Preface

This dissertation is submitted for the degree of Doctor of Philosophy at the University of Cambridge. The research described in this dissertation was conducted under the supervision of Dr H. K. D. H. Bhadeshia in the Department of Materials Science and Metallurgy, Cambridge, between October 1995 and September 1998. This work is to the best of my knowledge original, except where acknowledgement and reference is made to previous work. Neither this, nor any substantially similar dissertation has been or is being submitted for any degree, diploma or other qualification at this, or any other, university. This dissertation contains less than 60,000 words.

Parts of this work are published in the conference proceedings of the 5th International Conference on Trends in Welding Research, Atlanta, Georgia, USA, 1998 (in press).

Work detailed within Chapter 5 was awarded the *1998 International Institute of Welding Henry Granjon Prize* in Category B.

Michael Lord

March 1999

Acknowledgements

I would like to dedicate this work to my parents and sister for their love and support.

Abstract

Ultra–high strength steel weld deposits are currently produced using low carbon levels (<0.1 wt%) and significant additions of Mn, Cr, Si and Ni. These materials combine high strength (>700 MPa) with good toughness properties. The purpose of the work presented in this thesis was to investigate the means by which such properties are produced with a view to designing superior welds.

The microstructures of this class of weld were found to contain fine–plates of ferrite and occasionally martensite, separated by films of retained austenite with virtually no carbides. A series of welds, based on a commercially available electrode, was produced and tested to investigate the effect of compositional variations upon mechanical properties. Reductions in carbon and alteration of manganese, nickel and chromium levels in this series produced many interesting results but did not deliver significant improvements in strength. Neural network modelling, metallurgical interpretation and dilatometry revealed the cause of the often observed strength variations in such welds, found to be attributable to insufficient control of the interpass temperature. This was subsequently proved in careful experiments.

A model developed for estimating the strength of steels containing mixed microstructures of bainite and martensite was investigated in the context of these welds. This model considers the linear summation of strengthening effects resulting in an estimate of yield stress. Great discrepancies were found between predictions and measured strengths. The cause of such discrepancies was investigated using long tempering treatments to remove the microstructure. These experiments showed that the solid solution aspect of the strengthening model was not at fault. Much improved results were obtained by more correctly calculating the effect of the fine scale microstructure due to the realisation that the dislocation density and carbon content of bainite and martensite are not separable in the model.

A novel weld microstructure comprising predominantly bainite plates separated by austenite films was produced having a higher carbon content and high levels of silicon (≈ 1.6 wt%) to prevent carbide formation. Tests indicated rival strength but inferior toughness. Studies were performed into the role of the austenite films in such an alloy

and their resistance to carbide precipitation. The 'as–welded' microstructures showed no decomposition as a result of the welding process. Tempering of 1 h at 500 °C was necessary to promote notable decomposition into carbides, later identified as cementite with electron diffraction.

Modifications to thermodynamic data used in conjunction with thermodynamic modelling software allowed calculation for the first time of the effect of silicon additions on the paraequilibrium Fe-Si-C phase diagram. Silicon was found to greatly increase the extent of the single phase (austenite) field under paraequilibrium conditions thus retarding or preventing the precipitation of cementite by this mechanism. Comparison with experimental data showed that the number of paraequilibrium carbides and their tempering resistance in an alloy can be explained in terms of the distance from the calculated paraequilibrium single phase boundary. Hence an upper bound in preventing paraequilibrium precipitation can now be evaluated in terms of temperature or composition.

The production of a weld containing significant levels of Cu provided much interest as considerable strengthening resulted. A model was produced as a first step to predicting the complicated precipitation strengthening phenomenon in welds. This model considers the effects of nucleation, growth and coarsening of ε–Cu particles in a ferrite matrix as a function of composition, time and temperature. Varying agreement was found between predictions and experimental data from Fe–Cu alloys. However, trends were correctly modelled and a reason for the discrepancies highlighted, allowing possible further development and application to HSLA steels and weld alloys.

A number of new welds were designed and tested with the aid of thermodynamic modelling software and the results of experiments. In the conventional welds, tungsten was found to have a strong solid solution strengthening effect but toughness was reduced. However, superior results were produced by an increase in nickel partly at the expense of manganese.

In the novel bainitic weld, a composition containing half the previous level of silicon was found to have similar properties indicating that very high silicon levels are not required. Attempts were made at improving the experimental weld by reducing silicon levels and increasing the extent of the bainite reaction using cobalt whilst reducing the hardenability. A reduction in the level of silicon was not detrimental to mechanical properties although a reduction in hardenability was thought to have caused some reduction in strength.

Contents

Nomenclature List

α	low temperature ferrite
α'	martensite
α_1	one-dimensional parabolic rate constant
α_3	three-dimensional parabolic rate constant
γ	austenite
γ_1	angle between the normal to an interface and a dislocation in medium 1
γ_2	angle between the normal to an interface and a dislocation in medium 2
γ_p	surface free energy of precipitate / matrix interface ($\mathrm{J\,m^{-2}}$)
δ	high temperature ferrite
Δ	carbide particle spacing (m)
ΔG	critical free energy change due to capillarity ($\mathrm{J\,mol^{-1}}$)
ΔG_c	critical free energy change for nucleation (J)
ΔG_v	volume free energy change on nucleating a second phase ($\mathrm{J\,m^{-3}}$)
Δg_a	activation energy for solute transfer across interface (J)
ε	pure copper phase
ϵ_l	bainite / martensite lath width (μm)
ζ	Avrami type tempering function describing martensite
η	weld arc transfer efficiency
θ	angle between Burgers vector and dislocation line vector
θ_1	angle between dislocation line vector and the normal to an interface in medium 1
θ_2	angle between dislocation line vector and the normal to an interface in medium 2
κ	thermal conductivity ($\mathrm{J\,m^{-1}\,s^{-1}\,K^{-1}}$)
$\mu^{\mathrm{A}}_{\mathrm{eqm},\alpha,\beta}$	chemical potential of component A in α evaluated at composition x^{α}_{eqm}
$\mu^{\mathrm{B}}_{\mathrm{eqm},\alpha,\beta}$	chemical potential of component B in α evaluated at composition x^{α}_{eqm}
$\mu^{\mathrm{A}}_{\alpha}$	chemical potential of component A in α evaluated at composition $\bar{x}$
$\mu^{\mathrm{B}}_{\alpha}$	chemical potential of component B in α evaluated at composition $\bar{x}$
ν	Poisson's ratio
ξ	coordinate measuring translation of heat source (m)

ρ_D	dislocation density ($\mathrm{m^{-2}}$)
σ	general term for yield strength (MPa)
σ	interfacial energy ($\mathrm{J\,m^{-2}}$)
σ_α	yield strength of allotriomorphic ferrite (MPa)
σ_γ	yield strength of austenite (MPa)
σ_θ	yield strength contribution from cementite precipitates (MPa)
σ_ρ	yield strength contribution from dislocations (MPa)
σ_a	yield strength of acicular ferrite (MPa)
σ_B	yield strength of constrained bainite (MPa)
σ_B'	yield strength of unconstrained bainite (MPa)
σ_c	yield strength contribution from dissolved carbon (MPa)
σ_{Fe}	yield strength in tension or pure ferrite lattice (MPa)
σ_G	yield strength contribution due to ferrite lath size (MPa)
σ_m	yield strength contribution from microstructure (MPa)
σ_M	yield strength of untempered martensite (MPa)
σ_{Meq}	yield strength of martensite containing equilibrium ferrite carbon concentration (MPa)
σ_{MT}	yield strength of tempered martensite (MPa)
σ_{ss}	yield strength contribution from substitutional solutes (MPa)
$\sigma_{ss,Cu}$	yield strength contribution in ferrite from dissolved copper (MPa)
σ_w	yield strength of Widmanstätten ferrite (MPa)
σ_y	yield strength in tension (MPa)
τ	shear stress applied on a slip plane (MPa)
τ_c	critical shear stress required on a slip plane to allow for dislocation passage (MPa)
ϕ	angle between straight sections of dislocation on opposite sides of a precipitate (rad)
ϕ'	180-ϕ (rad)
ϕ_c	critical angle for dislocation passage (rad)
χ	angle between interface normal and matrix dislocation line vector in the cubic precipitate approximation
Ω	function describing atomic bonds ($\mathrm{J\,mol^{-1}}$)
a	thermal diffusivity ($\mathrm{m^2\,s^{-1}}$)
Ac_1	$\gamma + \alpha/\alpha+$ Fe$_3$C phase boundary during heating
Ac_3	$\gamma/\gamma + \alpha$ during heating
Ae_1	equilibrium $\gamma + \alpha/\alpha+$ Fe$_3$C phase boundary
Ae_3	equilibrium $\gamma/\gamma + \alpha$ phase boundary
at%	atomic%
b	Burgers vector

bcc	abbreviation for 'body-centred cubic'
bct	abbreviation for 'body-centred tetragonal'
$\bar{c}$	alloy average carbon concentration (wt%)
c_γ	carbon concentration in austenite (wt%)
c_0	bulk solubility of solute in a matrix (mol m^{-3})
CE	carbon equivalent (wt%)
D	diffusivity of solute in the matrix (m^2 s^{-1})
d_p	bainite / martensite packet diamter (μm)
E	dislocation line tension ignoring the effect of θ (J m^{-1})
$E(\theta)$	dislocation elastic energy per unit length (J m^{-1})
E_1	dislocation elastic energy per unit length in medium 1 (J m^{-1})
E_2	dislocation elastic energy per unit length in medium 2 (J m^{-1})
F	force on a dislocation due to a precipitate particle (N)
fcc	abbreviation for 'face-centred cubic'
G	shear modulus (MPa)
G^α	free energy of α phase
G^ε	free energy of ε phase
h	Planck constant (6.626 $\times 10^{-34}$J s)
H	Vickers hardness (MPa)
H_v	Vickers hardness (kgf mm^{-2})
$^\nu I$	homogeneous nucelation rate per unit volume (m^{-3} s^{-1})
k	function used within $\zeta(t)$
k_B	Boltzmann constant (1.380 $\times 10^{-23}$ J K^{-1})
L	distance between obstacles (m)
$\bar{L}_3$	mean lineal intercept (μm)
l	half the side length of precipitate approximated as a cube (m)
$\bar{M}$	similar to $\bar{L}_3$ but considering both lath and packet diameters (μm)
M_s	martensite start temperature
M_s^o	M_s for martensite with a carbon content of $\bar{x}$
$^\nu N$	homogeneous nucleation site density (m^{-3})
n	number of moles of atoms in a particle (mol)
n_∞	far–field concentration of solute
n_1	solute composition in the matrix in equilibrium with the precipitate
n_0	solute composition in the precipitate in equilibrium with the matrix
n_s	number density of particles on a slip plane (m^{-2})
P	point source energy input rate (J s^{-1})
Q	weld heat input (J m^{-1})

$\bar{r}$	average particle radius (m)
R	universal molar gas constant ($8.314\,\mathrm{J\,mol\,K^{-1}}$)
R_0	outer cut–off radius for dislocation energy evaluation (m)
r	radius of curvature of a dislocation (m)
r	polar coordinate with respect to point heat source (m)
$\bar{r}$	average radius of particles in a system (m)
r_0	dislocation inner core radius (m)
S	radius of spherical precipitate (m)
S_v	grain boundary surface area per unit volume ($\mathrm{m^{-1}}$)
t	time (s)
t_1	tempering time (h)
T	absolute temperature (K)
T_0	temperature at which austenite and ferrite of the same composition have identical free energy (K)
T_0	far field temperature (K)
T_0'	T_0 temperature but allowing for $\approx 400\,\mathrm{J\,mol^{-1}}$ stored energy
T_{eqm}	equilibrium transformation temperature (K)
T_i	weld interpass temperature (K)
v	velocity of point heat source ($\mathrm{m\,s^{-1}}$)
V_1	minimum cooling rate at $700\,^{\circ}\mathrm{C}$ giving 100% martensite ($^{\circ}\mathrm{C\,h^{-1}}$)
V_α	volume fraction of allotriomorphic ferrite
V_β	molar volume of β phase ($\mathrm{m^3\,mol^{-1}}$)
V_θ	volume fraction of cementite
V_a	volume fraction of acicular ferrite
V_b	volume fraction of bainite
V_m	volume fraction of martensite
V_p	molar volume of precipitate ($\mathrm{m^3\,mol^{-1}}$)
V_w	volume fraction of Widmanstätten ferrite
wt%	weight%
x	carbon concentration (wt%)
x^α	atomic fraction of Cu in α
$\bar{x}$	alloy average atomic fraction of carbon
x_γ	atomic fraction of carbon in austenite
x_b	atomic fraction of carbon in bainite
$x^{\alpha\beta}$	atomic fraction of solute in α in equilibrium with β
$x^{\beta\alpha}$	atomic fraction of solute in β in equilibrium with α
x_{ss}^α	initial atomic fraction of Cu in supersaturated α

x^{α}_{eqm} atomic fraction of Cu in α in equilibrium with β

x^{β}_{eqm} atomic fraction of Cu in β in equilibrium with α

$x^{\alpha}_{S,eqm}$ atomic fraction of Cu in α in equilibrium with β taking into account capillarity

$x^{\beta}_{S,eqm}$ atomic fraction of Cu in β in equilibrium with α taking into account capillarity

Chapter 1

Introduction

Steel is arguably the world's most useful material. It is found in thousands of applications from the superstructure of oil platforms to the simple paper clip. World annual production of iron and steel is approximately one billion tonnes, second only to concrete and two orders of magnitude greater than that of aluminium or of all the other metals combined.

The success of steel is due to its incredible versatility and low production costs. This versatility is a consequence of the natural complexity of the iron–carbon alloy system. Alloying with other elements and using suitable mechanical and heat treatments it is possible to produce a range of steels with very diverse properties such as yield strengths ranging from 200 MPa to 5000 MPa.

In many applications, particularly those on a large scale, the formation of strong joints between steel components is essential. Welding is the most effective method of joining steel in that it forms a continuous joint, reducing the stress concentrations and corrosion problems associated with fasteners and allows the transfer of large loads between components.

Since its beginnings in the late 19th century research into welding technology has become increasingly active following the general trends in the steel industry. In the last 30 years great advances have been made due to microscopy and phase transformation theory. Despite scientific advances there is still a large emphasis upon the skill of the welder, automation of the process being particularly difficult in many cases.

Modern welds are produced with mechanical properties designed to match or exceed those of the components being joined. A great research effort is directed at improving weld mechanical properties, enhancing their reproducibility and ensuring safety to match the demands of modern design. Driving down the costs of the welding process is also desirable as for example approximately half of the cost of a new ship can be due to welding.

The scope of this project lies within the field of high–strength steel welds. These welds are required to join components in specialist applications many of which are involved with the marine industry. For example, submarine hulls are constructed from high strength steel, allowing operation at greater speeds and depths (Fig. 1.1). Typically, the hull sections are welded together manually.

Figure 1.1: A typical application — at 172 m long, the Russian Navy's latest Typhoon class nuclear submarines are the largest ever constructed [1].

As wrought steels have superior mechanical properties in comparison with welds, the improvement of welds is likely to remain the focus of much research. Many different processes can be used to weld steels, but manual metal arc (MMA) welding is still the most versatile, as it can be performed in confined spaces, in many positions using only one hand and requires only a simple portable power supply. This project involves the development of ultra–high strength weld metals, those with strengths in excess of 700 MPa, fabricated with the MMA process.

1.1   Aims of this work

The aim of this work was to further the understanding of ultra–high strength weld microstructures with a view to producing welds with superior mechanical properties. At the outset a series of welds was produced for study, based upon an electrode (OK75.78) known to have good strength and toughness properties, with an approximate composition:-

Fe–0.05 C–2 Mn–3 Ni–0.3 Si–0.4 Cr–0.6 Mo   (values in wt%)
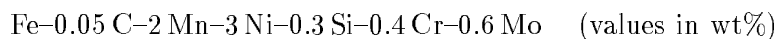
The compositions and microstructures of these welds were to be investigated and related to their mechanical properties. Drawing upon the results of such experiments it was hoped to design welds with improved mechanical properties. Additionally, there were some questions concerning the reproducibility of the tensile properties of such welds and it was hoped to both highlight the cause and provide a solution.

A further aim was to use modelling techniques in conjunction with experimental data. Specifically, it was hoped to further the development of a physical model currently used for predicting tensile properties by comparison with data from appropriate experiments. Models were also considered a valuable research tool and were to be used in the interpretation of data.

As another major aim of this project it was intended to produce and investigate a new class of high–strength weld microstructure based on carbide–free bainite. Such a microstructure has never been used in welds but could provide strong competition to the more conventional lower–carbon alloys. In a similar manner, microscopy and mechanical testing experiments were planned with a view to producing further improved welds.

A final aim was the novel consideration of using copper to precipitation strengthen high–strength welds. The focus here was to be upon modelling as a first step towards the incorporation of such a model into a more general tensile properties model.

Chapter 2

Formation of Weld Microstructures

2.1 Introduction

Fusion welding of steel is of paramount importance in the fabrication of engineering structures. It can be achieved using a variety of techniques but fundamentally they all involve the deposition of a small amount of liquid steel in a gap between components.

This project involves welds fabricated using the manual metal arc (MMA) process (also called shielded metal arc welding or SMAW) in which an electric arc is struck between an electrode and the work piece, the electrode containing not only the metal required to fill the joint but also compounds to control the arc, generate a suitable protective slag and to generate a gas shroud to protect the weld pool from the atmosphere (Fig. 2.1). Electrode technology is therefore complicated but it nevertheless provides an elegant simplicity to the process, requiring in addition only a suitable power supply.

2.1.1 MMA electrodes

An MMA electrode comprises a central metallic core surrounded by a complex coating. The core wire is usually made of mild steel, alloying additions found in the final weld deposit coming from powders such as ferrosilicon and ferromanganese, added to the coating. There are four main types of coating, basic, cellulosic, rutile and acid, which in addition to metallic powders, contain various quantities of minerals such as rutile, fluorospar, quartz, carbonates and organic compounds including cellulose. Their choice is determined by the characteristics of the arc, the welding position and the type of weld produced.

4

a)

Electrode

Electrode
Holder

Power
Source

Work Piece

b)

Slag

Electrode

Gas Shroud

Electric Arc

Core Wire

Weld Pool

Weld Deposit
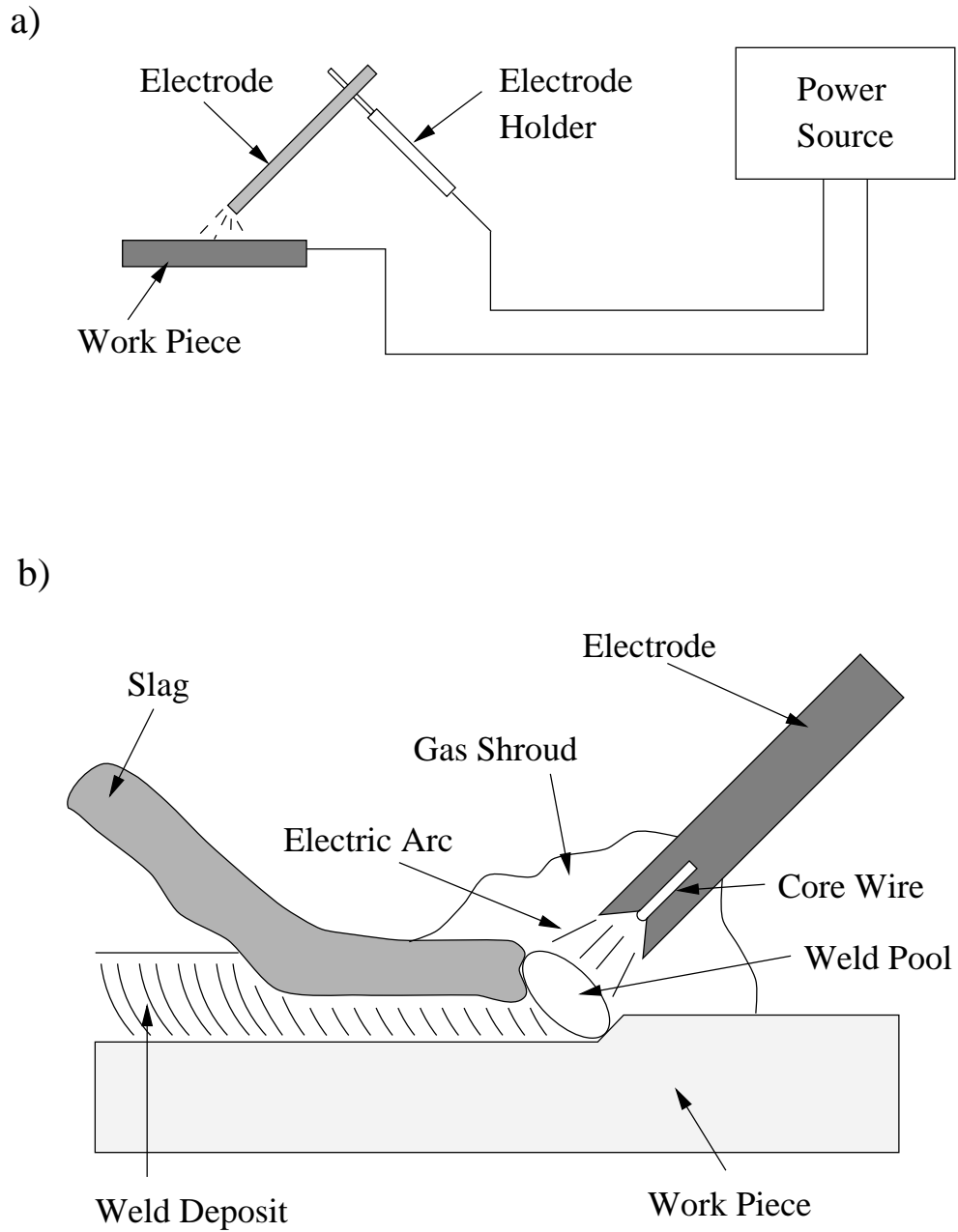
Work Piece

Figure 2.1: a) The principle of the MMA process and b) interaction of the electrode with the work piece.

The coatings form a cover slag which protects the hot metal from the atmosphere during cooling and provides physical support to the weld metal. The slag is effective in removing elements such as oxygen, sulphur and phosphorus from the weld pool.

Due to the high temperatures involved in the welding process it is necessary to protect the weld metal from environmental attack during fabrication. This is achieved using mineral fluxes or shrouds of inert gases such as CO_2. These measures are never fully effective and the oxygen content of welds is much higher than in wrought steels (Table 2.1). The oxygen is present in the form of oxides which become trapped as the weld solidifies. Elements such as manganese and silicon form manganese silicates and magnesium, zirconium, calcium and aluminium frequently form very stable oxides. Although the deoxidation process is efficient with an estimated 90% of oxygen removed prior to solidification [173], the remainder which is locked in non–metallic 'inclusions' can be detrimental to the toughness, although in some cases they may cause a favourable change in microstructure promoting acicular ferrite. However, oxygen is sometimes not found to have a significant effect upon the as–deposited microstructure [38, 39].

Table 2.1 also shows that the weld copper content is high as the electrode in this case had a copper coating to improve electrical contact. Weld metal silicon levels are also higher because silicon is used as a deoxidising element. The final composition of the weld metal thus has a complex dependency upon the compositions of the wire, the flux and the plate being welded.

	C	Mn	Si	Cu	Al	N	O
Plate	0.21	1.0	0.2	0.05	0.04	0.01	0.004
Wire	0.14	1.5	0.2	0.31	0.01	0.01	0.001
Weld	0.16	1.1	0.3	0.16	0.01	0.01	0.053

Table 2.1: A comparison of the chemical composition (wt%) of a submerged arc weld with that of the plate being welded, and the wire used as the consumable electrode.

2.1.2   The welded joint

Detailed examination of a welded joint reveals two distinctive regions, the 'fusion zone' and the 'heat affected zone' or HAZ (Fig. 2.2). The 'fusion zone' is a region in which both the deposited metal and metal melted during welding can be found. Adjacent to this lies the heat affected zone in which the microstructure of the unmelted metal in the welded components has undergone significant changes due to the influence of heat.
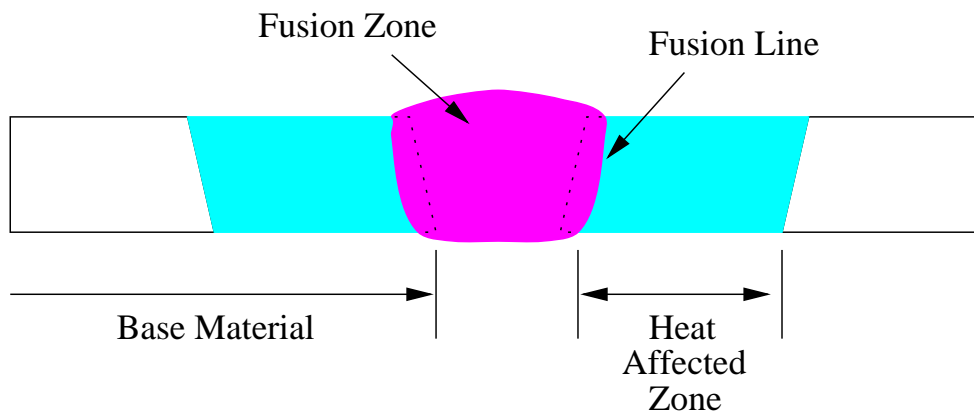
Figure 2.2: Definition of terms describing a welded joint.

This chapter and indeed this project is concerned primarily with the metallurgy of the fusion zone in steel welds. This includes solidification and subsequent solid–state phase transformations.

2.2 The fusion zone

2.2.1 Equilibrium phases of Steel

Pure iron is ferritic (δ) with a body–centred cubic lattice at temperatures just below the melting point (1534 °C). As it cools, the ferrite then transforms to austenite (γ), with a face–centred cubic lattice at 1390 °C. Further cooling to below 910 °C causes a transformation back to ferrite (α) which is the stable phase at all lower temperatures (Fig. 2.3). α and δ ferrite are identical in crystal structure but the latter symbol is used conventionally for the higher temperature form.

The strong influence of carbon upon this system is fundamental to the widespread use of steels. Carbon's atomic radius is only approximately 60% that of iron and consequently it enters both the ferrite and austenite lattices as an interstitial solute [89]. However, in either case the interstices are not large enough to accommodate carbon atoms without some local distortion. In the body–centred cubic ferrite lattice, tetrahedral and octahedral interstices exist, the latter being occupied preferentially despite their smaller size as this allows easier accommodation of strain. The austenite face–centred cubic lattice has larger interstices, reducing lattice strain, the important distinction being that the strain in austenite is isotropic whereas that in ferrite is tetragonal. In any case, although it is

7
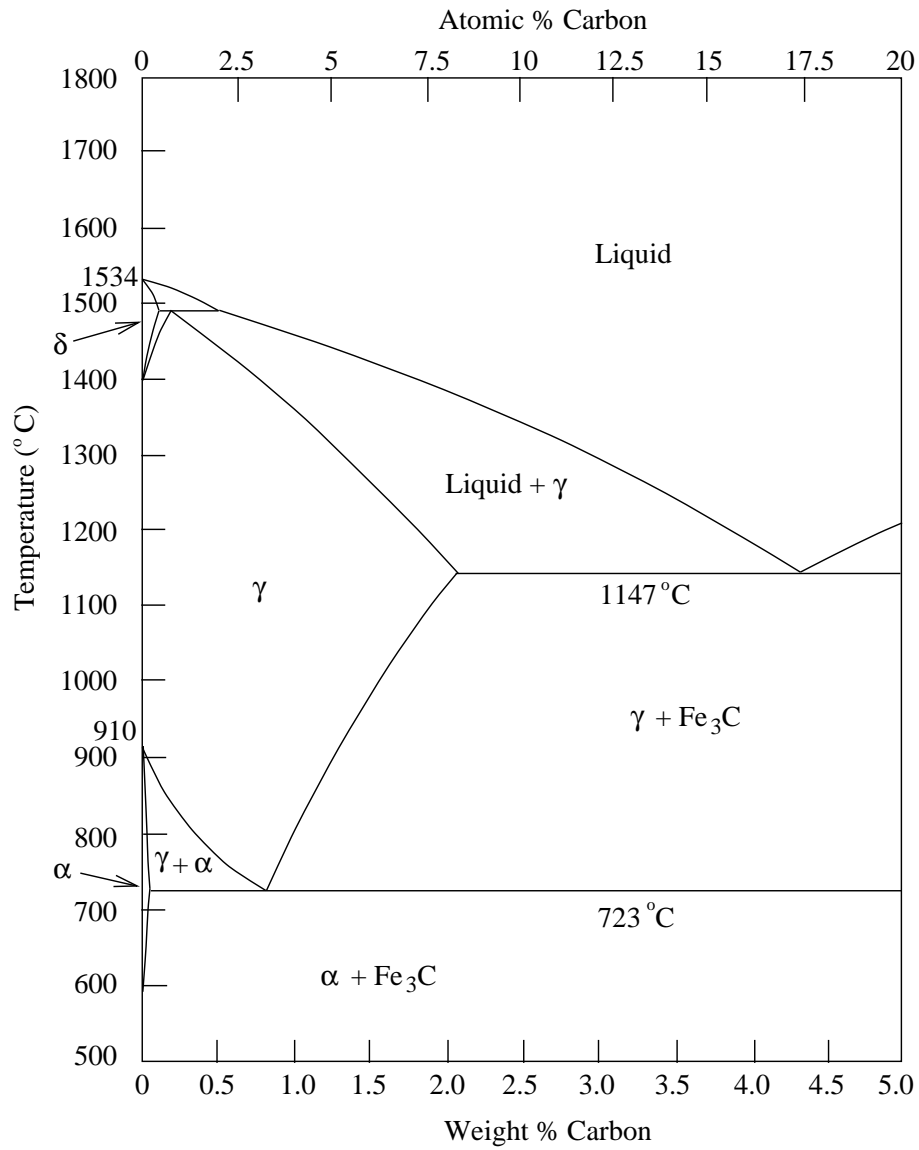
Figure 2.3: The Fe–rich end of the Fe–C equilibrium diagram. δ and α denote the high and low temperature ferrite stability fields respectively, whereas γ denotes austenite.

an oversimplification to discuss solubility purely in terms of size factors, austenite has a maximum carbon solubility of approximately 2 wt% in comparison with 0.02 wt% for ferrite (Fig. 2.3). The figure also indicates the presence of an iron carbide phase with fixed stoichiometry of Fe_3C. This iron carbide, cementite, is thermodynamically metastable but is nevertheless conventionally represented on the equilibrium diagram as it is almost always obtained rather than the equilibrium phase graphite for typical steel compositions (< 1.5 wt% C).

Solution treating a steel in the austenite phase field allows complete carbon dissolution. Subsequent cooling to ambient temperature, produces either a mixture of ferrite and precipitated iron carbide or a metastable supersaturated ferrite with a distorted lattice, depending upon the cooling rate. This transformation, its various mechanisms and the relative carbon solubilities in ferrite and austenite, produce the incredible range in the mechanical properties of steels.

The addition of small amounts of alloying elements to the iron produces similar phase changes but at modified temperatures. Unlike carbon, these elements are almost exclusively substitutional in that they take up similar positions as iron in the lattice. Common substantial additions to steels are silicon, manganese, nickel, molybdenum and chromium. These affect the free energies of the component phases and therefore can be used to control transformation behaviour. Both transition temperatures between phases and the sizes of phase stability fields are affected. A distinction is often made between elements that stabilize austenite such as C, Ni, Mn and those that stabilize ferrite such as Mo and Cr, termed austenite and ferrite stabilizers. Alloying has many other effects on properties particularly in terms of strength, toughness and corrosion resistance.

2.2.2   Weld Solidification

Many weld deposits begin their formation by solidifying as δ–ferrite. The solidification occurs epitaxially at the edge of the fusion zone and progresses inwards in a columnar manner along thermal gradients [38, 57, 157]. Grain selection occurs because those oriented with their <100> directions aligned with the direction of maximum heat flow stifle the growth of other grains. Hence the width of the columnar grains is observed to increase as a function of the distance from the fusion zone boundary.

It is possible to prevent the formation of the δ–ferrite phase by increasing the cooling rate, carbon content or levels of alloying additions such as manganese or nickel [63, 69]. In the majority of cases where the solidification product is δ–ferrite, austenite forms on the columnar δ–δ grain boundaries. The appearance of these columnar austenite grains is very similar to that of the original microstructure. The resultant size and shape of the austenite

grains affects all subsequent transformations since the number density of austenite grain boundary nucleation sites changes inversely with the grain size [89]. The morphology of the austenite grains can be idealized as long hexagonal prisms, typically around $100\,\mu$m wide and around 5 mm in length [38]. There are fewer grain junctions in such a structure in comparison with an equiaxed one and therefore the hardenability is larger than in an equivalent wrought alloy. In welds that solidify as austenite the grain size is expected to be larger than that formed by transformation from the δ–ferrite phase.

2.2.3   Solidification–Induced Segregation

Solidification produces inhomogeneities in the resultant microstructure. This chemical segregation occurs in welds due to their high cooling rates and fluctuations in process parameters [33]. The effects of the latter are extremely difficult to predict but some estimate of segregation due to non–equilibrium solidification can be made. This is based upon the partition coefficient κ_i which is simply the ratio of the solute element in the solid phase to that of the liquid [147]. Diffusion is assumed not to have time to occur during solidification with the exception of interstitial solutes such as carbon and consequently the solid phase does not contain a homogeneous solute distribution. This affects later transformations as regions low in solute content will transform at higher temperatures. Chemical segregation is not desirable as it causes localised variations in the microstructure and properties which are difficult to predict.

2.2.4   The as–deposited microstructure

The microstructure which forms as a steel weld cools from the liquid phase to ambient temperature is called the 'as–deposited' or 'primary' microstructure. In general allotriomorphic, acicular and Widmanstätten ferrite form the majority of this microstructure (Fig. 2.4). In the case of strong welds ($\approx 400\,$MPa) acicular ferrite and even martensite may be dominant. Small amounts of degenerate pearlite, retained austenite and martensite are also observed which are collectively termed 'microphases'. Acicular ferrite is common in welds because of the non–metallic inclusions which provide intragranular nucleation sites.

2.2.5   Allotriomorphic ferrite

Allotriomorphic ferrite is the first phase to form on slow cooling of the austenite grains below the Ae_3 temperature (Fig. 2.5) [48, 120].
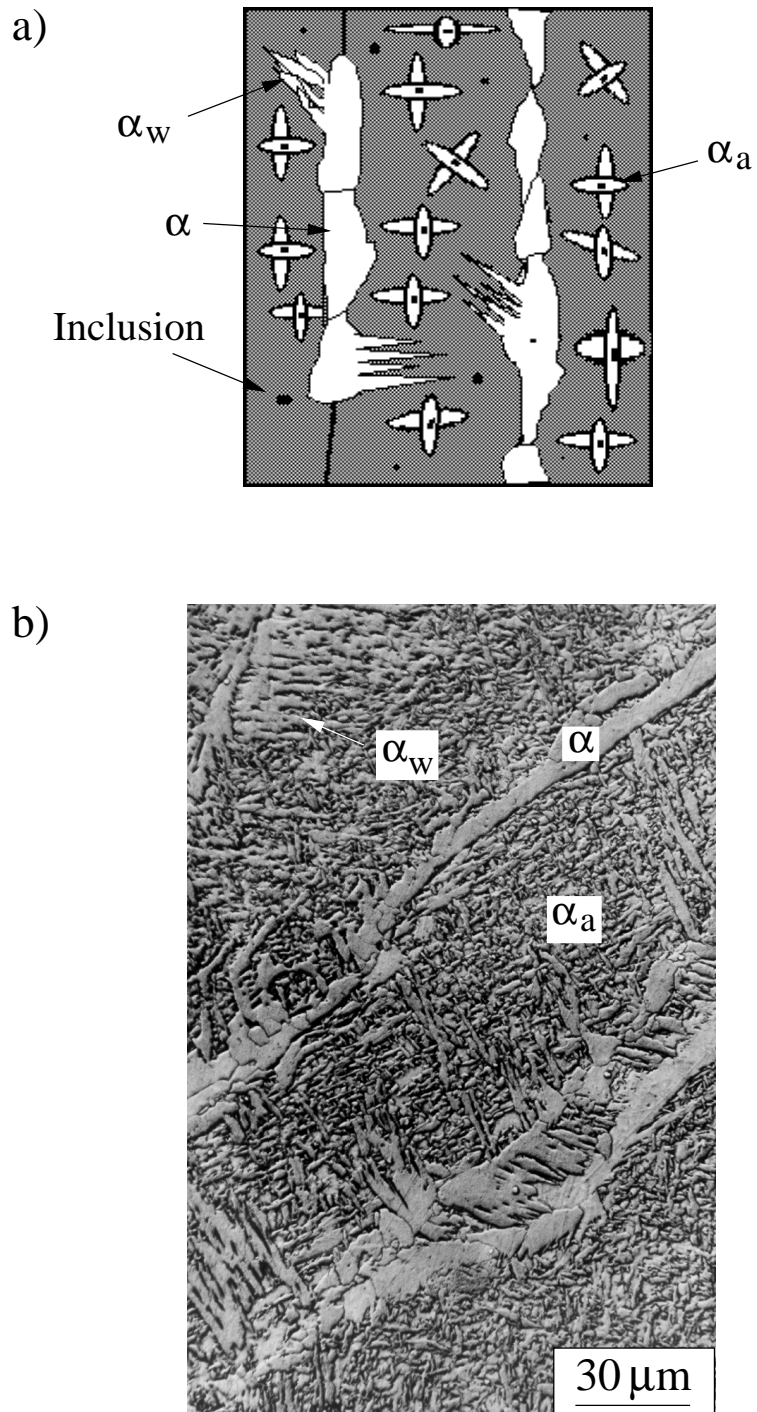
Figure 2.4: a) Illustration of the morphology of allotriomorphic (α), acicular (α_a) and Widmanstätten ferrite (α_W) and b) scanning electron micrograph of a weld microstructure [149].
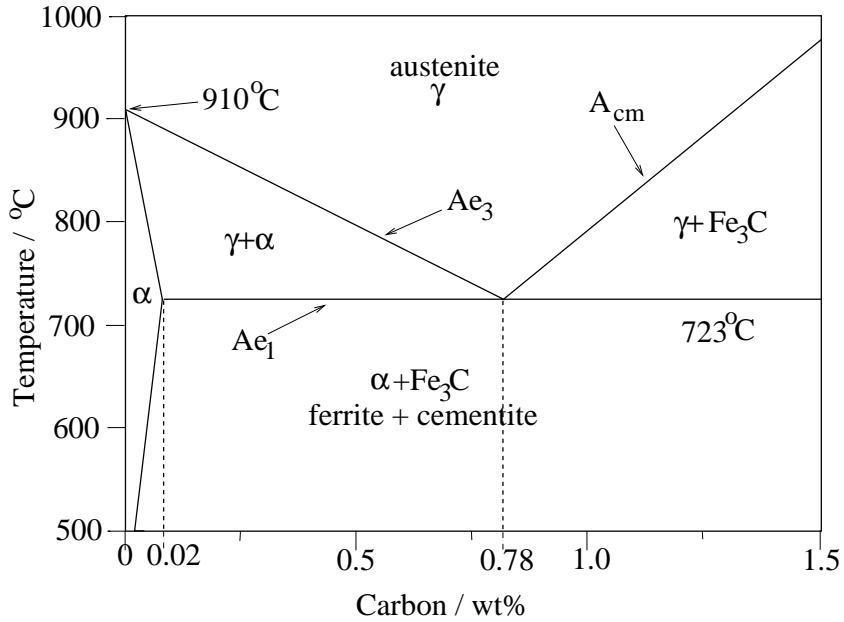
Figure 2.5: Schematic Fe–C equilibrium diagram at low carbon concentration.

Nucleation occurs at the columnar austenite grain boundaries which become decorated with thin layers of ferrite that thicken at a rate controlled by the diffusion of carbon in the austenite ahead of the advancing interface [12, 40]. Under isothermal conditions the thickness of the ferrite, S changes parabolically as a function of time, t [203]:-

$$S = \alpha_1 t^{\frac{1}{2}} \tag{2.1}$$

where α_1 is called the one–dimensional parabolic rate constant and takes the form:-

$$\alpha_1 \approx 2^{1/2} \left\{ \frac{\bar{x} - x^{\alpha\gamma}}{x^{\gamma\alpha} - x^{\alpha\gamma}} \right\}^{1/2} \tag{2.2}$$

where $x^{\gamma\alpha}$ is the solute concentration in the ferrite in equilibrium with the austenite and $x^{\alpha\gamma}$ the corresponding concentration in the austenite. $\bar{x}$ is the solute composition of the austenite far from the interface.

In this approximation an assumption is made that the solute concentration rises linearly from $x^{\alpha\gamma}$ to $\bar{x}$ as a function of distance into the austenite ahead of the interface (Fig. 2.6).

The high cooling rates found in welds do not allow transformation to ferrite under equilibrium conditions [45]. However, the transformation under 'paraequilibrium' conditions is possible, in which the partitioning of substitutional solute atoms does not have

12
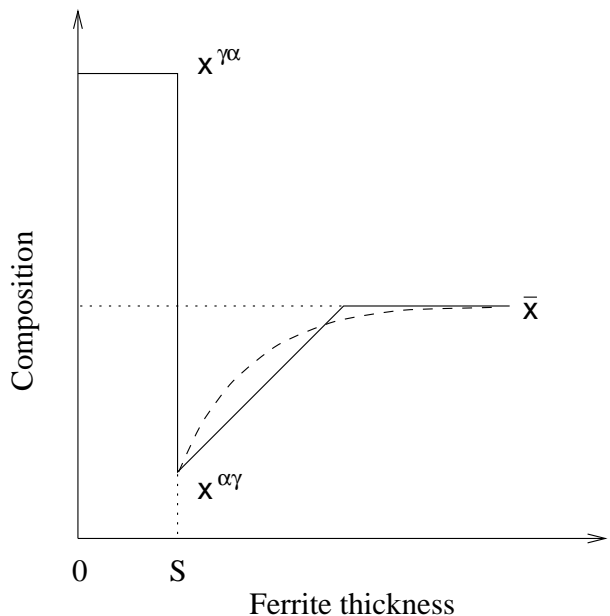
Figure 2.6: Actual (dashed curve) and approximate (solid curve) carbon concentration profiles ahead of the α–γ interface.

time to occur [5]. Paraequilibrium is a kinetically constrained equilibrium in which the adjoining phases have identical X/Fe atom ratios, where X represents substitutional solute elements. The substitutional lattice is configurationally frozen but the greater diffusivity of interstitial solutes such as carbon allows them to partition and attain equilibration of chemical potential in both phases. Substantial undercoolings are required to produce paraequilibrium transformations avoiding a mechanism involving the diffusion of sluggish substitutional solutes.

The growth of allotriomorphic ferrite in welds is therefore controlled by the diffusion of carbon. Hence the values $\bar{x}$, $x^{\alpha\gamma}$ and $x^{\gamma\alpha}$ in Eqn. 2.2 refer to carbon concentrations. It can be seen from Eqn. 2.2 that carbon levels only slightly in excess of the solubility limit in ferrite $x^{\alpha\gamma}$ will cause large variations in the rate constant α_1 (Fig. 2.7). Such low carbon levels are typically used in welding applications.

In welding, transformations are not even approximately isothermal, but nevertheless, because nucleation is often not rate limiting, the fraction of allotriomorphic ferrite obtained correlates directly with the parabolic rate constant [37].

Eqn. 2.2 also shows that the growth rate slows as transformation proceeds. This is because the distance over which carbon has to diffuse increases with time. The growth rate for a given alloy goes through a maximum as a function of temperature, because the driving force for transformation increases with undercooling whereas the diffusivity decreases.

2.2.6 Lower temperature transformations

As the weld cools to temperatures less than about 600 °C, the reconstructive growth of ferrite becomes sluggish and consequently the layers of allotriomorphic ferrite reach a limiting thickness. At this point displacive transformation mechanisms become kinetically (though not thermodynamically) favoured. Widmanstätten ferrite, bainite and acicular ferrite form by the co–ordinated movement of iron and substitutional atoms and hence can occur at lower temperatures. Figure 2.8 shows a mechanism by which the austenite can transform to ferrite without the need for large movements of atoms. Considering two adjacent face–centred cubic (fcc) cells of austenite, a body–centred tetragonal (bct) cell of austenite can be defined within the same structure as shown in Fig. 2.8, in which some lattice points have been removed for clarity. Transformation to a body–centred cubic (bcc) ferrite lattice can then be achieved by expansion along the a_{bct} directions, accompanied by a contraction along c_{bct}. This is known as the Bain Strain. No diffusion is required by this mechanism but in a constrained system further deformation is required to ensure a minimisation in strain energy. The observed *macroscopic* shear is therefore not the one described by the Bain Strain, but is rather an invariant–plane strain (IPS) in which the homogeneous lattice deformation required to convert the parent lattice into the product is coupled with a inhomogeneous lattice–invariant deformation. This latter deformation leaves the respective unit cells unchanged but macroscopically produces the correct structure. The resultant strain energy with this mechanism is still considerable and sufficient driving force is required to enable it to become feasible. Such a driving force is provided by significant undercooling below the equilibrium transformation temperature.

2.2.7 Widmanstätten Ferrite

At relatively low undercoolings plates of Widmanstätten ferrite form by a displacive paraequilibrium mechanism. Transformation of polished austenitic specimens to Widmanstätten ferrite causes surface relief indicative of a displacive mechanism often doubly tilted but occasionally singly tilted consistent with an IPS mechanism [195]. However, at such low undercoolings it has been shown that there is insufficient free energy available for the formation of a single plate by this mechanism [7]. Transformation involves co–operative growth of pairs of mutually accommodating plates reducing the strain energy involved to a value of around $50 \, \mathrm{J \, mol^{-1}}$ [27, 28] (Fig. 2.9). Carbon diffusion is still required during the formation of Widmanstätten ferrite but growth with a plate morphology prevents the build up of carbon ahead of the advancing interface. The carbon is accommodated at the sides of the advancing plate such that the plate tip always encounters fresh austenite in which to advance. Plate lengthening therefore occurs at a constant rate for this phase.
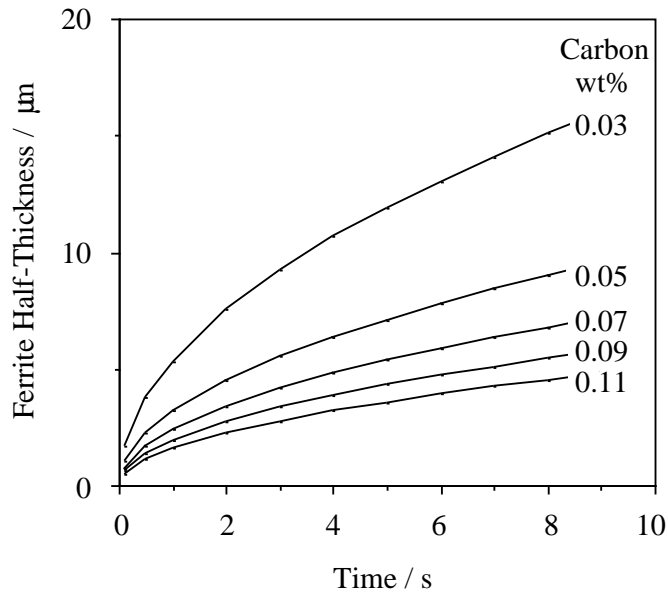
Figure 2.7: An illustration of the parabolic thickening of ferrite during isothermal transformation at 740 °C. Each curve represents a Fe-1Mn–C wt% steel with the carbon concentration as indicated.
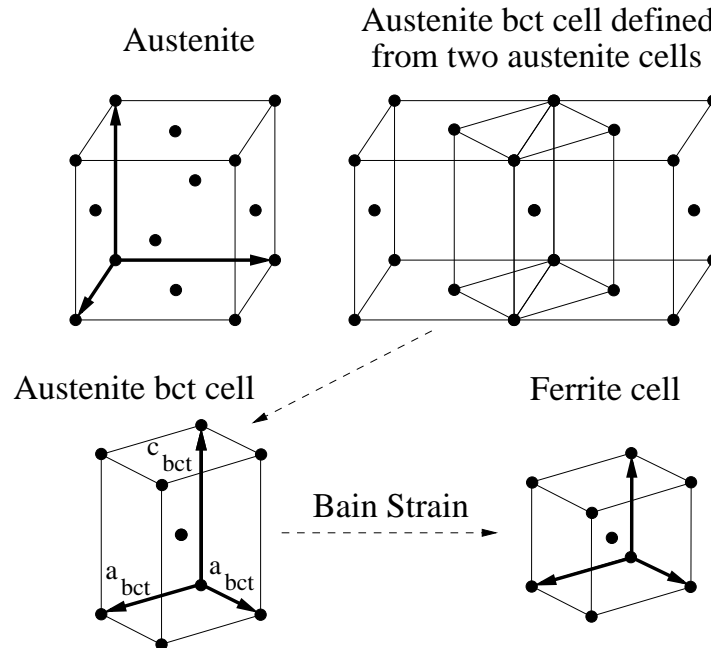
Figure 2.8: Illustration of the Bain deformation. "bct" denotes a body–centred tetragonal lattice. Note that some lattice points have been removed for clarity.
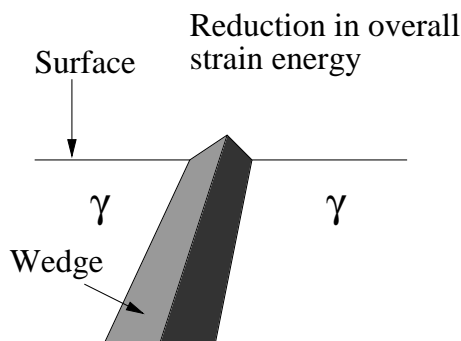
Figure 2.9: Typical Widmanstätten ferrite morphology showing mutually accommodating plates.

Measured growth rates are very large for most weld compositions such that the transformation is completed within a fraction of a second (Fig. 2.10) and is often considered to be essentially isothermal for this reason [33]. The growth rate is again strongly dependent upon the austenite carbon content at values close to the solubility limit in ferrite.

It might be thought that this reaction would complete the transformation processes within the weld. However, much less Widmanstätten ferrite forms than would be expected due to hard impingement with acicular ferrite plates growing towards the grain boundaries from their nucleation sites upon inclusions [33].

2.2.8   Bainite

Bainite is an interesting phase as its mechanism has been the cause of much debate. This centred upon the role of diffusion in the transformation, one side arguing strongly for a reconstructive mechanism, the other holding that it was a two stage reaction being displacive and diffusionless, followed by the later decarburisation of the ferrite by diffusion [2, 31, 32, 84, 108]. It is now clear that the bainite forms by a shear transformation. Repeated nucleation and growth of platelets collectively form larger aggregate structures known as sheaves (Fig. 2.11). The individual platelets are not resolvable by optical microscopy, the sheaves giving the appearance of thin wedges. Transmission electron microscopy reveals the individual sub–units. Sheaves macroscopically appear to grow by a lengthening and thickening process but this is misleading as it is actually due to the nucleation of platelets (sub–units) at the tips of and adjacent to those already present (also shown in Fig. 2.11). Nucleation appears to be favoured at the tips giving the overall impression of continuous growth of a sheaf [29].

The growth rate of bainite sheaves shows similar sensitivity to carbon concentration as
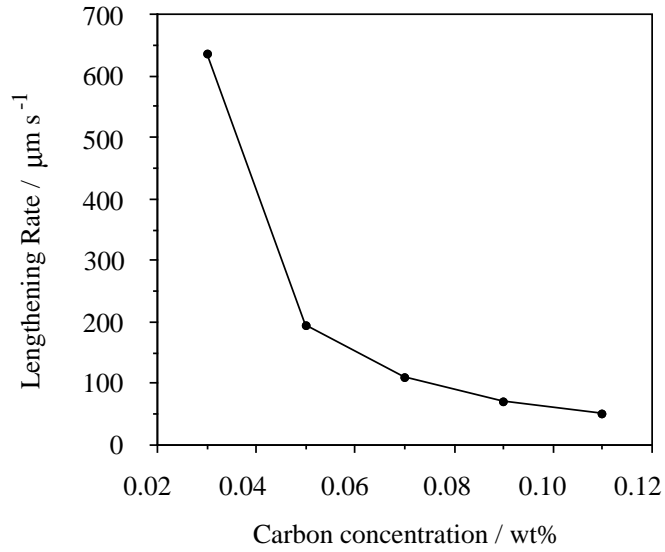
Figure 2.10: Sensitivity of Widmanstätten ferrite lengthening rate to carbon concentration in a Fe–1Mn–C wt% steel at 600 °C. Note the growth rate sensitivity at low carbon levels [33].
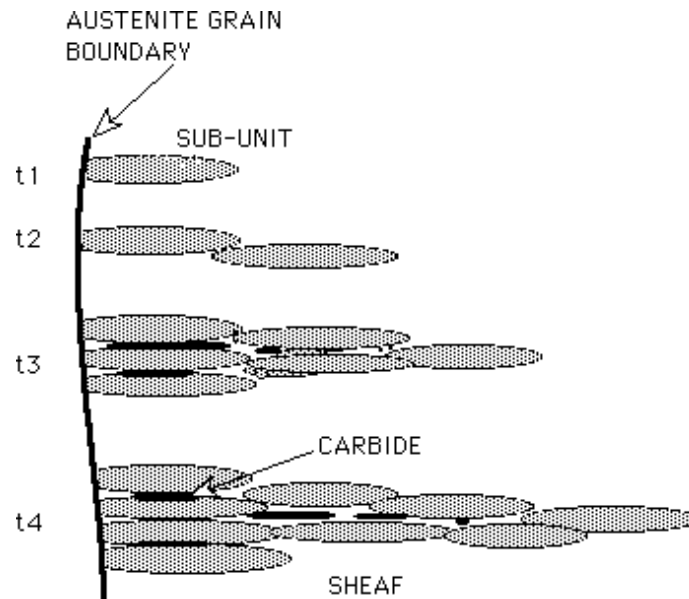
Figure 2.11: Schematic illustration of bainitic sheaves formed by sub–units of ferrite [25].

17

higher temperature phases (Fig. 2.12). However, the observed lengthening and thickening rates of sheaves have not as yet been adequately explained. Measurements have revealed approximately constant lengthening rates [83]. Thickening rates appear related to lengthening rates but this does not imply a dependence as thickening can be observed to continue after lengthening has stopped [83]. The growth rates of sub–units might be expected to occur at a rate limited by the velocity of sound propagation in steel, as is the case for some martensites. Measured growth rates are far less than this limiting velocity but still a number of orders of magnitude greater than diffusion controlled growth velocities. This is due to plastic deformation associated with the transformation.
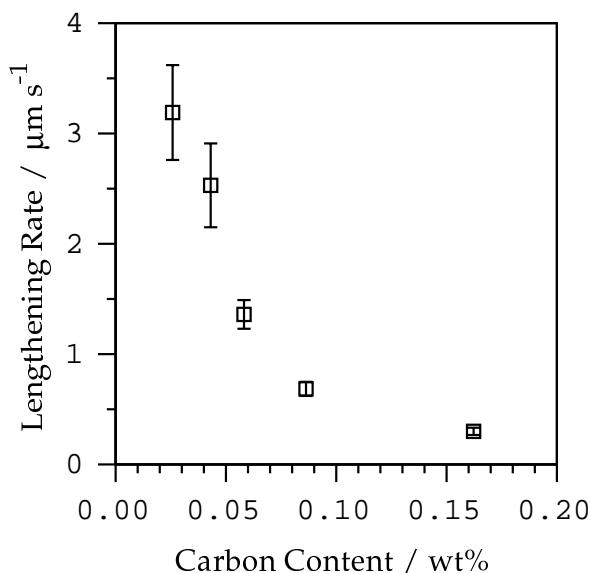
Figure 2.12: Dependency of bainite lengthening rate upon the carbon concentration in a Fe–10Ni–C wt% alloy at 400 °C [148].

The sub–units also form with a full supersaturation of carbon inherited from the austenite [31, 32]. The ferrite then decarburizes either by diffusion of carbon back into the austenite phase and/or by the precipitation of carbides within the ferrite. These two possibilities form the classical upper and lower bainite microstructures (Fig. 2.13).

In the case of upper bainite no carbides precipitate within the ferrite rather precipitating from the thin layers of austenite trapped between sub–units [114]. Upper bainite forms at higher transformation temperatures due to enhanced carbon diffusion. The carbon enriched austenite may then transform to a ferrite/carbide aggregate, transform to martensite or remain as retained austenite. Generally in upper bainite the precipitated carbide is cementite.

Lower bainite comprises two main kinds of carbides. Like upper bainite there is pre-
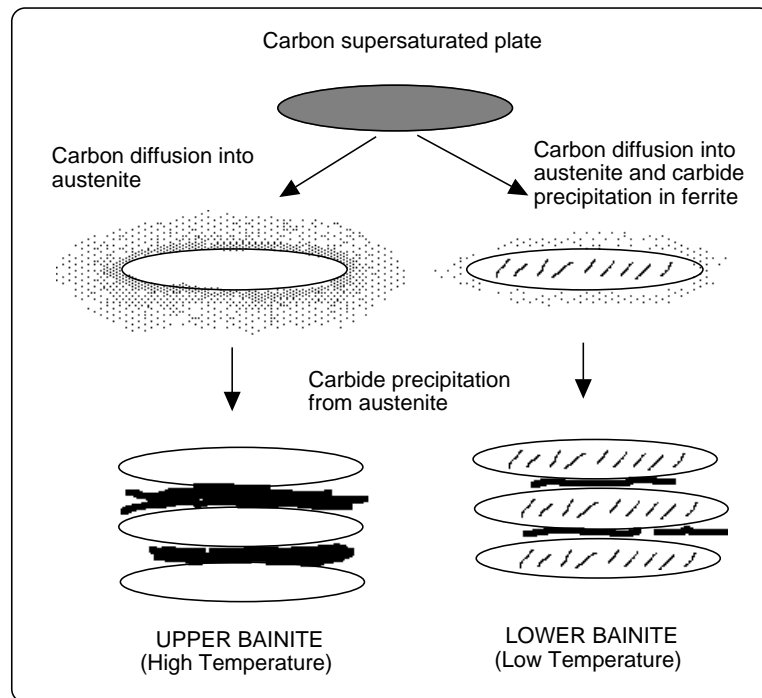
Figure 2.13: Schematic illustration of upper and lower bainite platelets [25].

cipitation of carbides between individual sub–units and in addition a fine dispersion of plate–like carbides can be found within the lenticular plates of ferrite. These carbides are generally either ϵ–carbide or cementite.

It has been suggested that the time taken to decarburize the ferrite in comparision with that required for precipitation within ferrite distinguishes between the two possibilities [176].

Calculations indicate that the strain energy due to the bainite reaction is around $400 \, \text{J mol}^{-1}$ [28], a corresponding value for martensite being $600 \, \text{J mol}^{-1}$ [55]. The smaller value for bainite reflects the smaller aspect ratios of platelets. Hence, transformation to bainite is prevented when insufficient driving force is available to overcome this strain term. Such conditions might arise from insufficient undercooling below the austenite phase boundary, Ae_3 (as shown earlier in Fig. 2.5) or due to the constraint that the carbon content of the ferrite cannot cannot be so high as to cause the free energy of ferrite to exceed that of austenite. The latter leads to the well documented *incomplete reaction phenomenon* in which the bainite reaction fails to go to completion due to enrichment of austenite during transformation (the phenomenon is more fully discussed in Chapter 7) [25, 109]. This is consistent with the theory describing a diffusionless first stage followed by later carbon partitioning. On the other hand a reconstructive transformation would be expected to continue until the austenite carbon content reached the paraequilibrium Ae_3 boundary. Thus a self–consistent picture is developing that bainite is the product of a displacive invariant–plane strain transformation involving an initial diffusionless stage followed by the partitioning of carbon.

Bainitic microstructures are found in applications where high strength and toughness are required. For example, weld deposits containing bainite are common in power plant applications as this microstructure is quite temper resistant.

2.2.9   Acicular Ferrite

'Acicular ferrite' is a phase most commonly found due to austenite transformation in low alloy steel weld deposits [34, 76]. It is prominent in welds as it nucleates on non–metallic inclusions which are far less common in wrought steels [100]. However, acicular ferrite can be formed in such steels by deliberate inoculation with non–metallic inclusions [133]. The term 'acicular' means shaped and pointed like a needle but this is really a misnomer derived from its appearance in two–dimensional microscopy sections (Fig. 2.14). The true three–dimensional morphology is thought to be that of thin, lenticular plates that are arranged in an interlocking pattern [33, 59]. Random planar sections reveal typical plate

lengths of $\approx 10\,\mu$m and widths of $\approx 1\,\mu$m and consequently the true aspect ratio is likely to be much smaller than 0.1.
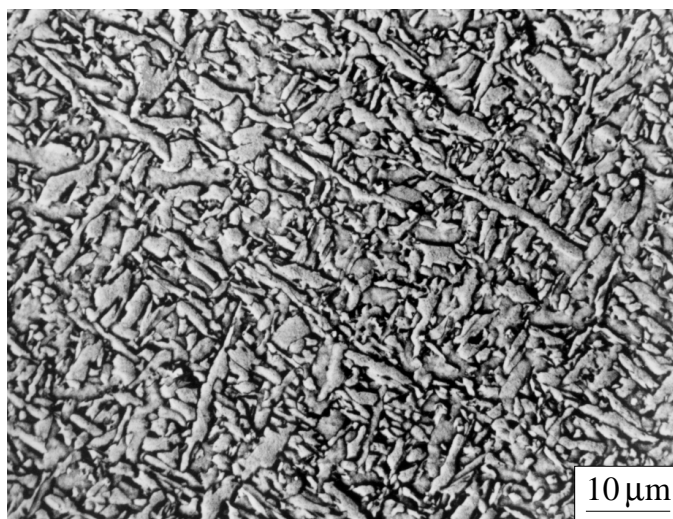
Figure 2.14: Morphology of acicular ferrite [149].

Weld deposits are well known to contain large prior–austenite grains, reducing the grain boundary area available for intergranular nucleation of bainite. As acicular ferrite nucleates intragranularly in direct competition with bainite the promotion of one phase at the expense of the other should be possible by control of the austenite grain size (Fig. 2.15). This has been demonstrated elegantly by reaustenitizing weld microstructures at low and high temperatures, the latter promoting larger grains [198]. Alternatively, vacuum remelting of a weld deposit that originally transformed to acicular ferrite under similar heating conditions has been shown to promote bainite by removal of inclusions [81].

Acicular ferrite shows similar relief on polished surfaces due to the transformation and this is consistent with an IPS shape change [171]. Microanalysis experiments also indicate that there is no bulk partitioning of substitutional alloying elements during transformation [171]. Acicular ferrite exhibits a high dislocation density and measurements indicate the stored energy has a similar value to that of bainite at $\approx 400\,\mathrm{J\,mol^{-1}}$ [171, 199]. There are further similarities with bainite as upper and lower variants of acicular ferrite can be promoted by adjusting the weld chemistry [168]. The lower variant was only observed recently (1989) as high carbon levels are required whereas they are usually kept low in welds to prevent formation of high–carbon martensite. An important characteristic of bainite is the 'incomplete reaction phenomenon' [25] where the degree of reaction tends to zero as the transformation temperature approaches the bainite start temperature; this is also observed in acicular ferrite [25, 171, 199]. Bainite nucleates on γ–γ grain surfaces and continues to grow by repeated formation of sub–units to generate the classical sheaf

morphology [198]. This morphology is not found in acicular ferrite and this is possibly due to hard impingement as independent nucleation upon inclusions must by necessity occur in a localised area. However, secondary nucleation upon previously transformed regions is also common, increasing the number of possible nucleation sites.

There is strong evidence therefore that the mechanisms of transformation to acicular ferrite or bainite are identical, the only difference being that the former nucleates on inclusions.

Some recent work has argued that acicular ferrite in some cases may comprise intra-granularly nucleated Widmanstätten ferrite rather than bainite [182] which can be easily distinguished, the scale of the former being much larger. Transmission electron microscopy should reveal two mutually accommodating plates if Widmanstätten ferrite is present and it may be necessary to make the distinction between this intragranularly nucleated Wid-manstätten ferrite and acicular ferrite as their transformation mechanisms are different. Conventional acicular ferrite will remain the superior microstructure in terms of properties due to its finer scale.

The fine chaotic nature of the acicular ferrite microstructure is ideal for mechanical properties as it imparts great strength to the material whilst exhibiting good toughness levels by presenting a tortuous path to cracks [101].

2.2.10 Martensite

Martensite is formed by a diffusionless transformation in steel and occurs when there is sufficient driving force to cause diffusionless nucleation and growth. Martenite forms with a plate morphology that can extend across austenite grains. However, spanning of austenite grain boundaries cannot occur without separate nucleation in the adjacent grain. Austenite is retained between the plates in a similar manner to bainite and surface relief is also observable due to the invariant plane strain transformation. Transformation velocities can be of the order of the speed of sound in austenite which far exceeds diffusional velocities therefore trapping the carbon. Martensite in steel is generally too brittle to use in its virgin state, a tempering treatment relieves some of the strain, improves toughness and reduces the strength by carbide precipitation.

Martensite is not generally a major constituent in welds because it is hard and brit-tle. Solidification and segregation during welding produce inhomogeneities which, when combined with the possibility of martensite formation, can lead to extremely hard regions occurring within the weld metal causing toughness and cracking problems. Martensite is however difficult to avoid as a microconstituent but can be tolerated in small quantities.

In specialist applications such as ultra–high strength alloys low carbon martensites can be formed with acceptable properties but their great strength is often compromised to allow reasonable toughness levels to be attained. Martensite, bainite and acicular ferrite all become rather difficult to distinguish at very low carbon concentrations ($\approx 0.05\,\mathrm{wt\%}$).

2.2.11   Other constituents

Most of the austenite will have transformed by the time the temperature of the weld metal has fallen to $500\,^{\circ}\mathrm{C}$. The residual austenite will be stabilized by enrichment with carbon and this may transform to the hard martensitic phase or it may form degenerate pearlite (not having the time to form the more familiar lamellar structure). Lower cooling rates favour pearlite but it is also possible to retain austenite to room temperature depending upon the weld chemistry. These 'microphases' can be considered as inclusions due to their relatively high hardnesses and they are consquently particularly important when considering the fracture behaviour of the weld metal [173].

2.3   Control of Microstructure

Techniques for the promotion of particular phases in weld microstructures are more limited in welds than wrought steels. The use of thermomechanical processing in welding is obviously limited. As welding permanently fixes components within a structure there is little that can be done subsequently to the microstructure of either the base plates or the weld metal. Simple preheating and post weld heat treatments can be used but as the cooling rate of the weld metal cannot be altered greatly the weld microstructure has to be controlled mainly by the chemical composition. As a further constraint, the level of alloying additions in weld deposits is usually kept low to prevent cold cracking and other defects caused by the formation of brittle phases [174]. The microstructure is therefore determined by the cooling rate and composition. The cooling rate is controlled by the welding parameters which include the joint geometry, welding process, energy input and speed. The time required for the weld to cool from $800\,^{\circ}\mathrm{C}$ to 500 is often used to describe the cooling rate, typical values for welds lying in the range 5–40 s [175].

The kinetics of transformations in the weld must be controlled such that the natural weld cooling rate promotes the formation of the desired microstructure. This can be considered in terms of the continuous cooling transformation (CCT) diagram for the weld deposit (Fig. 2.16). With a characteristic cooling rate, the positions of the diffusional and displacive transformation curves must be moved to promote the desired microstructure.

High strength welds require fine microstructures so the diffusional transformations must be retarded.

The hardenability is critical in that it must be low enough to avoid transformation during cooling of residual austenite to high–carbon untempered martensite. An alloy's hardenability can be expressed in terms of the carbon equivalent (CE). Two commonly used expressions exist for carbon equivalent as a result of the sensitivity of transformation kinetics at low carbon contents discussed earlier. The relationship due to Ito and Bessyo (for <0.18 wt% C) is presented here [99]:-

$$\mathrm{CE} = \mathrm{C} + \frac{\mathrm{Si}}{30} + \frac{\mathrm{Mn} + \mathrm{Cu} + \mathrm{Cr}}{20} + \frac{\mathrm{Ni}}{60} + \frac{\mathrm{Mo}}{15} + \frac{\mathrm{V}}{10} + 5\mathrm{B} \qquad \mathrm{wt\%} \qquad (2.3)$$

As Equation 2.3 indicates, carbon is the most important alloying addition as this has the greatest effect upon strength and hardenability. Control of hardenability to create a fine, temper–resistant microstructure such as acicular ferrite is vital for high strength welds.

The ferrite structure in pure iron is relatively weak. Alloying elements added to control hardenability also strengthen the lattice and in the case of nickel can also improve toughness [160, 173]. In a typical high–strength weld deposit, a large solid solution strengthening effect results from alloying elements, raising the lattice strength to more than double that of pure iron ($\approx$200 MPa) [121, 167].

2.3.1 Multi–run welds

In practice, the gap between the components to be joined often has to be filled by a sequence of several weld deposits. These multi–run welds can therefore have a complicated macrostructure (Fig. 2.17). The deposition of each successive layer heat–treats the underlying microstructure, the volume fraction of the reheated zone depending upon the number and size of beads deposited [62]. Some of the regions of original primary microstructure are reheated to temperatures high enough to cause the reformation of austenite (reaustenitization), which during the cooling part of the thermal cycle may transform into a different microstructure denoted as 'reheated' or 'secondary' microstructure. Other regions may simply be tempered by the deposition of subsequent runs. Consideration must be given to this 'secondary' microstructure and ideally its mechanical properties should be engineered to approach those of the primary microstructure.

The multi–run process limits the development of more martensitic welds as the inherent reaustenitizing and tempering can cause unwanted inhomogeneities, a homogeneous microstructure also favours toughness [192].
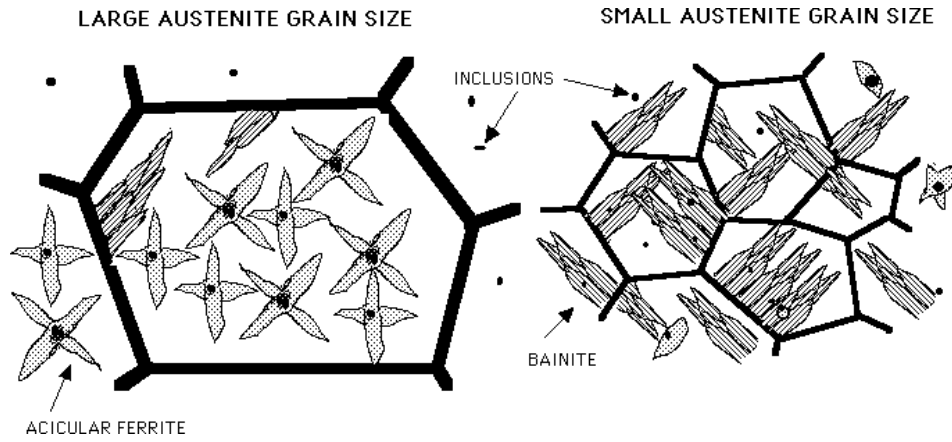
Figure 2.15: Illustration of the effect of prior–austenite grain size on the competing acicular ferrite and bainite reactions.
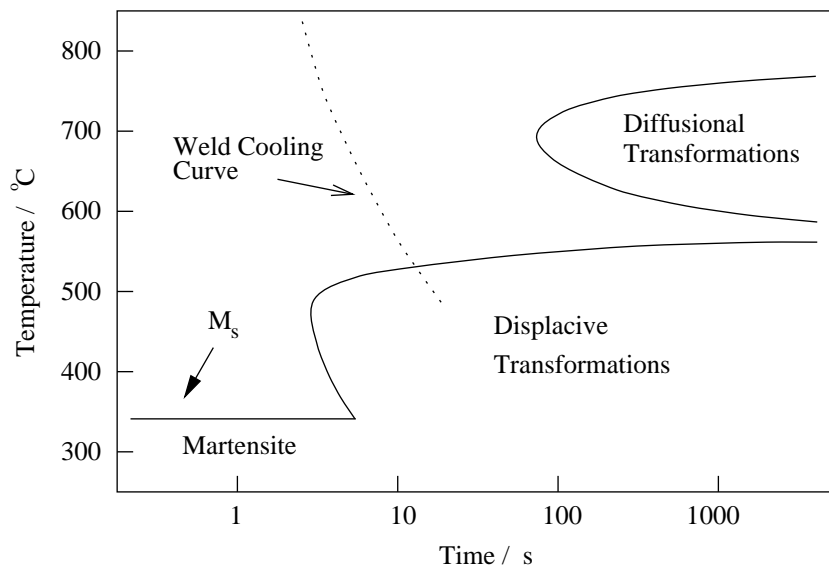
Figure 2.16: Schematic CCT curve for a high strength weld.

1 cm
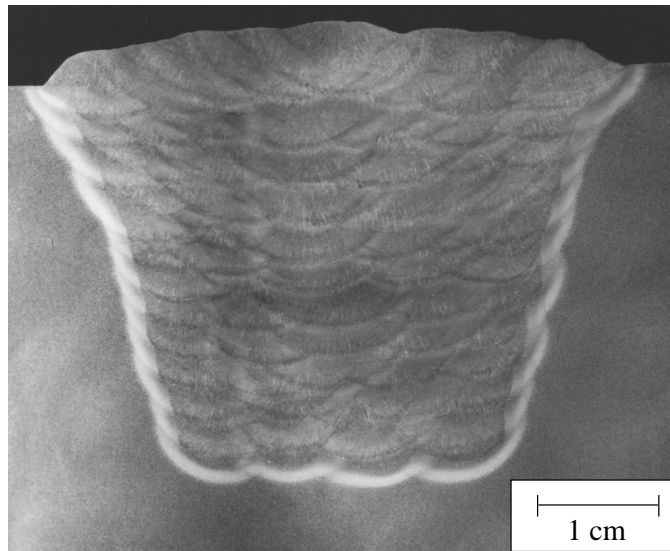
Figure 2.17: The macrostructure of a multirun weld, made by sequentially depositing a number of beads [151].

2.4 High strength weld microstructures

Good welding practice stipulates that the joint should have superior mechanical properties to the base material [173]. Traditionally the yield strength of weld deposits has been kept quite low ($\approx$ 350–550 MPa) to avoid cracking and formation of brittle martensite islands which plague higher carbon compositions [174]. This approach is therefore rather limiting as there are many applications in which the use of stronger steels would be beneficial. The increased use of high strength steels in applications such as pipelines, ships and oil platforms has necessitated the development of weld deposits with much greater strength (> 750 MPa). Such weld deposits are typically rather heavily alloyed, for example Ni and Mn contents may be in excess of 2 wt%.

The design of such high strength weld deposits must firstly involve a choice of microstructure. It is well known that the strengthening effect of the microstructure is reciprocally related to the grain size. The Hall-Petch relationship of $\sigma \propto d^{-1/2}$, relating the yield stress of a material σ to the grain diameter d, indicates that fine microstructures of predominantly acicular ferrite, bainite or martensite are required for such applications. The fundamental strengths of allotriomorphic and Widmanstätten ferrite are insufficient for this reason [174].

The multi–run fabrication technique favours the choice of acicular ferrite over martensite as the major phase. Acicular ferrite has excellent toughness but its maximum strength

has been estimated to be around 600 MPa [64] whereas greater strengths are desired. Hence a mixed microstructure of acicular ferrite and martensite can be used to increase the strength. In practice mixed microstructures are often naturally formed due to carbon partitioning and conveniently these give superior properties even to those of individual phases [202]. Low carbon contents (< 0.1wt %) are required to ensure sufficient toughness and ductility of the martensite, the volume fraction of acicular ferrite for the higher carbon contents in this range must also be kept to about 0.5 to prevent excessive austenite enrichment [25]. The lowering of the Ae_3 temperatures by alloying and the accompanying high hardenability ensures that the microstructures of high–strength welds in as–deposited and reaustenitised beads are quite similar [149].

A series of high strength welds formed by a multi–run manual metal arc process was studied by Yang [200], the significant alloying levels being 0.03–0.05 wt% C, 0.3–0.4 wt% Si, 2.4–2.6 wt% Ni and 1.6–2.0 wt% Mn. The microstructures were found to contain approximately 90% acicular ferrite and measured yield strengths were in the range 650–850 MPa. Good impact toughness values were also reported (≈ 70 J at -50 °C for the highest strength weld). The absence of any classical bainite morphology was noted. Approximately 30% of the microstructure was reaustenitized emphasising the importance of this effect. This work demonstrated that acicular ferrite can be used to produce weld deposits with strengths sufficient for high strength applications, the benefits to toughness of this microstructure being apparent.

High strength welds using more martensitic microstructures have been studied by Oldland *et al.* [139]. In this case a single pass submerged arc welding process was used on two alloys with compositions in the range 0.08–0.09 wt% C, 0.2–0.4 wt% Si, 2.1–2.4 wt% Ni, 1.5–1.7 wt% Mn and 0.6–0.8 wt% Mo. Yield strengths of around 940 MPa were produced with much lower toughness levels than in the former case at ≈ 20 J at -50 °C for a similar heat input. A predominantly martensitic microstructure was reported for a comparable energy input, higher values producing more bainite.

These two studies indicate the relative benefits of the rival microstructures but a strict comparison cannot be made as a multi–run techniques was not used in the latter case.

2.5   Conclusions

An overview of the formation of steel weld deposits has been presented. The cooling of such alloys from the austenite phase field can produce a number of possible phase transformation products which have been discussed individually. The transformation rates of many of these phases has been shown to be particularly sensitive to the carbon content

at the low concentrations typically used in high strength weld alloys. This is of particular concern as it is likely to cause inhomogeneity within the microstructure. In addition, the relative desirability of such phases as weld constituents has also been considered. The constraints placed upon weld design due to natural cooling rates have been highlighted particularly in the context of hardenability. Despite the constraints of the welding process it has been shown that careful control of alloy chemistry can produce fine, homogeneous microstructures with remarkable mechanical properties.

Chapter 3

Microstructure and Mechanical Properties of Experimental Welds

This chapter details the fabrication and examination of a series of six experimental welds in addition to a seventh, which was designed using an alternative strategy. The purpose was to examine the effects of altering chemical composition on elementary mechanical properties.

3.1   Production of experimental welds

All of the welds were fabricated using the manual metal arc (MMA) process from experimental electrodes produced to our composition specification at ESAB AB Central Laboratories, Gothenburg, Sweden. As this work focuses upon the weld metal itself, a joint geometry (ISO 2560) was chosen to reduce the effects of dilution due to mixing with the base metal (Fig. 3.1). The welds were fabricated using 20 mm thick plates. Approximately 30 runs were required to fill the gap, with 2–4 beads per layer. Welding was performed using a current of 174 ± 1 A, at a potential of 25 ± 1 V DC to give an electrical energy input of 1.08 ± 0.05 kJ mm^{-1}. An interpass temperature of 250 °C was specified. 'Buttering' of the plates was performed prior to welding, involving the deposition of a layer of weld beads along the edge of the plates [136]. Carbon diffusion into the weld metal from the base material can reduce toughness and cause cracking. Buttering provides a boundary layer that is not constrained during fabrication and is less likely to crack than the weld metal.

Six of the welds, denoted H1–H6, had chemical compositions based on that of a commercial electrode OK75.78, which in the present work is designated H1. Weld H7, was
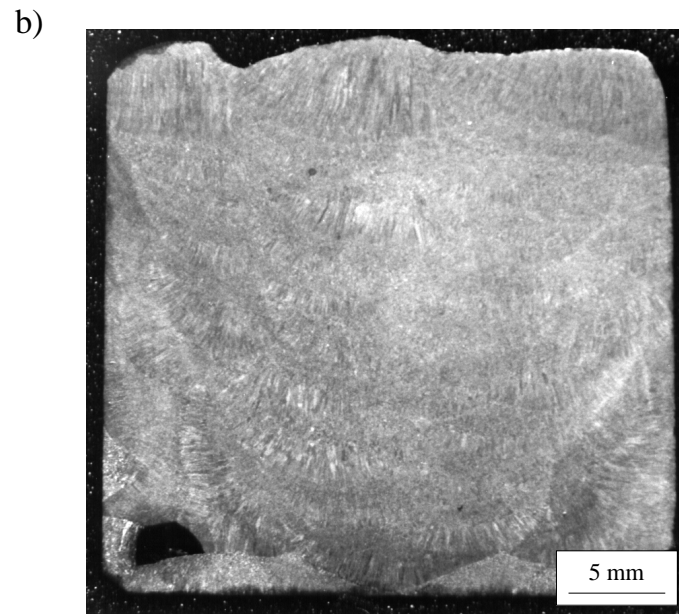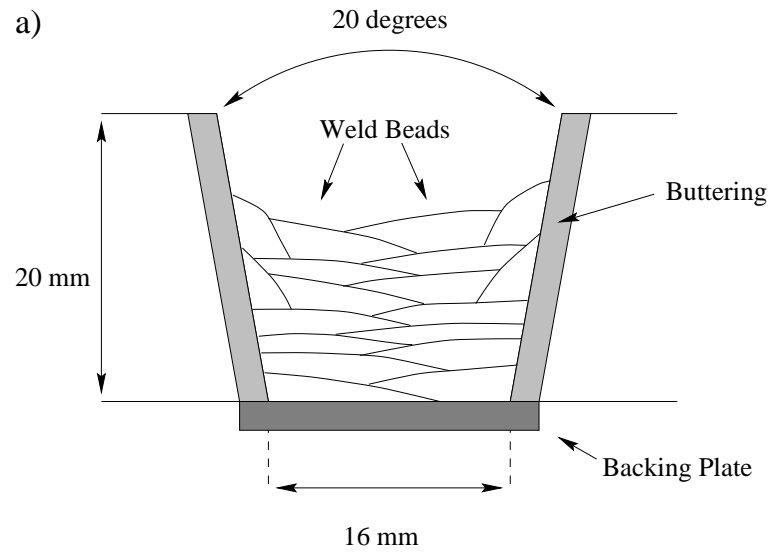
Figure 3.1: a) Geometry of an ISO 2560 weld. b) Image of the weld metal etched to reveal the weld beads.

designed as a high–silicon, high–carbon, carbide–free bainitic weld which ought to have a different microstructure which has never been investigated in the context of welds. Table 3.1 lists the proposed compositions of H1–H7; the actual compositions achieved are listed in Table 3.2 where all concentrations other than oxygen and nitrogen were determined using spark emission spectroscopy. Oxygen and nitrogen levels were measured using Leco furnaces.

Element	Weld Name						
/ wt%	H1	H2	H3	H4	H5	H6	H7
Carbon	0.05	0.02	0.05	0.02	0.02	0.02	0.10
Manganese	2.0	2.0	1.0	1.0	1.0	1.0	2.0
Silicon	0.30	0.30	0.30	0.30	0.30	0.30	1.75
Chromium	0.45	0.45	0.45	0.45	0.00	0.00	0.00
Nickel	3.0	3.0	4.0	4.0	4.0	4.0	2.0
Molybdenum	0.6	0.6	0.6	0.6	0.6	0.6	0.2
Copper	0.0	0.0	0.0	0.0	0.0	2.0	0.0
Iron	bal.	bal.	bal.	bal.	bal.	bal.	bal.

Table 3.1: The intended chemical composition of welds H1–H7.

Weld H2 was produced to study the effect of reducing the carbon concentration relative to H1. At 0.02 wt% the concentration is close to the maximum solubility of carbon in ferrite. Consequently, phase transformations which lead to the partitioning of carbon should not enrich the residual austenite, thus avoiding the subsequent formation of any hard martensite. H3 was designed with a higher nickel concentration with the aim of enhancing toughness since nickel is known to have a beneficial influence on the ability of ferrite to absorb energy during fracture [160]. Weld H4 provides a similar comparison to the lower carbon variant H2 with the emphasis on manganese. H5 is similar to H4 but without a deliberate addition of chromium. Copper can be used to precipitation harden steel. Copper precipitates are relatively soft so may not be too detrimental to toughness. It was in this context that weld H6 was made. With the exception of Cu, H6 is similar to H5. Weld H7 has a relatively large carbon concentration and significantly, a much higher silicon content which prevents carbide precipitation due to the higher carbon level. The idea is to have a microstructure containing fine plates of bainitic ferrite, each of which is separated by thin films of stable retained austenite. Such microstructures have in the past been proven to give a good combination of strength and toughness but never in the context of welds.

Comparison between Tables 3.1 and 3.2 shows that generally the measured levels of alloying additions did indeed match the target values. The largest discrepancies occurred with welds H2, H6 and H7. The carbon content of H2 was higher than intended at $0.037\,\mathrm{wt\%}$ (c.f. $0.02\,\mathrm{wt\%}$). Such a difference is significant because it is known that transformations are sensitive to the carbon at low concentrations [89]. The molybdenum level in weld H6 unfortunately turned out to be only $0.13\,\mathrm{wt\%}$ compared with the intended concentration of $0.6\,\mathrm{wt\%}$. Weld H6 was designed to test the effect of copper; a possible consequence of the lower molybdenum content would be a reduction in any secondary hardening effects. Some secondary hardening is expected in a multi–run weld; otherwise the alloy has sufficient hardenability.

Element	Weld						
/ wt%	H1	H2	H3	H4	H5	H6	H7
Carbon	0.049	0.037	0.045	0.026	0.025	0.022	0.102
Manganese	2.09	2.13	1.11	0.97	0.85	0.78	2.18
Silicon	0.29	0.27	0.29	0.23	.022	0.17	1.63
Phosphorus	0.005	0.010	0.008	0.010	0.010	0.010	0.009
Sulphur	0.012	0.006	0.006	0.010	0.009	0.011	0.005
Chromium	0.43	0.46	0.43	0.44	0.03	0.03	0.02
Nickel	3.04	3.03	3.91	4.00	3.91	4.25	2.07
Molybdenum	0.59	0.60	0.58	0.61	0.60	0.13	0.23
Vanadium	0.019	0.019	0.016	0.015	0.015	0.011	0.019
Copper	0.03	0.03	0.03	0.03	0.03	2.18	0.03
Titanium	0.014	0.014	0.014	0.012	0.012	0.010	0.039
Tin	0.007	0.010	0.007	0.004	0.002	0.001	0.010
Arsenic	0.012	0.012	0.012	0.006	0.005	0.000	0.013
Boron	0.0005	0.0006	0.0004	0.0002	0.0001	0.0000	0.0007
Oxygen	0.0267	0.0307	0.0310	0.0348	0.0299	0.0423	0.0205
Nitrogen	0.0118	0.0143	0.0101	0.0143	0.0148	0.0125	0.0113
Iron	bal.	bal.	bal.	bal.	bal.	bal.	bal.

Table 3.2: Results of chemical analysis of welds H1–H7.

3.2   Tensile tests

Tensile test specimens were machined along the welding direction (Fig. 3.2) with the dimensions illustrated in Figure 3.3. All specimens were degassed at 250 °C for 16 h prior to testing to failure at an applied stressing rate of $13 \pm 1\,\text{N}\,\text{mm}^{-2}\text{s}^{-1}$. Data for 0.2 % and 1.0 % proof stresses, ultimate tensile strength (UTS), elongation and reduction in area were obtained from pairs of tensile tests from each weld. The results are shown in Table 3.3 and the strength data are illustrated in Figure 3.4.
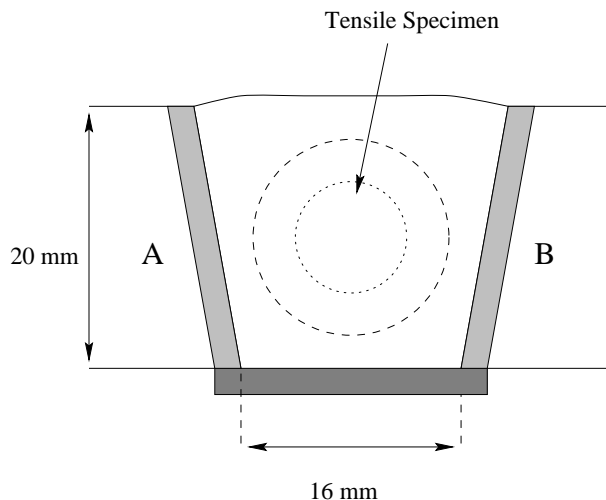
Figure 3.2: Cross–section of an ISO 2560 weld indicating the position from which tensile test specimens were machined.
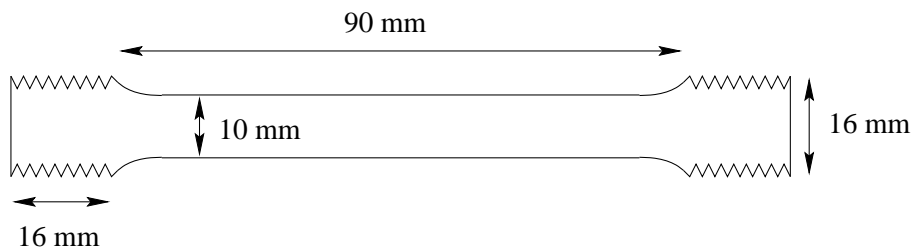
Figure 3.3: Geometry of tensile test specimens.

There is slight scatter in the data, the largest due to the yield strength of H1, discussed more fully in Chapter 5. It is clear from Figure 3.4 that welds H2–H6 have inferior strength to that of H1. A reduction in carbon could be expected to reduce the strength of such

welds. Replacement of manganese with nickel did not maintain strength levels as was hoped. The only comparative improvement was gained in H6 compared with weld H5, where the addition of 2 wt% Cu improved the strength by over 100 MPa. Encouragingly high strength levels were attained in weld H7, particularly in terms of the UTS.

Weld	0.2% Proof / MPa		1.0% Proof / MPa		UTS / MPa	
	Test 1	Test 2	Test 1	Test 2	Test 1	Test 2
H1	872	838	874	844	922	918
H2	827	837	830	845	903	909
H3	803	809	800	810	841	851
H4	714	723	713	731	776	788
H5	627	626	641	630	703	695
H6	750	763	749	762	804	807
H7	845	827	857	843	969	971

Weld	Elongation / %		Reduction in Area / %	
	Test 1	Test 2	Test 1	Test 2
H1	22.0	21.6	67	64
H2	21.0	22.8	65	64
H3	21.0	20.6	66	64
H4	21.6	24.4	66	68
H5	23.0	25.0	71	72
H6	20.6	22.2	60	62
H7	23.6	23.3	62	60

Table 3.3: Comparison between tensile test results for H1–H7.

Ductile deformation consists of two essential components; there is an initial stage of uniform elongation during which the work hardening caused by plastic deformation adequately compensates for any increase in stress due to reduction of area. This is followed by non−uniform elongation and the formation of voids which generally nucleate at inclusions. If the voids are few and far between there there is considerable elongation before they link and cause ultimate failure (Fig. 3.5).

Elongation should decrease as the inclusion content of the weld metal increases [36]. Assuming that the number density scales with the inclusion content, Barba [19] has shown that the elongation should be inversely proportional to the sum of the oxygen and sulphur contents of the welds [19]. Figure 3.6 shows that this is indeed the case. The welds all
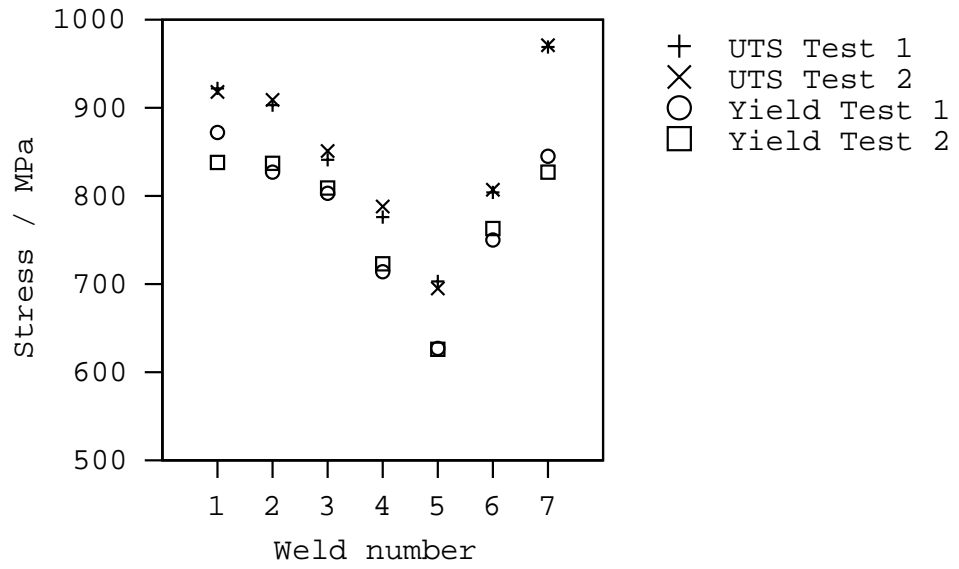
Figure 3.4: Comparison of yield and UTS data for welds H1–H7.
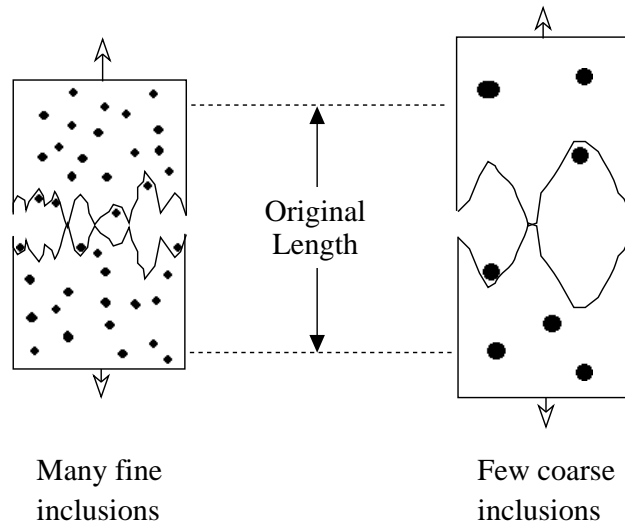
Figure 3.5: An illustration of a low ductility fracture caused by a high inclusion density.

had acceptable levels of elongation.
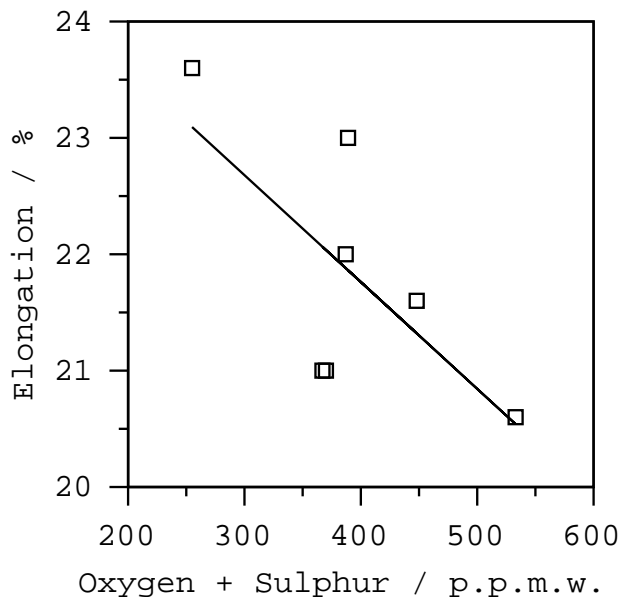
Figure 3.6: Inverse relationship between elongation and the sum of oxygen and sulphur contents of welds H1–H7. 'p.p.m.w.' denotes 'parts per million by weight'.

3.3 Charpy Impact Toughness

Standard 10 mm × 10 mm Charpy V-notch specimens were machined from all–weld metal samples (Fig. 3.7). The position of the notch lay within the weld metal and the axis of the specimen was normal to the welding direction. Between 2 and 5 samples were fractured at each temperature, greater numbers of specimens being used at temperatures of interest.

The fracture surfaces were examined using a Philips XL30 scanning electron microscope (SEM) operating at 20 kV, imaging with secondary electrons.

3.3.1 Results

As expected, the commercial weld H1 exhibited excellent impact toughness at all test temperatures (Fig. 3.8); the yield strength of ≈ 850 MPa is high in the context of welds. Charpy impact curves are often described as being sigmoidal in shape owing to the ductile– brittle transition in bcc iron. Fractographic examination (Fig. 3.9) shows that such a transition does indeed occur but is very gradual with mixed ductile and cleavage failure even at -60 °C. This is probably responsible for the smooth appearance of the impact

Charpy Specimen

20 mm

16 mm

55 mm

10 mm

10 mm

2 mm

2 mm
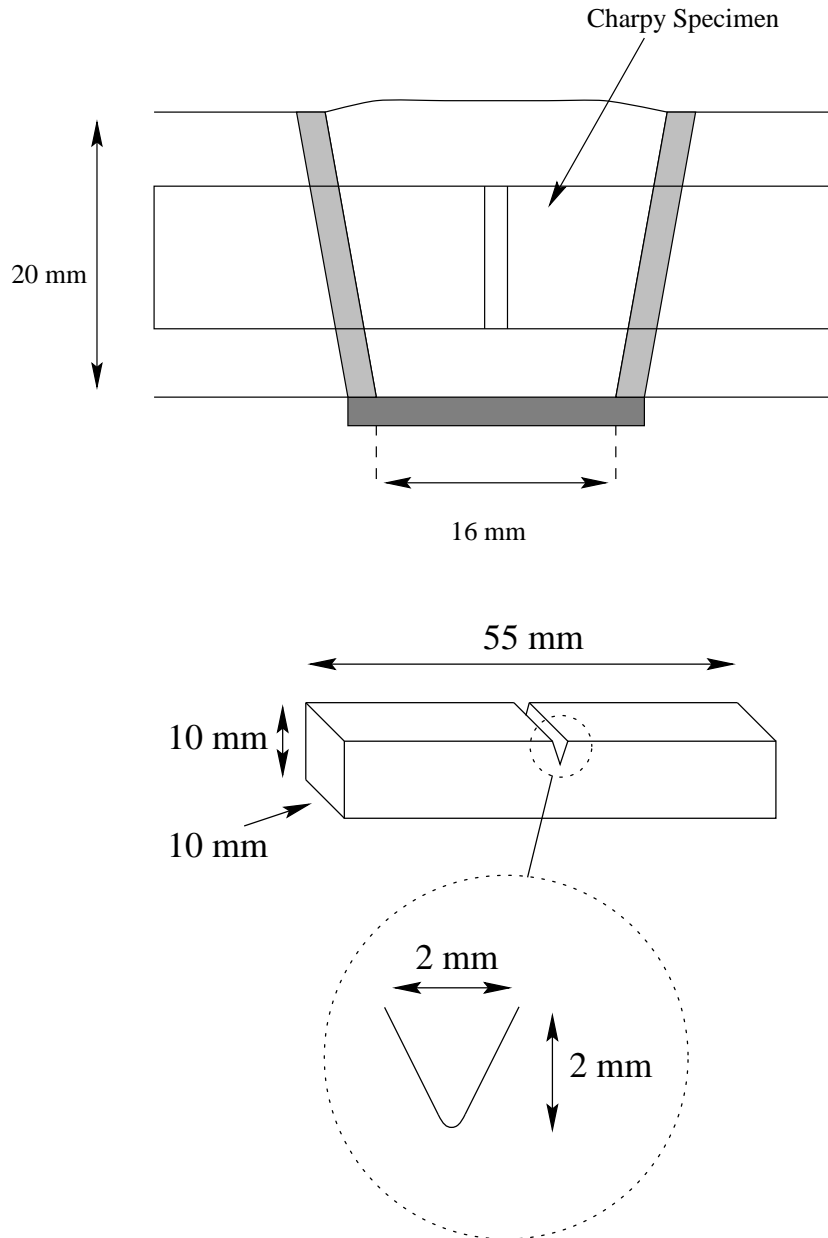
Figure 3.7: Specifications of Charpy impact specimens.

toughness vs. temperature curve (Fig. 3.8). Average impact energy values are presented in the following figures.
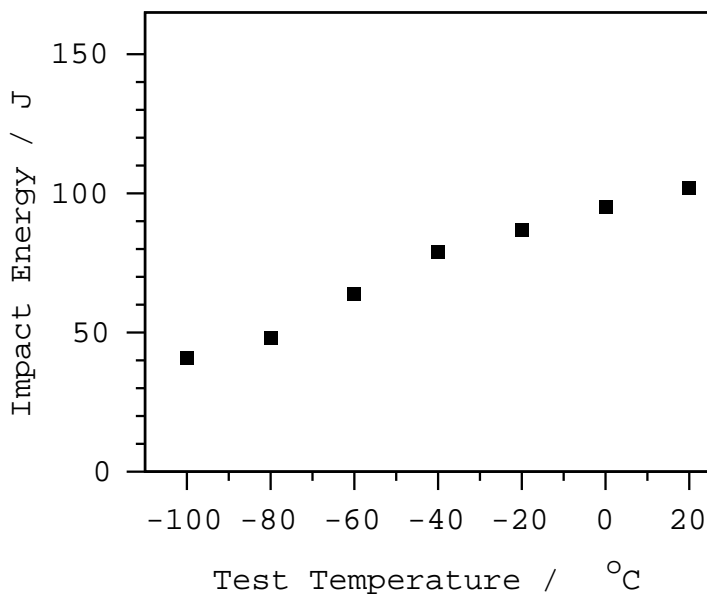
Figure 3.8: Effect of temperature upon impact toughness in H1.

Since the overall composition of weld H2 is similar to that of weld H1, it is not surprising that they have comparable toughness (Fig. 3.10).

On the other hand, the lower strength of weld H3 in which a portion of Mn was replaced with Ni, resulted in a higher toughness in the ductile regime (Fig. 3.11).

The reduced carbon concentration in weld H4 (0.02 wt% C) relative to that of weld H3 (0.05 wt%) led to a reduction in the strength by approximately 10%. The associated coarser microstructure leads to a sharper definition of the ductile–brittle transition in weld H4 (Fig. 3.12), causing a reduced cleavage fracture but better toughness in the ductile fracture regime in spite of the somewhat larger inclusion content relative to weld H3.

The weld with the highest toughness (and the lowest strength) was H5. The composition of weld H5 was similar to H4 but with chromium removed. The toughness of H5 was superior to H4 across the entire temperature range (Fig. 3.13). The removal of chromium caused a large reduction in yield strength (≈ 100 MPa). Comparison between the micrographs in Figures 3.14 shows perhaps a slight increase in dimple size in the H5 specimen, consistent with a lower inclusion content.

A drastic reduction in toughness was caused in weld H6 by the addition of 2 wt% Cu to H5 (Fig. 3.15). Weld H6 not only has a higher strength (by 120 MPa) but also a much greater oxygen content (H6: 0.0423 wt% compared with 0.0299 wt% in H5). Both of these
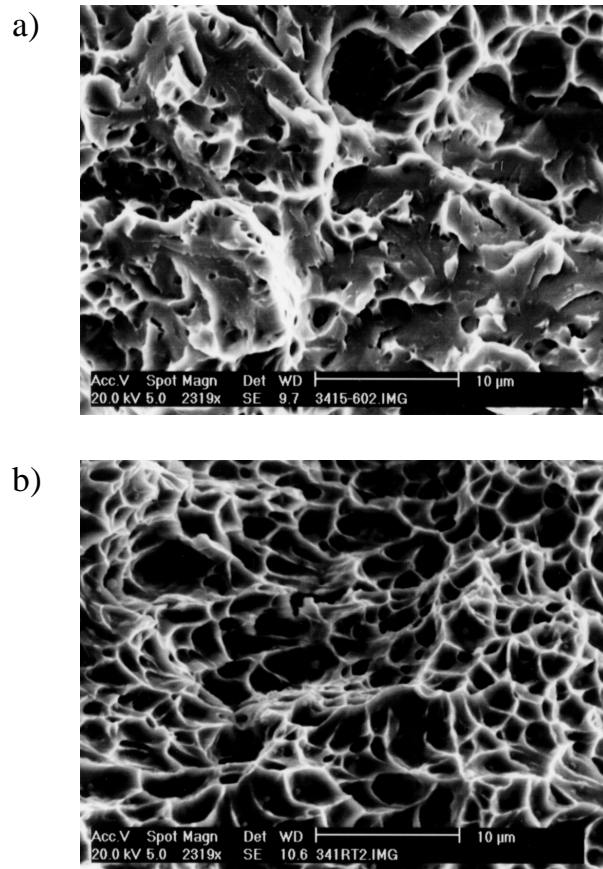
Figure 3.9: H1 specimens fractured at a) -60 °C indicating a more brittle fracture and b) room temperature showing more ductile dimpled regions.
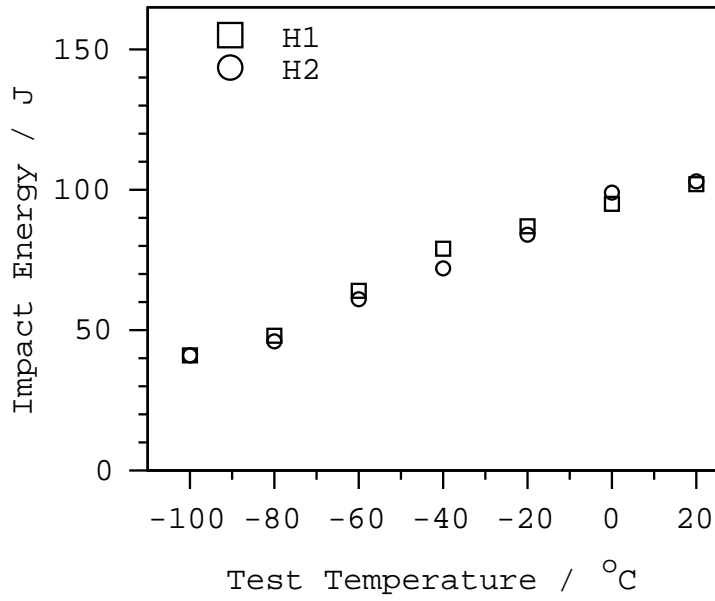
Figure 3.10: Comparison between the impact toughnesses of welds H1 and H2.
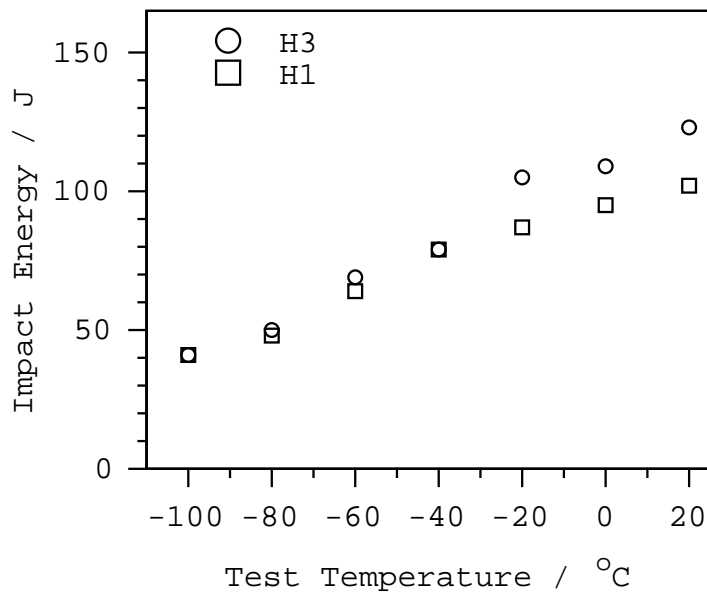
Figure 3.11: Comparison between the impact toughnesses of welds H1 and H3.
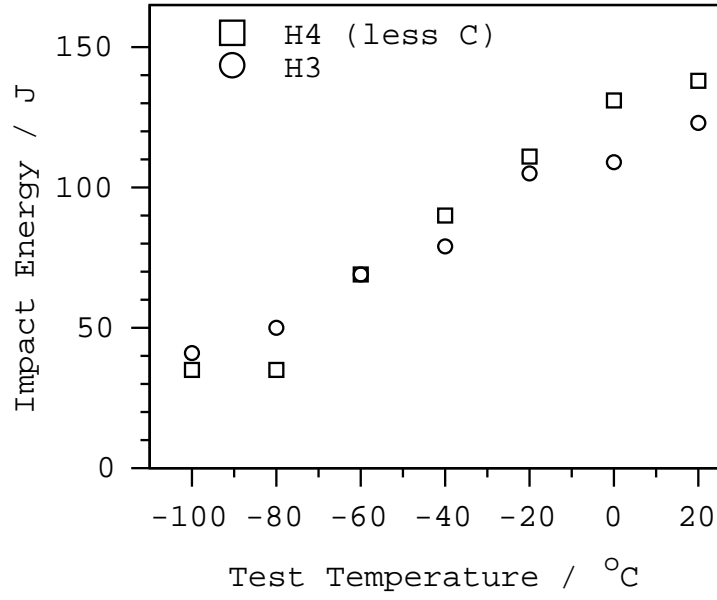
Figure 3.12: Comparison between the impact toughnesses of welds H3 and H4.
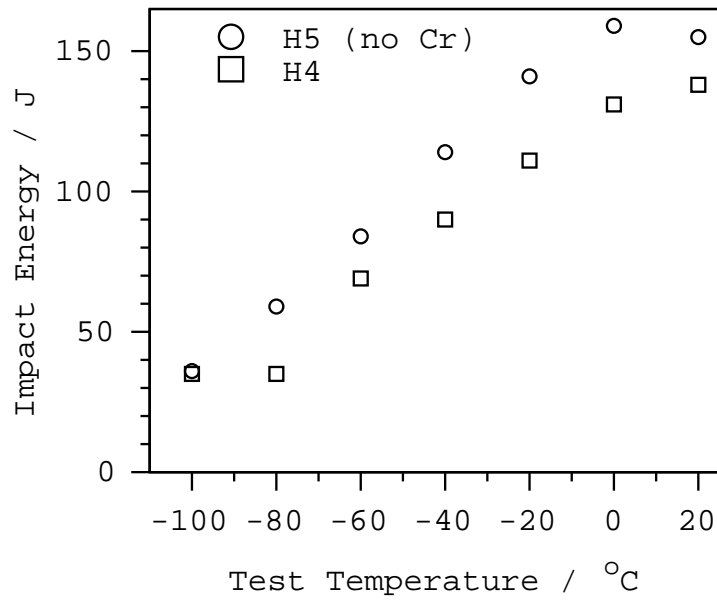
Figure 3.13: Comparison between impact toughness levels of welds H4 and H5.
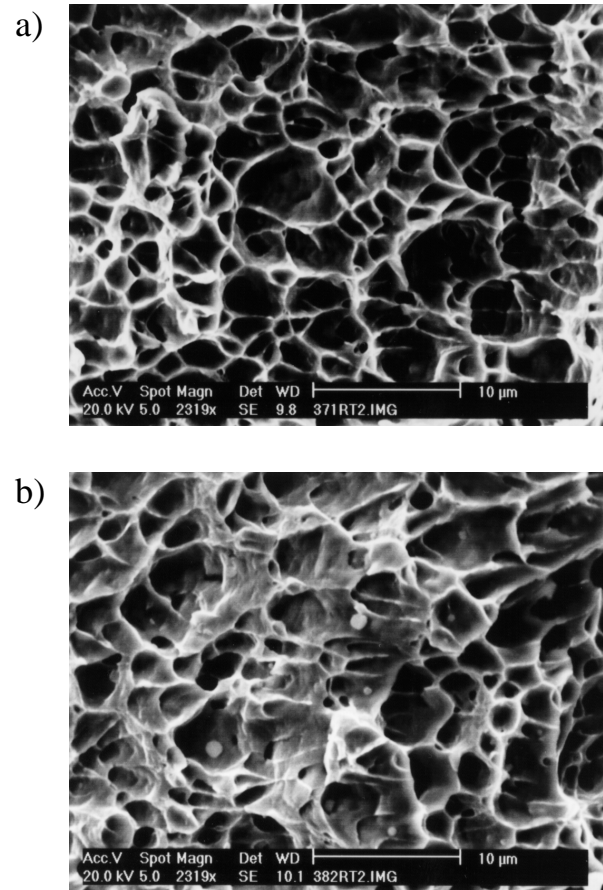
Figure 3.14: Room temperature fracture behaviour of welds a) H4 and b) H5.

might lead to a reduction in toughness. It is unfortunate that the comparison could not be made at a constant oxygen content.
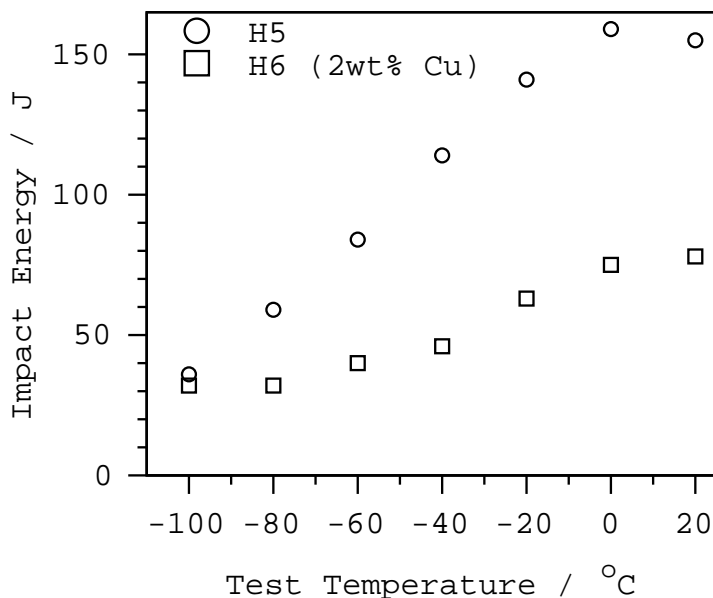
Figure 3.15: H5 absorbed energy values are higher than H6 over the entire range of tested temperatures.

Weld H7 has a yield strength which is comparable to that of H1 (Table 3.3), a much lower inclusion content (Table 3.2) and yet has much worse Charpy toughness at all temperatures (Fig. 3.16). As will be seen later, its microstructure is quite different with regions of high–carbon retained austenite. It is likely that some of these regions are unstable to martensitic transformation under the influence of stress, leading to the formation of very high–carbon, brittle martensite. This may explain the reduction in toughness.

Data from all of the Charpy tests are given in Table 3.4.

3.4 Specimen preparation for microscopy

Full weld cross–sections ('macros') of approximate dimension 20 mm×20 mm were cut from the weld metal of H1–H7. These were hot mounted in a conductive particulate copper–polymer matrix, a medium allowing scanning electron microscope (SEM) examination. A 7–stage grinding and polishing schedule was performed using an autopolisher, a final sub–micron polish being applied using a suspension of silica particles in water. Specimens were etched with 'Nitamyl' - a solution of 2.5% by volume of 65% HNO_3 in isoamylalcohol. Optical microscopy was performed using a Leitz microscope in 'interference contrast' mode
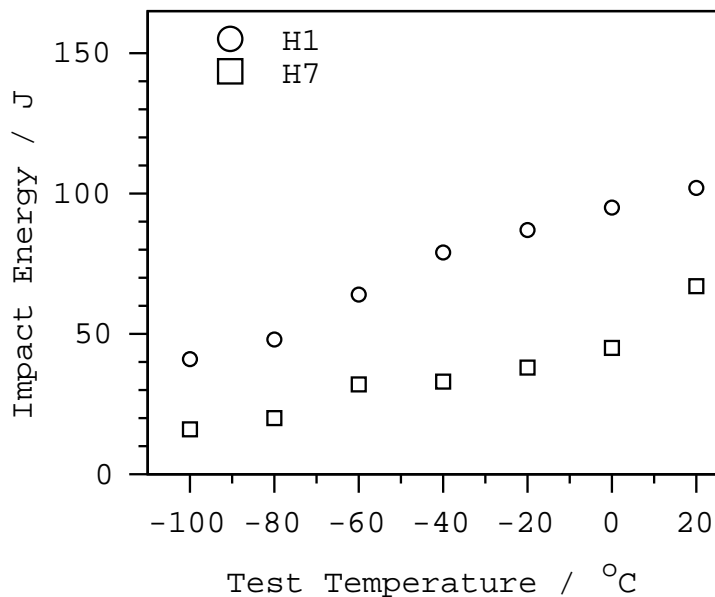
Figure 3.16: The toughness of H1 is superior to that of H7 despite their similar strengths.

Weld	Test temperature °C						
	-100	-80	-60	-40	-20	0	20
H1	40, 42	50, 46	66, 62, 63	77, 81, 78	88, 88, 89, 87, 85	93, 97,	101, 104, 100
H2	38, 44	49, 43,	59, 63, 61	76, 70, 70	87, 86, 81, 86, 82	95, 102	107, 100, 101
H3	40, 41	45, 55	65, 69, 74	72, 71, 95	106, 108, 107, 100, 102	109, 108	124, 120, 124
H4	43, 27	46, 24	71, 63, 72	87, 94, 88	111, 111, 121, 107, 104	132, 130	135, 144, 136
H5	33, 39	56, 62	88, 91, 73	106, 123, 114	140, 138, 142, 141, 146	157, 161	152,155, 157
H6	30, 33	32, 31	38, 41, 40	48, 46, 45	67, 61, 61, 60, 67	79, 70	80, 78, 77
H7	17, 14	14, 26	30, 32, 34	34, 35, 29	39, 39, 37, 37, 39	45, 45	74, 66, 62

Table 3.4: Charpy impact data for welds H1–H7. All values are in Joules.

to give better contrast. A Philips XL30 scanning electron microscope was used for high resolution imaging.

For transmission electron microscopy (TEM) a number of 3 mm diameter circular rods were machined from longitudinal sections of the centres of welds H1 and H7. An Al_2O_3 saw was used to remove thin discs of thicknesses between 100 and $120\,\mu$m. An '800–grit' mechanical polishing paper was used to manually thin the specimens to a thickness of $<60\,\mu$m with the aid of a specially designed holder and water as a lubricant. A twin–jet electropolisher was used in conjunction with two polishing solutions. A 5% perchloric acid– 10% glycerol – 85% ethanol solution was used at ambient temperatures for H1 specimens, typical polishing conditions being 45 V and 25 mA. Weld H7 proved difficult to polish and a more corrosive solution of 5% perchloric acid in 95% glacial acetic acid was used. Optimum polishing conditions were found at around 50 V and 23 mA. Imaging was performed in a 120 kV Philips 400ST microscope and a JEOL 200CX instrument operating at 200 kV.

3.5   Optical microstuctures

General features of the macrostructure are illustrated in Figure 3.17 which shows classical columnar prior–austenite grains in the last bead welded during the fabrication of weld H1, these grains having a fine substructure. The equiaxed grains also shown are due to the reheating of the previously deposited bead. The entire weld therefore consists of a mixture of columnar and equiaxed austenite grains, both of which have the same fine scale microstructure (Fig. 3.18a,b). As can be seen from Figure 3.19, little further information is revealed by optical microscopy other than the fact that the microstructures were fine.

3.6   Scanning and transmission electron microscopy of H1 and H7

Further microscopy was confined to welds H1 and H7 as welds H1–H6 are similar in philosophy but weld H7 was designed to have a radically different microstructure.

Figure 3.20 shows SEM images of the top beads of welds H1 and H7 at similar magnifications, with bainitic and martensitic regions identified. However, only limited information was provided by such micrographs and further investigations were performed using transmission electron microscopy.

Weld H1 revealed a microstructure of fine plates typically of thickness 200–500 nm (Figure 3.22). The plates were often separated by fine films of austenite identified using
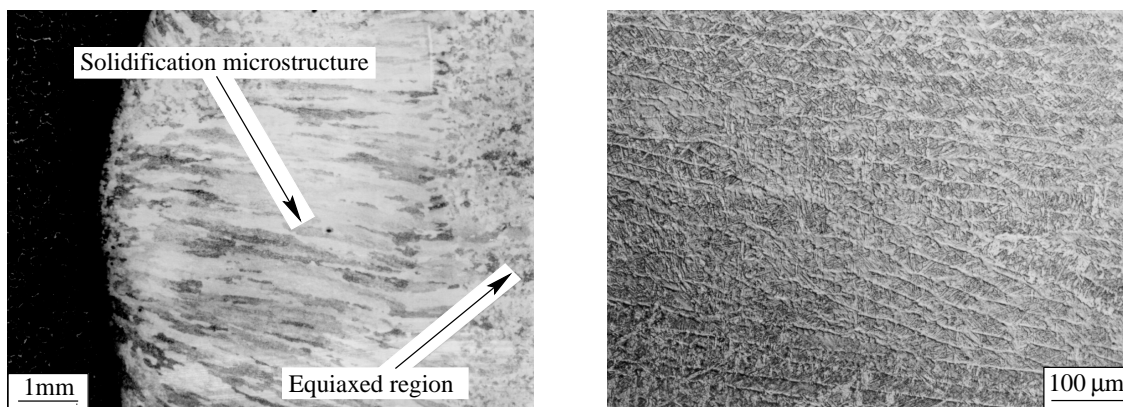
Figure 3.17: Solidification microstructure in H1 indicating elongated and equiaxed prior–austenite grains (left). Higher magnification reveals a fine substructure within these regions (right).

electron diffraction (Fig. 3.21).

Carbides were not detected because of the low average carbon content, which also makes it difficult to distinguish bainite and martensite. At such a low carbon composition bainite and martensite would be expected to have similar properties and be virtually indistinguishable. The apparent thickness of the plates depends upon the angle at which they are sectioned. Figure 3.22b shows a region in which the plate–like microstructure is less obvious. Here, as in most micrographs there are roughly spherical inclusions or holes left behind wherever the 'inclusions' were removed during electropolishing.

Micrographs of weld H7 are similar to those of H1 other than the fact that austenite regions were somewhat bigger and easier to identify (Fig. 3.23). Extensive microscopy failed to reveal any carbides, consistent with the large silicon concentration. The carbon partitions into the austenite during the formation of bainite, so the austenite is expected to be enriched in carbon. Some of the austenite decomposes into high carbon martensite; twinned martensite is shown in Figure 3.23d.

3.7 Hardness Data

It has already been emphasised that because of the very low carbon concentrations involved, it is very difficult to distinguish martensite and bainite from microstructural observations. Martensite is fully supersaturated with carbon whereas the excess carbon partitions into the retained austenite (or precipitates as carbides) during the bainite reaction. The amount of carbon partitioned decreases with the average carbon concentration,

a)

b)
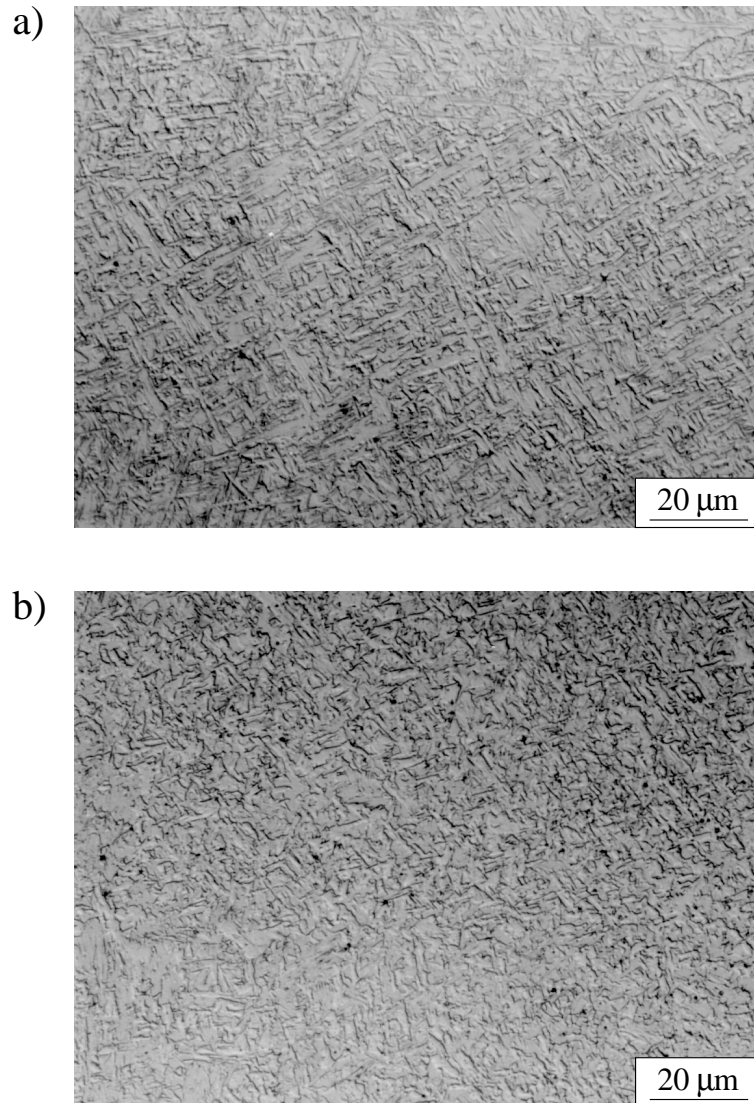
Figure 3.18: Examples of the fine microstructure of H1 in both a) the last welded bead and b) reaustenitized regions.
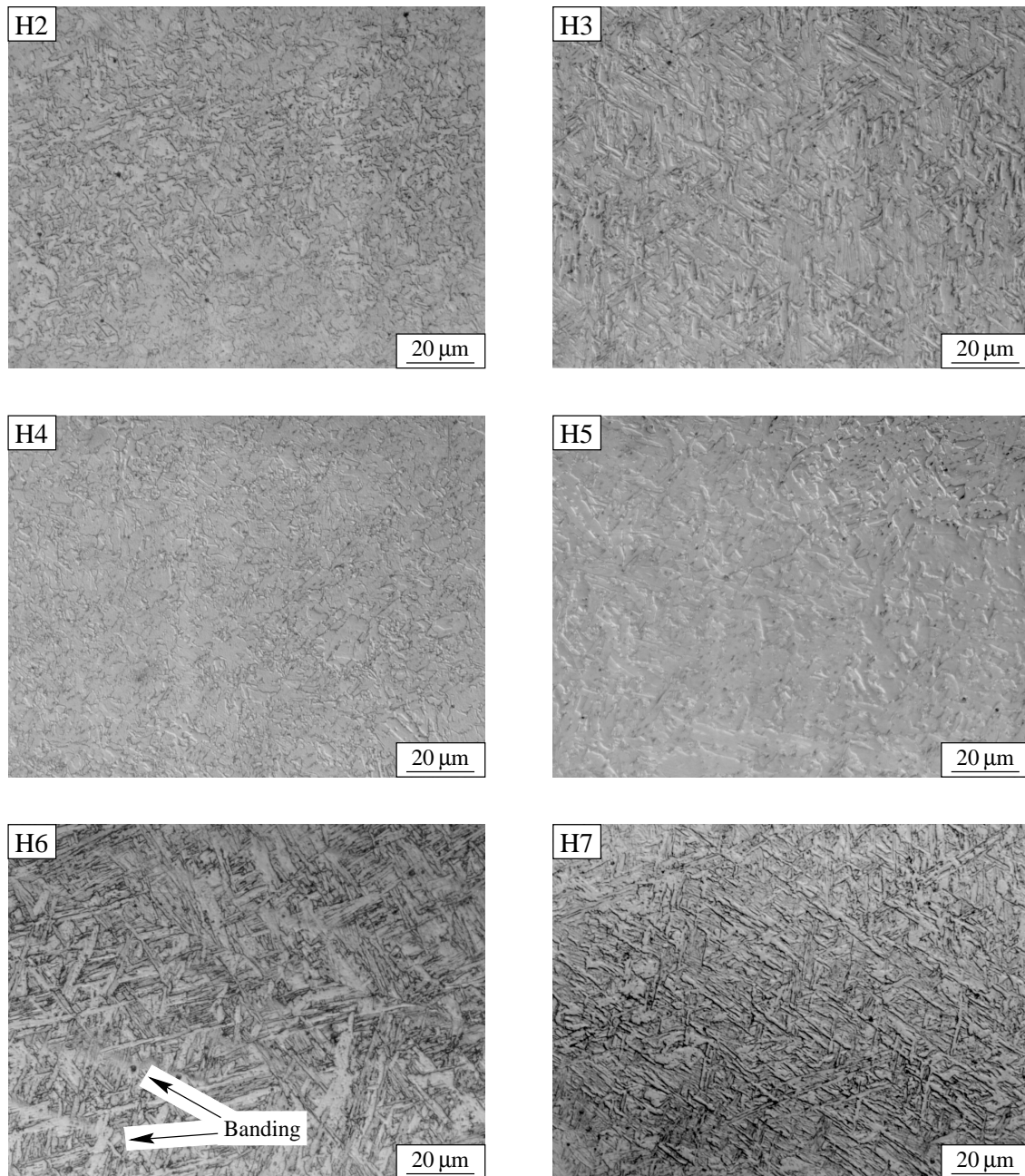
Figure 3.19: Optical micrographs of welds H2–H7. A fine microstructure is found in all cases. Some typical segregation effects are also visible in the H6 micrograph.
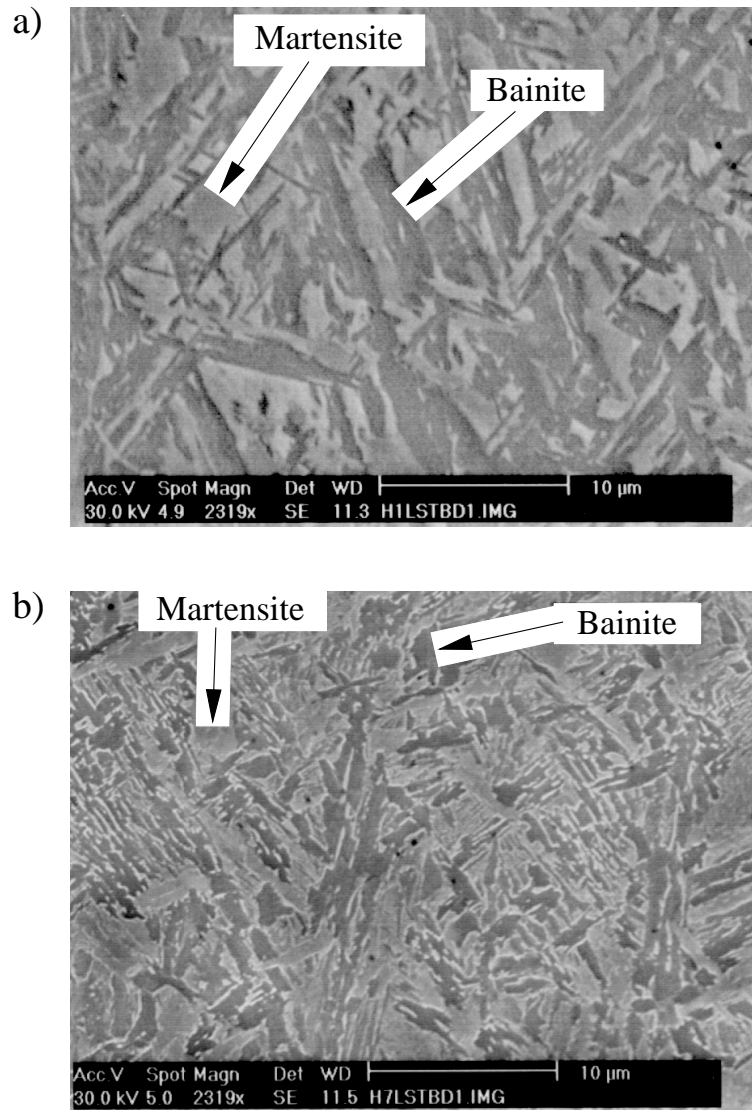
Figure 3.20: Comparison between a) H1 and b) H7 weld microstructures imaged with an SEM.
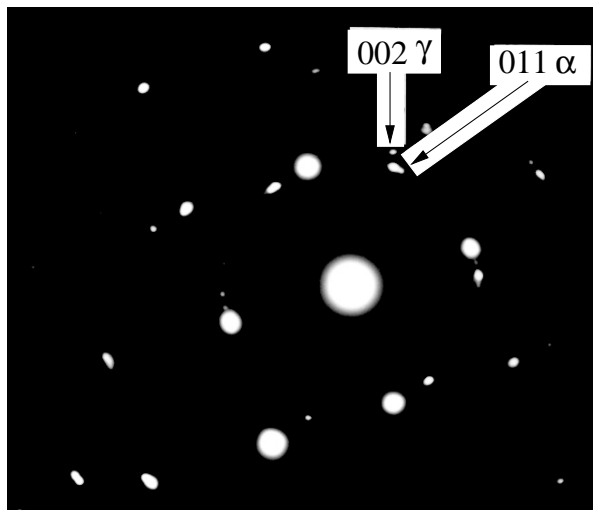
Figure 3.21: Electron diffraction pattern from H1 showing spots from ferrite and austenite.

making microstructural distinctions imprecise. Nevertheless, the hardness is very sensitive to the carbon concentration so a comparison of the sample hardness with that of a fully martensitic specimen can be very revealing.

Fully martensitic specimens were obtained by austenitizing 5 mm×5 mm×10 mm samples at 1000 °C for 5 minutes prior to quenching into water at ambient temperature. Hardness measurements on the quenched samples were then compared with corresponding data from the last weld bead and from the equiaxed austenite region below the last bead for all specimens. Six measurements were made for each region.

There are a number of interesting results illustrated in Figure 3.24. Firstly there is very little difference in the hardness between the as–deposited and reaustenitized microstructures. This is to be expected [35, 150] given the low Ae_3 temperatures (e.g. ≈ 760 °C calculated for H1 [88]) and high hardenability. The former ensures that that tempering effects are minimised and the latter that the reaustenitized regions eventually transform back into the as–deposited microstructure on cooling. This is a good feature of high–strength weld deposits in that they tend to be mechanically relatively homogeneous [150].

The hardness of as–deposited welds was always lower than of the directly quenched samples. This can be taken as good evidence that the as–deposited microstructure is a mixture of bainite and martensite (see Chapter 4). It is notable that the differences between the as–deposited and quenched samples is largest for H7 which has the largest carbon concentration.
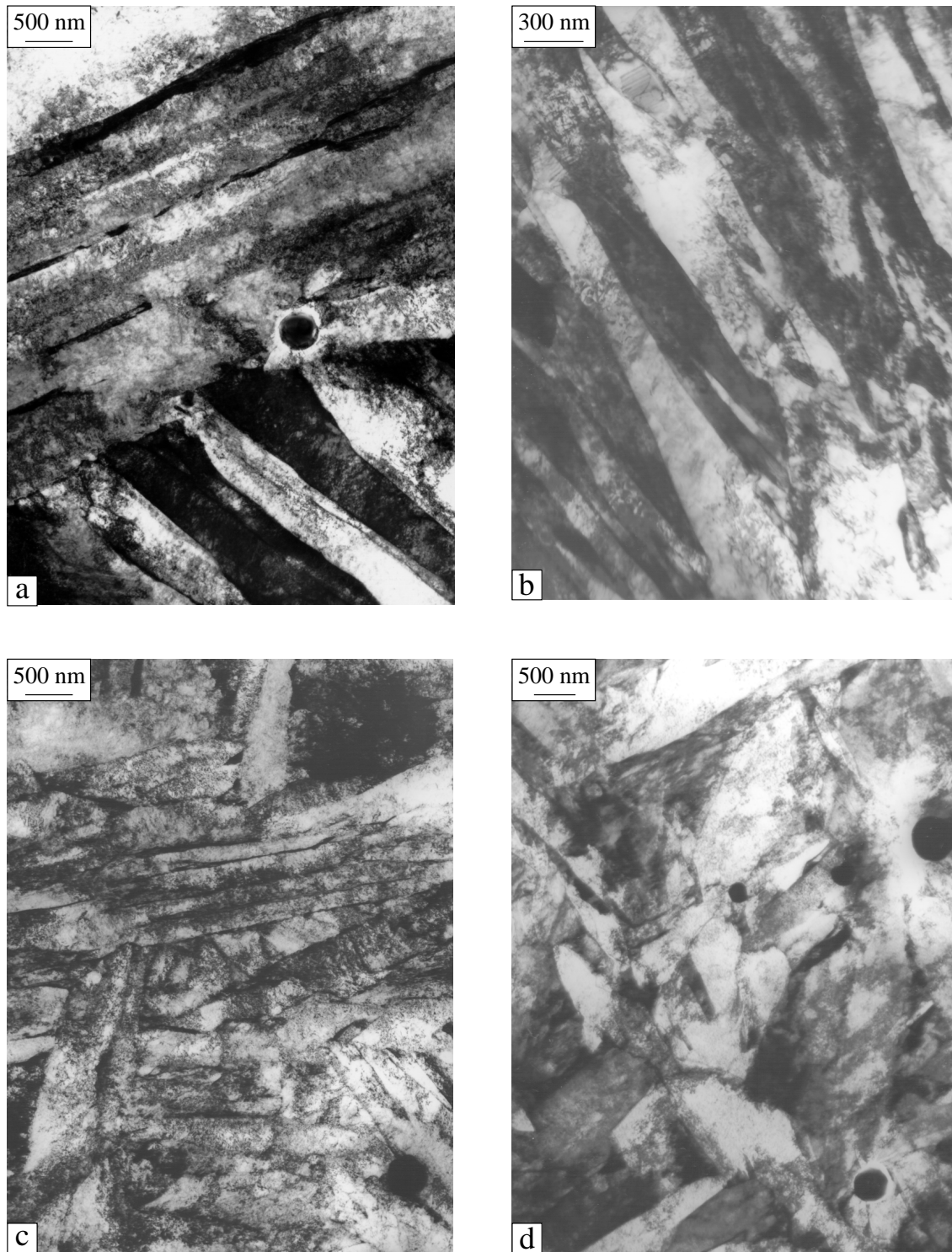
Figure 3.22: TEM micrographs of H1 showing a microstructure comprising packets of plates. Holes due to inclusions can be seen in micrographs a,c, and d.
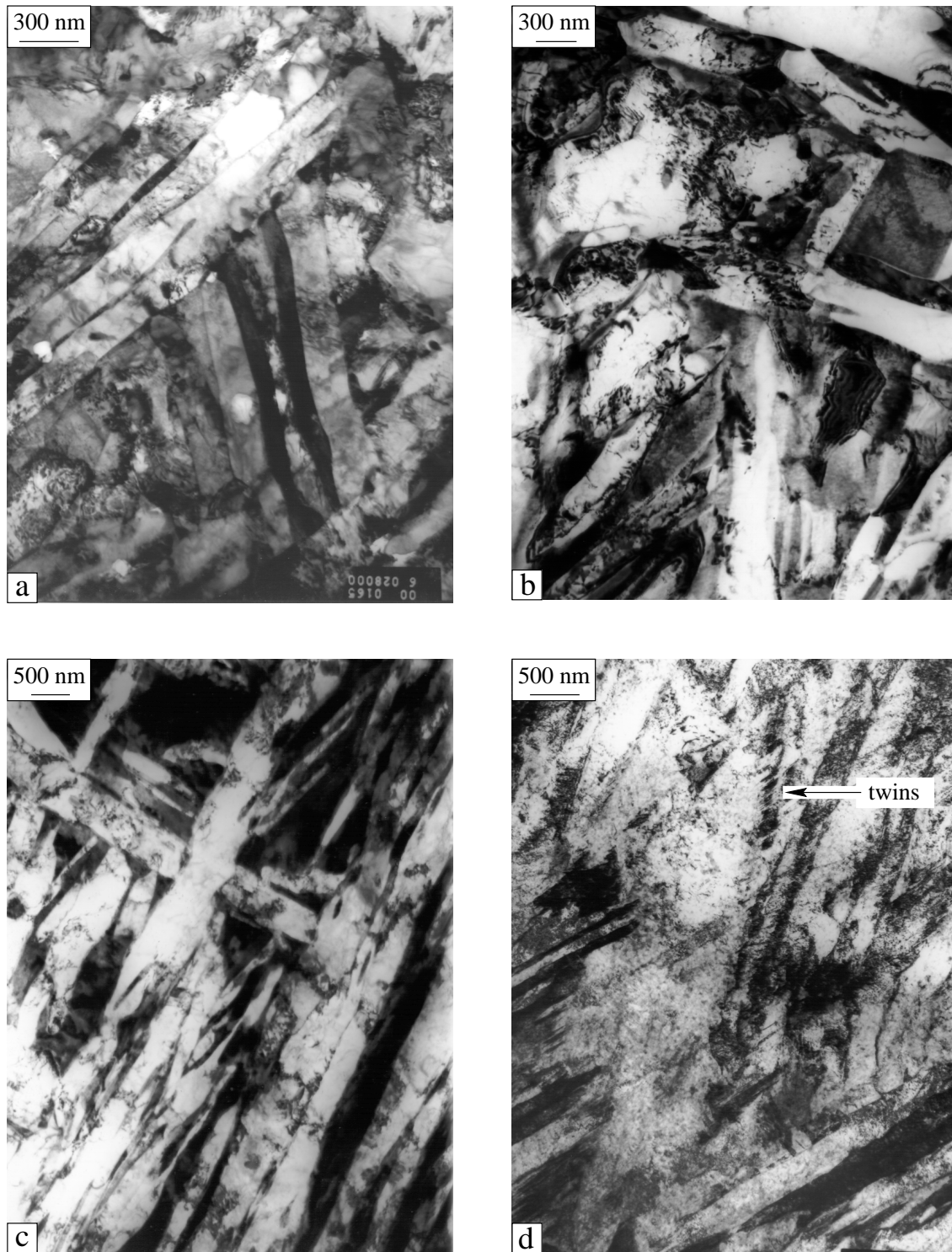
Figure 3.23: TEM micrographs of H7. Plates are visible particularly in micrographs a and c. Micrograph d shows fine twinning behaviour indicating martensite.
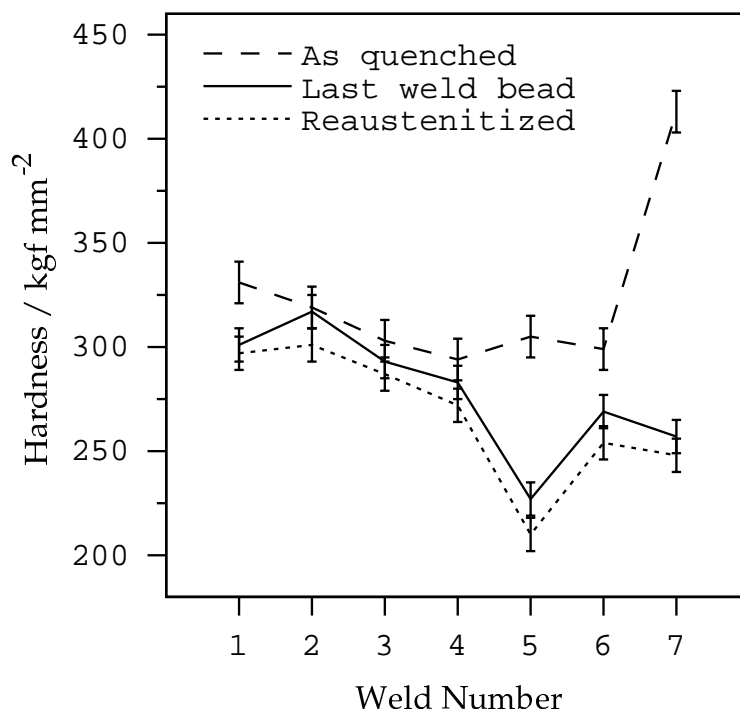
Figure 3.24: Hardness measurements taken from weld macros in comparison to 'as-quenched' values. Data points have been removed for clarity, the bars representing the standard deviation of 6 measurements for each point.

The microhardness of H1 was measured as a function of distance from the surface of the last welded bead. Microhardness values in fine grained materials would be expected to exhibit considerable variation but the aim of this experiment was to evaluate the average hardness of the weld through its cross–section. A Mitutoyo HKV–3 microhardness testing machine was used with a load mass of $100\,\mathrm{g}$ to take hardness readings at $200\,\mu\mathrm{m}$ intervals from the surface of the last bead through the cross–section of H1 (Fig. 3.25). The data show large local variations indicating the effect of a fine scale microstructure. There is some evidence of the equiaxed zone below the last bead at around $2000\,\mu\mathrm{m}$. The most important result of this experiment is the scale of the reduction in hardness from the top of the specimen to the bottom. An average reduction of only $20\,\mathrm{kgf\,mm^{-2}}$ is measured indicating that the cyclic heating of weld beads due to the deposition of later beads has only a limited effect upon the hardness and therefore the strength.
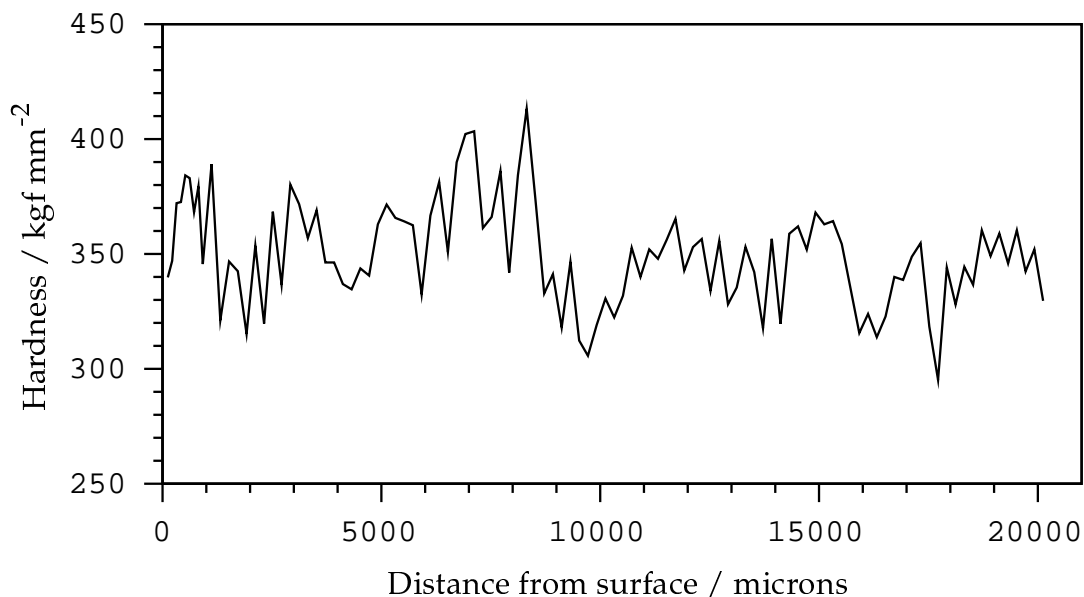
Figure 3.25: The measured hardness across a cross section of H1 normal to the surface.

3.8   Summary

Analysis of the microstructure and properties of the weld series indicated that five variations in the composition of H1 failed to produce an enhancement in tensile properties. The competitive strength and toughness properties of H1 appear to be due to a fine microstructure comprising probably bainitic rather than martensitic plates although at low carbon levels the distinction between these is of little consequence. The absence of carbides and a reasonably low oxygen content promoted good toughness levels which exhibited a low gradient as a function of temperature. Analysis using hardness tests showed only a slight drop in hardness across the weld and also little difference between as–deposited and reaustenitized regions. Weld H1 proved to be an excellent composition despite its original specification being based upon very little data.

Reductions in the levels of alloying additions generally did not help to maintain strength and improve toughness, in fact the toughness improved rather due to reductions in strength. Additions of copper showed some promise in terms of strengthening although the higher oxygen content in the weld prohibited a fair investigation into the effect of Cu on toughness.

Weld H7 showed some promising strength values although the toughness values could not compete with those of H1. The microstructures did indicate that the higher carbon content had promoted martensitic regions in this specimen although hardness values indicated that these did not comprise the majority of the microstructure and such martensitic

regions may in part be responsible for the poor toughness values as the low oxygen content could not be blamed.

Alterations to the chemistries of H1 and H7 were planned based upon the results of these investigations. In the case of H7 it was hoped to eventually produce rival properties to those of H1 whereas H1 was hoped to be improved in terms of yield strength without losing the good toughness properties. These modifications are detailed fully in Chapter 7.

Chapter 4

Models for Yield Strength

4.1 The Sugden–Bhadeshia and Young–Bhadeshia Models

A model designed to predict the strength of an 'as-deposited' steel weld as a function of composition, microstructure and temperature was produced by Sugden and Bhadeshia in 1988 [167]. The strength was in effect factorised into an intrinsic strength of pure annealed iron, solid solution strengthening and a microstructural component. The materials on which the model was based were not specifically 'high strength' welds but the methodology used was general. However, the contributions from individual phases were simply added after scaling according to their volume fractions. Later, Young and Bhadeshia [202] produced a more detailed model by allowing for plastic constraint but this model was not specifically aimed at welding alloys. The purpose of the work presented in this chapter was to see whether these models could be used for the development of high strength steel welds. As will be seen later, the predictions were found to differ significantly from experimental measurements so a good deal of effort was devoted to the investigation of the cause of the discrepancies.

4.1.1 Linear summation approximation

Like many authors, Sugden and Bhadeshia assumed components of strength can be determined independently and then summed to give an overall prediction. Although this may not be strictly true in reality it serves as a good first approximation. Thus the strengths can be modelled as the sum of the contributions from the pure ferrite lattice (σ_{Fe}), the solid solution strengthening (σ_{ss}) and microstructural components (σ_m):-

$$\sigma_y = \sigma_{Fe} + \sigma_{ss} + \sigma_m \tag{4.1}$$

4.1.2   Solid solution strengthening

Solid solution strengthening can be represented as a sum of the contributions from each solute:-

$$\sigma_{ss} = a \text{ wt\% Mn} + b \text{ wt\% Si} + ... \tag{4.2}$$

and the coefficients a, b, ... define the role of the alloying elements. The values for these parameters are usually found by regression analysis of measured data in published literature [98, 121], or directly from experimentation.

4.1.3   Microstructural effects

The microstructure can have a large strengthening effect. Thus a weld metal can have a large range of properties simply by controlling the welding conditions and heat treatment, factors which alter the microstructure. Many of these effects are difficult to quantify so Sugden and Bhadeshia studied three welds, all made with identical heat input, weld geometry, welding speed and interpass temperature. The compositions were adjusted to give different fractions of component phases in order to deduce the strengthening due to each phase. A summation was again assumed as follows:-

$$\sigma_m = \sigma_\alpha V_\alpha + \sigma_a V_a + \sigma_w V_w \tag{4.3}$$

where α, a, w denote allotriomorphic, acicular and Widmanstätten ferrite respectively. V_α, V_a and V_w are the corresponding volume fractions and σ_α, σ_a and σ_w their individual yield stresses obtained from the three experimental welds, so that:-

$$\sigma_y = \sigma_{Fe} + \sigma_{ss} + 27V_\alpha + 402V_a + 486V_w \quad \text{(MPa)} \tag{4.4}$$

σ_{Fe} and σ_{ss} were obtained from the published literature [10, 47, 49, 98, 107, 110, 134, 177, 178].

4.1.4   Comparison with other experimental data

Figure 4.1 shows a comparison of the model against published data [167]. There is considerable scatter in the data but the source of the noise in terms of the different components of the model is not clear.
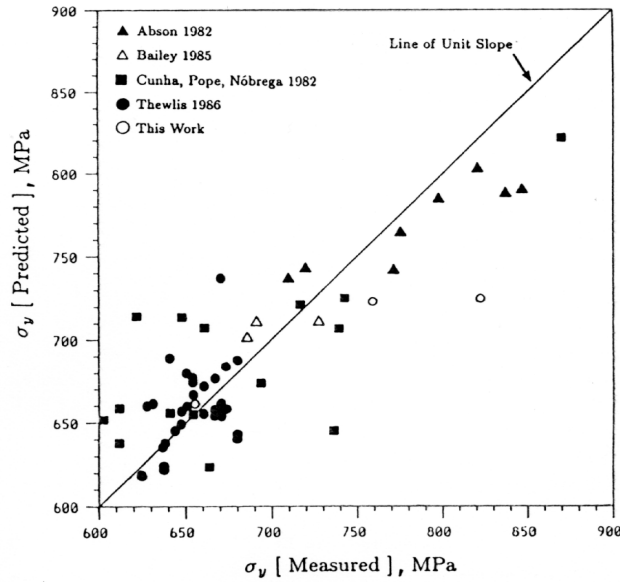
Figure 4.1: Graph of calculated and measured yield strengths of welds [167].

4.2 The Young–Bhadeshia Model

Young and Bhadeshia [202] noticed that a rule of mixtures may not be a good approximation in mixed microstructures, since some experimental data due to Tomita and Okabayashi [186]–[191] indicated a more complex behaviour when the fraction of martensite in a mixture of martensite and bainite was varied.

4.2.1 The strength of martensite and bainite

Adopting similar methods to those described earlier the total strength of either martensite or bainite σ, as individual phases was written as follows [202]:-

$$\sigma = \sigma_{Fe} + \sigma_{ss} + \sigma_c + K_L(\bar{L}_3)^{-1} + K_D\rho_D^{1/2} + K_p\Delta^{-1} \qquad (4.5)$$

where σ_{Fe} and σ_{ss} are as in Eqn. 4.1. σ_c is the solid solution strengthening effect of carbon, $\bar{L}_3$ is a measure of the bainite/martensite plate size, ρ_D is the dislocation density and Δ the distance between carbide particles if any are present. The constants K_L, K_D and K_p were obtained from the literature. Notice that microstructural effects are dealt with more explicitly in terms of dislocation and precipitation hardening theory and a grain size effect via $\bar{L}_3$ (this is different from the normal Hall–Petch equation because of the fine scale of bainite and martensite plates).

58

4.2.2 Carbon in bainite and martensite

For bainite the maximum solubility of carbon is assumed to be 0.03 wt%, whereas martensite inherits and retains the composition of the parent austenite. For bainite with its small concentration of carbon, there is justification for the strength to vary with the square root of the carbon concentration [53, 165]:-

$$\sigma_c = 1722.5x^{1/2} \tag{4.6}$$

where σ_c is carbon's contribution to the solid solution strength (in MPa) and x is the concentration of carbon in wt%. For martensite with its higher concentrations of carbon, an equation due to Winchell and Cohen [196] was used to avoid the overestimation of strength by adopting an $x^{1/3}$ relationship (identical units):-

$$\sigma_c = 1171.3x^{1/3} \tag{4.7}$$

Figure 4.2 indicates how Equation 4.6 would overestimate the strength at high carbon concentrations in comparison with Equation 4.7.
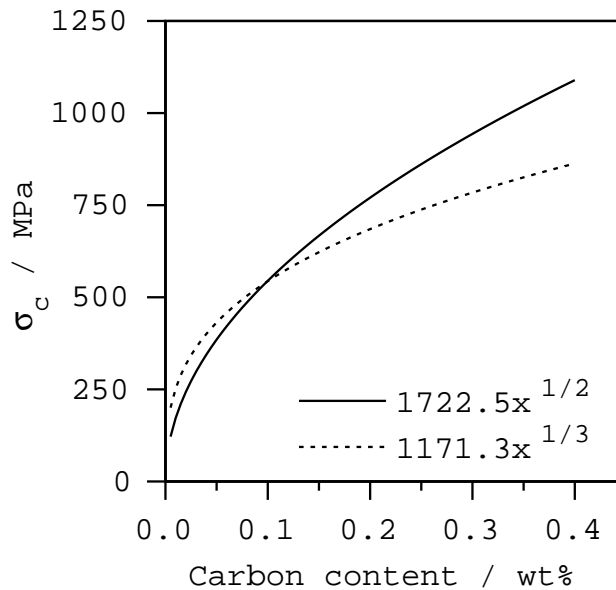
Figure 4.2: Solid solution strengthening effect of carbon due to Equations 4.6 and 4.7.

4.2.3 The effect of dislocations

The bainitic and martensitic transformations are associated with a shape deformation. If this deformation is plastically accommodated then the final microstructure may contain

a large density of dislocations. Plastic accommodation and recovery effects are both temperature dependent and consequently an equation representing the dislocation density should be a strong function of temperature as shown by Takahashi and Bhadeshia [176]:-

$$\log(\rho_D) = 9.2840 + \frac{6880.73}{T} - \frac{1780360}{T^2} \tag{4.8}$$

where T is in K and ρ_D is the dislocation density in m^{-2}. This equation relates to data taken in the range 570–920 K. Whilst for the most part this equation is sufficient, some martensites form below this temperature if the parent austenite has become highly enriched due to extensive bainitic transformation for example. Rather than extrapolating this equation to low temperatures, the dislocation density at all temperatures below 570K was taken as being identical to that at 570 K. From Keh and Weissmann [103], the strengthening due to dislocations is given by:-

$$\sigma_\rho \approx 7.34 \times 10^{-6} \rho_D^{1/2} \tag{4.9}$$

where σ_ρ is in MPa.

4.2.4 The effect of the lath size

In sub-micrometre sized grains, the mechanism of yielding is found to be different to the classical effect described by the Hall–Petch equation where dislocation sources act within individual grains. Here the dislocation sources are found at the grain boundaries. Bainite and martensite are found in high strength steels in the form of plates with typical aspect ratios of 0.02–0.05 (thickness to length). The increase in strength due to the plate size is given by:-

$$\sigma_G \approx 115(\bar{L}_3)^{-1} \tag{4.10}$$

where σ_G is in MPa and $\bar{L}_3$ is the mean lineal intercept taken on random sections and at random angles to the length of any plate section. The coefficient 115 has been obtained from regression analysis of measured data from martensitic and bainitic microstructures [117, 132]. A typical trend is illustrated in Fig. 4.3. It is obvious from this that the strength is very sensitive to $\bar{L}_3$, which is typically $\approx 0.3\,\mu$m. Errors in $\bar{L}_3$ will lead to considerable errors in the calculated strength.

The final term in Equation 4.5 assumes a uniform dispersion of cementite particles so precipitation hardening is given by:-
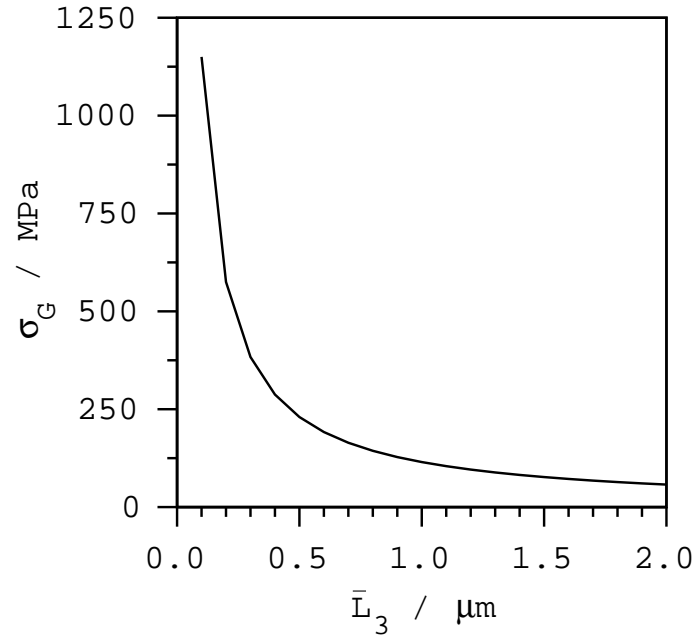
Figure 4.3: Sensitivity of strengthening to $\bar{L}_3$.

$$\sigma_\theta \approx 0.52 V_\theta \Delta^{-1} \quad \text{MPa} \tag{4.11}$$

where V_θ is the cementite volume fraction and Δ is the cementite interparticle spacing.

4.2.5 Partitioning of carbon

There are many cases where the formation of a phase changes the chemical composition of the residual austenite. This is relevant in the present work where bainite formation is not accompanied by the precipitation of carbides. Thus, the carbon content of the residual austenite (x_γ) is from a mass balance argument given by:-

$$x_\gamma = \frac{\bar{x} - V_b x_b}{1 - V_b} \tag{4.12}$$

where $\bar{x}$ is the atomic fraction of carbon in the alloy, V_b and x_b are the volume fraction of bainite and the atomic fraction of carbon within the bainite respectively.

The M_s temperature of the austenite is therefore modified from its original value M_s^o. Steven and Haynes [166] found that the M_s temperature could be represented as:-

$$M_s = M_s^o - 564(c_\gamma - \bar{c}) \tag{4.13}$$

where the coefficient 564 comes from the work of Steven and Haynes [166] and c_γ and $\bar{c}$ denote the carbon concentrations of the austenite alone and the average for the alloy

in weight% respectively. The actual M_s temperature is important because it is used to estimate the dislocation density ρ_D of martensite.

Many strong alloys are used in a tempered condition to improve toughness. Bainite is relatively unaffected by tempering treatments that do not significantly alter the grain size because the amount of carbon in solution is very small. This is not the case for martensite, whose strength in the tempered condition, σ_{MT} is given by [176]:-

$$\sigma_{MT} = \sigma_M - \zeta(t_1)\{\sigma_M - \sigma_{Meq}\} \tag{4.14}$$

where σ_M is the strength of virgin martensite, σ_{Meq} is the strength of martensite containing the equilibrium carbon concentration of ferrite (equal to bainite) and the Avrami function ζ is:-

$$\zeta = 1 - \exp[-kt_1{}^{n_1}] \tag{4.15}$$

with the time exponent $n_1 = 0.62$ [176]. t_1 is the tempering time in hours and k is a function of the form:-

$$k = k_0 \exp\{-Q_k/RT\} \tag{4.16}$$

the value for k_0 being $4.07 \times 10^4\, \bar{x}^{0.635}\, h^{-0.62}$. R is the gas constant, T the absolute temperature and $Q_k = 33598\,\mathrm{J\,mol^{-1}}$. Note that the fitting constants n_1 and k must depend upon the steel.

4.2.6 The strength of austenite

The model deals with austenite in a less comprehensive manner than in the cases of bainite and martensite. The strength of austenite (σ_γ) is expressed empirically as:-

$$
\begin{aligned}
\sigma_\gamma \;=\;& 15.4 \times \{4.4 + 23.0\,\mathrm{C} + 1.3\,\mathrm{Si} + 0.24\,\mathrm{Cr} + 0.94\,\mathrm{Mo} \\
& + 1.2\,\mathrm{V} + 0.29\,\mathrm{W} + 2.6\,\mathrm{Nb} + 1.7\,\mathrm{Ti} + 0.82\,\mathrm{Al} + 32.0\,\mathrm{N}\}
\end{aligned}
\tag{4.17}
$$

where elemental compositions are in weight% and σ_γ is in MPa. Note the relative magnitudes of the coefficients.

It is assumed that small volume fractions of austenite have little effect upon the overall strength of mixed microstructures. σ_γ is typically $\approx 230\,\mathrm{MPa}$, which in a 95% bainite 5% austenite microstructure accounts for only 1% of the total strength assuming a law of mixtures.

4.2.7   Combination of microstructures

The yield strength of a multiphase material can be increased by plastic constraint effects. The effect of plastic constraint is illustrated by the fact that the strength of a brazed joint frequently exceeds that of the braze material alone. A similar effect is expected in a mixed microstructure. Tomita and Okabayashi [186] found a peak in strength as a function of bainite volume fraction in a mixture of martensite and bainite (Fig. 4.4).
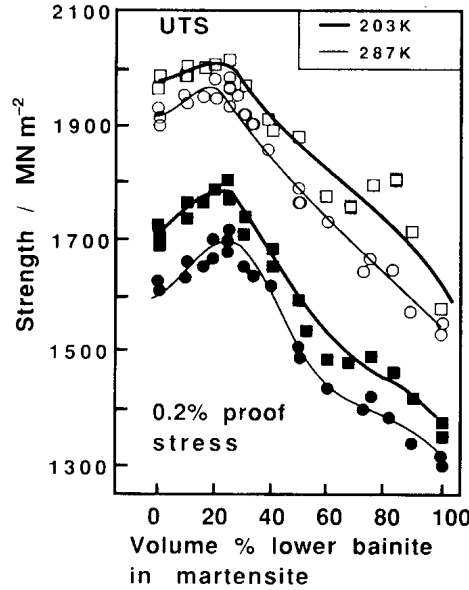
Figure 4.4: Variation in yield stress as a function of bainite volume fraction (data from Tomita and Okabayashi [186]).

To obtain a simple solution for constraint, Young and Bhadeshia assumed that the normalised thickness of the braze is equivalent to the volume fraction of bainite:-

$$\sigma_B \approx \sigma'_B(0.65\exp\{-3.3V_b\} + 0.98) \le \sigma_M \tag{4.18}$$

where σ_B and σ'_B are the strengths of constrained and unconstrained bainite respectively and V_b is the volume fraction of bainite. The net yield stress value is calculated as in [167]:-

$$\sigma_y = V_b\sigma_B + V_m\sigma_M + V_\gamma\sigma_\gamma \tag{4.19}$$

where V_b, V_m and V_γ are the volume fractions of bainite, martensite and austenite respectively. Figure 4.5 shows that the model correctly predicts experimental data [186].
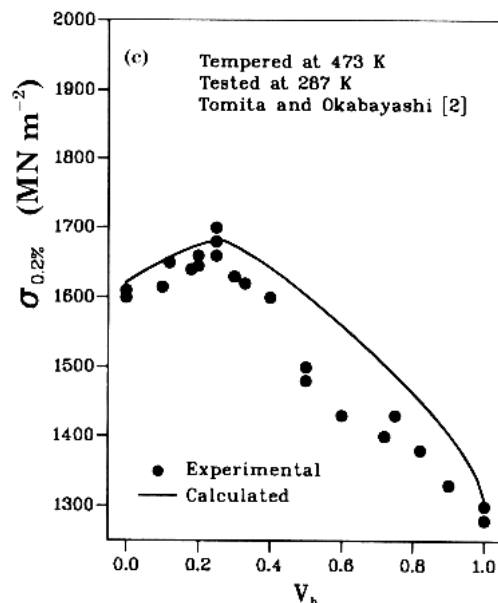
Figure 4.5: Example of the predicted and measured [186] strengths of mixed bainite-martensite microstructures as a function of bainite volume fraction, showing good agreement.

4.3 Application to ultra-high strength welds

The experimental welds contain little carbon so there should be little difference in the strength of martensite and bainite. Bainite would be expected to be weaker due to the partitioning of carbon to austenite. Figure 4.6 is a comparison of calculations against experimental tensile tests, with the former greatly exceeding the experimental data. The calculations assumed a microstructure comprising 90% bainite and 10% austenite, and a plate thickness of $0.3\,\mu$m. Reducing the austenite content to 5% increased the calculated strength by less than 50 MPa. When the bainite was replaced with martensite, the estimated strength of H1 and H7 increased by more than 300 MPa. Note that H1 is representative of welds H1–H6.

4.4 Cause of discrepancies

A possible cause for the overestimation of strength could be that the weld microstructures are not known with sufficient accuracy. An experiment was designed to allow a better test of the model using a fully martensitic microstructure. The strength of the martensite had to be estimated using hardness tests because of material limitations.

It is often stated that the hardness H and the yield stress (σ_y, MPa) are related as
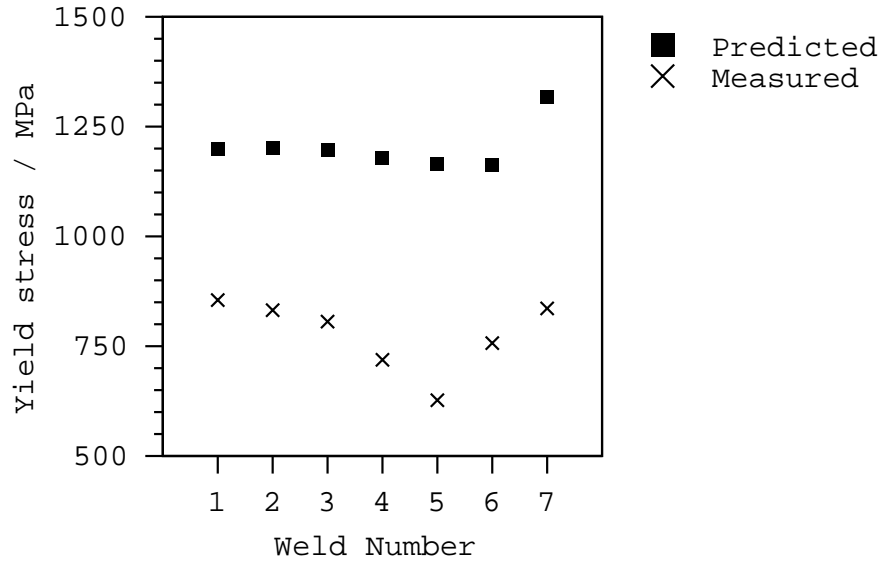
Figure 4.6: Comparison between the predictions of the Young–Bhadeshia model and the measured yield stresses of the weld series. Here H1–H7 welds are denoted by numbers 1–7.

follows [60]:-

$$\sigma_y \approx \frac{H}{3} \tag{4.20}$$

The factor of three can be justified on the basis of plastic constraint [60] but the estimate is based upon zero work hardening. Speich and Warlimont [165] thus deduced the relationship empirically based on low carbon martensites (Fig. 4.7). It was this which was used to interpret the hardness data.

Speich and Warlimont described their data with the following equation:-

$$\sigma_y = 2.59H_v - 80 \tag{4.21}$$

where σ_y is in MPa and H_v in kgf mm^{-2}.

Small specimens $6 \times 6 \times 2$ mm were heated for 5 minutes at 1000 °C and then quenched into water. Vickers Hardness was measured using a 1 kg load. Fig. 4.8 compares the results with two microstructural calculations assuming a mixed microstructure of 90% α' and 10% γ and fully martensitic specimens. It is interesting that although the discrepancy with experiments remains, the trend seems to be correctly predicted. The calculated components for a fully martensitic H1 weld are shown in Table 4.1.
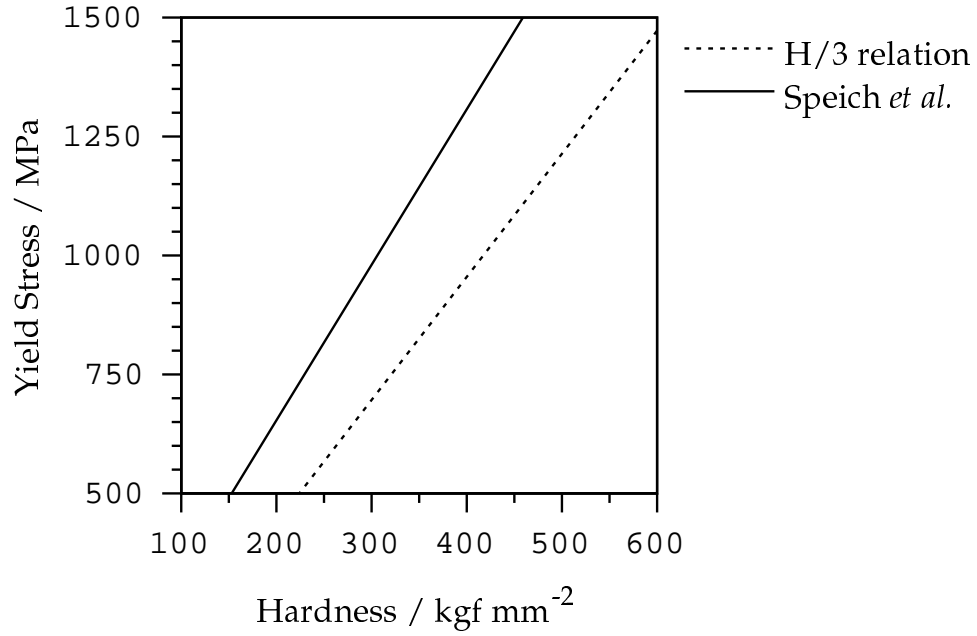
Figure 4.7: A comparison of two relationships between yield stress and hardness.
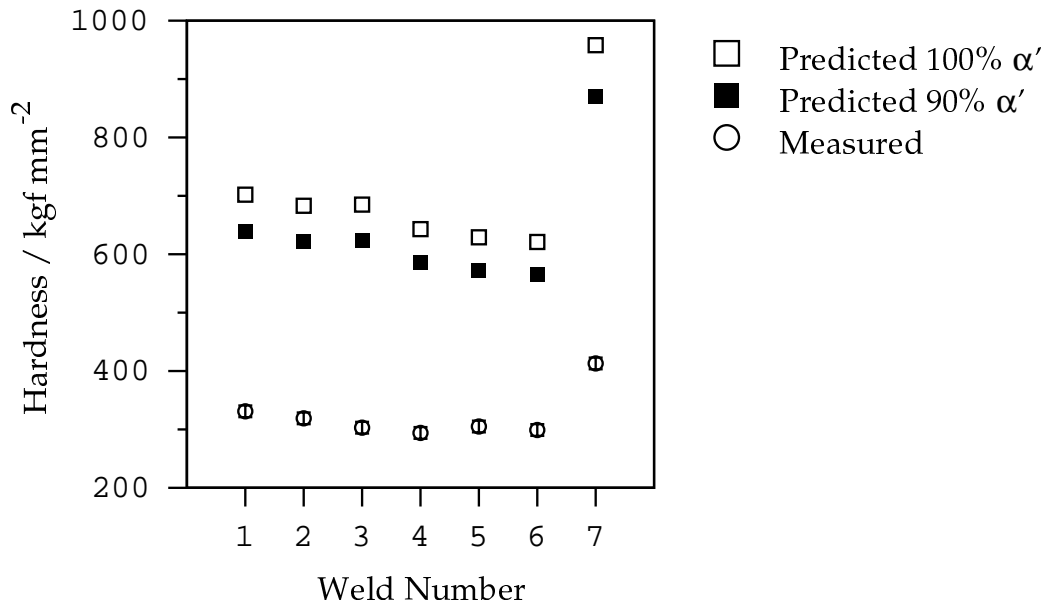
Figure 4.8: Measured and calculated (90% and 100% martensitic) hardness values for the weld series.

Mechanism	Strength Contribution / MPa
Lattice strength	221
Solid solution	290
Dislocations	463
Grain size	383
Dissolved carbon	381
Total	1738

Table 4.1: Calculated contributions to the yield strength of H1 with a fully martensitic microstructure.

It was decided to measure the fundamental strength of the lattice, that of iron with solid solution strengthening, as this provided the greatest contribution to the predicted strength.

4.5 Measurement of the intrinsic lattice strength

A direct measurement of the intrinsic strength (that is, in the absence of any microstructure) can be made after severe tempering. The tempering temperature was chosen on the basis of dilatometric data.

4.5.1 Determination of the Ac_1 and Ac_3 temperatures

Tempering must naturally be performed at a high temperature but one which is below Ae_1, beyond which austenite begins to form. Although Ae_1 corresponds to the equilibium transformation temperature, it is approximated here by Ac_1 determined during continuous heating at $0.05\,°C\,s^{-1}$. A *Thermecmastor Z* thermomechanical simulator (Chapter 5) was used to measure Ac_1 for H1 and H7 which are representative of the entire series. Figure 4.9 shows an example of the measured dilatation of H1 as a function of temperature. The results of these experiments are presented in Table 4.2. The Ae_1 temperature should be somewhat below Ac_1, so to be absolutely certain of avoiding austenite formation, the heat treatment was carried out at a lower temperature of $550\,°C$. It is nevertheless high enough to promote grain growth.
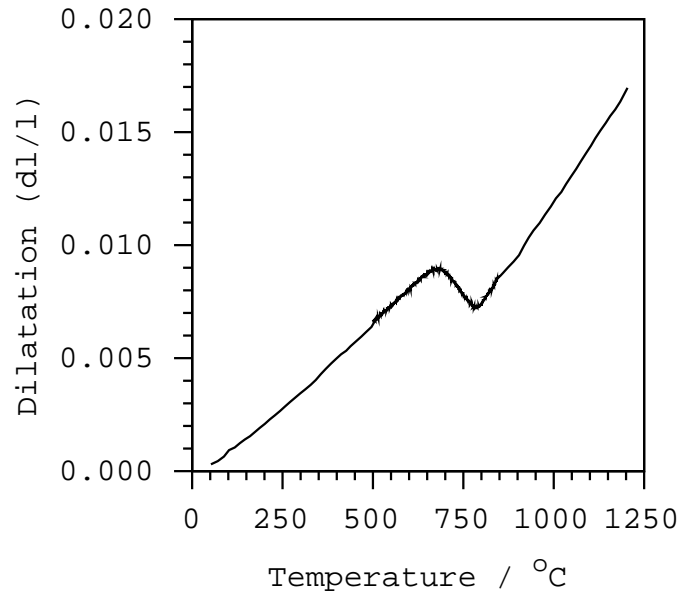
Figure 4.9: Example dilatometer data for H1 during a heating cycle.

Specimen	Ac_1 / °C	Ac_3 / °C
H1	645 ± 10	780 ± 10
H7	790 ± 10	830 ± 10

Table 4.2: Measured Ac_1 and Ac_3 temperatures for H1 and H7 at a heating rate of $0.05\,°\mathrm{C\,s^{-1}}$.

4.5.2   Experimental procedure

Specimens of H1–H7 of approximate dimensions 4 mm × 4 mm × 10 mm were sealed in silica tubes in a protective argon atmosphere at a pressure of $\approx$ 0.1 bar. The heat treatment consisted of 2 months at 550 °C, followed by air cooling. Small sections (4 mm × 4 mm × 4 mm) of material were removed from each sample after 2 months. Grinding and polishing operations were performed to a 1 μm diamond grit finish. All specimens were etched with a 4% Nital solution and examined using a reflected light microscope.

4.5.3   Results after 2 month heat treatment

Optical microscopy revealed that the 2 month heat treatment was not sufficient to remove all of the fine scale microstructure (Figs. 4.10, 4.11). The microstructures were remarkably stable. Local recrystallisation was seen in some areas (arrows, Fig. 4.10). However, in general the recrystallised grains could only be found in isolated regions of specimens H1–H7. The fine scale microstructures persisted as the majority of the microstructure, fine plates about 1 μm thick being visible in many of the micrographs.

The tempering heat treatment was therefore continued for a further 2 months in order to greatly increase the scale of the microstructure.

4.5.4   Results after 4 month heat treatment

Fig. 4.12 shows that after four months the fine plate microstructure had been removed in specimens H1 and H4. However, H2 and H5 showed some recrystallised grains but remnants of a finer grain structure persisted. Steel H6 resisted coarsening with many fine grains still visible in the microstructure. It is likely that the temper resistance of H6 may be due to copper precipitates as H6 is otherwise similar to H4 and H5 which are less resistant to tempering. The copper precipitates are expected to Zener pin grain boundaries [96].

4.6   Hardness testing of tempered specimens

The purpose of the tempering experiments was to "remove" the microstructure so that the lattice strength could be measured. Hardness measurements were made in regions that had obviously recrystallised. Such regions could not be found in H2 and H5. Figure 4.13 shows the considerable drop in hardness when compared with the 'as–welded' values. The results represent the mean of six hardness measurements from each specimen after 2 and
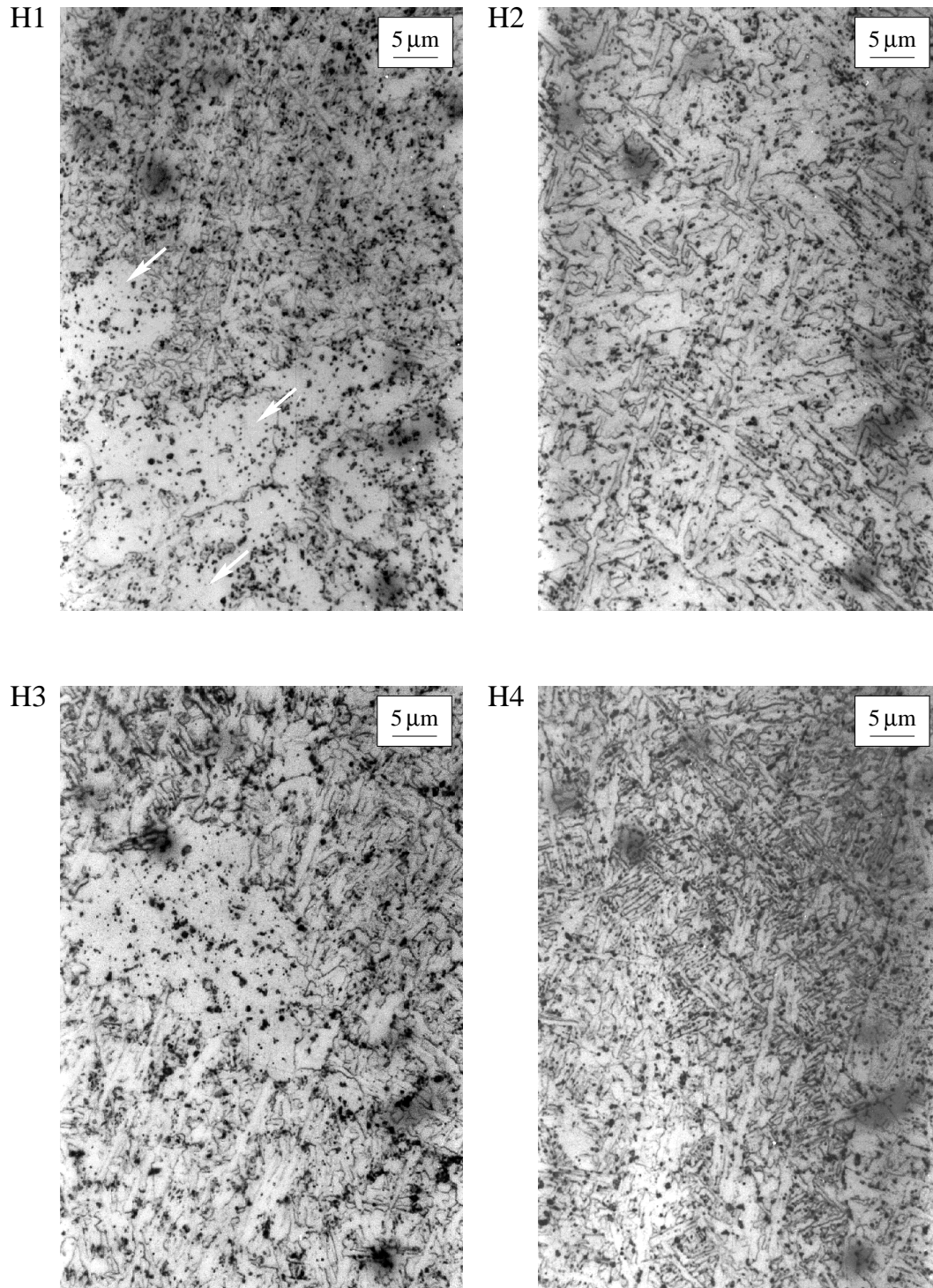
Figure 4.10: Optical micrographs of specimens from welds H1, H2, H3 and H4 after 2 months in a 0.1 bar Ar atmosphere at 550 °C.
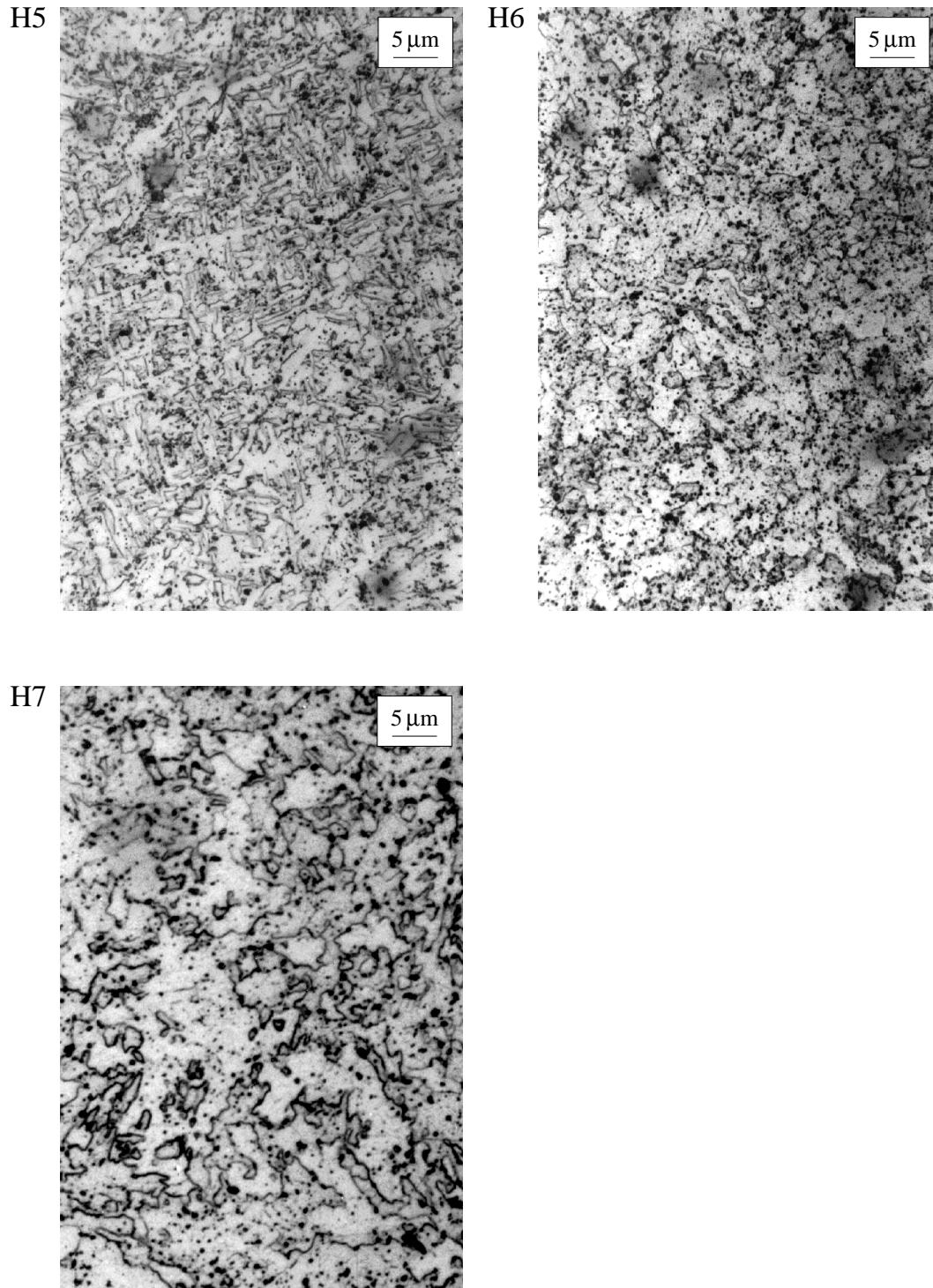
Figure 4.11: Optical micrographs of specimens from welds H5, H6 and H7 after 2 months in a 0.1 bar Ar atmosphere at 550 °C.
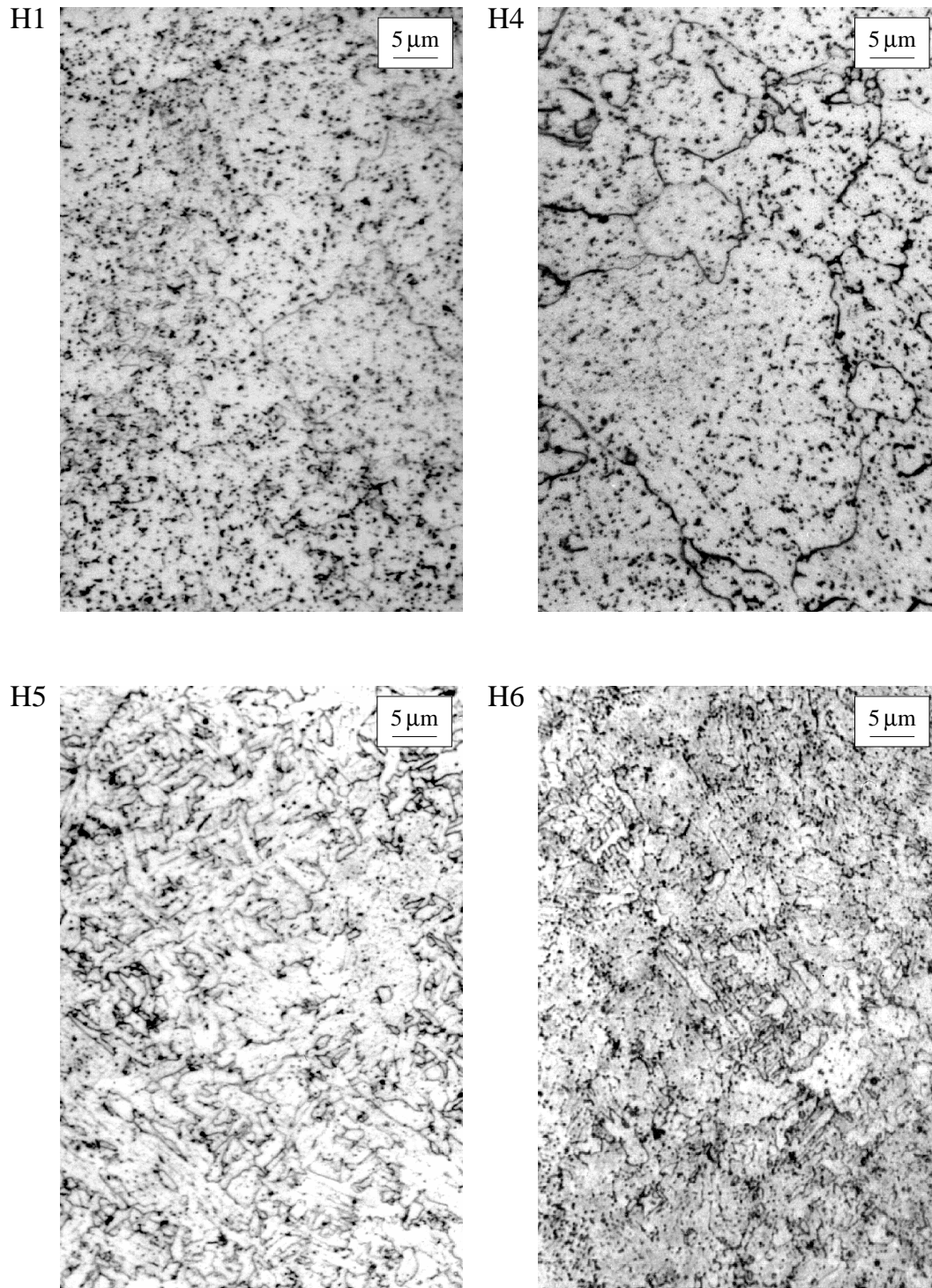
Figure 4.12: Optical micrographs of specimens from welds H1, H4, H5 and H6 after 4 months in a 0.1 bar Ar atmosphere at 550 °C. Specimen H6 exhibits a strong tempering resistance.

4 months of tempering. They correlate with optical microscopy evidence in that, after 2 months specimens H4 and H5 showed the smallest reduction in hardness.
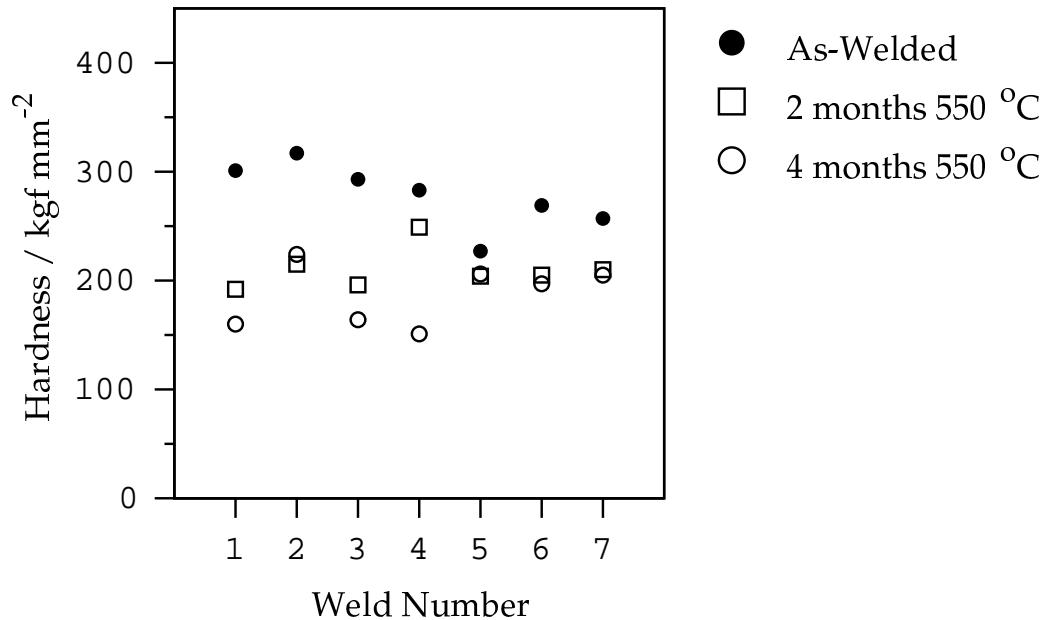
Figure 4.13: Macrohardness measurements on H1–H7. Error bars have been removed for clarity.

A further drop in hardness was generally evident after 4 months. It is to be expected that H1–H5 should exhibit approximately similar hardness values as their compositions are closely related. Variations in the carbon concentration should not show up significantly after such severe tempering. The higher values of H2, H5 and H6 were thought to be due to fine microstructure retention.

4.6.1 Comparison of Macro and Microhardness values

Due to incomplete recrystallisation, microhardness measurements were performed on the welds tempered for 4 months using a $100\,g$ load. A minimum of 5 measurements were taken only in regions of recrystallised grains. The data are presented in Figure 4.14. Welds H1–H5 show similar levels of microhardness (≈ 160 VPN). Equivalent macrohardness measurements correlate well except in H2 and H5 where few recrystallised regions were found. No sufficiently recrystallised regions were found in H6 sample and the corresponding measurments indicate higher hardness levels. H7 exhibited a higher hardness even in recrystallised regions which could be explained by carbide precipitation. Macrohardness and microhardness values are not generally equivalent, the latter often being

higher [14, 142]. However, in the microhardness experiments a high enough load was used to give comparative values with macrohardness data.
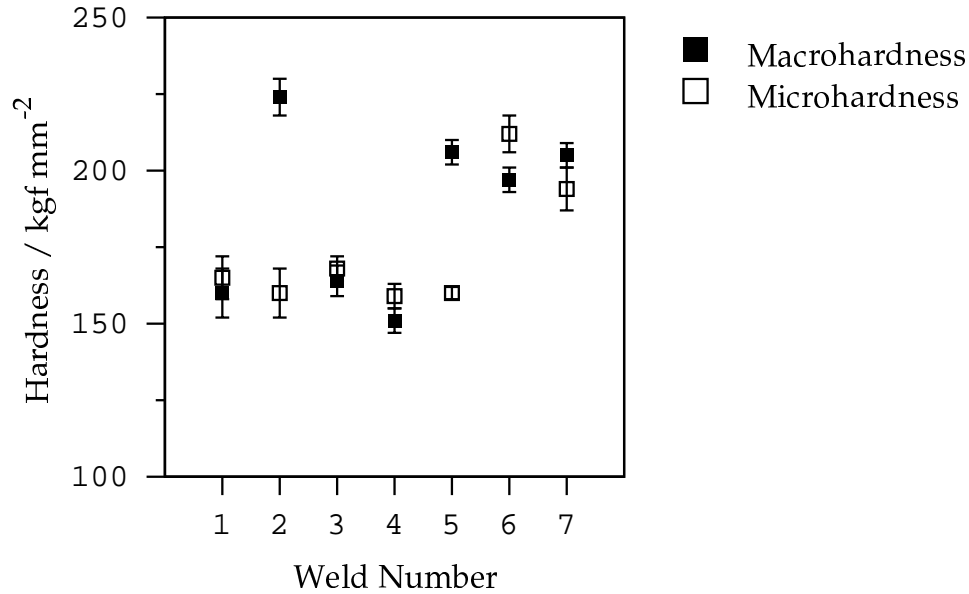
Figure 4.14: Comparison between macrohardness and microhardness measurements on the weld series.

4.7 The lattice strength

Comparison between calculated lattice strengths and measured values converted from microhardness data (Eqn. 4.20) show good agreement (Fig. 4.15), the H6 value showing great discrepancy due to the lack of suitable data from recrystallised grains.

It is evident that the intrinsic lattice strength is therefore not responsible for the discrepancy between calculated and measured strengths.

4.8 Other causes of discrepancies

Four other strength contributions are considered in Equation 4.5, although the last, $K_p \Delta^{-1}$ deals with carbide precipitate strengthening and is therefore not relevant here. Examination of the literature revealed some causes of error in the model.

The model uses data from Naylor [132] to incorporate the strengthening due to the lath size, σ_G :-
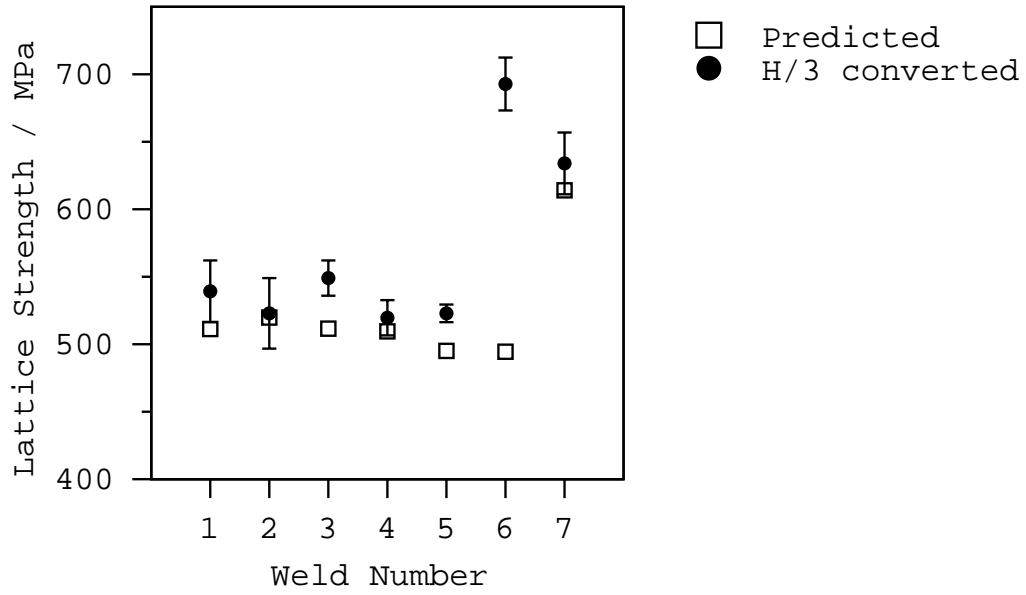
Figure 4.15: The strength of the lattice shows good agreement in terms of both predicted and converted measured values.

$$\sigma_G \approx k_L(\bar{L}_3)^{-1} \qquad \text{MPa} \qquad\qquad (4.22)$$

where $\bar{L}_3$ is taken as a mean lineal intercept (μm) and $k_L = 115\,\mu$m MPa. However, this equation was found to be incorrect as the actual equation due to Naylor was:-

$$\sigma_G \approx k_M(\bar{M})^{-1/2} \qquad \text{MPa} \qquad\qquad (4.23)$$

where $\bar{M}$, detailed below, was originally taken as being equal to $\bar{L}_3$ in the model and $k_M = 115\,\mu$m$^{1/2}$ MPa. Note the different exponent which has a large effect upon σ_G ($\approx$150 MPa) when typical values of $\bar{L}_3$ are used such as $0.3\,\mu$m (Fig. 4.16):-

In addition, the model assumed equality between $\bar{L}_3$ and $\bar{M}$ used by Naylor. $\bar{M}$ represents the average slip plane length in a lath of width, ϵ_l and length, d_p (i.e. the packet diameter) and is evaluated as:-

$$\bar{M} = \frac{2}{\pi}\left\{\epsilon_l \ln\left|\tan\left(\frac{\arccos(\epsilon_l/d_p)}{2}\right)\right| + \frac{\pi}{2}d_p - d_p\arccos(\epsilon_l/d_p)\right\} \qquad (4.24)$$

This function takes into account both the large strengthening effect of the lath size and the lesser effect of the packet as a whole. Values of $\bar{M}$ are thus larger than those of $\bar{L}_3$ giving a smaller strengthening effect. The use of $\bar{M}$ has better justification as the
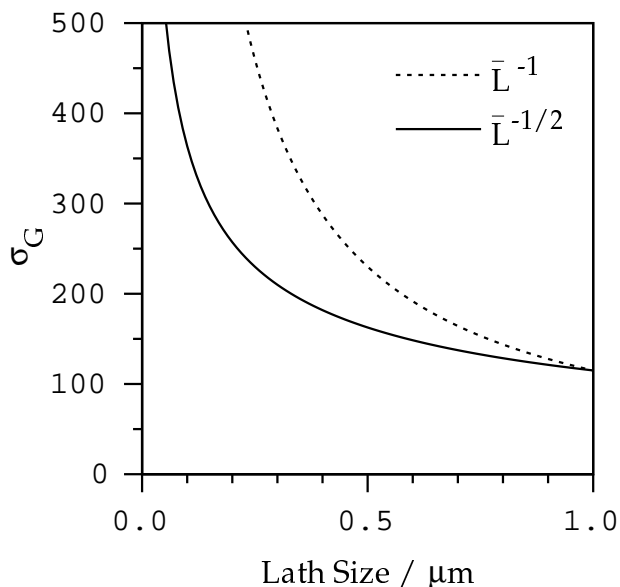
Figure 4.16: Comparison between lath strengthening terms.

coefficient in Equation 4.22 was evaluated using this parameter. Modifications to the model were made to implement the use of $\bar{M}$.

The model considers the effects of dislocations and carbon 'solid solution' strengthening separately. However, literature indicates an implicit relationship between these two parameters [134, 104]. Whilst the data used to describe the effect of carbon did separate the intrinsic lattice strength and the lath size effect, dislocations were not considered in isolation [165]. An improvement to the model was therefore made by assuming a dislocation strengthening effect via that observed due to carbon.

The predictions of the original and modified model in comparison to measured yield strengths of H1–H7 are shown in Figure 4.17 in which 95% bainitic 5% austenitic microstructures are assumed. Generally the predictions were much improved. As before similar strengths are predicted for welds H1–H5, the H6 value also being similar as the model does not consider copper. It should be noted that the behaviour of very low carbon alloys (below ≈ 0.03 wt% i.e. H4–H6) becomes inaccurate with this model due to the effects of carbon's solubility in ferrite.

Similar calculations for fully martensitic microstructures also exhibit improvement as shown in Figure 4.18. Here the trends are well modelled despite the overprediction of the values which again notably rely upon the empirical conversion between yield strength and hardness (Eqn. 4.21).

76
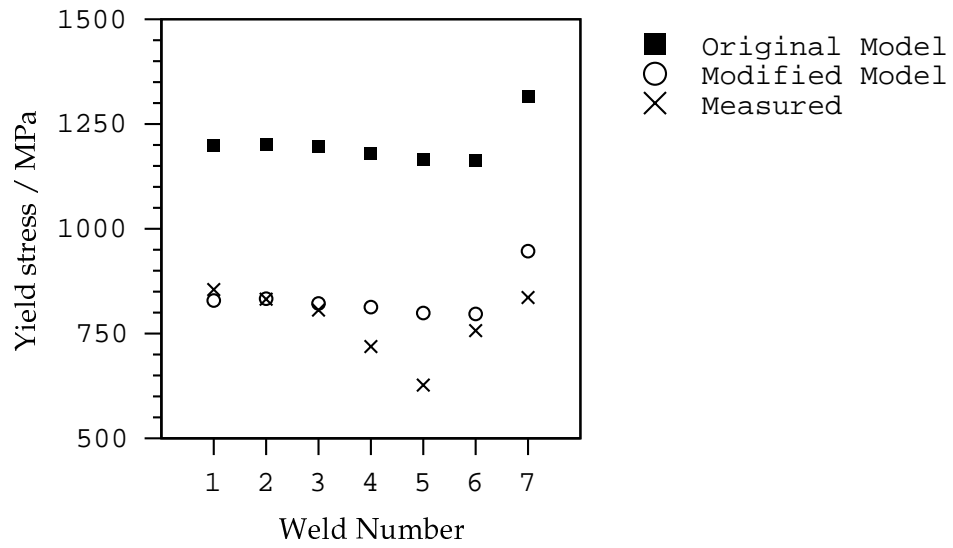
Figure 4.17: Effect of modifications upon model strength predictions of weld H1–H7.
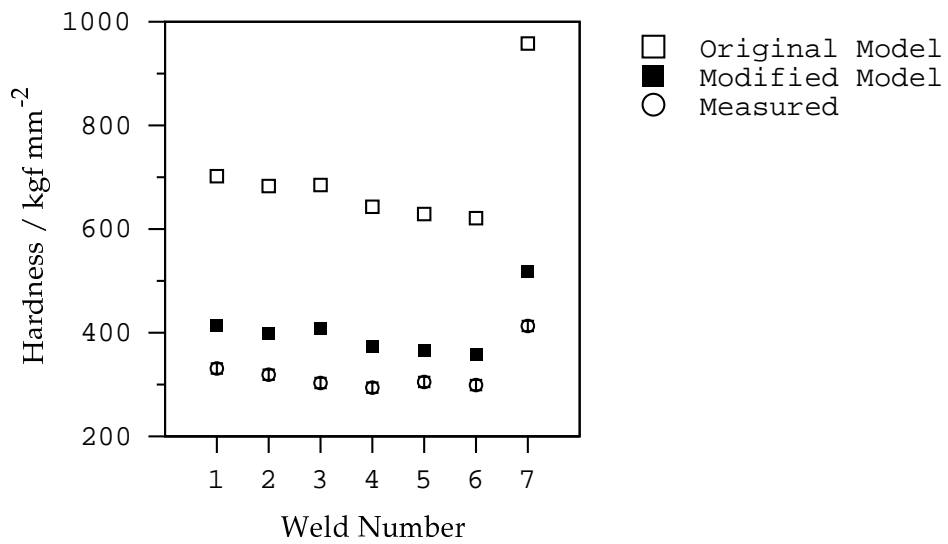
Figure 4.18: Predicted and measured hardness values for 100% martensitic specimens.

4.9   Conclusions

A large discrepancy was found between the predicted and measured strengths of high strength weld alloys both in the 'as–welded' and quenched states. The 'removal' of microstructures using long heat treatments indicated the validity of linear summation of alloy solid solution strengthening effects. Following identification of possible causes for overprediction, modifications were made to more accurately model the effect of the fine scale microstructure and to more realisitically consider the role of dislocations. Use of the modified model indicated that the strength of low carbon weld microstructures can be predicted with reasonable accuracy.

Chapter 5

The effect of the Interpass Temperature upon weld H1

It has been noticed during production that weld deposits of composition similar to H1 sometimes exhibit large variations in their yield strength (Table 5.1). Weld 15 in this table shows a particularly low yield strengths but high ultimate tensile strength (UTS). Despite weld 16's similarity in composition to 15, the yield strength is higher by over 200 MPa.

As with all welds, some scatter is to be expected within experimental results due to the combination of complicated thermal histories, microstructures and defects. In this case, the observed variations were, on the basis of experience, judged to be too large to be attributed to such effects. Occasional reductions in the yield strength are not tolerable from either a design or a safety standpoint and hence there is a desire to identify the cause of this effect, which is not appreciated by customers.

The purpose of the work detailed within this chapter was to investigate the possible causes for the scatter in the yield strength. A combination of modelling and experimental techniques are described culminating in the production of experimental welds in an attempt to produce a variable yield strength in a controlled manner.

5.1 Measured yield strength variations

Weld H1 typically has a yield strength of around 850 MPa with an ultimate tensile strength (UTS) of 920 MPa. However, it has been observed that reductions of up to 150 MPa can occur in the yield strength. The corresponding UTS values appear to change to a much smaller extent. The variations in the tensile properties are not explained by minute

Weld	C	Mn	Si	Cr	Ni	Mo	Yield / MPa	UTS / MPa
1	0.049	1.95	0.27	0.38	2.93	0.53	887	903
2	0.048	1.81	0.28	0.38	2.45	0.50	828	892
3	0.043	2.09	0.28	0.46	3.07	0.61	898	964
4	0.044	2.23	0.33	0.53	3.25	0.64	960	1005
5	0.043	1.81	0.28	0.45	3.32	0.67	923	963
6	0.048	2.07	0.28	0.44	2.65	0.55	952	967
7	0.050	2.02	0.27	0.46	2.65	0.58	923	956
8	0.056	2.12	0.29	0.45	2.77	0.59	948	987
9	0.054	1.96	0.27	0.46	2.65	0.55	879	906
10	0.039	1.83	0.21	0.41	3.01	0.58	934	956
11	0.039	1.70	0.30	0.45	2.87	0.55	875	895
12	0.051	1.71	0.14	0.44	3.25	0.62	836	875
13	0.060	1.91	0.17	0.61	3.12	0.67	889	937
14	0.078	1.94	0.65	0.63	1.94	0.46	902	953
15	0.070	2.06	0.30	0.46	3.10	0.65	698*	1049
16	0.070	1.99	0.31	0.44	3.00	0.65	904	974

Table 5.1: The major alloying additions and tensile properties of 16 welds of similar composition to OK75.78. Elemental values are in weight%. Weld 15 has a particularly low yield strength value. Data from ESAB AB [172]. All welds were fabricated with the MMA process using a heat input of $1\,\mathrm{kJ\,mm^{-1}}$.

variations in the metal composition. The apparent sensitivity of the yield strength in H1 to one or more unidentified factors was first tackled using a trained neural network. The nature of a neural network is described first, to be followed by the application of the method towards the understanding of the strength variations.

5.2 Neural network method

In regression analysis, data are best–fitted to a specified relationship which is usually linear. The result is an equation in which each of the inputs x_j is multiplied by a weight w_j. The sum of all such products and a constant θ then gives an estimate of the output, y:-

$$y = \sum_j w_j x_j + \theta \qquad (5.1)$$

It is well understood that there are dangers in using such relationships beyond the range of fitted data.

A neural network is a much more general method of regression analysis. As before, the input data x_j are multiplied by weights, but the sum of all these products forms the argument of a hyperbolic tangent. The output y is therefore a non-linear function of x_j, the function usually chosen being the hyperbolic tangent because of its flexibility [123]–[127]. The exact shape of the hyperbolic tangent can be varied by altering the weights (Fig. 5.1a). Further degrees of non–linearity can be introduced by combining several of these hyperbolic tangent functions (Fig. 5.1b), so that the neural network is able to capture almost arbitrarily non–linear relationships. For example, the effect of chromium upon the microstructure of steels at large concentrations is quite different to that at low concentrations and such behaviour cannot be modelled using ordinary regression analysis.

A neural network is 'trained' on a set of examples of both input and output data. The outcome of the training is a set of coefficients (weights) and a specification of the functions which, in combination with the weights, relate the input to the output. The computer in-tensive training process involves a search for the optimum non–linear relationship between the input and the output data. However, once the network is trained, estimation of the outputs for any given inputs is rapid.

As with most blind data modelling techniques, difficulties are often encountered with 'overfitting', in which spurious details and noise within the training data are overfitted by the model (Fig. 5.2). This gives rise to solutions that generalise poorly. MacKay [123] has developed a Bayesian framework for neural networks in which the appropriate model

complexity is inferred from the data. The Bayesian framework has two further advantages. Firstly, the significance of the input variables is automatically quantified and consequently the significance perceived by the model of each input variable can be compared against metallurgical theory, where such theory is known. Secondly, the network's predictions are accompanied by error bars which depend on the specific position in input space. These quantify the model's certainty about its predictions.

5.3   Application of neural network modelling

Neural network models due to Cool and Bhadeshia [50] were used to analyse the tensile properties of weld H1. The models give an estimate of the yield and ultimate tensile strength as a function of the weld composition and process parameters. Table 5.2 details the variation of these variables within the data on which the models were trained.

Figure 5.3 shows that the yield strength model is capable of accurate predictions on welds of the type considered here. Two separate tensile test results are included with each figure to give some idea of the scatter in the tensile properties.

A similar prediction of the ultimate tensile strengths of the weld series shows an even better correlation of predicted and measured values (Fig. 5.4). In this case there is a slight and constant overprediction of the values but the trends within the weld series are well modelled. Given the good agreement, it may be possible for the networks to indicate the effects of individual parameters upon the yield and ultimate tensile strength properties of welds such as H1.

The effects of individual parameters upon the tensile properties of H1 were systematically varied. The full results of these calculations are presented in Fig. 5.5.

The most interesting prediction was the effect of the interpass temperature (Fig. 5.6). The neural networks clearly predicted a divergence of the yield and ultimate tensile strengths of H1 as a function of increasing interpass temperature. This parameter was the only one of all the input parameters, to cause a large variation of the yield strength with a much smaller effect upon the UTS. This is precisely consistent with observations [172].

Comparison between the predicted and measured yield and UTS data for welds detailed in Table 5.1 are shown in Figure 5.7. Here some assumptions have been made concerning minor alloying additions (assumed similar to H1) and critically, the interpass temperature, which was set at 250 °C. The neural network models consistently underpredicted the strength of the welds in this case except for weld 16 which showed a much lower measured yield strength and a slightly higher UTS than predicted. Such occasional unpredictability was thought to be caused by variations in the interpass temperature.
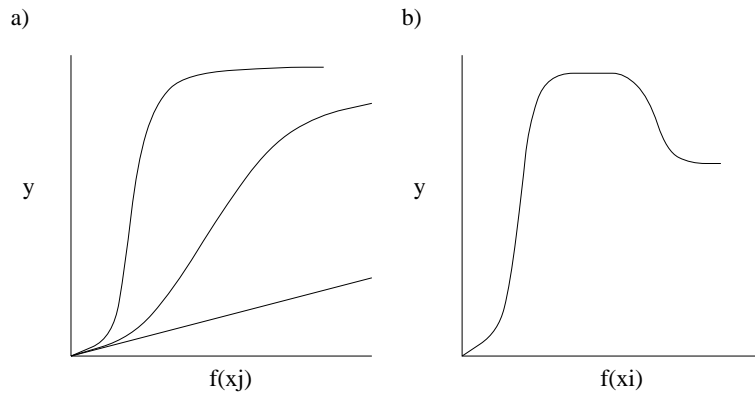
Figure 5.1: (a) Three different hyperbolic tangent functions; the 'strength' of each depends on the weights. (b) A combination of two hyperbolic tangents to produce a more complex model.
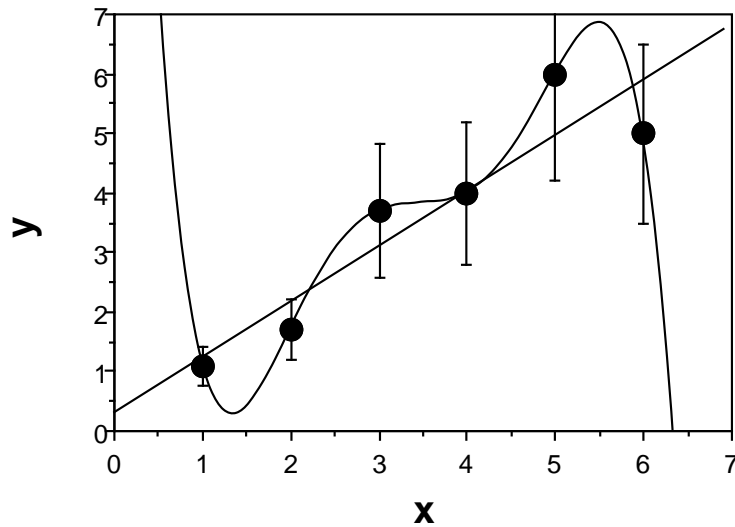
Figure 5.2: A complicated model may overfit the data. In this case, a linear relationship is all that is justified by the noise in the data.

Variable	Range	Mean	Standard Deviation
Carbon weight %	0.029–0.160	0.076	0.018
Silicon weight %	0.04–1.14	0.35	0.14
Manganese weight %	0.27–2.22	1.23	0.36
Sulphur weight %	0.004–0.14	0.010	0.007
Phosphorus weight %	0.004–0.25	0.012	0.012
Nickel weight %	0.00–3.15	0.16	0.53
Chromium weight %	0.00–9.35	0.62	1.91
Molybdenum weight %	0.00–1.50	0.18	0.36
Vanadium weight %	0.00–0.24	0.02	0.04
Copper weight %	0.00–1.63	0.07	0.23
Cobalt weight %	0.00–2.80	0.02	0.18
Tungsten weight %	0.00–2.99	0.02	0.18
Titanium p. p. m. w.	0–690	49	91
Boron p. p. m. w.	0–69	1.15	6.18
Niobium p. p. m. w.	0–985	62	165
Heat Input kJ mm^{-1}	1–7.9	1.9	1.5
Interpass Temperature °C	100–300	205	51
Tempering Temperature °C	0–760	317	243
Tempering Time hours	0–16	6.1	6.2
Oxygen p. p. m. w.	132–1650	441	152
Yield Strength MPa	329–920	503	88
Ultimate Tensile Strength MPa	447–1151	599	92

Table 5.2: The variables used in the analysis of the yield strength. The oxygen content and yield strength are additional inputs for the UTS model. The abbreviation p. p. m. w. denotes parts per million by weight (Cool [50]).
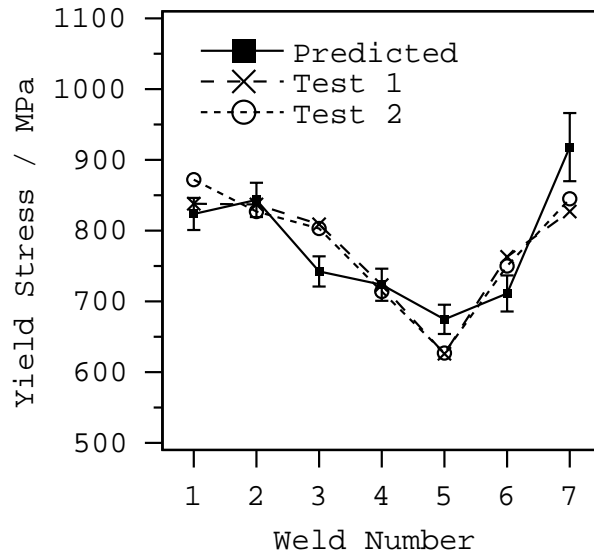
Figure 5.3: Predicted and measured yield stresses for a series of welds. Welds H1–7 are denoted by numbers 1–7. Error bars are set at a value of $\pm 1\sigma$ as perceived by the model.
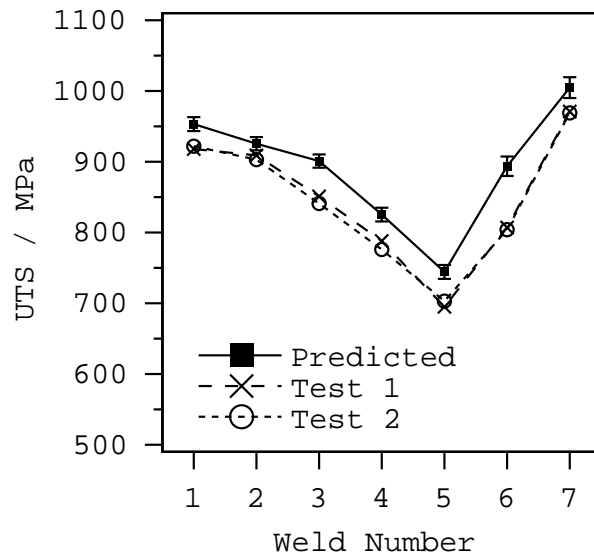
Figure 5.4: Predicted and measured UTS values of the weld series showing superior agreement than the yield strength experiments.

An important feature of neural network modelling is clearly shown in Figure 5.6 as below approximately 100 °C, and neglecting error bars, the yield strength is predicted to be higher than the UTS. Such a prediction is obviously not justified. The network recognises that the prediction is less certain in this region, with the larger error bars, but
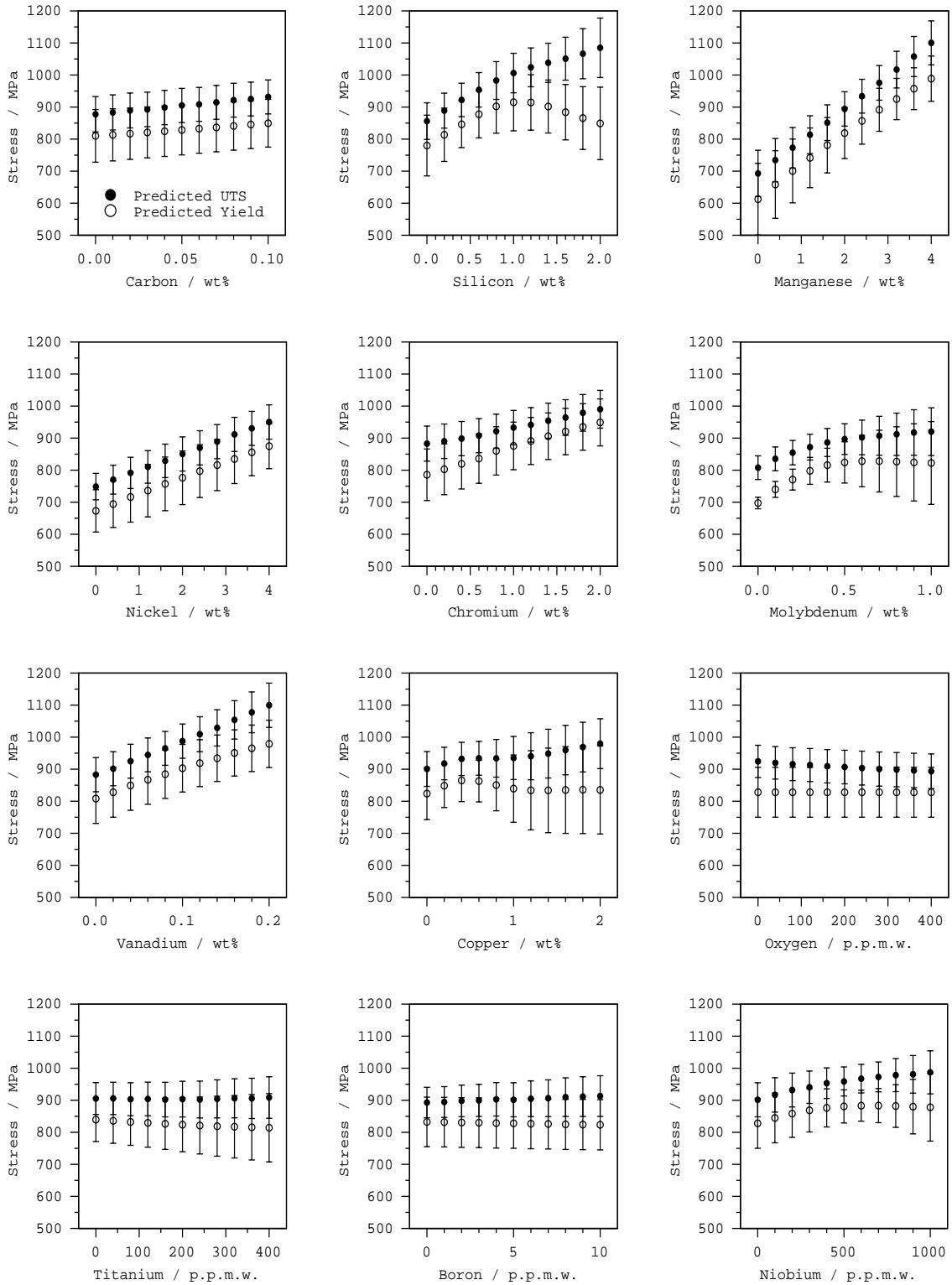
Figure 5.5: The effect of the variation of some individual neural network inputs upon the predicted yield and ultimate tensile strengths of H1. Error bars denote a 1σ uncertainty.
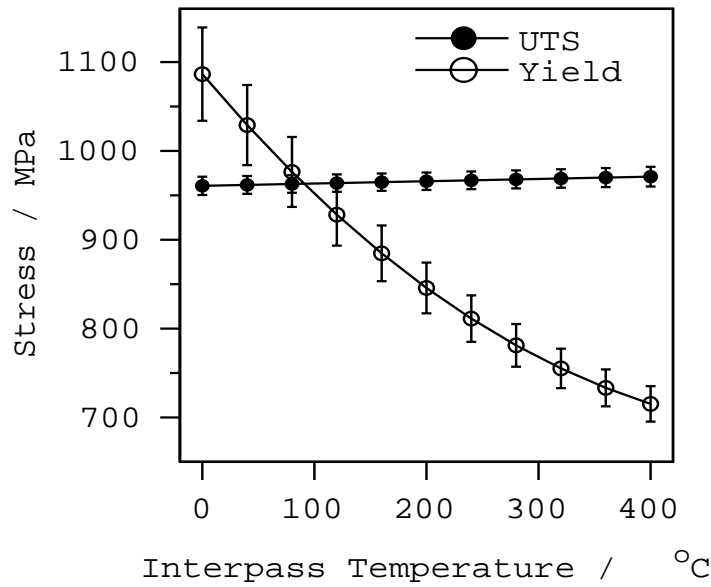
Figure 5.6: The predicted effect of the interpass temperature upon H1 with the single best neural network models.

obviously has no knowledge of metallurgy. It is clearly necessary to interpret the neural network output from a metallurgical viewpoint wherever this is possible. The divergence between the yield and UTS was clearly perceived by the models. It was therefore decided to investigate the role of the interpass temperature on the tensile properties of H1.

5.4   Production of an experimental CCT curve

The biggest effect of the interpass temperature during welding is to influence the cooling rate. This can be seen from the Rosenthal equation [116]:-

$$T - T_0 = \frac{P}{2\pi\kappa r}\exp\left\{-\frac{v(\xi + r)}{2a}\right\} \tag{5.2}$$

where T is local temperature due to a point source of power input P moving at velocity v. T_0 is the far-field plate temperature which is equivalent to the interpass temperature in this case. κ is the thermal conductivity and a is the thermal diffusivity. r is a polar co-ordinate measured from a reference frame attached to the moving heat source, related to the stationary frame by:-

$$r = \sqrt{\xi^2 + y^2 + z^2} \tag{5.3}$$
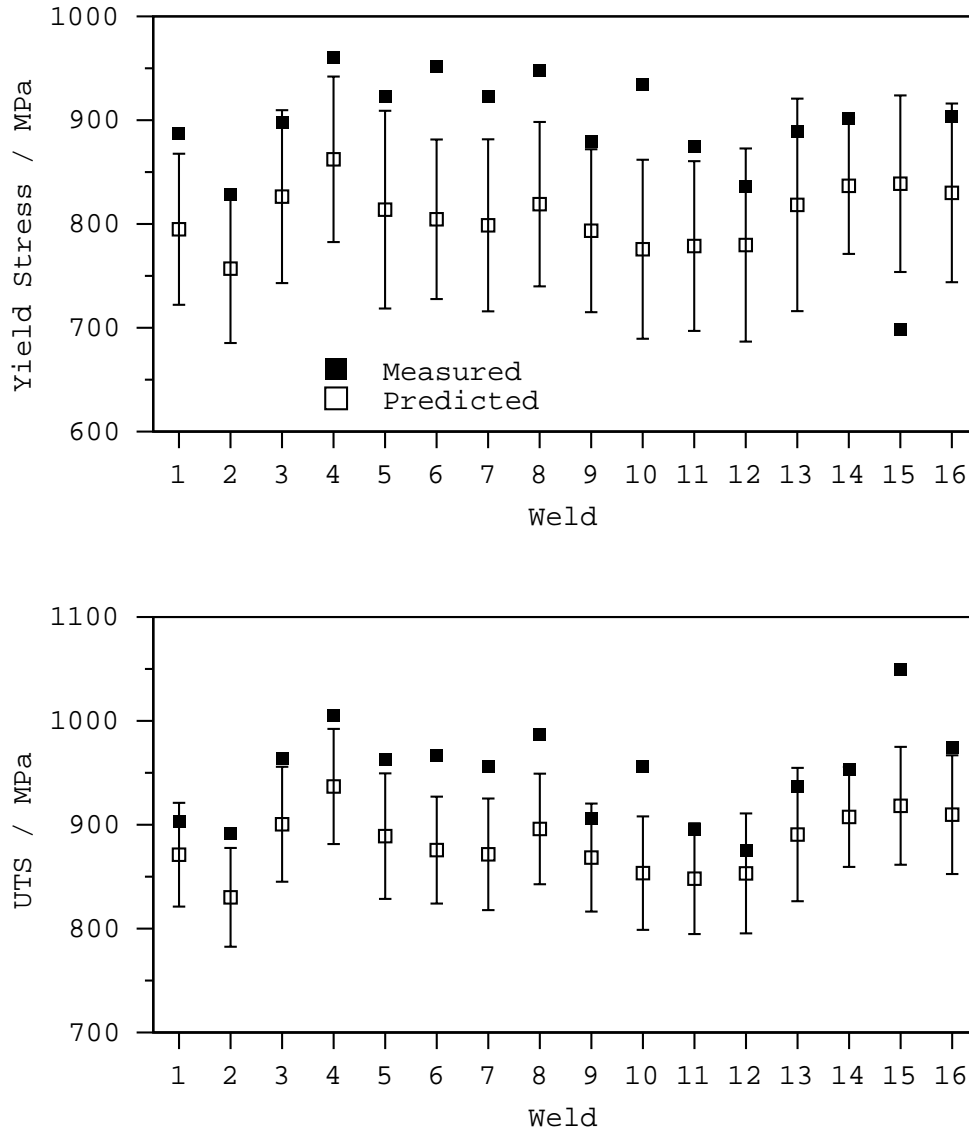
Figure 5.7: Predicted and measured weld yield and UTS data for welds detailed in Table 5.1.

where ξ is a coordinate measuring the translation of the heat source, x and z simply being coordinate axes orthogonal to ξ.

Thus the cooling rate is expected to decrease as the interpass temperature increases. It is possible that such variations in the cooling rate might lead to significant changes in the microstructure. This was investigated by measuring the continuous cooling transformation (CCT) diagram with a thermomechanical simulator.

5.4.1   The *Thermecmastor Z* thermomechanical simulator

The *Thermecmastor Z* allows computer controlled application of heat treatments and deformation to a sample of material. Laser dilatometry is used to follow phase transformations as they occur where the temperature is recorded using a Pt–PtRh thermocouple attached to the sample (Fig. 5.8). The experiments are performed in a sealed chamber which is usually evacuated to allow efficient cooling of the specimen and to prevent oxidation effects. The specimen is seated centrally between Si_3N_4 platens. Heating is via a water-cooled induction coil surrounding the specimen. The maximum heating rate that can be achieved is around $50\,°C\,s^{-1}$ but this is dependent upon the material. Cooling is controlled via helium jets, the prior evacuation of the chamber allowing greater cooling efficiency. Maximum measured cooling rates are found to be in excess of $110\,°C\,s^{-1}$. The specimens are usually solid cylinders of length 12 mm and diameter 8 mm. For experiments in which rapid cooling is required, better results are achieved using hollowed out specimens with an internal diameter of 5 mm. A scanning laser beam is used to measure the diameter of the specimen during testing. A thermocouple is attached to the specimen using spot welding and, on placing the specimen in the machine, the thermocouple is turned to face the scanning laser in order to prevent interference with the dilatometry measurements. The machine is also capable of applying both tensile and compressive stresses via the platens although this facility was not used in the determination of the H1 CCT curve. Data from the dilatometer, the thermocouple and the load cell are logged simultaneously by a computer for later analysis.

5.4.2   Experimental method

In the production of a CCT curve it is desirable to have an identical microstructure in all specimens prior to cooling. In this case all specimens were held for 10 minutes at $1200\,°C$ before controlled cooling rates were applied. Following transformation to the austenite phase upon heating, it was found that the specimens required approximately 2 minutes to reach a stable state.

The austenite grain size was measured in these specimens using 'thermal etching'. In this technique a flat surface is polished on one side of the dilatometer specimen. An austenitizing heat treatment is then applied in an inert atmosphere. Following quenching and no further surface preparation, optical microscopy reveals the prior–austenite grains as surface relief. The grains in a reaustenitized sample of weld material were equiaxed as would be expected. In contrast the austenite within an MMA weld is composed of long grains. S_v, the grain boundary surface area per unit volume of material, can affect
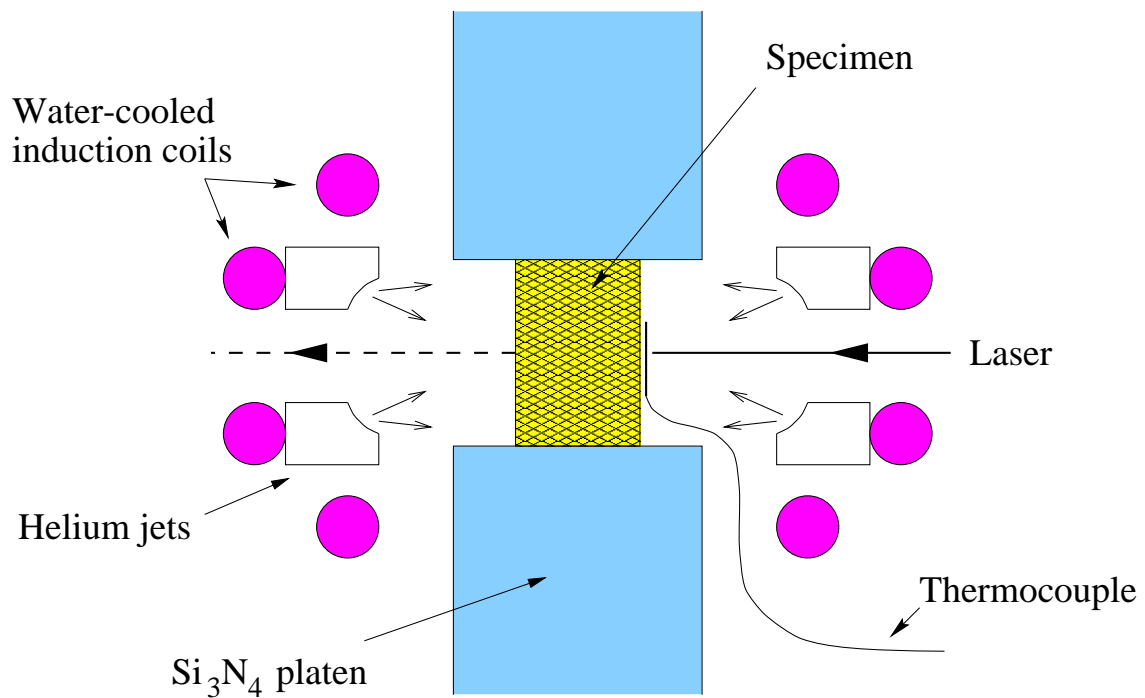
Figure 5.8: The arrangement of equipment within the *Thermecmastor Z* thermomechanical simulator. The specimen is situated between Si_3N_4 platens, inside an induction coil. Simultaneous temperature, dilatometric and load data can be measured.

the transformation temperatures. The methods of Bhadeshia *et al.* [38] were utilised in estimating the equivalent equiaxed grain size of the weld's prior–austenite grains.

Etching a polished 'macro' of H1 with 4% Nital revealed both the prior–austenite and the fine scale microstructure but this method did not allow accurate measurement of the prior–austenite grain size. Measured average widths of austenite grains varied between 40 and 160 μm. It was thought the true value would be closer to the lower end of this range as difficulties were encountered in identifying individual grains. The equivalent equiaxed grain size for the lower value was calculated as 49 μm. Measuring the intersection of thermally etched grain boundaries with randomly oriented test lines on three micrographs, revealed a 41 μm grain size. Although this was lower than the equivalent elongated grain value it was deemed accurate enough, as the effect of the prior–austenite grain size on transformations only becomes large for small grains.

In order to avoid oxidation problems, the chamber was flushed with helium and evacuated to a pressure of $< 5 \times 10^{-2}$ Pa before each test was performed. The evacuation was necessary because without it the chamber would quickly become positively pressurised during cooling and the cooling rate would then be controlled by the venting of helium through the safety valve. Such a cooling rate is certainly much less than the maximum achievable under vacuum conditions.

Constant cooling rates were applied to the specimens of H1. These ranged from above $100\,°\mathrm{C}\,\mathrm{s}^{-1}$ to $0.05\,°\mathrm{C}\,\mathrm{s}^{-1}$. Hollow specimens were used for all experiments to ensure rapid cooling. Figure 5.9 shows the measured temperature versus time data for cooling at $1\,°\mathrm{C}\,\mathrm{s}^{-1}$ and the fastest possible at approximately $125\,°\mathrm{C}\,\mathrm{s}^{-1}$ from the austenitization temperature.

The graphs span the phase transformation between austenite and ferrite. The constant cooling conditions are maintained by the equipment at the lower cooling rate but at the high cooling rates there are deviations from linearity due to recalescence effects and the action of the safety valve. An approximately linear cooling rate was achieved between $800\,°\mathrm{C}$ and $500\,°\mathrm{C}$ which are often quoted as points between which to measure cooling rates. The dilatometer data corresponding to Fig. 5.9 are shown in Figure 5.10. The detection of phase transformations within the material relies upon the fact that the high and low temperature phases have different densities.

Figure 5.10 shows two reasonably linear regions separated by a transient region. The gradients of the 'linear' regions denoting thermal contraction of austenite at the high temperatures and ferrite at the lower temperatures. The intermediate transition region represents the change from a high to a low density.
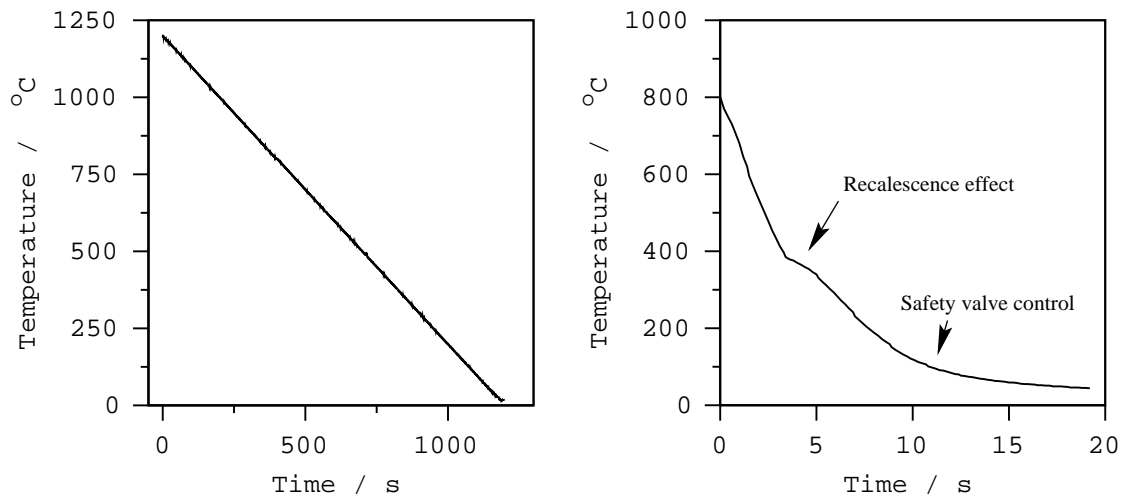
Figure 5.9: The measured linear cooling rates at $1\,°C\,s^{-1}$ (left) and $125\,°C\,s^{-1}$ (right). Linear cooling can be achieved at low cooling rates. The $125\,°C\,s^{-1}$ data show recalescence and reduced cooling at low temperatures due to the safety valve.
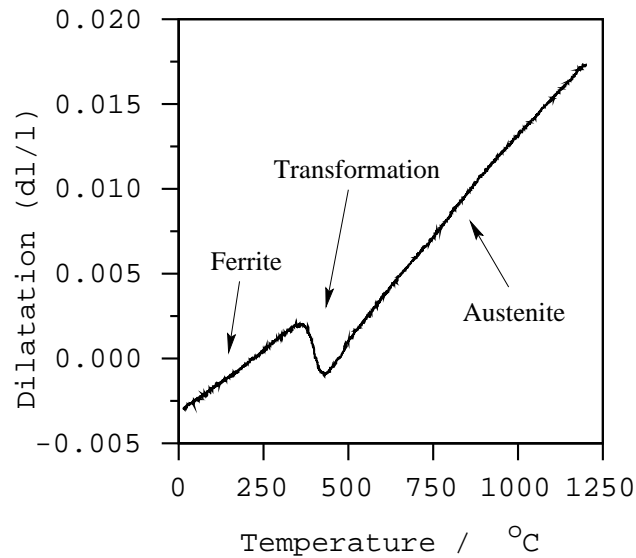
Figure 5.10: Dilatometric data for a $1\,°C\,s^{-1}$ cooling rate. The transformation is clearly revealed.

In the construction of a CCT diagram, the transformation start temperature is obtained from the point at which the dilatometer curve deviates from linearity (Fig. 5.11).

The measured diagram for H1 is shown in Fig. 5.12, which also shows the trace of a weld cooling curve calculated from a method due to Svensson *et al.* [175]. The interpass
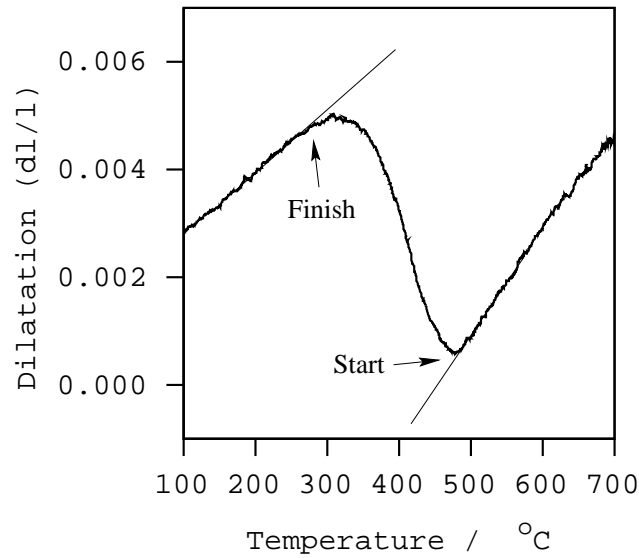
Figure 5.11: The transformation start and finish points marked on a dilatometric curve.

temperature for this calculated cooling curve was 250 °C, nominally identical to that at which H1 samples were welded. The calculated cooling curve uses an equation of the form:-

$$\frac{dT}{dt} = \left(\frac{C_1}{Q\eta}\right)(T - T_i)^{C_2} \tag{5.4}$$

where $C_1 = 1324.8\,\mathrm{J\,K^{-(C_2-1)}\,m^{-1}\,s^{-1}}$ and $C_2 = 0.083$ are fitted constants. T is the absolute temperature and t is the time in seconds. Q is the electrical energy input in $\mathrm{J\,m^{-1}}$ and $\eta = 0.775$ is the arc transfer efficiency for the manual metal arc process. T_i is the interpass temperature (K).

The CCT curve shows the expected 'C-curve' behaviour. The calculated martensite start temperature M_s is also shown [22, 23]. It would appear that even the very fastest cooling rate may not be sufficient to produce a fully martensitic specimen, assuming the validity of the M_s calculation. The error bars in the figure were produced from the estimated uncertainty in determining the start temperature from curves such as that illustrated in Fig. 5.11. Some dilatometric data were better behaved than others, possibly due to computer sampling effects and instability in the potential developed within the thermocouple.

It is interesting that the weld cooling curve lies in a region where the CCT curve has a large gradient. It is possible therefore that variations in the cooling rate could cause large variations in the transformation temperature. Transformation at higher temperatures

should generally give coarser microstructures and this would serve to reduce the yield strength of the material and allow a greater degree of work hardening to occur before the UTS is reached. The superimposed cooling curve in Figure 5.12 intersects the CCT curve at around 440 °C. This is only 200 °C above the interpass temperature of the material. It is thus conceivable that a relatively small variation in the interpass temperature could affect the natural cooling rate sufficiently to significantly influence the transformation temperature. Consequently it was decided to perform some experiments in which samples of H1 would be welded at three specific interpass temperatures in order to investigate the mechanical properties.
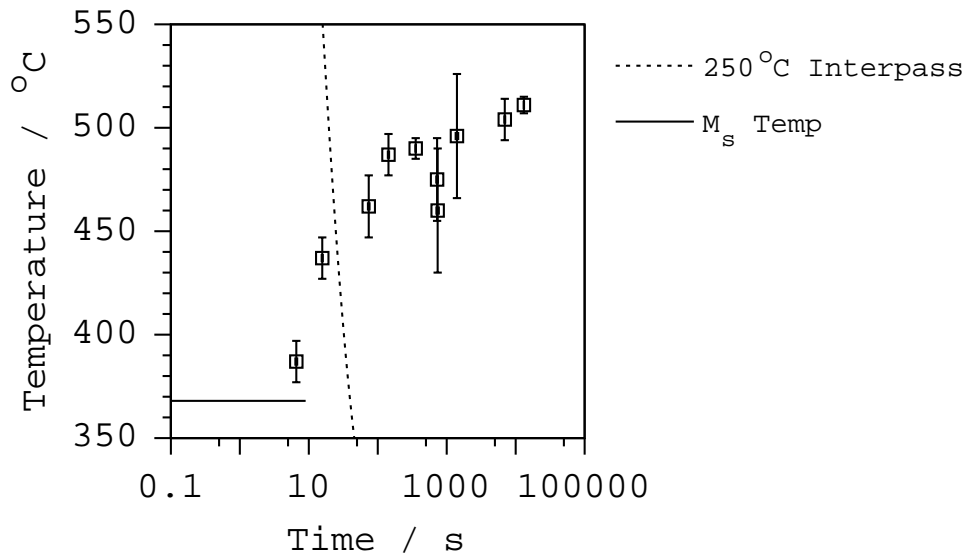
Figure 5.12: Experimental CCT curve for H1 showing. A fitted cooling rate curve is also presented for a 250 °C interpass temperature (Eqn. 5.4).

5.5 Production and testing of welds

Weld deposits were produced using H1 electrodes to similar specifications as described in Chapter 3. The interpass temperature was held at 38 ± 7 °C, 99 ± 7 °C, and 230 ± 20 °C in each case, measurements being taken with a thermocouple probe. Tensile and Charpy specimens were produced for mechanical testing.

5.5.1   Tensile test results

Figure 5.13 shows both the predicted and the measured yield and ultimate tensile strengths of H1 as a function of the interpass temperature. The yield strength does indeed drop as a function of the interpass temperature whereas the UTS is less variable. Table 5.3 shows that the specimen with a 38 °C interpass temperature exhibited a very high yield strength but a UTS which is only 5 MPa higher. Although the yield strength is extremely high in this case, the elongation is lower which has implications for safety. At an interpass temperature of 230 °C the gap between the yield and UTS had widened to 100 MPa and the yield strength value was 170 MPa lower. Such a reduction in yield strength is very large and represents a full 20% of the value at 230 °C. It is particularly interesting that whereas 230 °C is not considered to be a very high temperature in an industrial context, it certainly has an important effect on the mechanical properties. It is the proximity of the interpass temperature to the transformation temperature that is causing the problems.

Interpass Temperature °C	Yield / MPa	UTS / MPa	Elongation / %	RA %
38 ± 7	1003	1008	14.4	61
99 ± 7	978	987	16.8	64
230 ± 20	832	932	20.0	60

Table 5.3: The effect of the interpass temperature upon tensile properties of H1.

5.5.2   Charpy impact tests

Standard $10\,\text{mm} \times 10\,\text{mm}$ Charpy V-notch specimens were machined from transverse sections of the welds and tested at temperatures in the range -100 °C to -20 °C. As Figure 5.14 shows, the interpass variation has little effect upon the impact toughness of the specimens. It appears that the 99 °C specimens had slightly lower toughness. Considering the scatter in the data, the interpass temperature was found to have no discernible effect upon the low temperature impact toughness values. This is an important result as it indicates that the yield strength can be controlled independently of toughness at high strengths.

5.6   Summary

The tensile properties of high strength welds intended for use in situations where toughness is important, have been investigated with a view to explaining large variations in the yield
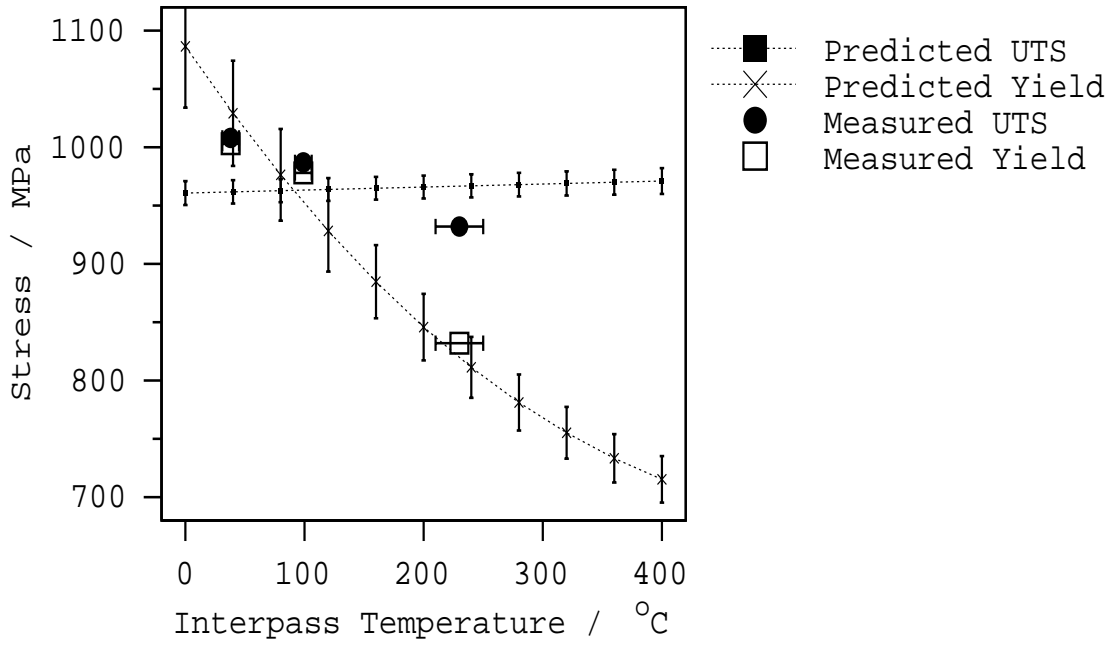
Figure 5.13: Tests at three interpass temperatures supported the predictions of the neural network models.
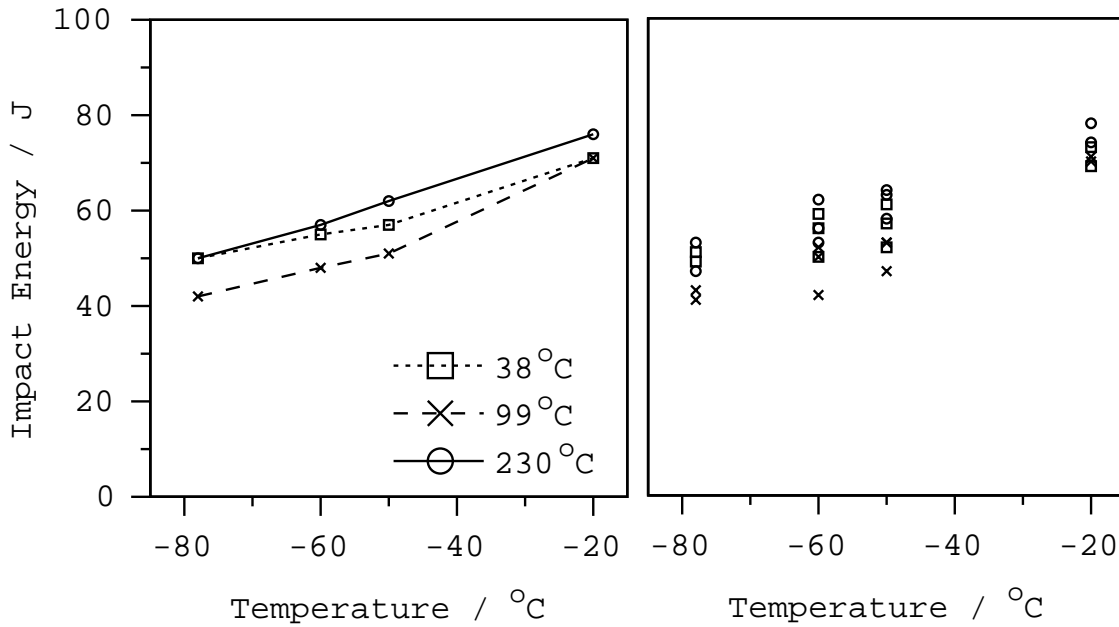
Figure 5.14: Charpy impact data showing both average values (left) and scatter (right).

strengths. The preliminary work utilised a neural network model to identify the particular variable (out of many possibilities) which might be responsible for the observed scatter

96

in mechanical properties. The neural network model was found to be remarkably good in predicting the yield stress and UTS of a whole series of experimental welds and further analysis indicated that the high strength welds are particularly sensitive to the interpass temperature.

The temperature of a weld asymptotically approaches the interpass temperature. It follows that the weld cooling rate must become very sensitive to the interpass temperature, T_i as the weld temperature approaches that of the interpass temperature. This may not matter in alloys where phase changes are completed at temperatures well above T_i. On the other hand, when transformation temperatures are suppressed by alloying, it is quite possible that the exact value of the interpass temperature significantly influences the development of microstructure and the mechanical properties.

This theoretical prediction was verified in two stages. The continuous cooling transformation diagram for alloy H1 was measured. This revealed that the development of microstructure occurs at temperatures close to the interpass temperature for typical welding conditions.

As a second stage of verification, a series of welds made with careful control of the interpass temperature demonstrated conclusively the large effect on the mechanical properties.

In conclusion, great care must be exercised in controlling the interpass temperature for welds where the phase transformations are suppressed by alloying additions to temperatures close to T_i.

Chapter 6

Austenite decomposition in a bainitic weld

The weld deliberately manufactured with a large silicon concentration (1.6 wt%, H7) has a microstructure which is essentially bainitic ferrite plates separated by carbon–enriched films of austenite (Chapter 3). Some of the austenite must inevitably decompose to martensite during cooling and such high–carbon martensite has also been observed during transmission electron microscopy, as discussed in Chapter 3.

The purpose of the work presented in this chapter was to examine the resistance of the microstructure to tempering heat treatments. The aim was to discover the resistance of the austenite to decomposition into ferrite and carbides. Tempering also provides a convenient method of checking the quantity of high–carbon martensite via the variations in hardness.

6.1 Tempering experiments

Small rods of diameter 3 mm and length 20 mm were cut longitudinally from the centre of the weld metal thereby intersecting both 'as–deposited' and reaustenitized regions due to the multi–run deposition process. These were sealed in silica tubes in a low pressure argon atmosphere prior to tempering at 500 °C for 0.5, 1, 2 and 3 hours. Substitutional atom mobility becomes significant in iron at temperatures in the vicinity of 500 °C, as is common knowledge in secondary hardening experiments. Transmission electron microscopy was performed on these heat treated specimens and also upon a rod of material in the 'as–welded' condition. Foils were prepared as in Chapter 3 and examined using a Philips 400ST microscope operating at 120 kV and a JEOL 200CX operating at 200 kV.

6.1.1 Microscopy results

Carbides were never positively identified in the as–welded microstructure. Thick austenite films were frequently observed separating plates of bainitic ferrite (Fig. 6.1). The austenite films were generally intact after tempering at 0.5 h at 500 °C (Fig. 6.2a). Partial decomposition to carbides occurred when tempered for 1 h, although many of the austenite films seemed to be unaffected. Figure 6.2b shows a dark field image of such a film. Where decomposition had occurred the majority of carbides observed were found at plate boundaries (Fig. 6.2c). Following 2 h at 500 °C the austenite films had decomposed and carbides were clearly visible on many plate boundaries (Fig. 6.2d). Much of the carbide precipitation was completed after 2 h at 500 °C with no obvious change in the microstructure following 3 h at 500 °C.

It was difficult to identify these fine carbides using selected area diffraction due to the strong diffraction from the ferrite. Convergent beam diffraction also did not help, so extraction replicas were prepared from each of the samples.
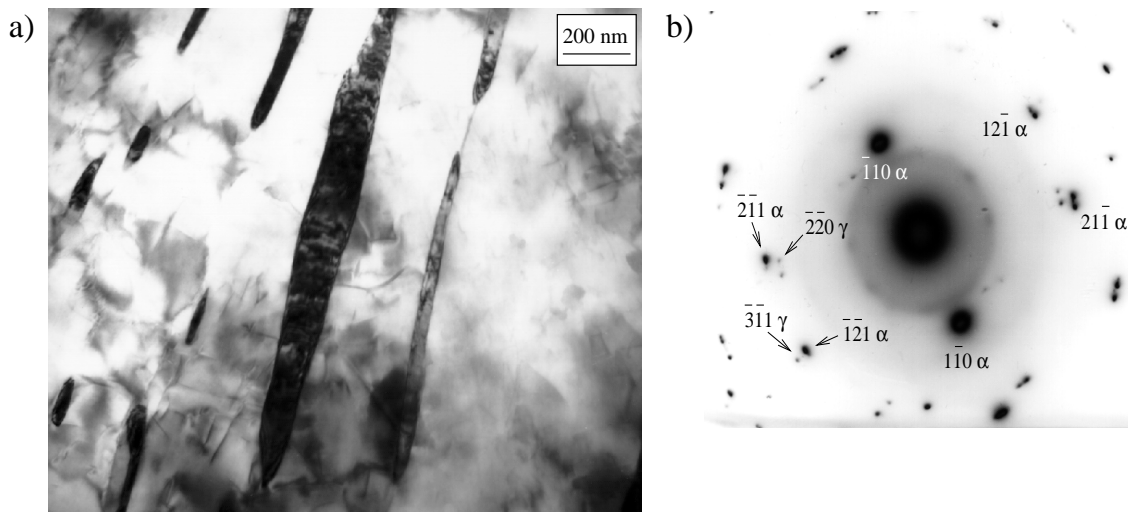
Figure 6.1: a) bright field image and b) diffraction pattern of austenite films lying between plates of ferrite in an 'as–welded' sample.

6.2 Carbide Identification

Metallographic samples were etched in 4% Nital before depositing a thin layer of carbon (200–300 Å) in a vacuum of 10^{-3} Pa onto the polished surface. Electrolytic etching in a
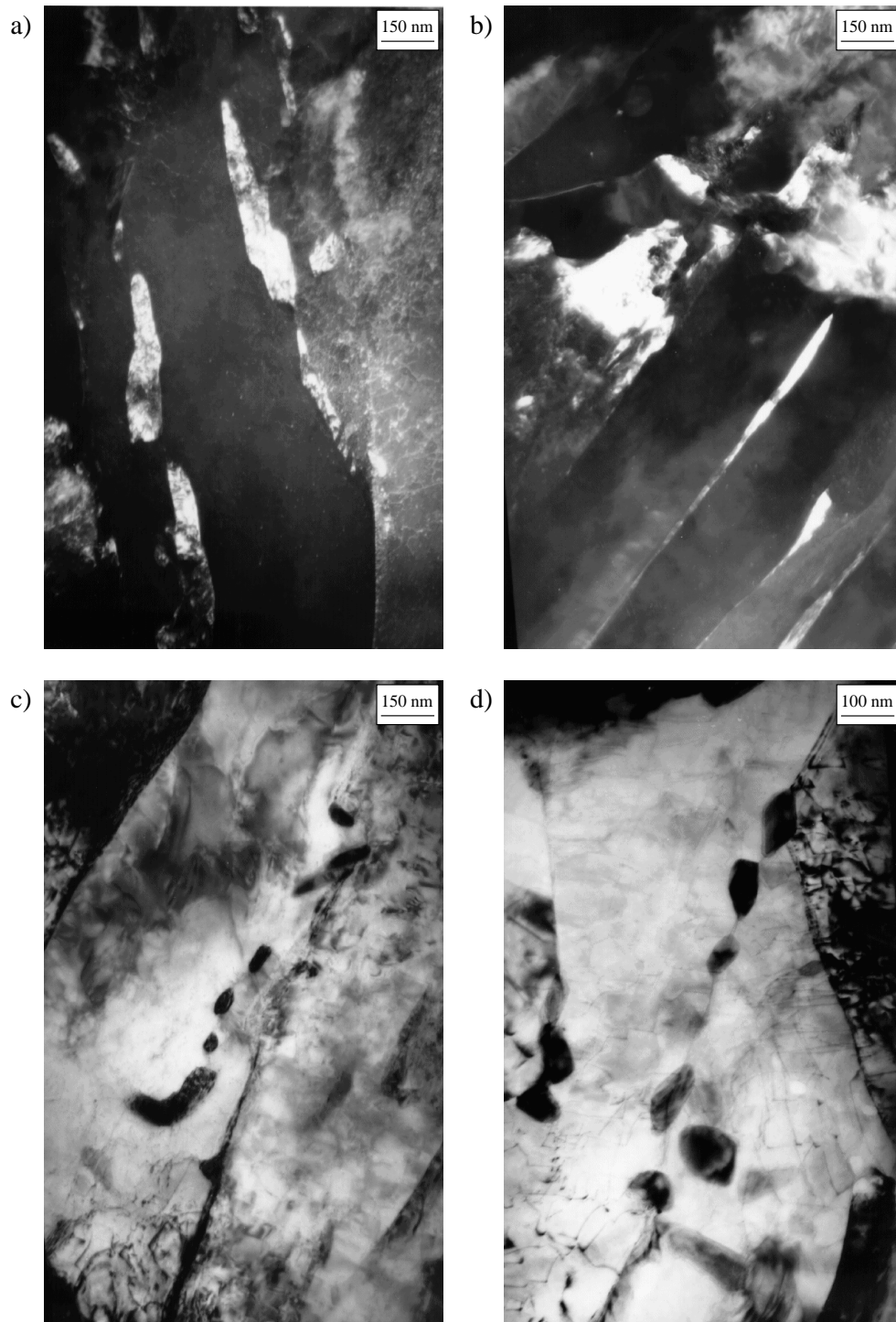
Figure 6.2: Effect of tempering at 500 °C on austenite films: a) 0.5 h (dark field 200 γ reflection) b) intact austenite films after 1 h (dark field 220 γ reflection) c) some decomposition after 1 h in another region (bright field) d) complete decomposition after 2 h (bright field).

solution of 5% hydrochloric acid in methanol with a potential of 1.5 V was used to loosen the carbon layer [161, 162]. Gently dipping the specimens in baths of methanol and then distilled water caused the carbon layers to float free. The replicas were placed on 400 square mesh copper grids and allowed to dry before observation in the TEM.

6.2.1   Electron diffraction

The extraction replicas were observed in a JEOL 200CX transmission electron microscope whose camera constant for specific lens settings was calibrated using a thin foil and diffraction from the ferrite. Identification of carbides was performed upon specimens in the untempered condition and those tempered for 2 h at 500 °C. As stated earlier, although carbides were not found in the foils of the as–welded microstructure, a few were extracted by the replicas. In both the as–welded and the 2 h specimens, the carbides were identified as cementite (Figure 6.3). It is believed that the relatively few carbides in the untempered samples arise during the tempering caused by sequential deposition of layers of weld metal as the weld gap is filled. Many more cementite particles were observed in the tempered microstructures; Figure 6.3c gives an example diffraction pattern.

These observations show that the majority of the carbon in the alloy is held within the austenite films. These films appear to be quite stable since it required a tempering heat treatment of 500 °C for an hour to induce significant decomposition.

6.3   Hardness of tempered specimens

In a primarily upper bainitic alloy, tempering to induce the precipitation of carbides from the weaker austenite phase should have little effect upon the hardness. The conversion of some of the softer austenite to ferrite should help to compensate for any strength reductions due to recovery. Alloying elements such as Cr and Mo may cause secondary hardening, perhaps on an extremely fine scale not observable using conventional TEM techniques [36]. Conversely, the strength of high–carbon martensite should drop sharply during tempering. Vickers hardness values were measured on specimens tempered at 500 °C for 0, 0.5, 1, 2, and 3 h respectively using a 10 kg load, six indents being made in each sample. Figure 6.4 shows that there was no discernible drop in hardness despite the precipitation of carbides observed during tempering.
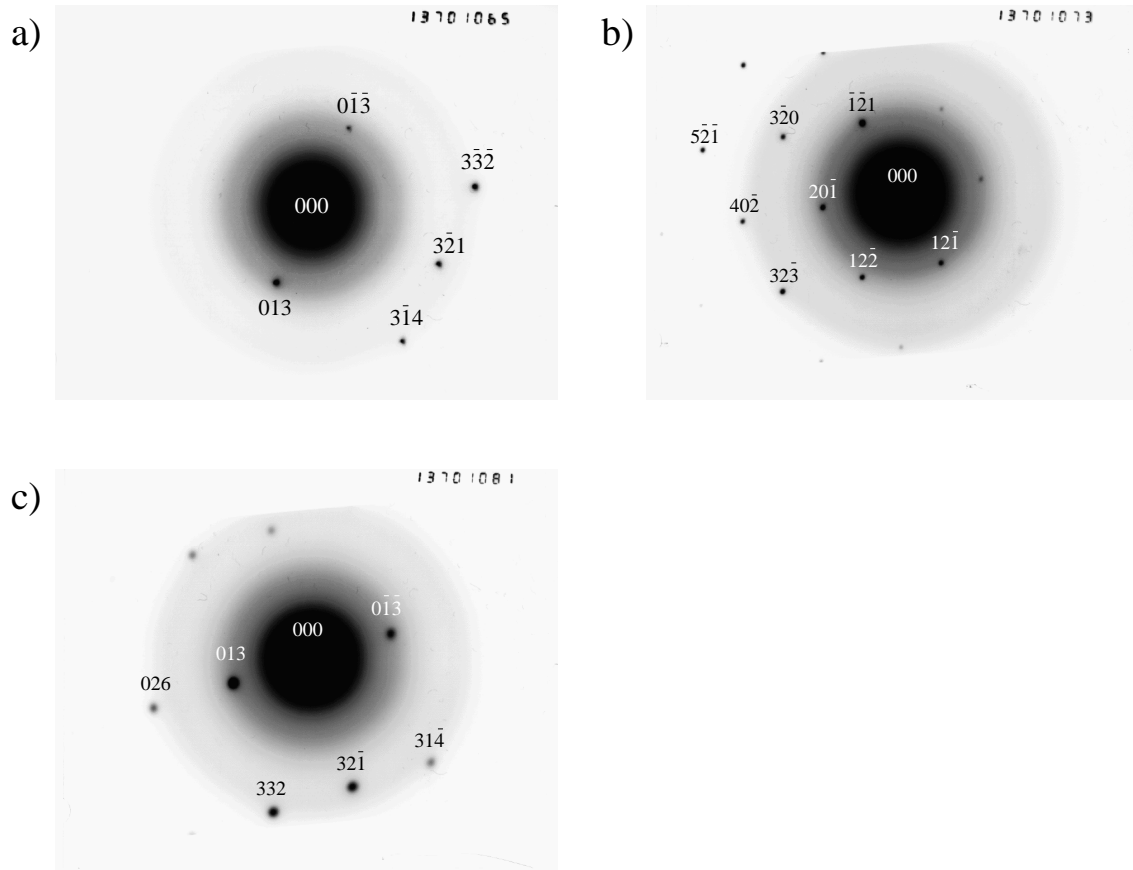
Figure 6.3: Carbide diffraction patterns from an 'as–welded' specimen consistent with a) [79$\bar{3}$] and b) [234] cementite zones, and c) from a specimen tempered for 2 h at 500 °C consistent with a [7$\bar{9}$3] cementite zone.

Time / h	Hardness / kgf mm^{-2}
0	314 ± 5
0.5	317 ± 10
1	302 ± 10
2	312 ± 8
3	309 ± 8

Table 6.1: Macrohardness data from specimens tempered at 500 °C.
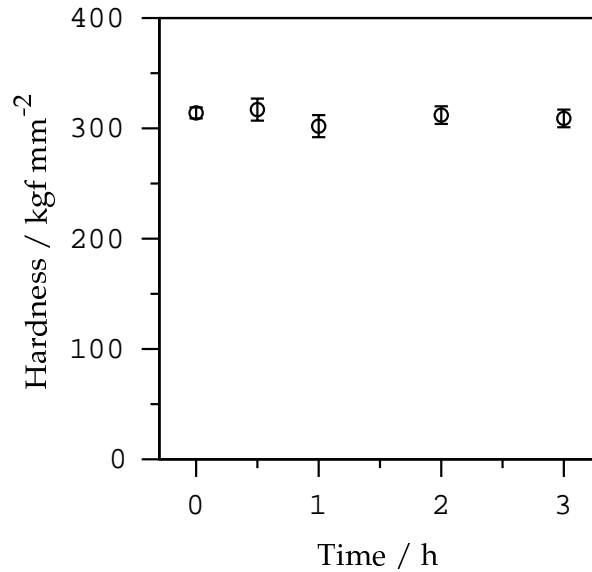
Figure 6.4: Effect of tempering at 500 °C on the hardness of weld H7.

6.4 Toughness of tempered specimens

The microstructure of the high–silicon bainitic weld (H7) is not as tough as that of the more conventional material (H1). There was concern that the promotion of a bainitic microstructure may produce very hard 'martensitic islands' due to the 'incomplete reaction phenomenon'. Such regions may act as initiation sites for cracks during fracture. Thus, tempering should improve the toughness. However, Table 6.2 shows a considerable drop in impact toughness. This was thought the be due to precipitated carbides in the tempered specimens. If hard martensitic regions had increased in toughness, this effect was secondary to the effect of carbides.

Further evidence that the carbides are detrimental to toughness comes from tensile test data (Table 6.3). A similar yield strength and a slight increase in UTS were observed. However, the elongation was lower in the tempered specimen which is consistent with the smaller dimple size observed in a tensile fracture surface (Fig. 6.5).

Charpy impact testing promotes brittle fracture mechanisms whereas tensile testing favours a more ductile failure. Tensile fracture surfaces were examined using a JEOL 5800LV scanning electron microscope operating at 20 kV. Observations of dimples showed a smaller average size in the tempered specimen indicating a higher density of nucleation sites for microvoids (Fig. 6.5). This effect could only be attributed to carbide precipitation as the number of inclusions should remain constant, indicating that carbides can strongly affect toughness in the tempered specimens [30].

Impact Energy / J								
-60 °C			-20 °C			20 °C		
H1	H7	H7*	H1	H7	H7*	H1	H7	H7*
66	30	26	88	39	28	101	74	47
62	32	12	88	39	27	104	66	41
63	34	–	89	37	27	100	62	42
–	–	–	87	37	–	–	–	42
–	–	–	85	39	–	–	–	–
64	32	19	87	38	27	102	67	43

Table 6.2: Comparative toughnesses of the commercial electrode (H1) with the higher silicon bainitic material in the 'as–welded' (H7) and tempered (1 h 500 °C, H7*) conditions. Average values are also shown (final row).

Weld	Yield / MPa	UTS / MPa	Elongation / %
H1 as–welded	838	918	21.6
H7 as–welded	827	971	23.2
H7 tempered	783	1026	21.0

Table 6.3: Comparison between tensile test results. The 'tempered' specimen was held at 500 °C for 1 h.

a)

b)
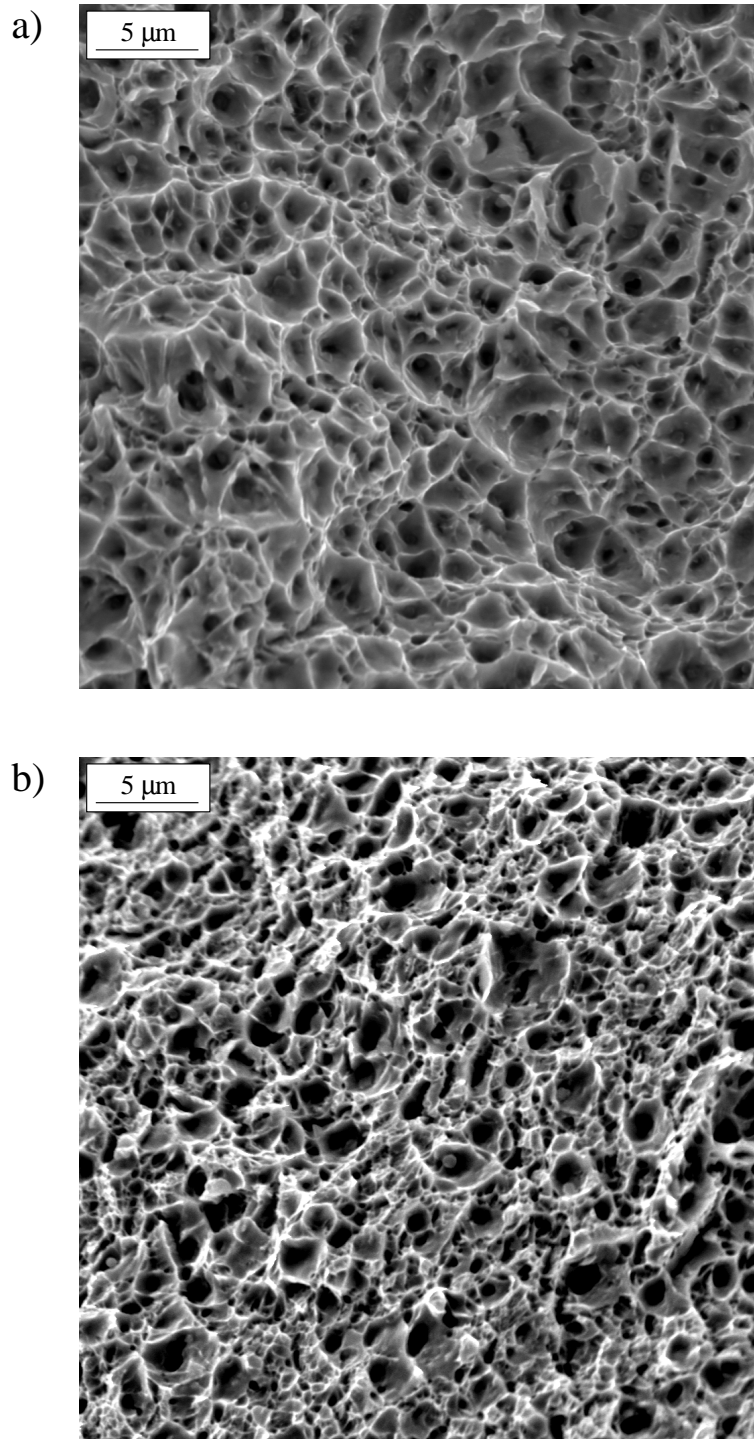
Figure 6.5: Tensile fracture surfaces of H7 in the (a) 'as–welded' condition and (b) after 1 hour at 500 °C.

6.5   Conclusions

Experiments and TEM observations of H7 indicated some resistance of the austenite films to tempering. The silicon level was high enough to prevent carbide precipitation in the 'as–welded' condition as intended. The constant hardness levels during tempering indicated that the microstructure did not contain large volume fractions of martensite. Few carbides were present in the 'as–welded' specimens indicating that they are probably not the cause of the lower toughness in comparison with H1.

Chapter 7

Design of New Welds

The design and testing of new weld compositions is discussed in this chapter. In addition to some neural network modelling, extensive use was made of 'MTDATA', a computer program that can be used to describe thermodynamic data.

7.1 MTDATA

The assimilation of thermochemical data has made phase equilibria calculations relatively straightforward. 'MTDATA' allows computation of phase equilibria for multicomponent systems in which many phases may co–exist [88]. This is achieved by combination of data from unary, binary and sometimes ternary systems, with theoretical methods to estimate phase stabilities for more complex systems. The reliability of the estimates is dependent upon the data available, simpler systems being more accurately predicted, but in more complex cases MTDATA does report missing interaction data. Mass conservation and a minimisation of Gibbs free energy allow calculation of volume fractions of phases present and their chemical compositions. Phases can be suppressed during a calculation to permit metastable equilibria to be investigated. The calculations can be done with respect to changes in composition, temperature and pressure. As MTDATA uses thermodynamics, equilibrium conditions are always assumed and no kinetic information is produced. Welds are formed under conditions far from equilibrium but as will be seen, thermodynamic calculations are extremely useful.

7.2   Modifications to Weld H1

Experimental data presented in Chapter 3 indicated that weld H1 exhibited excellent strength and toughness properties. It was thought however that the strength might be improved either by increasing solid solution strengthening or by enhancing the hardenability of the weld. Two appropriate alloys were therefore produced and their properties compared with those of H1.

MTDATA was used to calculate the equilibrium phases in H1 as a function of temperature. Some δ–ferrite is predicted at around 1500 °C although this is not an issue because there is a large temperature range over which the alloy is fully austenitic (Fig. 7.1). The avoidance of δ–ferrite in the final microstructure is desirable as its strength is lower due to a large grain size [51]. Figure 7.1 also indicates that there is a possibility that some 5% of austenite may be retained at room temperature.
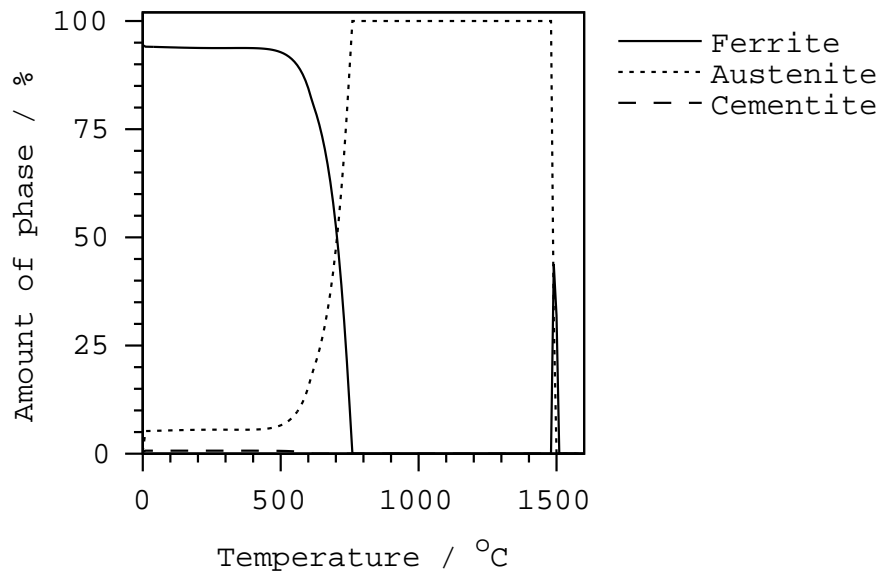
Figure 7.1: Calculated equilibrium phases for H1 as a function of temperature.

7.2.1   Addition of tungsten

It was decided to enhance the strength of H1 by addition of tungsten as a solid solution strengthener. There are few published data although Sawaragi *et al.* [158] indicated that tungsten is more potent than molybdenum. Gregg [75] in his studies found that the addition of tungsten to low-alloy steel welds did not adversely influence the toughness. Hence, an addition of tungsten to H1 was expected to be beneficial.

Strength was estimated using the neural network models described in Chapter 5 but trained on a larger data set of 1200 alloys due to Harsha [82]. Table 7.1 shows a predicted increase in both the yield and UTS due to tungsten, the latter being considerably larger. Considering the conclusions of Sawaragi [158], the Young–Bhadeshia solid solution model predicted that a comparative atomic fraction of molybdenum would produce a 36 MPa yield strength increase. An alloy of H1 containing tungsten was produced for investigation.

A value of 4 wt% (1.3 at%) W was chosen for addition to H1. As tungsten is a ferrite stabilizer, MTDATA was consulted to examine its effect on the δ–ferrite phase field. Only a slight increase in stability was predicted (Fig. 7.2).
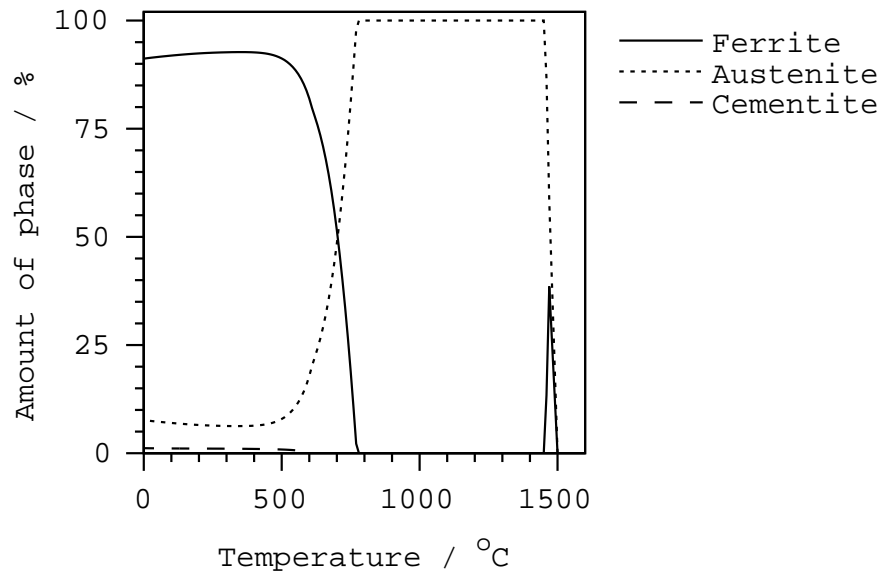
Figure 7.2: Calculated equilibrium phases for H1 + 4 wt% W as a function of temperature.

An experimental weld of this nominal composition was produced to specifications as in Chapter 3. The measured chemical composition of this weld is presented in Table 7.7. In addition another test weld was made from H1 under similar conditions. Specimens were produced for both tensile and Charpy impact testing. Tensile test data are shown in Table 7.1.

Element	Yield Stress / MPa		UTS / MPa	
	Predicted	Measured	Predicted	Measured
H1	811	769	904	939
H1 + 4 wt%W	852	819	1050	1056

Table 7.1: Predicted [82] and measured yield and UTS values for H1 and H1+4 wt% W.

The weld containing tungsten showed both a higher yield strength (by 50 MPa) and UTS (by 117 MPa) which is in agreement with the earlier neural network predictions. The Charpy data (Fig. 7.3) showed that the significantly higher strength of weld H1 containing tungsten led to a reduction in toughness.
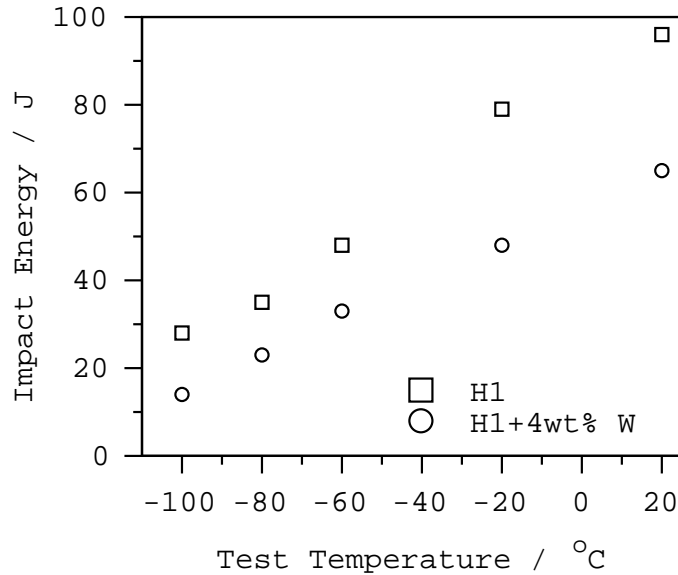
Figure 7.3: Effect of tungsten addition upon toughness in H1.

7.2.2 Increased Hardenability

Increasing the volume fraction of low carbon martensite may provide additional strength to H1. The experimentally determined CCT curve with a superposed estimated MMA weld cooling rate (Chapter 5) indicated that a small increase in hardenability may significantly affect the properties due to the large gradient of the cooling curve in the region of intersection (Fig. 7.4).

The hardenability of a steel can be controlled by the grain size or composition, in welding the latter option being the more practical. Generally additions of metallic elements increase the hardenability by retarding the austenite–ferrite transformation. Maynier *et al.* studied hardenability by analysing the cooling curves of low–alloyed steels and determined an equation giving the minimum cooling rate required at 700 °C, V_1 (°C h^{-1}), to give a fully martensitic microstructure [129]:-

$$\log V_1 = 9.81 - \{4.62 \text{ C} + 1.05 \text{ Mn} + 0.54 \text{ Ni} + 0.5 \text{ Cr} + 0.66 \text{ Mo} + F(T, t)\} \qquad (7.1)$$
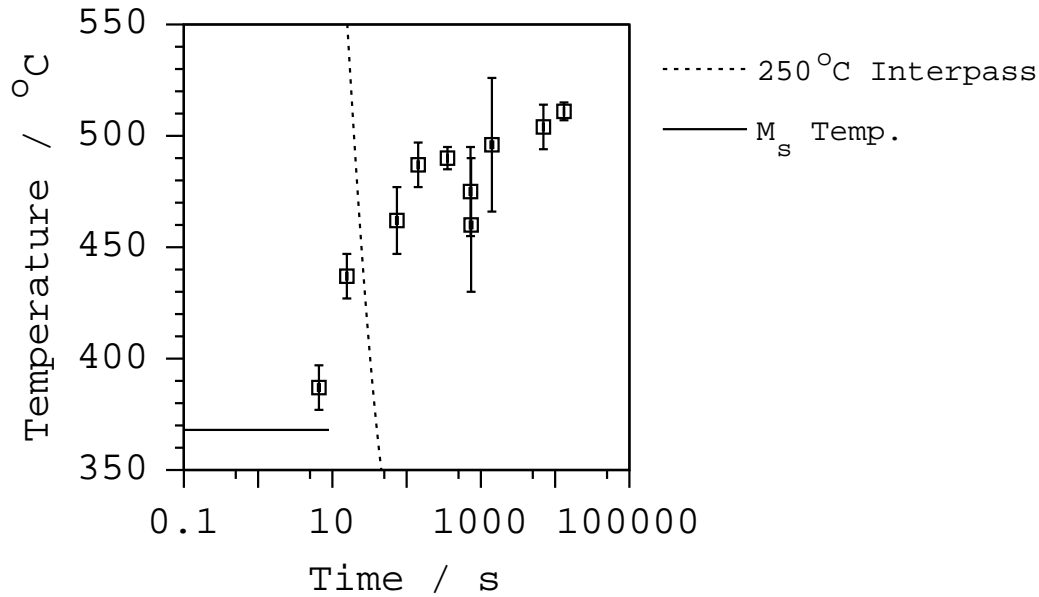
Figure 7.4: Experimentally determined CCT curve for H1.

where all elements are given in weight% and $F(T, t)$ is a function of time and temperature allowing comparison between differing thermal conditions. The coefficients show the relative effects of alloying additions on hardenability. Nickel and manganese are used together to control hardenability. However, although the influence of nickel is the smaller, it is advantageous because it tends lower the ductile–brittle transition temperature and increase the resistance to cleavage fracture [160, 173].

Stabilisation of austenite by nickel may lead to a greater retention of austenite as shown in Fig. 7.5 in which calculated quantities of equilibrium phases are presented for an H1 alloy containing 4.5 wt% Ni. The high temperature δ–ferrite region is eliminated. Using the neural network model due to Harsha [82] the higher nickel alloy was predicted to have considerably higher yield (by 85 MPa) and UTS (by 119 MPa) values (Table 7.2).

An experimental alloy was produced and tested to identical specifications as those discussed in Chapter 3). The composition of this weld is shown in Table 7.7. Tensile data showed an increase in yield stress (by 89 MPa) and UTS (by 80 MPa) values relative to H1 (Fig. 7.2). These data are in reasonable agreement with the predictions of the neural networks. Charpy impact data were also encouraging, showing similar values at low temperatures and a smooth transition to slightly lower values at higher temperatures (Fig. 7.6). Such behaviour is expected on increasing nickel levels. Full impact testing results for this and the high tungsten alloy are shown in Table 7.3.
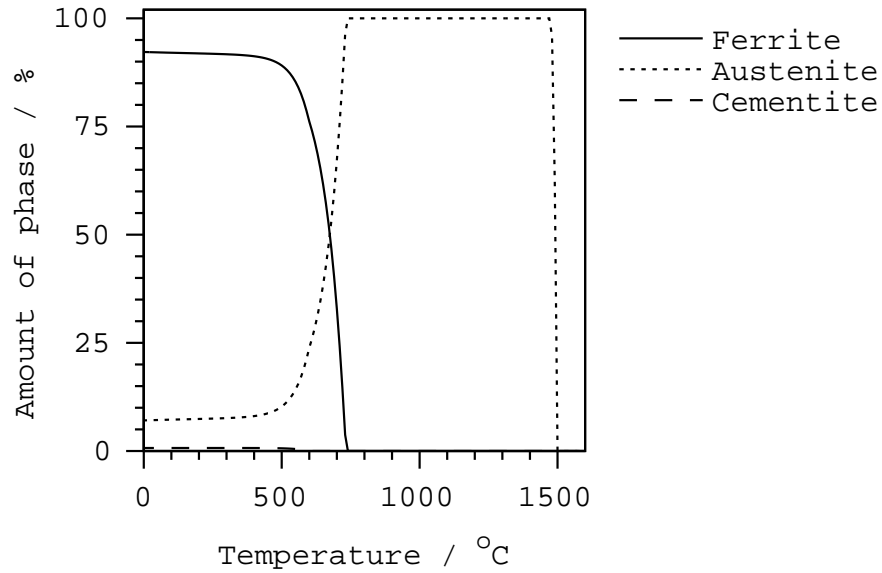
Figure 7.5: Calculated equilibrium phases for H1 containing 4.5 wt% Ni.

Element	Yield Stress / MPa		UTS / MPa	
	Predicted	Measured	Predicted	Measured
H1	811	769	904	939
H1 − 4.5 wt% Ni	896	858	1015	1019

Table 7.2: Predicted [82] and measured yield and UTS values for H1 and H1 containing 4.5 wt% Ni.

Weld	Test temperature °C				
	-100	-80	-60	-20	20
H1	30, 26	34, 36	47, 48,	78, 80,	97, 94
H1 + 4 wt% W	15, 12	25, 21,	34, 31,	50, 45,	63, 67
H1 − 4.5 wt% Ni	17, 26	34, 35	46, 44,	63, 64,	70, 68

Table 7.3: Charpy impact values (J) for new welds.
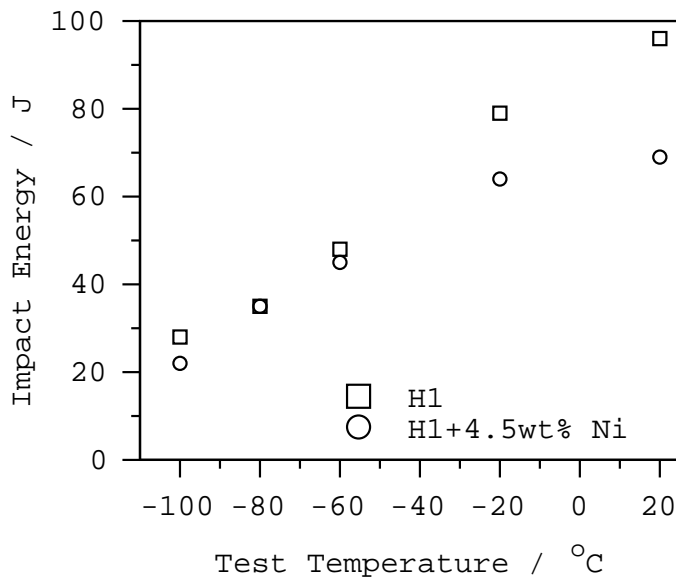
Figure 7.6: Effect of nickel addition upon toughness in H1.

7.3   Summary of H1 modifications

Improvements in tensile properties were produced by both solid solution strengthening and by increasing hardenability. If it is assumed that the contribution of tungsten to strength is solely due to solid solution strengthening then it's influence of around 40 MPa per at% is strong in comparison with other elements [121]. The improvement in strength is costly however in terms of toughness. In the case of nickel, a larger improvement in yield strength coupled with the better toughness performance makes this addition more attractive.

7.4   Modifications to weld H7

Bainitic microstructures can suffer from toughness problems due to the aligned nature of plates within packets. This is less of a problem for the more chaotic acicular microstructures found in welds but the inclusions which promote acicular ferrite also cause low toughness. Common to both bainite and acicular ferrite is a further problem due to the 'incomplete reaction phenomenon'.

113

7.4.1   The Incomplete Reaction Phenomenon

A feature of the bainite transformation is that the amount of bainite decreases and eventually tends to zero as the isothermal transformation temperature is increased. Furthermore even after rapid initial growth the transformation can quickly cease. The remainder of the microstructure may then comprise large areas of 'blocky austenite' with the potential of transforming to martensite. This effect can be explained by a two–stage transformation mechanism involving a diffusionless initial stage followed by rejection of carbon into the remaining austenite. In principle a diffusionless transformation in which parent and product have identical compositions should go to completion. In reality this does not occur due to slow kinetics. Carbon trapped within bainite has enough time to diffuse into the austenite. Thus subsequent diffusionless transformation of increasingly enriched austenite occurs. This is eventually prevented by thermodynamics at the T_0 line, beyond which the transformation would require an increase in free energy. The T_0 line on a phase diagram is the locus of points at which ferrite and austenite of the same composition have identical free energy. Often a T_0' line is used which takes into account the additional strain energy cost of forming bainite ($\approx 400 \, \mathrm{J \, mol^{-1}}$). Hence the theory predicts that the bainite reaction may be prevented from going to completion. The T_0 line also predicts the impossibility of forming bainite above a particular temperature. Figure 7.7 relates schematic free energy curves for α and γ phases to the dual phase $\alpha + \gamma$ region of the phase diagram. A second curve for α, includes the effect of strain energy. The form of the T_0 and T_0' curves is also shown.

It was thought that the toughness of weld H7 may be improved by increasing the extent of the bainite transformation. This may be achieved by moving the T_0 curves to the right in the phase diagram without altering the average carbon concentration.

7.4.2   Promoting bainite in H7

Investigation of the equilibrium phases in H7 using MTDATA showed that δ–ferrite should not form (Fig. 7.8).

Dilatometric measurements were made upon H7 in order to produce an experimental CCT curve as in Chapter 3. Superposing a cooling curve representative of an MMA weld using a 250 °C interpass temperature shows that the CCT curve is cut in a region where the transformation temperature is independent of cooling rate (Fig. 7.9). The calculated M_s temperature is also shown [22, 23].

Metallographic evidence for the presence of martensite was presented in Chapter 3. A martensitic microstructure is not desirable in this alloy due to its higher carbon content.
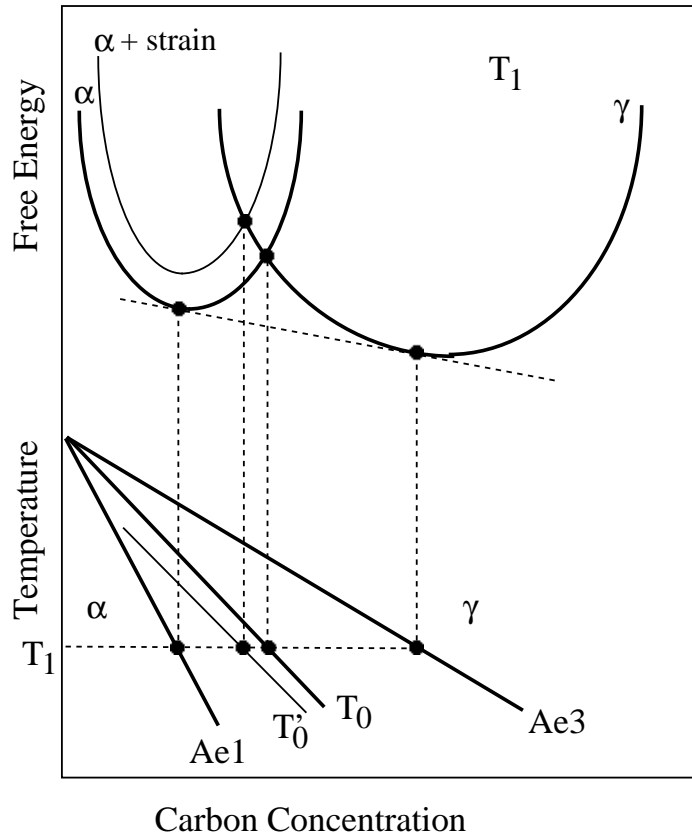
Figure 7.7: Schematic relationship between free energy curves and aspects of the Fe–C equilibrium phase diagram [25].
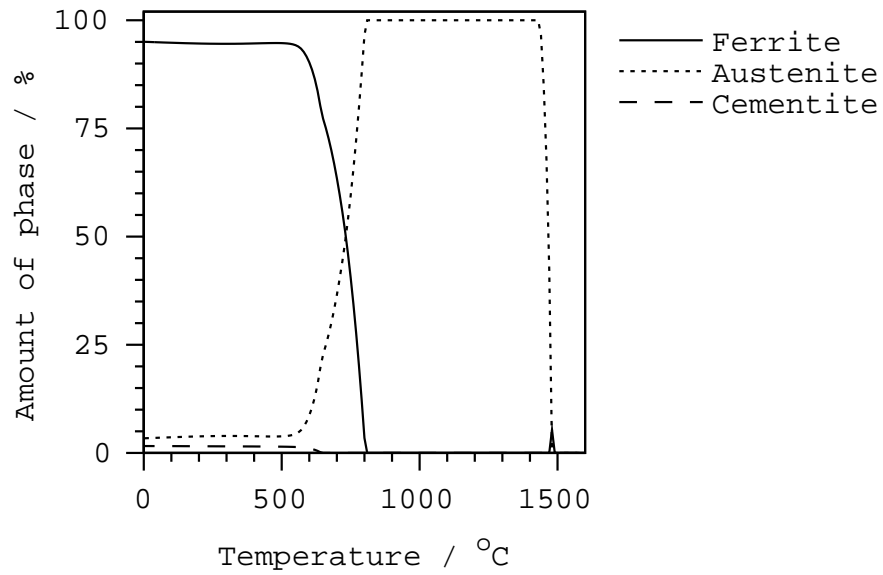
Figure 7.8: Calculated equilibrium composition of H7 as a function of temperature.
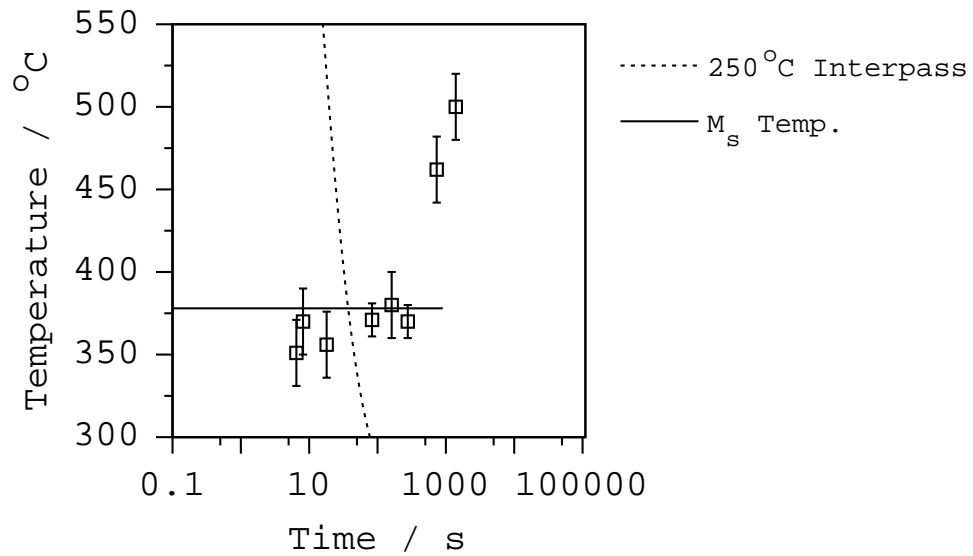
Figure 7.9: Experimentally determined CCT curve for H7.

Referring to the work of Aaronson *et al.* [4], an addition of Co would increase the extent of the bainite reaction by increasing the free energy change of the γ–α transformation and thus pushing the T_0 lines to higher carbon concentrations. Addition of 1.5 wt% Co was planned for H7 and to further reduce hardenability, reductions in Mn (by 0.5 wt%) and Ni (by 0.2 wt%) were also made. The new weld was denoted H71. MTDATA calculations indicated that a change in the composition would not lead to a retention of δ–ferrite to room temperature (Fig. 7.10).
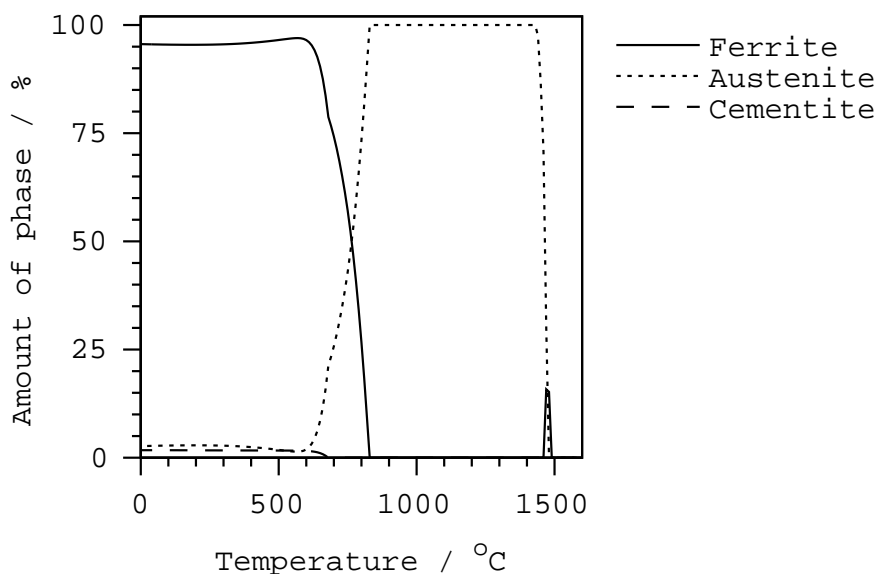
Figure 7.10: Effect of compositional changes of H71 on equilibrium phases.

An experimental weld was produced and tested according to previous specifications detailed in Chapter 3. The composition of this alloy is presented in Table 7.7. The experimental CCT curve shown in Fig. 7.11 shows an increase in the M_s temperature (calculated as 405 °C) and indicates that a reduction in hardenability relative to H7 was achieved.

A heat treatment of 1 h at 500 °C also allowed comparison with a similar treatment in H7. Table 7.4 shows the results of the tensile tests. The modification in composition appears to be detrimental to yield strength with little effect on the UTS. Considerable reductions in elongation were noted for the two untempered H71 samples.

Charpy impact testing revealed a reduction in toughness of the H71 specimens in both the as–welded and tempered conditions (Fig. 7.12). Tempering caused significant toughness reductions in both H7 and H71. In both alloys a reduction in toughness can be explained by carbide precipitation due to decomposition of retained austenite. Tempering promotes carbide formation particularly at interfaces causing a reduction in toughness.
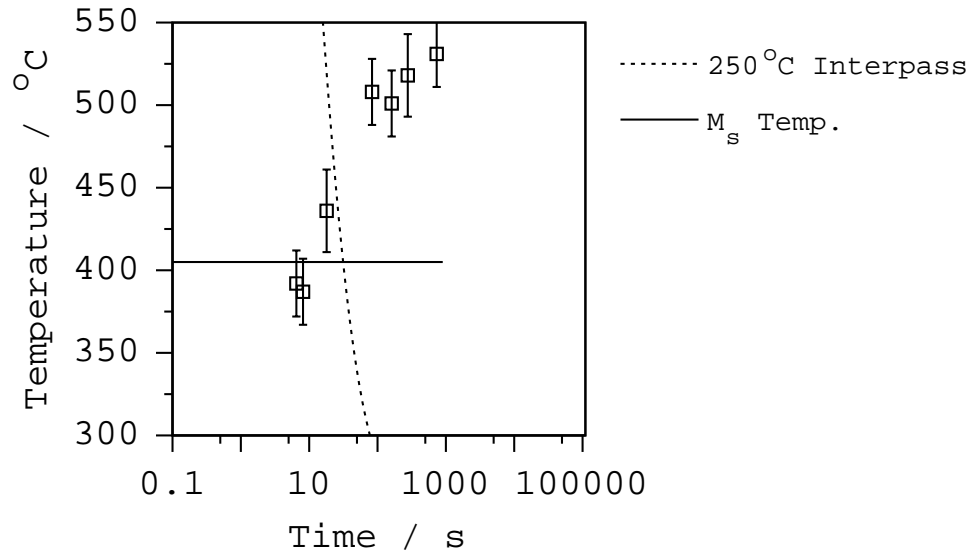
Figure 7.11: Experimentally determined CCT curve for H71.

Weld	Heat Treatment	Yield / MPa	UTS / MPa	Elongation / %
H7	-	845	969	23.6
H7	1 h 500 °C	779	1032	21.8
H7	1 h 500 °C	787	1019	20.2
H71	-	763	971	14
H71	-	758	959	15.2
H71	1 h 500 °C	754	968	18.6
H71	1 h 500 °C	734	961	20.4

Table 7.4: Tensile testing data for H7 and H71.

A simultaneous reduction in the strength of H7 can be attributed to the tempering of martensitic regions. The strength of H71 was apparently unaffected by tempering. This resistance to tempering coupled with the CCT cuve data indicates that a reduction in the volume fraction of martensite was achieved. Defects in the form of slag inclusions and gas pores were noted particularly in H71 Charpy specimens during testing despite a low oxygen content.
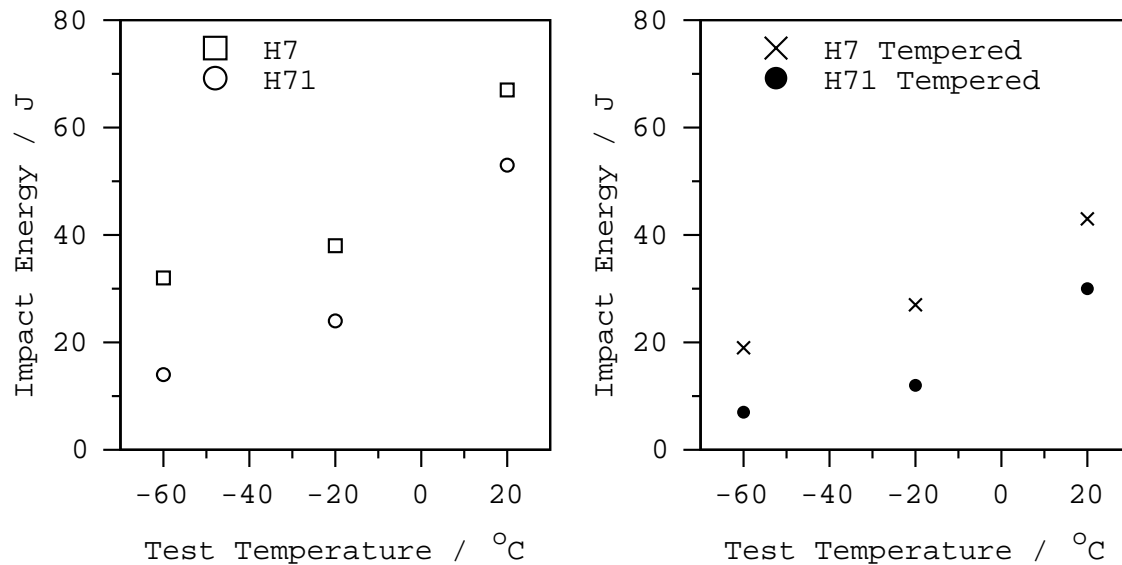
Figure 7.12: Comparison between impact toughness of welds H7 and H71 in the as–welded and tempered conditions.

7.4.3   Reductions in silicon

Transmission electron microscope studies detailed in Chapter 6 indicated that a nominal silicon content of 1.6 wt% in H7 is sufficient to retard the precipitation of carbides. It was decided to produce two further alloys of H7 using reduced silicon levels of 0.8 wt% and 1.4 wt% to investigate whether a beneficial effect upon mechanical properties would be produced. These welds were named H72 and H73 respectively. The welds were fabricated to the specifications detailed in Chapter 3. Details of measured compositions and welding conditions for these and other welds discussed in this chapter are presented in Table 7.7.

Tensile testing results indicated that no significant effect was produced by halving the silicon content (Table 7.5). Charpy impact data did however show that some improvement in toughness may result from reducing silicon levels which provides further evidence that carbides do not control the toughness of as–welded specimens of H7.

7.4.4   Conclusion of H7 modifications

A reduction in both the hardenability and the martensite content of H7 was successfully achieved by modifying the composition. However, the mechanical properties of the modified weld were not superior to those of H7. A greater number of defects were found in H71 which may have adversely affected some of the toughness measurements. Further experimentation into the manufacturing process is required before welds of equal quality of both H7 and H71 can be produced. Further investigations into the effect of the silicon content in H7 suggested that carbides do not control the toughness of H7 specimens in the as–welded condition. The production of further welds and detailed examination using transmission electron microscopy are required to resolve the relationship between the microstructure and the toughness of H7. However, the achievement of this goal will be greatly aided when the problems of manufacturing alloys of this type are overcome.

Weld	Yield Stress / MPa	UTS / MPa
H7 (1.6 wt% Si)	836	970
H73 (1.4 wt% Si)	853	954
H72 (0.8 wt% Si)	843	958

Table 7.5: Tensile test data for H7 containing reduced levels of silicon.

Weld	Test temperature °C			
	-78	-60	-40	-30
H7 (1.6 wt% Si)	20	32	33	-
H73 (1.4 wt% Si)	19	26	32	38
H72 (0.8 wt% Si)	26	33	45	47

Table 7.6: Charpy impact values (J) for H7 welds containing reduced silicon.

Element	Weld Name				
/ wt%	H1+4 wt% W	H1 - 4.5 wt% Ni	H71	H72	H73
Carbon	0.053	0.049	0.098	0.100	0.120
Manganese	2.00	2.31	1.72	2.24	2.30
Silicon	0.29	0.32	1.61	0.86	1.38
Phosphorus	0.008	0.009	0.010	0.009	0.009
Sulphur	0.011	0.011	0.007	0.011	0.011
Chromium	0.45	0.77	0.05	0.03	0.03
Nickel	2.97	4.57	1.89	2.11	2.12
Molybdenum	0.14	0.53	0.23	0.21	0.21
Vanadium	0.015	0.018	0.015	0.017	0.017
Copper	0.02	0.02	0.05	-	-
Titanium	0.015	0.016	0.029	0.024	0.033
Tin	0.002	0.005	0.006	0.011	0.010
Arsenic	-	0.010	0.003	0.005	0.005
Boron	-	0.0003	0.0003	-	-
Cobalt	-	-	1.88	-	-
Tungsten	3.857	-	-	-	-
Oxygen	0.0412	0.0325	0.0223	0.0249	0.0261
Nitrogen	0.0099	0.0076	0.0130	0.0108	0.0121
Iron	bal.	bal.	bal.	bal.	bal.

Table 7.7: Measured chemical composition of the new welds. All welds were fabricated to ISO 2560 using 20 mm thick plates. Approximately 30 runs were required to fill the gap, with 2–4 beads per layer. Welding was performed using a current of 174 ± 1 A, at a potential of 25 ± 1 V DC to give an electrical energy input of 1.08 ± 0.05 kJ mm^{-1}. An interpass temperature of 250 °C was specified. 'Buttering' of the plates was also performed prior to welding.

Chapter 8

Retardation of Cementite Precipitation due to Silicon

8.1 Introduction

The fact that a large concentration of silicon ($\simeq$ 2wt%) retards the precipitation of cementite has been exploited widely. For example, in the conversion of cementite–rich white cast iron into graphite–rich grey cast iron. The silicon somehow prevents the precipitation of cementite during the solidification of cast iron.

It is also well known that martensite tempers at a slower rate in silicon–rich steels, so that silicon also hinders the formation of cementite from supersaturated ferrite [9, 87, 102]. This is the basis of a highly successful ultra–high strength steel, $300M$, containing about 1.6 wt% Si [146]. Silicon also retards the precipitation of cementite from austenite. Therefore, in silicon–rich steels and in austempered ductile cast irons, the growth of upper bainite may not be accompanied by the precipitation of cementite. The microstructure at the transformation temperature is carbide–free, consisting of a simple mixture of bainitic ferrite and carbon–enriched residual austenite [31, 97, 128, 155, 156]. Silicon has its effect because of its remarkably low solubility in cementite, so small that it is frequently assumed to be zero in phase diagram calculations. The need to partition silicon during the growth of cementite might explain the observed retardation of the precipitation rate [143]. It has also been argued that silicon favours the formation of metastable transition carbides in which it has a greater solubility [74, 152] but it has now been shown that the transition carbides are not particularly enriched with silicon [20]. However, this last observation has to be considered in the light of the mechanism by which the transition carbides form. If they form by a displacive mechanism then they are expected to contain less silicon than

might be the case under equilibrium conditions; the result does not necessarily contradict the proposition that the transition carbides have a high solubility for silicon. The work detailed below focuses on cementite precipitation at relatively low temperatures, for example, during the tempering of martensite or during the bainite transformation. Prior to this a short review of the carbide precipitation mechanism is given in order to establish a working hypothesis for the effect of silicon.

8.2   Mechanism of Carbide Formation

There is a great deal of evidence that the carbides associated with these transformations form by a displacive mechanism without the partitioning of substitutional solutes. The mechanism must obviously involve the diffusion of carbon, but not of substitutional solutes or iron atoms. Considerable experimental data show that the carbide precipitation associated with bainite and martensite does not lead to a partitioning of substitutional solutes [24, 46]. The precipitation can occur under conditions where the diffusion rates of iron and substitutional atoms are incredibly small compared with the rate of precipitation. It has in fact been believed for some time that the cementite lattice may be generated by the deformation of the ferrite lattice, combined with the necessary diffusion of carbon into the appropriate sites. The Fe/X ratio thus remains constant everywhere and subject to that constraint, the carbon achieves equality of chemical potential; the cementite is then said to grow by *paraequilibrium* transformation. The way in which the ferrite lattice could be deformed to produce the right arrangement of iron atoms needed to generate the cementite has been reviewed by Yakel [197]. High–resolution transmission electron microscopy supports the idea that the carbide particles grow by displacive transformation [131, 180, 181]. In a remarkable experiment, Babu *et al.* [17] have shown using the atom–probe technique that the cementite obtained by tempering martensite is forced to inherit the silicon concentration of the martensite. This is in spite of the fact that the equilibrium solubility of silicon in cementite is negligible. The number of carbide variants which grow in any given plate of martensite decreases when the virgin martensite is tempered under the influence of the stress. This response of the microstructure to an externally applied stress is consistent with a displacive mechanism of transformation.

To summarise, it appears that substitutional solute atoms are trapped in the cementite when the latter precipitates during the bainitic or martensitic transformations in steels. That is, the cementite grows by a paraequilibrium transformation mechanism. In silicon containing steels the free energy change associated with the paraequilibrium precipitation of cementite must be much smaller than when the cementite is free of silicon. It is proposed

here that this is what leads to the suppression of cementite in high–silicon bainitic or martensitic steels.

8.3   The Hypothesis

In an ordinary steel which is free of silicon, the formation of upper bainitic ferrite is accompanied with the precipitation of cementite (θ) from the adjacent carbon–enriched austenite (γ). It follows that at the transformation temperature the alloy must lie within the $\gamma + \theta$ phase field of the paraequilibrium phase diagram. Note that the term "paraequilibrium" is used instead of "equilibrium" since as discussed earlier there is no redistribution of substitutional solutes during the formation of cementite in bainite or martensite. A common experimental result is that the addition of silicon stops the precipitation of cementite, leaving a microstructure of just bainitic ferrite and carbon–enriched retained austenite. There are two possible explanations for this observation:-

1. The addition of silicon causes a change in the phase diagram so that the alloy now lies in the single–phase austenite field. There is no driving force for cementite precipitation by a paraequilibrium mechanism.

2. The addition of silicon causes the $\gamma + \theta$ phase field to decrease in extent so that the driving force for the precipitation of cementite is reduced greatly, making the precipitation process extremely slow compared with the rate at which the bainitic ferrite forms.

The latter scenario is likely in some steels where experiments suggest that prolonged heat treatment at the bainite formation temperature causes the enriched austenite eventually to decompose into a mixture of carbides and ferrite [184, 199]. Austempered ductile cast–irons fall into this category since there is a well–defined heat treatment window where the microstructure initially consists of the desired bainitic ferrite and austenite, with the latter decomposing to carbides and ferrite as the austempering is continued to longer times.

8.4   Experimental Method

Thermodynamic calculations were to be performed on steel compositions using MT-DATA [88], the software package (discussed in Chapter 7) which uses critically assessed

thermodynamic date for calculation of phase equilibria. A recent development of this package allows calculation of phases under the constraint of paraequilibrium conditions.

The original MTDATA software contained no data concerning the equilibrium composition of silicon in cementite. As a result, calculations did not predict any silicon within it and paraequilibrium predictions could not be made as no thermodynamic data were available. It was necessary to provide the software with further data concerning silicon before useful calculations could be performed. Investigations have shown that the solubility of Si in the cementite phase is extremely low. An equilibrium cementite silicon content of 1 ppm was chosen as being a reasonable composition at 298 K and other interactions were assumed to be ideal. These modifications allowed the calculation of both equilibrium and paraequilibrium phase fields.

Initially the calculation of ternary phase diagrams was performed for the Fe-C-Si system at two temperatures under both equilibrium and paraequilibrium conditions. The system was constrained to produce only cementite from the austenite parent phase.

Calculations were then performed on the precipitation reaction of cementite from the austenite films of two steels detailed in Table 8.1.

Specimen	C	Mn	Si	Cr	Fe
A	0.4	3.0	2.1	-	bal
B	1.0	0.5	2.2	0.8	bal

Table 8.1: Concentration (in weight%) of the major alloying elements in the steels investigated.

These compositions match alloys used in relevant literature [21, 156]. As these calculations concern the precipitation of cementite from the austenite phase, the concentration of carbon within the austenite films could not be taken to be that of the bulk material as the formation of ferrite would cause considerable rejection of carbon into the austenite. Prior to calculation of thermodynamic quantities it was necessary to calculate the approximate concentration of the carbon in the austenite. This was achieved for steel A using computer software to calculate the composition of the austenite at the T_0' temperature (the temperature at which the bainite reaction should cease including a consideration of strain energy). Experimental data were used in the case of steel B. The concentration of the carbon within the austenite was input into the MTDATA software and calculations were performed on this basis.

Predictions were made of the temperature at which it should become thermodynami-

cally impossible for the material to produce cementite via paraequilibrium transformation conditions. For each of the steels calculations were performed to investigate the effect of both the silicon and carbon concentrations of the austenite on the paraequilibrium single phase boundary.

8.5   Results

Calculated ternary phase diagrams for the Fe rich corner of the Fe-Si-C system show two prominent features. An increase in temperature from 573 K to 773 K produced a larger predicted single phase austenite region, Fig. 8.1. In both cases the phase field was approximately parallel to the Si axis. A marked increase in the size of the austenite phase field was predicted on constraining the system to paraequilibrium transformation conditions. The phase boundary was no longer parallel to the Si axis, the deviation being particularly marked at the higher temperature. Furthermore, as expected the equilibrium single phase field is small even at high temperatures and in the discussion below the description of an alloy lying within the paraequilibrium single phase field, implies lying within the equilibrium dual phase field for all alloys considered. Calculations of the paraequilibrium single phase boundary in steels A and B were performed.

The calculated paraequilibrium phase boundary for steel A as a function of carbon is shown in Fig. 8.2. The carbon content of the retained austenite was calculated [26] as 0.48 wt% at 350 °C (the temperature used by Bhadeshia in isothermal transformation of the steel to form upper bainite). It is clear that this point is close to the calculated paraequilibrium phase boundary in the figure. The effect of silicon was similarly investigated for steel A. It was found that additions of silicon could affect the size of the paraequilibrium single phase field, its boundary significantly extending to lower temperatures on increasing the silicon concentration, Fig. 8.3.

A second composition, B, was chosen for investigation with the model. Useful data are available [156] detailing the microstructure of this steel (denoted 'SiCr4' in the original paper). The material was transformed to an upper bainitic microstructure at 380 °C for 24 hours. Measurements were also made of the concentration of carbon within the austenite, giving a value of 1.6 wt%. The dependence of the paraequilibrium single phase temperature on the austenite carbon content was calculated (Fig. 8.4). The position of Steel B in terms of austenite carbon content and isothermal transformation temperature are also presented. As for Steel A, the effect of silicon on the single phase temperature was investigated, Fig. 8.5.

a) Equilibrium 573K
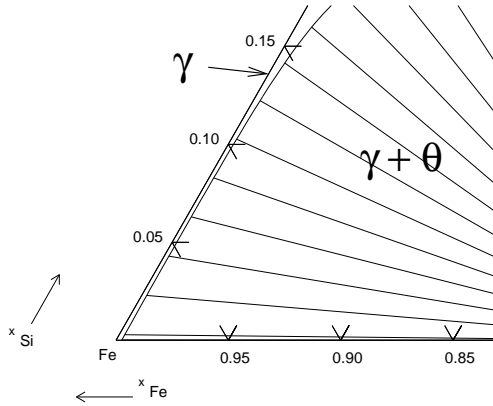
b) Equilibrium 773K
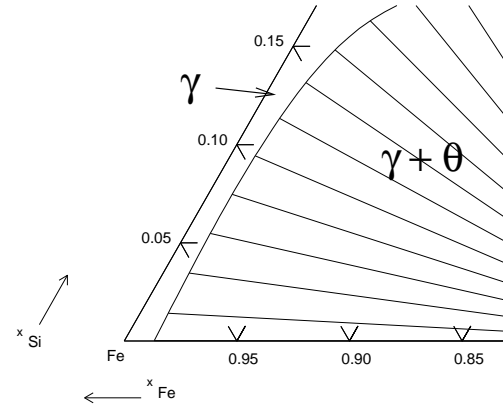
c) Paraequilibrium 573K
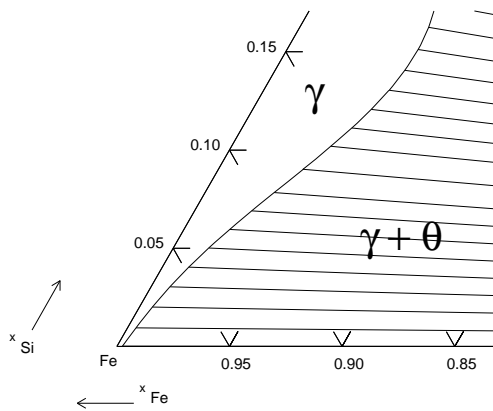
d) Paraequilibrium 773K
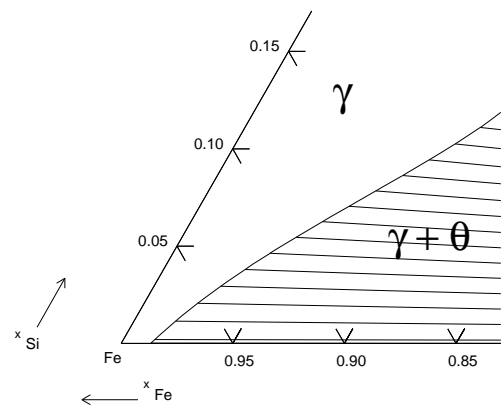
Figure 8.1: The Fe rich corner of the equilibrium (a,b) and paraequilibrium (c,d) Fe-Si-C phase diagram at 573 K and 773 K.

8.6 Discussion

The predicted effect of silicon is to expand the paraequilibrium single phase field. It is well known that silicon is instrumental in the retardation of cementite formation. Addition of enough silicon to an alloy to move the composition towards or into the single phase paraequilibrium region would retard or even prevent the paraequilibrium reaction mechanism
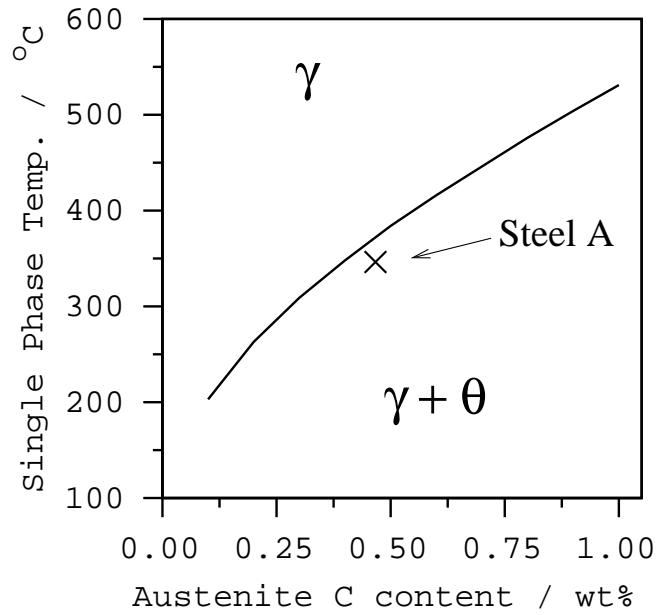
Figure 8.2: Predicted paraequilibrium phase fields for a composition based upon steel A as a function of austenite C content. The calculated position of steel A is also shown.
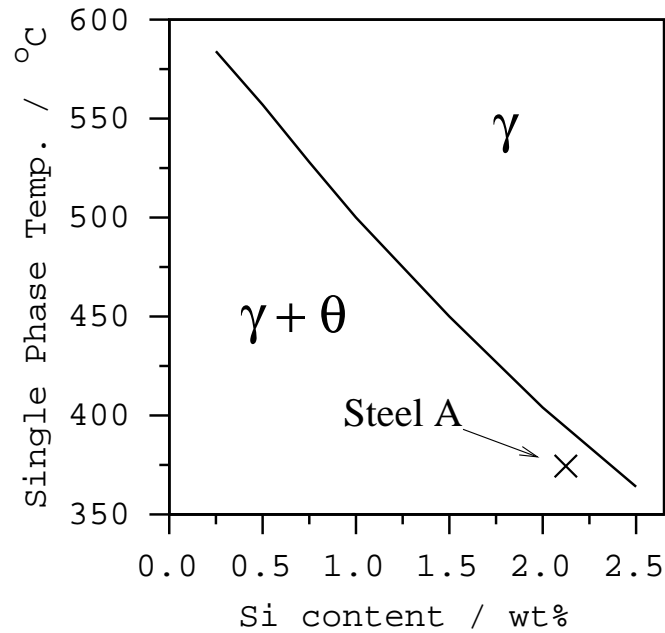
Figure 8.3: The calculated effect of Si on a composition based upon steel A.

which is often favoured over the slower equilibrium route.

Analysis of the ternary phase diagrams shows that the equilibrium austenite phase
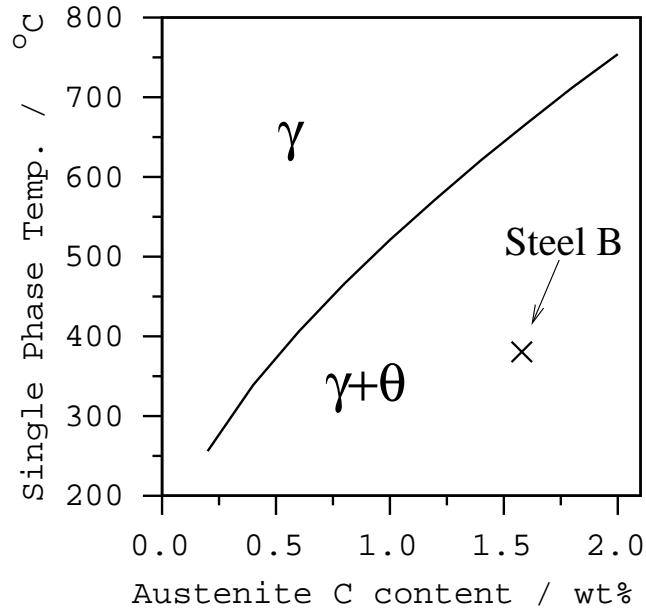
Figure 8.4: Dependence of paraequilibrium phase fields on austenite C content for a composition based upon steel B. The calculated position of steel B is also shown.
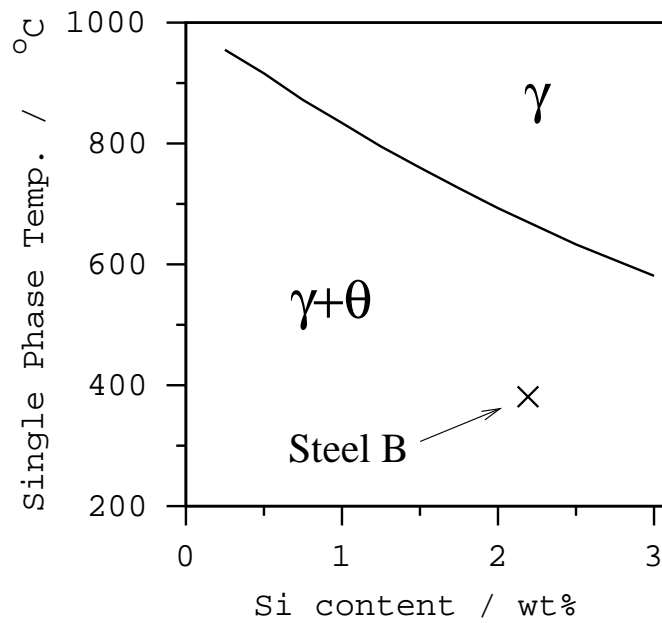
Figure 8.5: Predicted paraequilibrium phase fields for a composition based upon steel B as a function of Si content.

boundary is approximately parallel to the silicon axis, indicating that silicon has little effect on the austenite phase field at reasonable steel compositions ($< 10 \, \mathrm{at\%}$ Si). In the paraequilibrium case, increasing the silicon content moves the single phase boundary further from the Si axis, thus stabilising the austenite phase (Fig. 8.1). This effect was found to be particularly marked at the higher temperature (773 K). Theoretically it would be expected that the paraequilibrium austenite phase field should be larger than its equilibrium counterpart at a specific temperature due to the higher activities of the non-partitioned components [86]. Consequently, an alloy having a composition lying outside the equilibrium single phase region, but inside the paraequilibrium single phase region can only precipitate cementite via an equilibrium mechanism. In this manner a boundary condition can be applied to the silicon composition of the steel in that, ensuring the steel's composition lies within the paraequilibrium single phase field, any precipitation of cementite should be retarded until equilibrium conditions are approached.

The calculations are likely to become progressively inaccurate as the content of the alloying elements increases. The software was forced to calculate only austenite and cementite phases regardless of the relative stability of other possible phases. The effect on the phase diagram can be seen in Fig. 8.1 where the paraequilibrium phase boundary deviates towards the silicon axis at high Si levels.

Clearly predictions of this diagrammatical nature can only be applied to ternary alloy systems. However, the MTDATA software is capable of performing similar calculations for systems containing more than three elements although such calculations can not be easily represented graphically. The assumption of the accuracy of the calculations is a necessity which will become more severe as the number of alloying elements is increased. The question of the accuracy of the calculations is difficult to resolve purely due to the lack of available relevant experimental data. Although a number of investigations have been performed concerning the effect of silicon, many of these focus upon the precipitation of cementite from the ferrite phase as in the case of microstructures containing martensite and lower bainite. The calculations detailed here are relevant to upper bainite where the precipitation of cementite occurs from the austenite films between ferritic plates. The two steels used for the calculations were chosen as experimental data are available for them detailing the formation of upper bainite/austenite microstructures and their subsequent tempering.

Steel A was found to lie close to the paraequilibrium single phase boundary, indicating that at this temperature very few carbides should form via a paraequilibrium mechanism. Close to such a boundary in the two phase region, the driving force for the transformation will be low. A 30 min tempering treatment at 500 °C did produce small monoclinic carbides

but these reverted quickly to cementite on further tempering. The small volume fraction of non-equilibrium carbides and their rapid conversion to the 'equilibrium' phase is indicative of the unfavourable paraequilibrium reaction kinetics occurring within the material. A steel under conditions favouring a paraequilibrium mechanism is likely to exhibit a greater number of metastable carbides that form more rapidly and persist for long periods of tempering prior to formation of the stable cementite phase.

In the case of steel B, calculations indicate that the material lies well within the calculated paraequilibrium phase field (Fig. 8.4). The composition of this steel is wholly different to that of A. Examination of the figures indicates that the position of the single phase temperature as a function of C is quite similar in both cases. Steel B has over double the carbon content and similar levels of silicon to A. The steep gradient of the phase boundary as a function of carbon indicates that were the two steels to be identical in composition other than in C content, steel B would be expected to exhibit much greater evidence of a paraequilibrium transformation. The effect of silicon is similar in steel B to that exhibited in A, in that the form and the gradient of the phase boundary is similar in both cases. Sandvik's [155, 156] observations indicated the presence of a distribution of fine previously unidentified metastable carbides following the isothermal heat treatment. The resistance of this carbide to tempering was also investigated. Subjecting the specimens to a 4 hour temper treatment at 500 °C, it was noted that this time was not long enough to convert all of the carbides into cementite. In comparison to steel A, in which Bhadeshia [21] noted that complete conversion to cementite could be achieved with a 2 hour temper at 500 °C, steel B showed greater resistance to tempering. After double the time at 500 °C a significant although unquantified amount of the metastable carbide was still present.

The calculations performed for steels A and B predict this difference in behaviour. For steel A, it is apparent that the composition and conditions place the material near to the single phase region and it is to be expected that the driving force for a paraequilibrium transformation route is low. Hence the number of metastable carbides is low and the carbon remaining in solution within the austenite will increase the driving force for cementite formation when tempering at higher temperatures. In the case of steel B, the isothermal transformation temperature places the material well below the paraequilibrium single phase boundary, indicating that there will be an appreciable thermodynamic driving force for this reaction to occur. It would be expected therefore to observe carbides formed by a paraequilibrium route and that having formed, their relative stability would cause them to persist when tempered.

Tempering at higher temperatures as was performed in these cases, is likely to promote a mechanism which exhibits more of the characteristics of a diffusional equilibrium

transformation. However, the difference between A and B is that in the latter case the metastable carbides form during the original transformation, whereas the former contained no visible carbides after transformation. The calculations clearly show that steel B lies well within the dual phase region and even at 500 °C the paraequilibrium reaction should continue to occur. As a consequence it is to be expected that tempering at 500 °C has a more profound effect on steel A.

The calculations detailed above are based upon thermodynamics and can only be taken as indicating the limiting conditions governing the alloy systems. They do not provide kinetic data and can only be used as a guide for determining the possible reaction mechanisms. The formation of cementite via metastable carbides and the effect that silicon has upon the kinetics of these reactions is not as yet fully understood. The paraequilibrium and equilibrium reaction mechanisms represent limiting cases whereas in reality it is to be expected that the precipitation of cementite exhibits characteristics of both these mechanisms.

8.7   Conclusions

Modification of a thermodynamic database used by MTDATA [88], computer software for predicting thermodynamic quantities in alloy systems, has allowed the calculation of the effect of silicon on the Fe-Si-C ternary phase diagram and on two alloys under both equilibrium and paraequilibrium conditions. It has been shown that silicon greatly increases the single phase (austenite) field under paraequilibrium conditions and as a consequence cementite precipitation via this mechanism may be retarded or prevented. Comparison with experimental data shows that an alloy close to the calculated paraequilibrium single phase boundary does indeed exhibit far fewer carbides on isothermal transformation than an alloy lying well within the dual phase region. Further data confirm that the metastable carbides formed in this case are quite resistant to tempering, indicative of the alloy composition lying well within the paraequilibrium two phase region. This technique allows the calculation of an upper bound of temperature or composition which, when applied, should prevent the paraequilibrium precipitation reaction of cementite from upper bainite, thus producing clean carbide free microstructures.

Chapter 9

Copper in Steel

Copper is added to some High Strength Low Alloy (HSLA) steels for precipitation strengthening. This chapter presents a review of the effect of copper in iron and steel with a view to constructing a model for Cu precipitation, which can ultimately be applied to welding alloys.

9.1   The Iron–Copper system

Copper has a similar atomic radius to that of iron in the α phase and does not form an intermetallic compound. The mutual solid solubilities of both elements are very limited, that of Cu in α–iron reaching a maximum of 1.9 at% at 850 °C (Fig. 9.1). At the Cu–rich end of the equilibrium phase diagram, iron has a maximum solubility in the face–centred cubic (fcc) ε phase of around 4 at%. Ferrite can be supersaturated with copper by quenching from the austenite phase field. Such a supersaturation drives the precipitation of the Cu–rich ε phase, which leads to the usual peak in hardness as a function of isothermal aging time.

In contrast to many systems, the precipitated phase, Cu, has a lower yield strength than the iron matrix. Research on Fe–Cu alloys has generally involved quenching followed by aging treatments at temperatures in the range 400–700 °C. High temperatures produce an immediate increase in hardness as aging begins. At temperatures below about 500 °C, an incubation period appears to occur before the onset of hardening, particularly in dilute alloys (Fujii *et al.* [72]). This may be simply a reflection of the slow precipitation kinetics. X-ray diffraction studies show that the lattice parameter of aged copper-containing α–iron drops during aging and at long aging times extra reflections due to ε copper are observed [135]. Precipitates also change in morphology from spheres to rods with long term or high temperature treatments [90, 154].
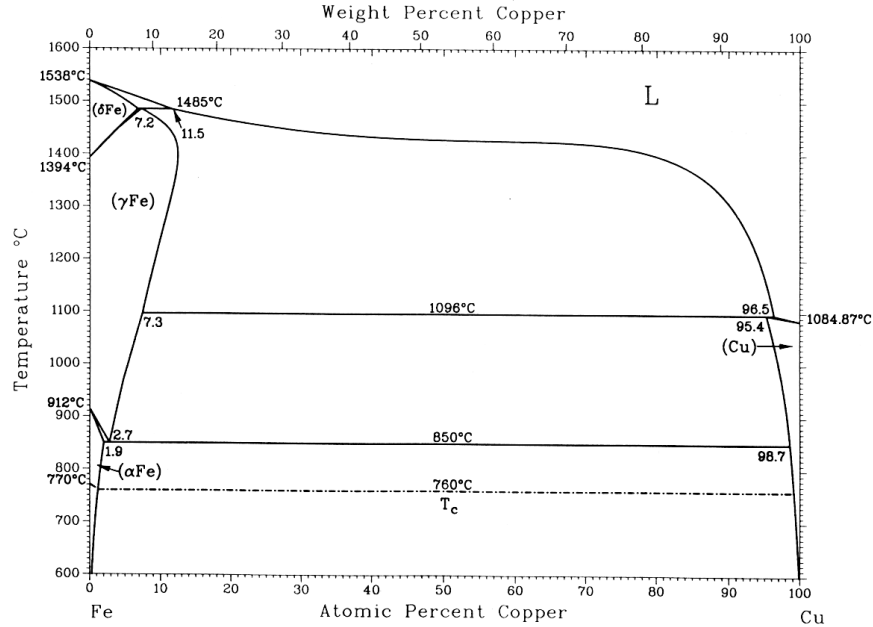
Figure 9.1: Equilibrium phase diagram for the Fe–Cu system [16].

9.2 Precipitation behaviour of Cu in Fe

In 1960, Hornbogen and Glenn [90] investigated the precipitation of copper from iron alloys using carbon extraction replicas. The alloys were quenched from both the γ (1000 °C) and α (840 °C) phase fields. Subsequent aging was performed at 500 °C, 600 °C and 700 °C. The hardness of the alloys as a function of aging time was monitored, the lower temperatures producing a stronger effect (Fig. 9.2). Similar behaviour is exhibited regardless of the parent phase.

A homogeneous distribution of precipitates was found in the replicas. Tempering at 700 °C caused rod-shaped particles to appear with an orientation relationship aligning the closest packed directions in α iron with the easy growth directions in the ε copper. After an hour at 600 °C transmission electron microscopy showed a dispersion of fine (≈ 90 Å) spherical copper precipitates which grew but reduced in number over time. X-ray diffraction revealed these to be ε copper, their composition remaining constant during tempering. At 500 °C and 600 °C two stages of precipitate growth were observed:

1. Particles of ε–Cu ≈ 90 Å diameter rapidly precipitate shortly after the start of the tempering - rapid coherent Cu clustering was thought to be aided by an excess of
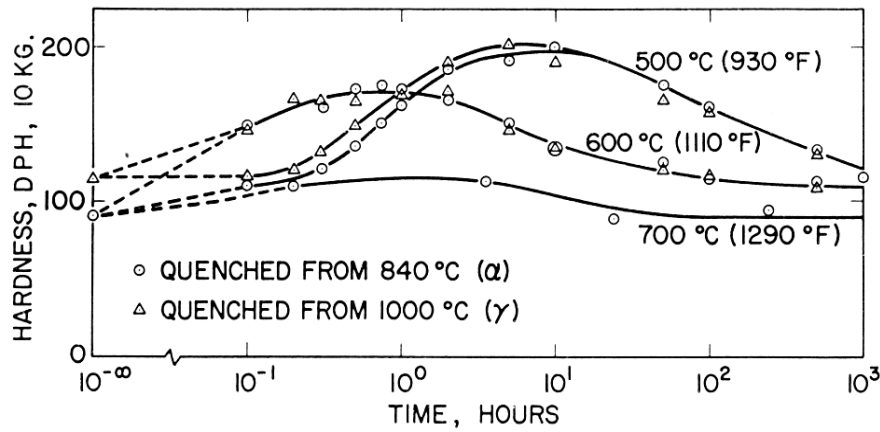
Figure 9.2: Hardness as a function of aging time and temperature for a Fe-1.23 wt% Cu alloy [90].

vacancies [73, 90].

2. Growth as a function of $\sqrt{t}$ as predicted by Zener [203] due to volume diffusion of Cu. This rate was later measured by Goodman *et al.* [73].

Little difference was observed between samples quenched from either phase field although some copper films were observed on the boundaries formed by the γ-α transformation.

Ricks [154] in 1979 also studied some Fe-Cu alloys and in a manner similar to Hornbogen, quenched specimens of Fe-2 wt% Cu from 1200 °C. He performed a number of tempering treatments (using temperatures of 600, 700 and 800 °C) but kept the duration of each constant at 2 hours. Transmission electron micrographs of the specimens showed that fine precipitates generally formed on dislocation networks at 600 °C. At 700 °C some rods were observed, the distribution being coarser, and at 800 °C large rods formed surrounded by dislocations indicating the strain that their growth had caused within the matrix.

Observations that particles in excess of 300 Å diameter became rod shaped [90, 154] were later confirmed by Speich and Oriani [163] to be due to interfacial energy. Rods can be aligned such that the cylindrical surface defining the interface between the sides of the copper rod and the matrix, is constructed from close–packed rows of atoms in both lattices, resulting in a reduction in the total interfacial energy.

Further experiments by Hornbogen [92] in 1962 compared the precipitation behaviours of copper and gold in iron. Both elements behave similarly except that the Au has a radius in excess of that of Fe by a factor of 1.126, whereas Cu is almost identical at

1.003. Hornbogen suggested that strain energy was critical in the precipitation of the Au and Cu, all other factors being approximately equal. He found that gold tended to nucleate upon dislocations alone whereas copper tended to nucleate on dislocations and also apparently homogeneously within the iron structure (although he suggested Cu may actually require vacancies to initiate nucleation). The strain energy effect of Au precipitates interacting with dislocations was cited as the cause for the observed differences in nucleation behaviour.

Hornbogen [93] in 1964 also examined the precipitation of copper in an Fe-0.9 at% Cu alloy. These studies revealed that small coherent precipitates form in large numbers and grow, thus depleting the matrix of copper. However, coarsening was evident even before the matrix was depleted to its equilibrium composition since the number density of particles decreased.

The tensile strength reaches a maximum early in the precipitation reaction and this high level of strength is maintained for a period of time up to a point where the matrix contains almost the equilibrium concentration of copper and further growth then occurs by coarsening. During overaging the yield stress drops as the interparticle spacing increases although this process is considerably slower due to coarsening kinetics.

Hornbogen later postulated that the early stage of precipitation occurred by the "formation of copper–rich coherent body–centred cubic zones which transform *in situ* into face–centred cubic particles" [91].

The similarity between the atomic radii of Fe and Cu caused problems for early work using TEM imaging as these elements have similar scattering factors and there is little strain imposed on the matrix, minimizing strain contrast. However, the advent of the Field Ion Microscope (FIM) allowed the early stage of precipitation to be studied on the finest scale. Youle [201] noted that precipitation occurred "randomly in the matrix, on line defects and at grain boundaries" those at the latter sites being larger. The peak strength in the material corresponded to an approximate precipitate diameter of 3 nm correlating well with the data of Goodman *et al.* [73] who also suggested that particles in excess of 50 Å in diameter showed no coherency with the matrix.

The FIM observations showed large number densities of body–centred cubic precipitates ($\approx 10^{24}\,\mathrm{cm^{-3}}$) prior to ε–Cu precipitation. The largest number densities observed in both cases coincided with the peak in strengthening. However, rival studies disagreed on the amount of the copper remaining in solution, Goodman *et al.* suggesting that half of the Cu remained, Youle suggesting very little. In the overaged condition when precipitates are all of the ε phase, it was shown that over 99 % of the particles have by that time redissolved. The data of Goodman *et al.* agreed well with the TEM data from alloys in the

overaged condition. FIM is superior to TEM for studying small coherent copper particles as the contrast between these and the iron matrix in a TEM is very small. Hence only non-coherent particles are observable whereas coherent ones may also be counted using FIM.

Since the time of such FIM studies the sequence of events associated with copper precipitation has been more clearly established [183]. The first precipitate to form is a metastable form of copper with a bcc structure containing less than 2 wt% iron. Peak aged specimens contain bcc precipitates of approximately 4 nm diameter whilst around 50 % of the copper remains in solution. Following growth to about 6 nm the precipitates transform to the equilibrium ε–Cu fcc phase which exhibits internal twinning and faulting. Generally it is the latter phase that was observed in much of the early TEM work in this field.

9.3   The strengthening effect of copper

There are three main methods by which particles can strengthen a matrix [141]:

1. The particles do not share the plastic deformation of the matrix and the strengthening is due to the average spacing of the particles.

2. Dislocation motion in the matrix is inhibited by coherency stresses due to the precipitates.

3. The particles are sheared during deformation and energy is required to produce this shear.

The behaviour of dislocations with respect to Cu precipitates has also been examined in the Fe–Cu system. Hornbogen noted the shearing of particles after 10 % deformation but found little evidence of dislocations within particles of diameter < 30 nm. Fujii *et al.* [72] discussed possible strengthening mechanisms involving the creation of new interface by dislocation cutting of the particles, or by local variations in shear modulus. Neither of these theories could sufficiently explain their data. Orowan's mechanism of dislocation bowing between particles fitted the data well but they failed to find dislocation loops around the particles. TEM micrographs did however show bowing of dislocations between the particles. The lower shear modulus of ε–Cu than α–iron is probably responsible for the lack of Orowan loops being observed around copper precipitates, it being energetically more favourable for them to enter the precipitate. Thus bowing of dislocations in the matrix may drag sections through the precipitates forming a hybrid mechanism between classical

bowing and cutting [79, 153]. The metastable bcc phase is an extra consideration but in this case cutting of precipitates by dislocations is to be expected due to greater coherency. On the one hand, for small coherent particles, the dislocation line will experience limited pinning in many places, whereas in the overaged state the spacing between particles will be larger and the dislocation will bow between them before the stress causes the pinned sections of dislocation to pass through the particles.

9.4   Cu in steels

It is to be expected that the addition of other elements to iron may alter the solubility of Cu in Fe and the precipitation reaction. Ohtani *et al.* [137] reviewed the effects of alloying elements on the Fe–Cu equilibrium phase diagram. These can be summarized as:-

- Ni, Co, and Al additions result in an increase in the solubility of Cu in austenite.

- V, Cr, Mn and Si decrease Cu solubility in austenite.

Many of these elements are present within steels, the general trend being that elements to the right of Fe in the Periodic Table tend to increase copper solubility in austenite, those to the left reducing it. Only drastic changes in solubility would affect the precipitation behaviour, a far greater effect of the elements being upon the precipitation reaction kinetics.

Recently, Ohtsuka *et al.* [138] and Fourlaris *et al.* [68] examined the effect of copper on the austenite to ferrite transformation in steels. Ohtsuka *et al.* [138] observed a considerable retardation of the isothermal transformation rate from austenite to ferrite due to the presence of copper. Both the nucleation and growth rates were reduced. It was suggested that the nucleation rate decreased because of a reduction in the austenite grain boundary energy due to Cu segregation at high temperatures, a deceleration of carbon diffusion by repulsion between C and Cu and, the formation of fine coherent precipitates at ferrite nucleation sites. These mechanisms were not fully investigated. The growth rate was thought to be retarded by a solute drag effect of the Cu atoms.

Fourlaris *et al.* observed a retardation in transformation kinetics from austenite to bainite but that the supersaturation of copper was constant in both bainite and cementite following transformation from an assumed homogeneous distribution in the austenite phase. As the solubility of copper in both phases is very small this observation provides further evidence for a diffusionless mechanism of the bainite transformation. The experiments showed that no observable copper precipitates were present when the temperature

was held at 350 °C for a number of days. Heating to above 500 °C for a number of hours was required to induce the precipitation which was favoured within the bainitic ferrite rather than the cementite phase. The precipitation of ε–Cu was found to occur in a similar manner to Fe–Cu alloys, the copper retaining it's inherited homogeneous distribution from the austenite phase.

9.5   HSLA Steels

High strength low alloy (HSLA) steels contain low concentrations of solutes, particularly carbon, and attain good mechanical properties by careful processing [80]. Cu is frequently added to these steels to increase strength by precipitation hardening, a typical composition being Fe–0.05 C–1.4 Mn–0.25 Si–0.85 Ni–1.1 Cu (values in weight%). Foularis *et al.* observed a homogeneous precipitation of ε–Cu in bainitic ferrite within such materials. Banadkouki *et al.* [18] studied the effect of microstructure on the copper precipitation hardening phenomenon. The hardness response to aging of an HSLA80 type steel containing 1.1 wt% Cu was compared in the 'as–quenched' martensitic, isothermally transformed bainitic and 'as–rolled' ferritic conditions. All microstructures showed an increase in hardness due to aging at 450 °C, 500 °C, and 550 °C. In martensite a more rapid response to tempering was observed than in the ferritic microstructures (attributed to a greater dislocation density) but the competing effects of tempering and precipitation strengthening produced a smaller hardness increase. Bainite showed the greatest hardness response, this phase being more resistant to tempering but also containing comparatively more Cu in solution than the 'as–rolled' specimens. The hot rolling procedure produced interphase precipitation which has a lesser strengthening effect. It was suggested that peak hardness was attained in all cases when small ε–Cu precipitates were present, their observation being possible in a TEM. Aging revealed precipitates randomly distributed upon dislocations in both bainite and martensite. Lower temperatures produced a slower but larger hardness response as in Fe–Cu alloys.

Further studies on an HSLA80 steel by Thompson and Krauss [183] showed precipitation on dislocations due to aging treatments applied following quenching from the austenite phase. However, slow continuous cooling experiments (< 10 °C s^{-1}) did promote interface precipitation during the austenite–ferrite transformation. The resulting precipitates were less favourably positioned for strengthening, often being found in rows on or close to the final grain boundaries with a common orientation relationship. The continuous cooling experiments were not however comparable to welding conditions in that the cooling rate was too low. Furthermore, high strength welds contain displacive transformation products

in which nucleation of ε–Cu is likely to occur on dislocations.

9.6   Application to Welding

Unlike HSLA steels, copper is not commonly used to strengthen welding alloys for structural steels. This may be in part due to a reported reduction in toughness [183], welding alloys having generally lower toughness than wrought steels of comparable strength.

Kluken *et al.* [111] in 1994 presented some data on the effects of Ni, B and Cu in multi–run submerged arc weld (SAW) steels containing up to 0.9 wt% Cu. With virtually no nickel the yield strength was increased by 50-60 MPa with the addition of copper, but for 0.45 and 1.5 wt% Ni the yield stress fluctuated slightly as a function of copper content and no significant trend could be established, probably due to changes in microstructure. Ultimate tensile strength data proved more consistent in that copper increased the strength in all samples. It was noted that copper additions did have a detrimental effect upon toughness. Any precipitation was not characterised.

Kimura and Takaki [106] recently provided evidence that beneficial tensile properties may be obtained via copper additions. A range of Fe-Cu wrought alloys were solution treated and allowed to cool from 1250 °C under various conditions. The levels of Cu used were up to 4 at%, considerably higher than in the case of Kluken *et al.* Importantly one of these was an air-cooling treatment (similar to a single-pass weld). Particles of 10-20 nm in diameter were found in the air-cooled specimen resulting in a 100 MPa increase in strength over a water quenched specimen (which would have a more martensitic nature and greater Cu solid solution strengthing). Thus it would appear that natural cooling rates can promote high strength levels due to a fine dispersion of ε–Cu precipitates.

9.7   Conclusions

Literature indicates that additions of copper can significantly strengthen iron alloys, heat treatment of a supersaturated solution producing a peak in strength. The greatest improvements in strength are found in transformation products formed at low temperatures where aging at around 500 °C promotes a fine dispersion of precipitates. The first precipitates to form are of almost pure Cu with a body–centred cubic crystal structure. These produce a peak in strength when they are typically 3–4 nm in diamter, further heat treatment converting them to the equilibrium ε fcc phase. Unlike in HSLA steels, Cu is rarely used in welds. There is some evidence however that the rapid cooling of weld alloys may allow significant strengthening with Cu precipitates but a reduction in toughness may be

expected. Additions of Cu may therefore allow attainment of greater levels of strength in ultra–high strength weld alloys.

Chapter 10

A Model for Copper Precipitation from Ferrite

As reviewed in Chapter 9, the strengthening effect of a dispersion of fine copper precipitates may provide a mechanism for the substantial strengthening of steel welds in a manner similar to high strength low alloy (HSLA) steels.

The purpose of the work detailed within this chapter was to construct a numerical model for estimating the number density, volume fraction and size distribution of copper precipitates using composition and thermal history as input variables. The following chapter details a second numerical model to estimate the strengthening effect of the precipitates.

10.1   Fundamentals of the model

Literature concerning the behaviour of the iron-copper system was examined in Chapter 9. This research indicates a precipitation behaviour determined by nucleation and growth of embryos, followed later by coarsening effects, although Hornbogen suggests simultaneous coarsening [92].

Some simplifying assumptions are necessary as follows:-

1. The system is treated as a Fe–Cu binary alloy.

2. The precipitates are assumed to be spheres of pure ε copper.

3. Precipitation is assumed to occur from a supersaturated solid solution of ferrite.

10.2   Calculation of Precipitation

10.2.1   The nucleation model

The nucleation rate, $^\nu I$, per unit volume of second phase embryos from a matrix can be expressed as a function [54]:-

$$^\nu I = {}^\nu N \left(\frac{k_B T}{h}\right) \exp\left\{-\frac{(\Delta G_c + \Delta g_a)}{RT}\right\} \tag{10.1}$$

where $^\nu N$ is a nucleation site density which may be adjusted according to a variety of assumptions. h and R are the Planck and gas constants respectively, T is the absolute temperature. The constant Δg_a is the activation energy for the transfer of atoms across the embryo/matrix interface. ΔG_c is the activation energy for nucleation. For spheres it can be related to the magnitude of the transformation free energy change per unit volume, ΔG_v by:-

$$\Delta G_c = \frac{16\pi\sigma^3}{3\Delta G_v^2} \tag{10.2}$$

where σ is the energy of a unit area of second phase interface.

The form of Eqn. 10.1 indicates a strong dependence of the nucleation rate upon both temperature and ΔG_v. In reality the interfacial energy, σ, will take a low value due to the high degree of precipitate coherency. A value for a typical semi–coherent interface of $0.1\,\mathrm{J\,m^{-2}}$ was chosen whilst testing the model. ΔG_v is a thermodynamic property describing the driving force for the formation of a unit volume of second phase. Figure 10.1 indicates the magnitude of ΔG_v at the onset of nucleation [6]. The phases α and β represent the iron-rich and copper-rich phases respectively. Similarly A and B are representative of pure Fe and pure Cu. As the nucleation reaction proceeds and the level of supersaturation decreases, the free energy of the α phase follows the G^α curve from the initial point (abscissa $\bar{x}$) to the final, equilibrium position (x^α_{eqm}) (Fig. 10.2). A tangent to the G^α curve at any position gives intercepts on the ordinate axes corresponding to the chemical potentials of the single phase solid solution components, μ_α^A and μ_β^B. This is an application of the 'common tangent construction' for a single phase which, when applied in the more conventional manner between the α and β curves, gives the equilibrium state. In the equilibrium case the intercepts now give the equilibrium chemical potentials of the component species $\mu^A_{\mathrm{eqm},\alpha,\beta}$ and $\mu^B_{\mathrm{eqm},\alpha,\beta}$. A value for ΔG_v is now simply obtained from the difference in ordinate between the solid solution and equilibrium tangents at a composition fixed by the equilibrium composition of the β phase (assumed as pure Cu in the model).
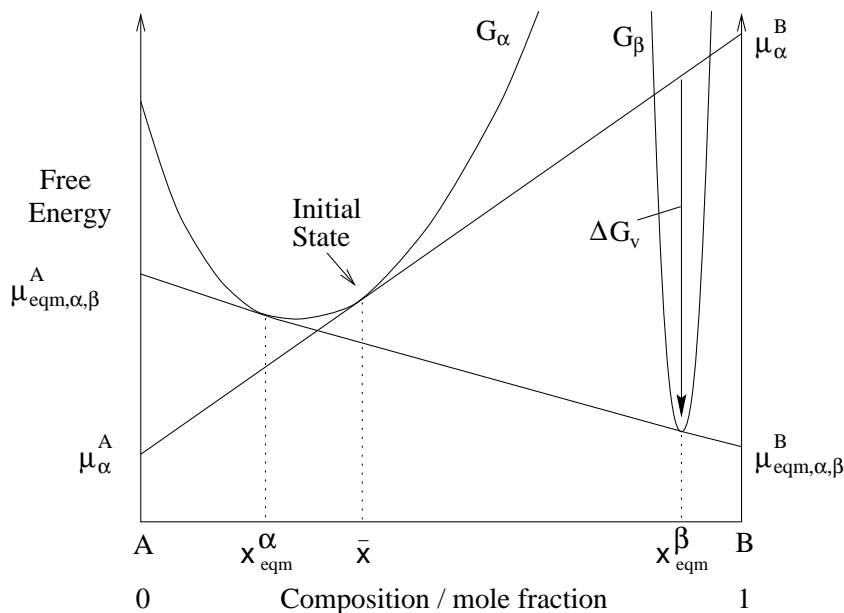
Figure 10.1: Schematic illustration of driving force for nucleation ΔG_v.

Detailed knowledge is required of G_α as a function of solute composition, as the tangent to this curve determines the value of ΔG_v. The assumption of pure copper precipitates ensures that the intercepts of the tangent with the G_β curve can be represented by calculating the chemical potentials $\mu^B_{\text{eqm},\alpha,\beta}$ and μ^B_α.

The form of the G^α curve as a function of temperature was calculated using MTDATA [88] (described in Chapter 7) and represented in the model using quartic polynomial equations. Preliminary MTDATA calculations of the form of the G^α curves showed that, as expected, the curve did not simply displace along the free energy axis as a function of temperature - it also changed its shape. A reasonable way to describe the free energy curve was to monitor the behaviour of certain points of constant composition as a function of temperature. However, rather than simply obtaining G^α values at each chosen composition, the corresponding chemical potentials calculated by MTDATA were recorded as these allow the calculation of ΔG_v.

Each curve was represented using 7 points. Calculations for approximately the full range of temperatures within the α phase field were performed (from 100 °C up to the phase boundary) in a composition range of 0 to 6 wt% Cu. Additional calculations were also performed in order to determine the position of the intercepts with the axes corresponding to the two–phase equilibrium state, and to represent the α / $\alpha+\varepsilon$ phase boundary. Quartic
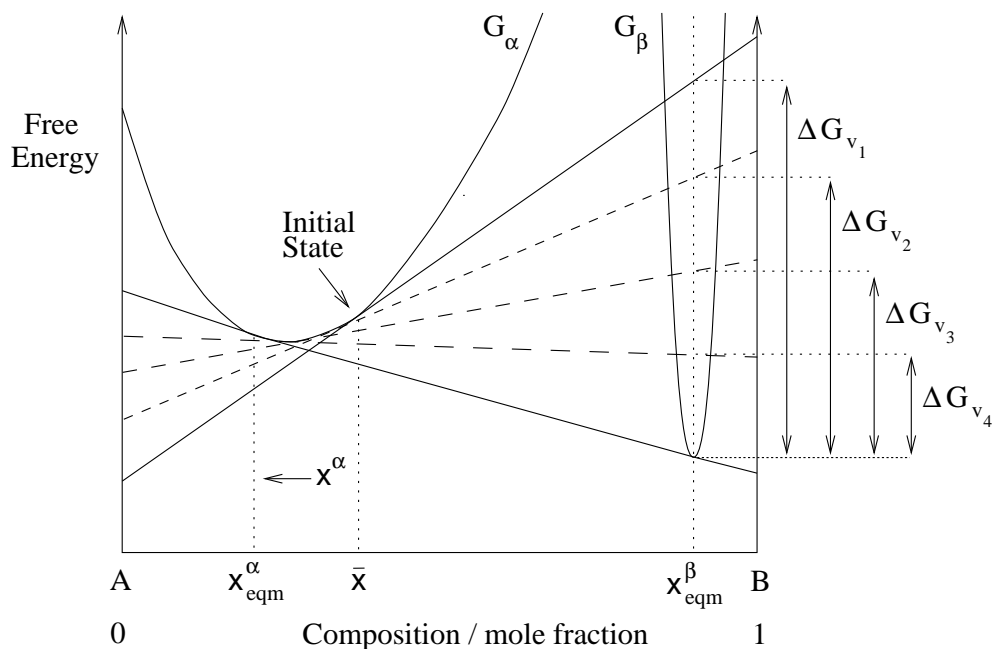
Figure 10.2: Reduction in driving force as nucleation proceeds.

polynomials were used represent the calculated data in all cases.

Whilst the thermodynamics of the system were modelled at length, it should be emphasised that this nucleation theory is only approximate [53]. Eqn. 10.1 is generally applicable to transformations in vapour, liquid and solid phase with appropriate adjustment of coefficients. However, in the case of a completely solid–state transformation the effect of strain energy is likely to become significant which was not taken into account. The approximately similar atomic radii of iron and copper go some way to reduce this effect but in reality the driving force for nucleation will be reduced [53]. Despite the small size of nuclei the free energy per unit area of interface is nevertheless assigned a constant value. Furthermore, the nature of interfacial chemical bonds is ignored and the activation energy for atomic transfer across the interface is assumed to be similar to that for diffusion within the matrix. Most importantly as detailed in Chapter 9 the copper–rich embryos are not initially composed of the face–centred cubic ε phase but rather a metastable phase with a body-centred cubic lattice. The initial presence of this phase implies more rapid kinetics which are not modelled. Hence some inaccuracies are to be expected during calculation of reaction kinetics.

10.2.2   The Growth Model

Growth was assumed to be controlled by the diffusion of Cu in ferrite. The radius of a spherical precipitate particle, S, during isothermal growth is given by [203]:-

$$S = \alpha_3 (Dt)^{1/2} \tag{10.3}$$

where D here is the diffusivity of Cu in ferrite, t is the time. Assuming a linear reduction in solute concentration ahead of the advancing interface α_3 is given by [78, 203]:-

$$\alpha_3 = 2^{1/2} \left\{ \frac{x^{\alpha} - x^{\alpha\beta}}{x^{\beta\alpha} - x^{\alpha\beta}} \right\}^{1/2} \tag{10.4}$$

where $x^{\beta\alpha}$ is the solute concentration in the precipitate in equilibrium with the matrix and $x^{\alpha\beta}$ the corresponding concentration in the matrix. x^{α} is the solute composition of the matrix at any time far from the precipitate (Fig. 10.3).
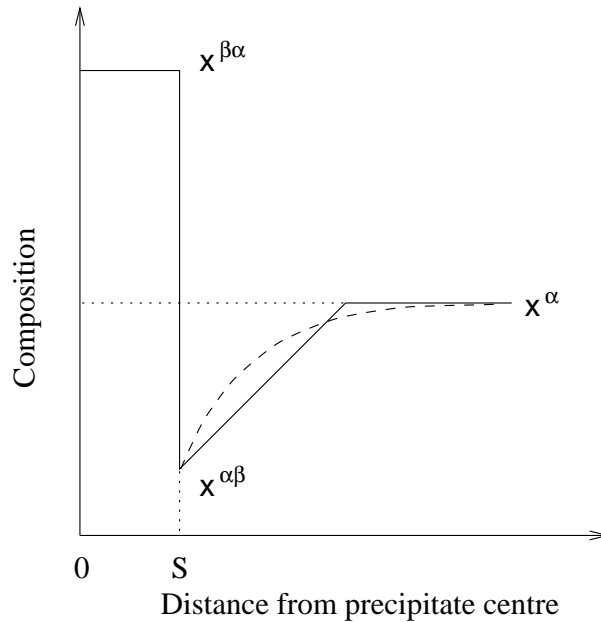
Figure 10.3: Approximate concentration profile of precipitation (solid line).

The diffusivity D of copper within ferrite was assumed to obey the equation:-

$$D = D_0 \exp \left\{ \frac{-Q}{RT} \right\} \tag{10.5}$$

D_0 and Q differ above and below the Curie temperature (759 °C), the values used are shown in Table 10.1. The diffusivity of Cu in ferrite is therefore greater than that of iron by a factor of about 1.6.

Temperature / °C	D_0 / $m^2 s^{-1}$	Q / kJ mol^{-1}
≥ 759 °C	13.5×10^{-4}	254
< 759 °C	2.0×10^{-4}	249

Table 10.1: Diffusivity data for Cu used in the model [70, 164].

Equation 10.4 evalutes α_3 using equilibrium solubilities for planar interfaces. However, in small precipitates the influence of the surface free energy of the interface becomes significant. This 'capillarity' effect alters equilibrium solubilities [53, 147].

10.2.2.1 Capillarity

Capillarity can be calculated by considering a matrix α containing two particles, P and Q of phase β, of identical composition. Let particle P have a spherical interface of radius S and particle Q have a planar interface ($S = \infty$). Assuming a constant surface free energy per unit area σ for all interfaces, transfer of a small amount of material dn from P to Q will reduce the free energy of the system by an amount dG. As the particles are of identical composition, dG arises solely due to a reduction in the total interfacial area. The addition of dn to particle Q causes no increase in its surface area (due to its infinite radius) but the surface area O of P is reduced by an amount dO which can be related to dG by:-

$$dG = \sigma dO \tag{10.6}$$

The free energy change dG is simply related to the molar free energy by:-

$$dG = \Delta G dn \tag{10.7}$$

Equating these expressions gives:-

$$\Delta G = \sigma \frac{dO}{dn} \tag{10.8}$$

The number of moles n of material in particle P is given by:-

$$n = \frac{4\pi S^3}{3 V_\beta} \tag{10.9}$$

where V_β is the molar volume of phase β. Using $O = 4\pi S^2$ leads to the equation:-

$$\Delta G = \frac{2\sigma V_\beta}{S} \tag{10.10}$$

Hence the free energy curve of the β phase is displaced by an amount ΔG which is a function of the precipitate radius. This results in new equilibrium compositions between the matrix and the precipitate phases denoted $x^\alpha_{S,\text{eqm}}$ and $x^\beta_{S,\text{eqm}}$ respectively (Fig. 10.4).
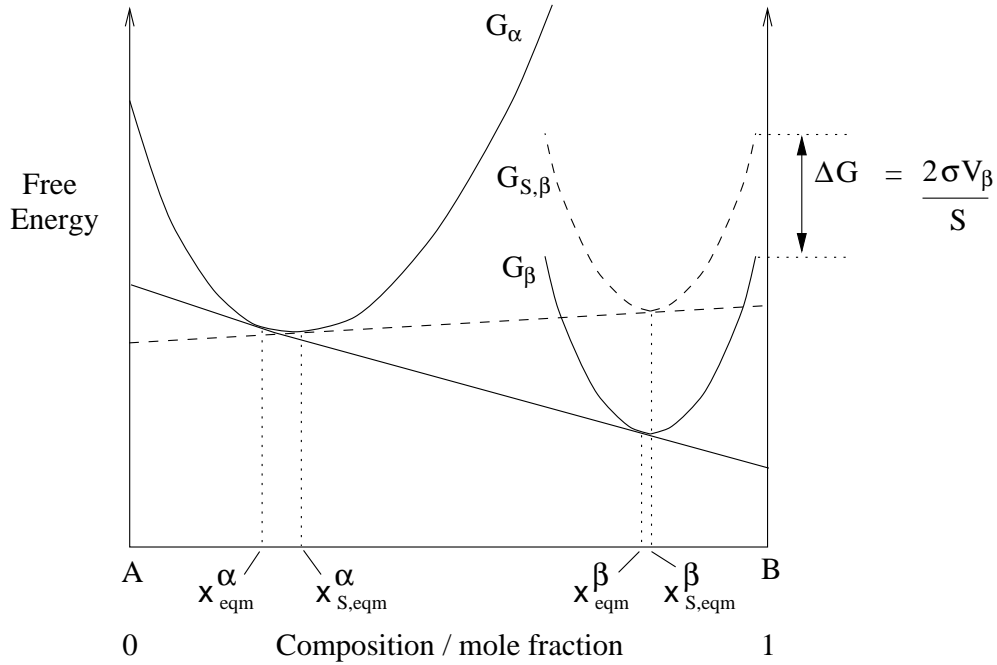
Figure 10.4: The effect of capillarity on the equilibrium between α and β phases.

The β phase is representative of ε–Cu, its equilibrium composition remaining unchanged as pure Cu. Assuming that the α phase is a regular solution, the composition of a planar interface in equilibrium with β can be written as [147]:-

$$x^\alpha_{\text{eqm}} = \exp\left\{\frac{\Delta G_B + \Omega}{RT}\right\} \tag{10.11}$$

where ΔG_B is the difference in free energy between the α and β phases for pure β (i.e. copper). $\Omega = z\epsilon$ where z is the number of bonds per atom and ϵ describes the energy difference between similar and dissimilar atomic bonds.

The additional free energy due to capillarity can be added to the exponent such that Eqn. 10.11 becomes:-

$$x_{S,eqm}^{\alpha} = x_{eqm}^{\alpha} \exp\left\{\frac{2\sigma V_{\beta}}{S}\right\} \tag{10.12}$$

As in the nucleation model, the approximation of a constant free energy per unit area of interface σ was necessary, a similar value of $0.1\,\mathrm{J\,m^{-2}}$ was used. Capillarity is included in the growth equation by sustituting $x_{S,eqm}^{\alpha}$ for $x^{\alpha\beta}$ in Eqn. 10.4:-

$$\alpha_3 = 2^{1/2}\left\{\frac{x^{\alpha} - x_{S,eqm}^{\alpha}}{x^{\beta\alpha} - x_{S,eqm}^{\alpha}}\right\}^{1/2} \tag{10.13}$$

The consideration of capillarity within the growth model automatically calculates the effect of coarsening. Early in the transformation all particles grow by depleting the matrix of solute (Fig. 10.5). At a later time as the reaction approaches completion the matrix solute will have fallen from its earlier level of x_0^{α} to a new level x_t^{α} crucially below the equilibrium solubility in the matrix at the interface $x_{S,eqm}^{\alpha}$ for some of the smaller particles. The value of α_1 thus becomes negative, causing a negative growth rate (Fig. 10.5). All particles for which $x_{S,eqm}^{\alpha} > x_1^{\alpha}$ therefore dissolve. In the model correct partitioning of solute to and from the matrix is ensured by a mass balance constraint.

10.2.3 The computer model

Calculations were carried out using discrete time steps δt. For each step the number of new embryos is calculated and the size of each particle updated as is the matrix composition using the mean field approximation. The average radius and volume fraction transformed are thus obtained as a function of time (Fig. 10.6). At each iteration, the model uses a second time variable τ to distinguish between groups of particles formed in previous time steps.

The adjustable parameters are as follows:-

- Homogeneous nucleation site density $^{\nu}N$ taken as $1 \times 10^{22}\,\mathrm{m^{-3}}$ - chosen to ensure realistic nucleation rates e.g. $10^{20}\,\mathrm{m^{-3}\,s^{-1}}$ [53].

- Precipitate interfacial free energy σ taken as $0.1\,\mathrm{J\,m^{-2}}$ (approximately that of a semi-coherent interface) which influences the critical nucleus size and the effect of capillarity.

- Activation energy Δg_a for solute transfer across the coherent particle interface. The value was assumed to equal to that of the activation energy for solute diffusion, Q ($240\,\mathrm{kJ\,mol^{-1}}$) [70]. This parameter controls the influence of temperature upon the nucleation rate.
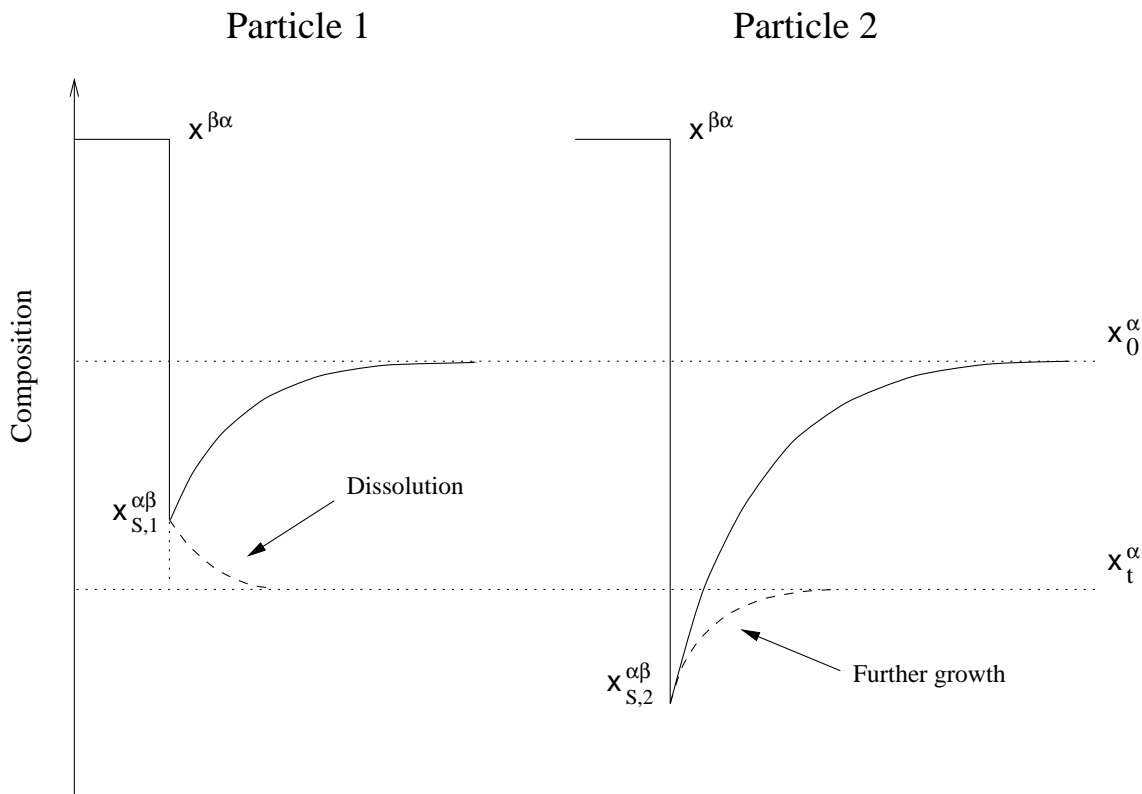
Figure 10.5: Reduction in solute concentration causes dissolution of the smaller particles (Particle 1) but continued growth of larger particles (Particle 2) due to capillarity.

Calculations of the isothermal nucleation rate are illustrated in Fig. 10.7.

During precipitation the nucleation rate $^\nu I$ exhibits a maximum as a function of undercooling below the transformation temperature T_{eqm} (Fig. 10.8). This is because as $\Delta G_c \propto 1/\Delta G_v^2$ so that $^\nu I$ increases rapidly with under–cooling. As the temperature decreases further the nucleation is reduced by the sluggish rate which atoms are transferred across the interface (the effect of Δg_a).

At 500 °C for a 2 at% Cu alloy, the initial driving force for precipitation ΔG_v is very high $\approx 20 \, \text{kJ} \, \text{mol}^{-1}$ giving ΔG_c from Eqn. 10.2 of $\approx 0.15 \, \text{kJ} \, \text{mol}^{-1}$. At this temperature this value is insignificant in comparison with $\Delta g_a \approx 240 \, \text{kJ} \, \text{mol}^{-1}$, being represented in the figure by a position to the right of the peak. Only in very dilute Cu alloys at temperatures close to the transformation temperature will a situation occur that is represented by a position to the left of the peak.

Higher temperatures also lead to more rapid growth kinetics, Fig. 10.9, which also

Entry of parameters to
describe the system

Start of main loop
t=0

Time increment

Evaluate thermodynamic quantities

Calculate number of new embryos

Calculate current growth rate
including capillarity effect
for embryos formed at time t-τ

Main time
loop from
t = 0 to end

Sub-loop running
backwards from time
τ= t to τ= 0

Evaluate the change in volume of
the embryos at time t-τ

Calculate the new composition
of the matrix by mass balance

Calculate the average radius
of all the embryos

Record the average radius and
volume fraction data or pass it
to the strengthening model

End program at a specific time
or when reaction complete

Figure 10.6: Flow diagram describing the structure of the precipitation model.
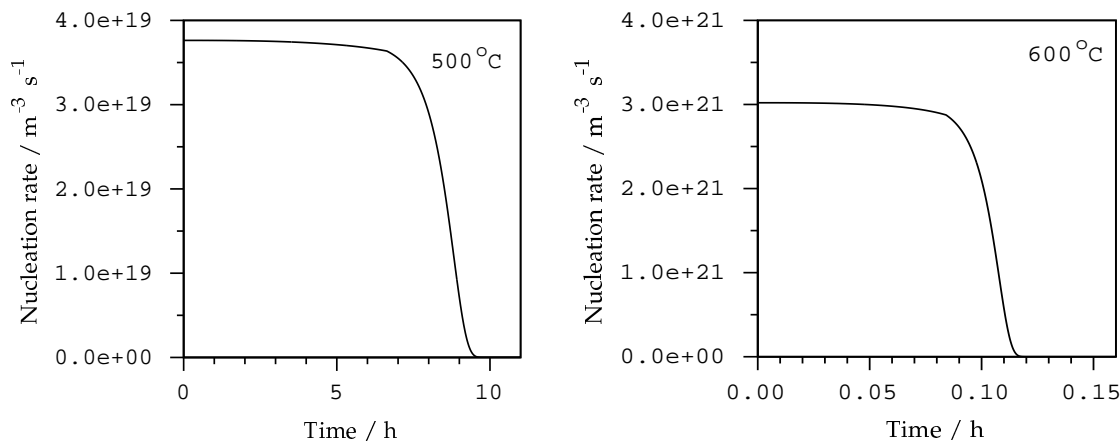
Figure 10.7: Comparison between calculated nucleation rates at 500 °C and 600 °C for a 2 at% Cu alloy.
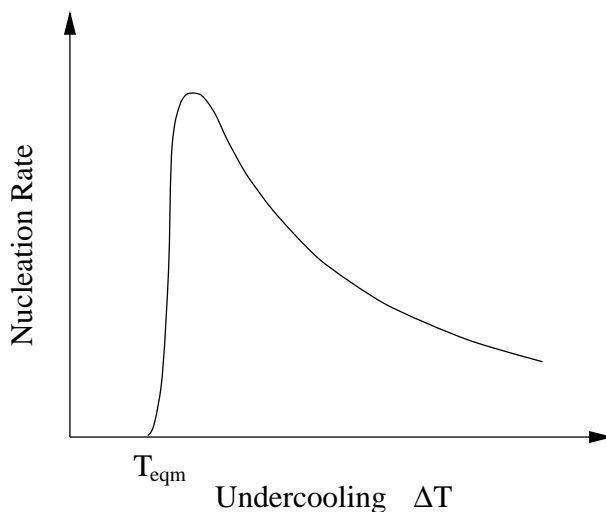
Figure 10.8: Schematic illustration of the effect of the undercooling upon the nucleation rate.

shows the greater solubility of Cu in ferrite at 600 °C.

The nucleation rate tends to zero as the reaction goes to completion. As this happens the coarsening of the precipitates begins to occur naturally, reducing the number of particles. Hence a peak in the number of embryos is to be expected at this point (Fig. 10.10).

During nucleation the average radius of the particles should increase at a rate determined by the combination of the nucleation and growth rates. As nucleation ceases a transition is observed to a rate governed solely by growth and coarsening (Fig. 10.11).
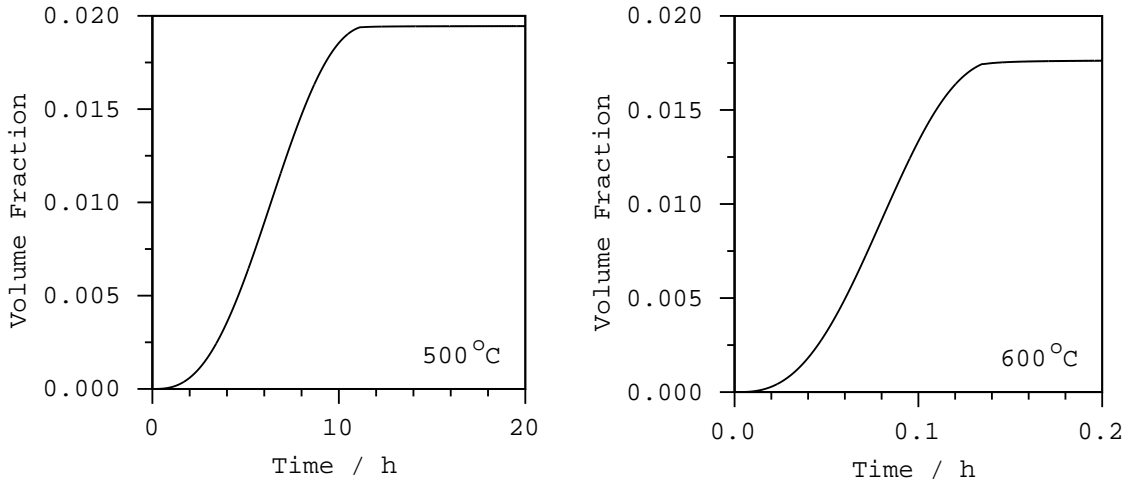
Figure 10.9: Volume fraction of precipitates as a function of time calculated at 500 °C and 600 °C for a 2 at% Cu alloy.
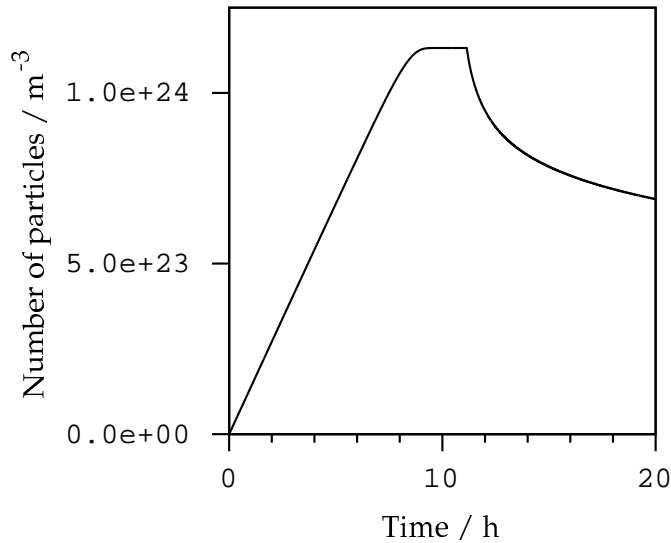
Figure 10.10: Total number of particles as a function of time at 500 °C for a 2 at% Cu alloy.

A theoretical treatment of coarsening has been produced independently by Wagner [194] and Lifshitz and Slyozov [122]. Their theory suggests the average radius, $\bar{r}$ of the particles within a system varies with time as:-

$$\bar{r} = \left(\frac{8 \sigma D x^{\alpha \beta} V_p^2}{9 RT} \right)^{1/3} t^{1/3} \tag{10.14}$$

where σ is the surface free energy of the matrix / precipitate interface, $x^{\alpha \beta}$ is the bulk sol-
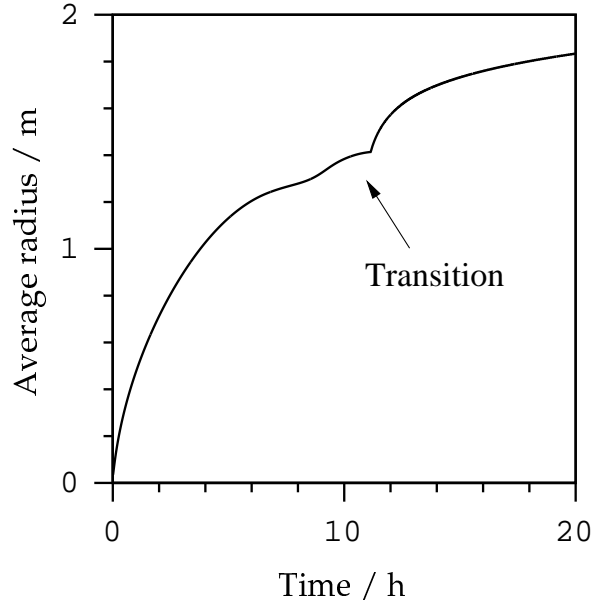
Figure 10.11: Calculated average particle radius as a function of time at 500 °C for a 2 at% Cu alloy.

ubility of solute with diffusivity D in the matrix, V_p is the molar volume of the precipitate, t is the time from the onset of coarsening and T the absolute temperature.

Defining a time t_0 with an average particle radius $\bar{r}_0$ beyond which coarsening is deemed to be dominant, the average radius of particles $\bar{r}$ at a later time t due to the above theory obeys the relationship:-

$$\bar{r}^3 - \bar{r}_0^3 \propto t - t_0 \tag{10.15}$$

Plotting $\ln(\bar{r}^3 - \bar{r}_0^3)$ versus $\ln(t - t_0)$ should give a line of unit slope. Figure 10.12 shows good agreement with Eqn. 10.15.

10.3   Comparison with experimental data

The field ion microscopy data of Goodman and Brenner [73] were chosen for comparison with the model, transmission electron microscopy data being shown to be inaccurate for such small particles [73]. Goodman and Brenner used a 1.4 at% Cu alloy quenched from 850 °C and tempered at 500 °C for periods up to 120 h. They measured the number density of particles and their average radii, using these values to calculate the volume fraction of
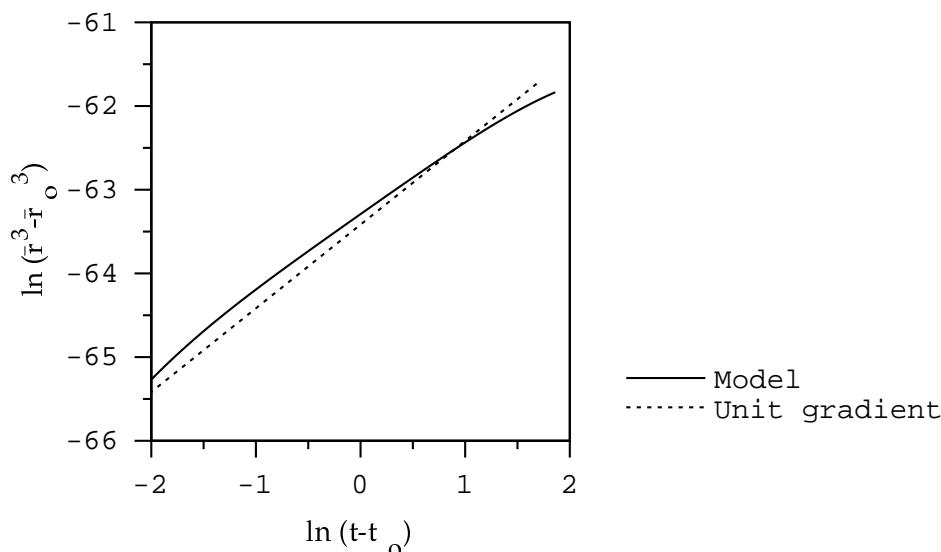
Figure 10.12: Comparison between the modelled coarsening effect and that expected using Eqn. 10.15, the prediction of theory [122, 194] is denoted by a unit gradient.

precipitate. Figure 10.13 compares their data with the calculations. Error bars were only presented for the particle diameter data.

The main differences between the predicted and measured values are that nucleation appears to be more rapid in the measured data and the coarsening similarly seems more severe. Considerable errors are to be expected in the number density data due to the assumptions used when calculating nucleation rates. A fine metastable phase was noted prior to ε–Cu formation, such a phase would have more rapid kinetics of formation and its later dissolution might cause the more rapid reduction in number density. The average particle diameter is also underestimated. As the smallest particles are difficult to image some overestimation of the average value might be expected. The model's inability to account for the metastable phase influences the particle diameter estimates.

Similar calculations were compared with the data of Youle and Ralph [201], for a 1.5 at% Cu alloy tempered at 450 °C. Figure 10.14 shows that the agreement with their data is rather poor. It is believed that there are discrepancies in the data which are not that much different from those of Goodman and Brenner [73] in spite of the different composition and heat treatment. It was found that the observed discrepancies could not be explained readily by adjusting either the interfacial energy or the activation energy Δg_a.

10.4 Conclusions

A numerical representation of the precipitation of copper in ferrite has been developed. This model captures the essential features of the precipitation process with respect to the influence of chemical composition upon transformation temperatures. It assumes homogeneous nucleation and the absence of any precursors to the formation of ε–copper. This latter simplification is probably unjustified in detail but is considered expedient given the lack of understanding associated with the early stages of transformation.

Coarsening effects have been incorporated naturally through the treatment of capillarity and this approach has shown encouraging consistency with standard coarsening theory.

Comparisons with experimental data are reasonable though it is admitted that they could be better. It is clear however that some of the data must contain inaccuracies since for example the number densities of particles are extremely difficult to evaluate accurately.
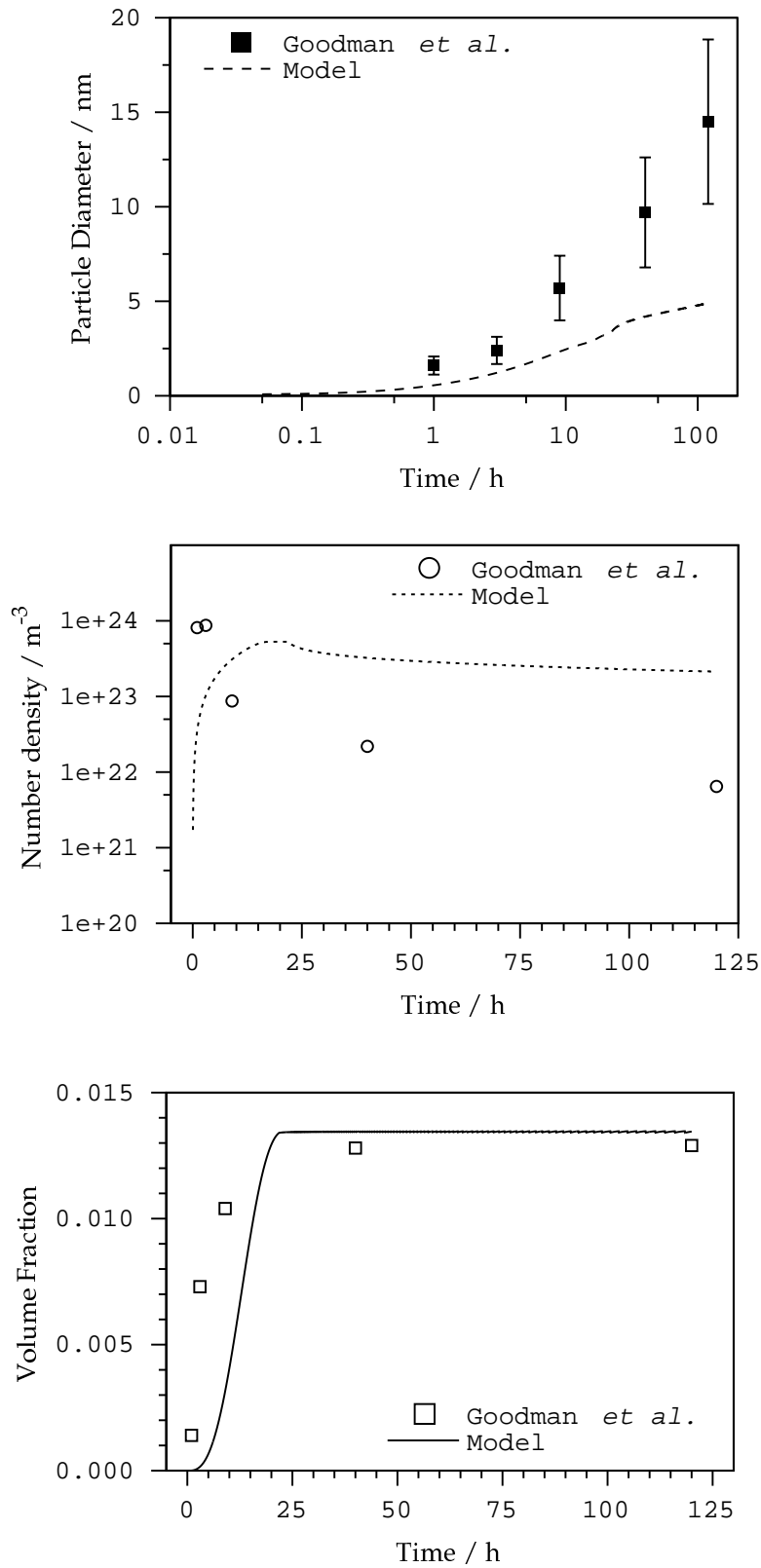
Figure 10.13: Comparison between model predictions and the data of Goodman *et al.* [73] for a 1.4 at% Cu alloy tempered at 500 °C.
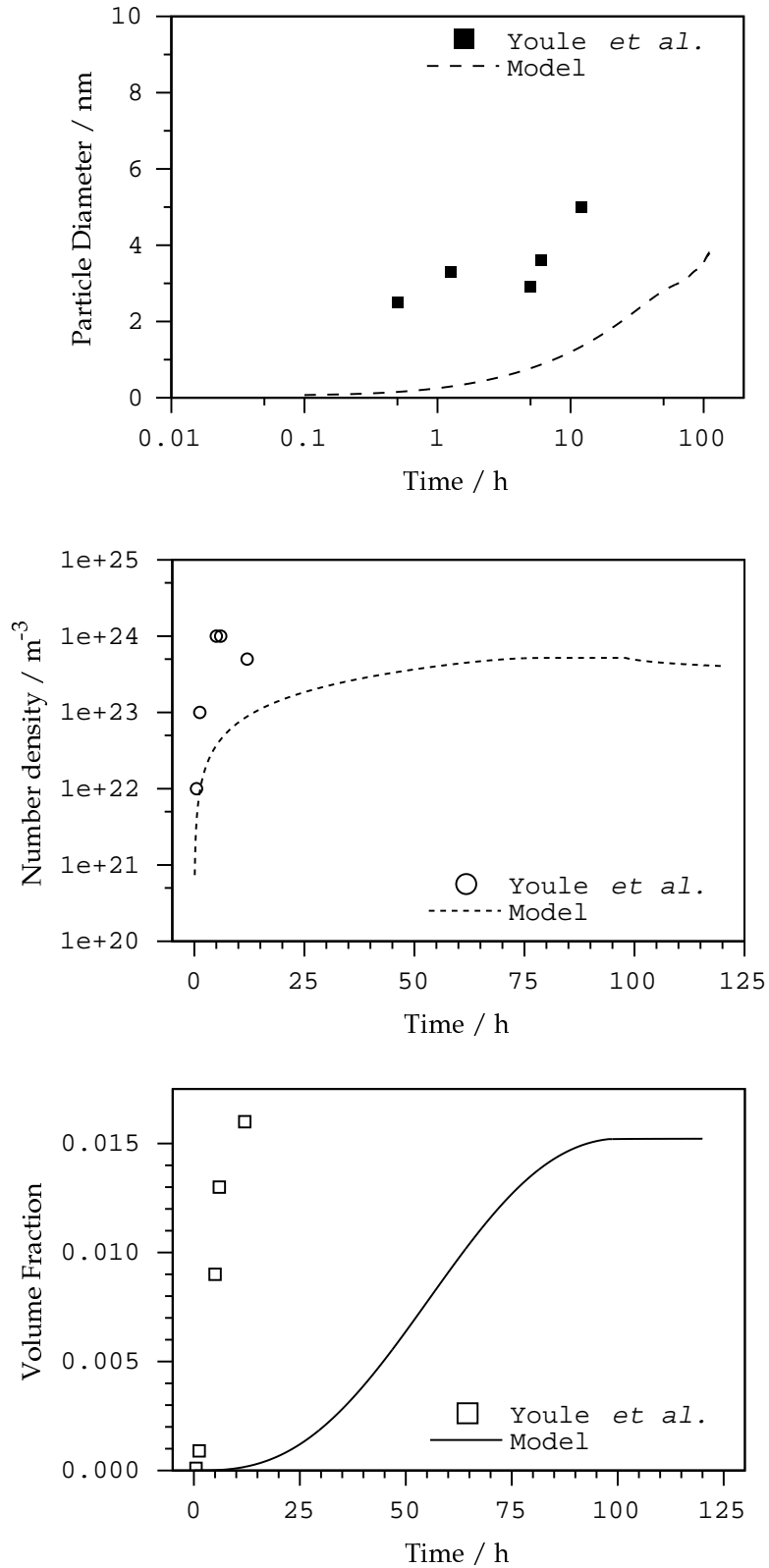
Figure 10.14: Comparison between model predictions and the data of Youle *et al.* [73] for a 1.5 at% Cu alloy tempered at 450 °C.

Chapter 11

Strengthening due to Copper Precipitates

The resistance of an obstacle to the motion of a dislocation can be measured by the extent to which the dislocation must bend before it can move on. An angle ϕ can be defined which measures the angle between the dislocation sections on either side of the obstacle, or alternatively a related angle ϕ' can be used as shown in Fig. 11.1.
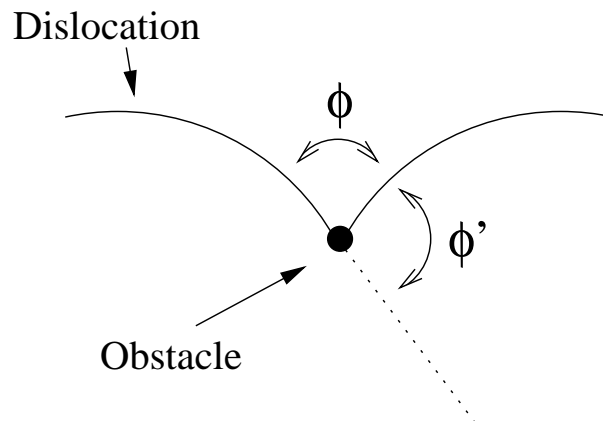
Figure 11.1: The relationship between angles ϕ and ϕ'.

Thus a straight dislocation can be described using $\phi = \pi$ or $\phi' = 0$. Hence, strong obstacles have low values of ϕ and weak ones have values approaching π. The bowing of a dislocation will statistically increase its probability of encountering another particle and theories have been developed to account for this. Firstly though it is more important to focus upon the shape of a dislocation as a function of the applied stress.

11.0.1 The 'Fixed Line Tension' model

A long straight dislocation in an infinite isotropic matrix has an elastic energy per unit length given by [65]:-

$$E(\theta) = \frac{Gb}{4\pi} \left(\frac{1 - \nu cos^2\theta}{1 - \nu} \right) \ln \left(\frac{R_0}{r_0} \right) \tag{11.1}$$

where G is the shear modulus and ν the Poisson's ratio of the matrix. θ is the angle between the dislocation line and the Burgers vector ($\theta = \pi/2$ for edge dislocations) and b is the magnitude of the Burgers vector. R_0 is an outer cutoff radius - approximately the distance to the closest parallel dislocation of opposite sign, and r_0 is an inner core radius (of the order of b) below which the elasticity theory breaks down.

A dislocation can be considered as a line defect within a matrix. If the assumption is made that the dislocation ends abruptly within an isotropic matrix then there must be a force on either end of equal magnitude to the energy per unit length, $E(\theta)$ in order to stop the dislocation collapsing. This force is the 'line tension'. If a shear stress, τ is applied on the slip plane parallel to the slip direction, then the dislocation can be approximately described as lying on arcs of radius, r given by:-

$$r = \frac{E}{\tau b} \tag{11.2}$$

This only applies if the change in the character of the dislocation as it bows is ignored. Hence E is described here as a constant rather than as a function of θ. Resolving forces, each obstacle must give rise to a force of:-

$$F = 2E\cos \left(\frac{\phi}{2} \right) \tag{11.3}$$

with,

$$E \approx \frac{Gb^2}{2} \tag{11.4}$$

and simply substituting $F = \tau bL$ where L is the distance between obstacles, the critical shear stress τ_c is fiven by:-

$$\tau_c = \frac{Gb}{L}\cos \left(\frac{\phi_c}{2} \right) \tag{11.5}$$

This indicates that a different mechanism must occur when $\phi = \pi$. In this case when the particles are extremely strong, the dislocation is in the Frank-Read configuration (the

arc becomes a semicircle). Such a configuration is unstable and leads to the combination of the two dislocation arms beyond the obstacle and the formation of a dislocation loop around the particle. The dislocation is then free to move on. The stress at which this occurs is [43]:-

$$\tau = \frac{Gb}{L} \tag{11.6}$$

here the cosine term has become unity as ϕ tended to zero.

The 'fixed line tension' model does not take into account the change in character of a dislocation as it bends around an object nor does it consider the elastic anisotropy of the α–iron lattice. More advanced models are available but these were considered too complex for the modelling purposes of this work, as they require greater knowledge of the character of dislocations interacting with particles [42, 43, 61].

11.1 Realistic particle distributions

It is unlikely that particles are regularly spaced in a real material; their sizes and shapes may also vary. Friedel [71] proposed a modification of Eqn. 11.5 due to a distribution of particles. As illustrated in Fig. 11.2, if a dislocation initially in a stable position pinned by particles O, P and Q is released from particle P to reach a new equilibrium lying in an arc along particles O, R and Q, it will sweep out an area $Z = OPQR$.
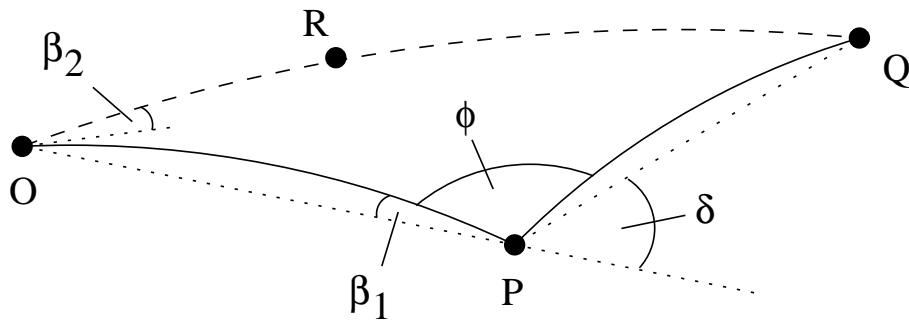
Figure 11.2: Cutting of an array of particles due to Friedel [71].

Assuming just one particle R is intersected during this process, and n_s is the number of particles per unit area then:-

$$Zn_s = 1 \qquad (11.7)$$

Assuming OP=PQ, for weak particles in which the dislocation is approximately straight and that angles β_1, $\beta_2 = 2\beta_1$ and δ are small, Z is given by:-

$$Z = 4\beta_1^3 r^2 \qquad (11.8)$$

As $2\beta_1 = \pi - \phi_c$, $n_s = 1/L^2$ and using Eqns. 11.2 and 11.4 we obtain:-

$$\tau_c \approx \frac{Gb}{L} \left(\cos\frac{\phi}{2} \right)^{3/2} \qquad (11.9)$$

In comparison to Eqn. 11.5 the cosine term now has a stronger effect. As this analytical approach is only applicable to weak particles the more generally accepted numerical method for investigating the effect of the particle distributions is given by Foreman and Makin [66] and Kocks [113]. A computer is programmed to randomly generate an array of obstacles. Drawing arcs between the obstacles and by iteratively applying Eqn. 11.2, the radii of these arcs are related to the applied shear stress. Gradually increasing the shear stress (increasing the radii of the arcs) then allows the dislocations to eventually break free from the obstacles.

The main result of numerical experiments such as these is that the stress required to cause a mass breakthrough of the array of dislocations is quite well defined and can be correlated with the yield stress of a material.

Foreman and Makin [66] in 1966 calculated the shear stress τ_c required to cause general yielding in arrays of random particles as a function of the angle ϕ from the Orowan ($\phi \approx 0$) to the Friedel ($\phi \approx \pi$) limiting cases. They proposed that a good representation of their numerical data was achieved by multiplying Eqn 11.9 by a function containing ϕ:-

$$\tau_c \approx \frac{Gb}{L} \left(\cos\frac{\phi}{2} \right)^{3/2} \left(0.80 + \frac{\phi}{5\pi} \right) \qquad (11.10)$$

This equation establishes a relationship between the critical shear stress τ_c on the slip plane and the angle ϕ.

The continuous nucleation and growth of precipitates will also give rise to a distribution in precipitate sizes. Foreman and Makin in 1967 investigated the effect of a square spectrum of particle sizes randomly arranged on the slip plane [67]. Their numerical experiments indicated that the average particle size was adequately representative of the distribution which is a convenient result for modelling purposes.

It was decided to use Equation 11.10 as a basis for a strengthening model due to its combination of generality and accuracy.

11.2 The role of particles

11.2.1 Copper as an 'attractive' particle

An 'attractive' particle is one which leads to a reduction in the energy of a dislocation on entering the particle. This might happen if the particle has a smaller elastic modulus than the matrix as in the case of ε–Cu with respect to ferrite (Table 11.1).

Material	Shear Modulus G / GPa	Poisson's Ratio
α–Fe	83	0.29
ε–Cu	49	0.35

Table 11.1: Shear moduli and Poisson's ratio values for ferrite and for copper precipitates [71].

The strengthening theories discussed above require a value for ϕ_c to be calculated for the copper particles. Russell and Brown [153] in 1972 utilised the attractive nature of the particles and the work of Siems *et al.* [159] to calculate their strengthening effect via ϕ_c. Siems *et al.* proposed that a dislocation running across an interface between media 1 and 2 will have an energy per unit length E_1 in medium 1 and E_2 in medium 2. For the dislocation to be in equilibrium, they argued that the dislocation line must make angles γ_1 and γ_2 with the normal to the interface in media 1 and 2 respectively (Fig. 11.3).

Hence the angles that the dislocation make with the interface are given by:-

$$E_1 \sin\gamma_1 = E_2 \sin\gamma_2 \tag{11.11}$$

Russell and Brown [153] used the following equations to describe the strengthening effect as a function of ϕ_c:-

$$\tau_c = 0.8 \frac{Gb}{L} \left[\cos\frac{\phi_c}{2} \right] \qquad \phi < 100° \tag{11.12}$$

$$\tau_c = \frac{Gb}{L} \left[\cos\frac{\phi_c}{2} \right]^{3/2} \qquad \phi \geq 100° \tag{11.13}$$
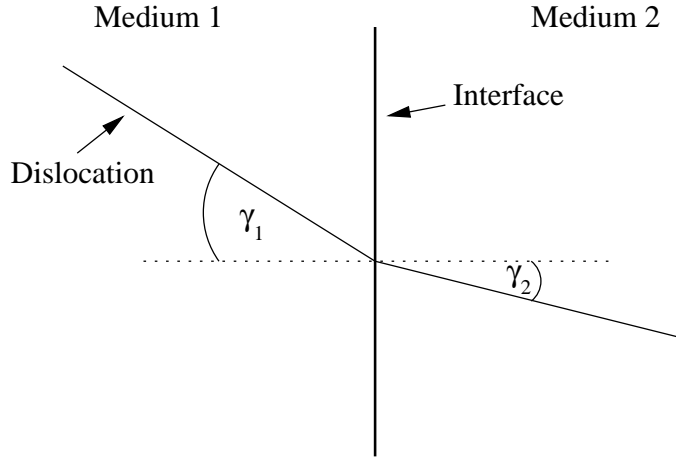
Figure 11.3: Equilibrium position of a dislocation crossing an interface [159].

They proposed that for a spherical precipitate the greatest strengthening occurs when the dislocation is about to leave the particle and therefore $\gamma_1 \approx \pi/2$ (Fig. 11.4). This assumption allows the strengthening equations to be expressed as:-

$$\tau_c = 0.8 \frac{Gb}{L} \left[1 - \frac{E_1^2}{E_2^2} \right]^{1/2} \sin^{-1} \frac{E_1}{E_2} \qquad \phi < 100° \tag{11.14}$$

$$\tau_c = \frac{Gb}{L} \left[1 - \frac{E_1^2}{E_2^2} \right]^{3/2} \sin^{-1} \frac{E_1}{E_2} \qquad \phi \geq 100° \tag{11.15}$$

Realising that the effect of the particle radius could not be ignored they produced the following relationship for the ratio of E_1 and E_2:-

$$\frac{E_1}{E_2} = \frac{E_1^\infty \log \frac{r}{r_0}}{E_2^\infty \log \frac{R}{r_0}} + \frac{\log \frac{R}{r}}{\log \frac{R}{r_0}} \tag{11.16}$$

where the subscript 1 denotes the matrix and 2 the precipitate, and the superscript ∞ denotes values for a dislocation in an infinite medium. This function causes the value of E_1 to approach that of the matrix E_2 for small particles and vice versa for particles with infinite radius. It is based upon the logarithmic nature of the function used in the free line tension model (Eqn. 11.1). Using this model, good correlation was observed with experimental data, the strengthening due to the precipitates $\Delta\sigma$ varying with the square root of the volume fraction of precipitates, f (Fig. 11.5).

In this work a somewhat similar method was used in the computer model for evaluating ϕ_c. However, here the precipitates are first approximated as cubes. The trace of
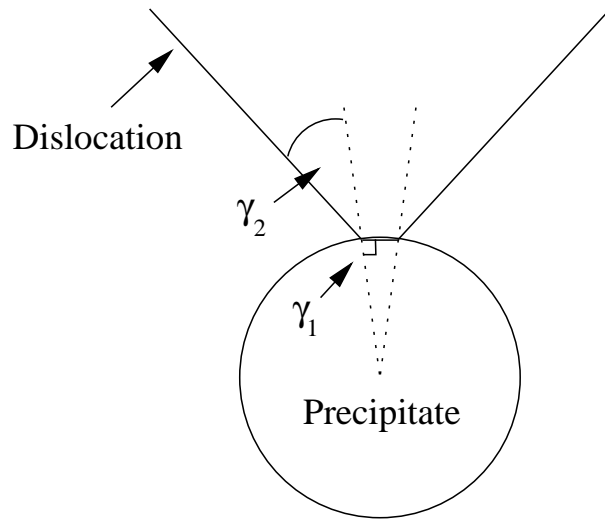
Figure 11.4: Position of maximum strengthening due to the assumptions of Russell and Brown [153].
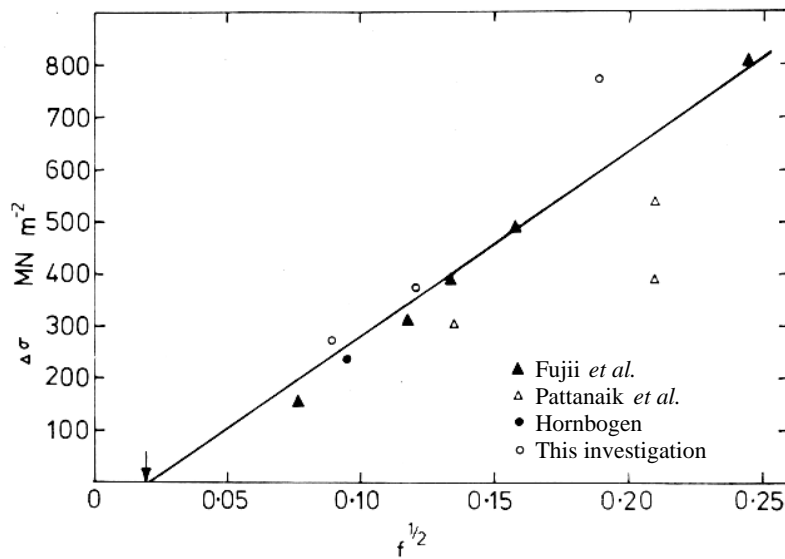
Figure 11.5: Correlation between Rusell and Brown's model with experimental data [153].

a sphere (precipitate) upon a slip plane is a circle, the average radius of which can be calculated due to the dependence on the position of intersection. This can then be related to the side length of a cube. A similar assumption is made to that used by Russell and Brown [153] in that $\gamma_1 = \pi/2$ (Fig. 11.6). Eqn. 11.1 is used to calculate the energy of the dislocation assuming it adopts a symmetrical position centrally within the precipitate.

The dislocation's energy is calculated by adding the energy due to a dislocation in copper, out to the cube edge, to that of a similar dislocation in ferritic iron out to a distance related to the precipitate spacing:-

$$
\begin{aligned}
E(\theta) \quad = \quad & \frac{G_p b_p}{4\pi} \left(\frac{1 - \nu_p cos^2\theta}{1 - \nu_p} \right) \ln \left(\frac{l}{r_0} \right) \\
& + \frac{G_m b_m}{4\pi} \left(\frac{1 - \nu_m cos^2\theta}{1 - \nu_m} \right) \ln \left(\frac{R_0}{l} \right) \quad (11.17)
\end{aligned}
$$

where p and m subscripts refer to the precipitate (ε–copper) and matrix (ferrite) values respectively (Table 11.1) and l is equal to half the side length of the cubic precipitate on the slip plane.

This approach has greater physical meaning than that used by Russell and Brown [153]. When the precipitate size reduces to that of a dislocation core r_0, a radius of the order of the Burgers vector, the dislocation is no longer affected by the precipitate. It can also be seen that smaller particles are weaker and should result in larger values of ϕ_c due to Eqns. 11.11 and 11.17.
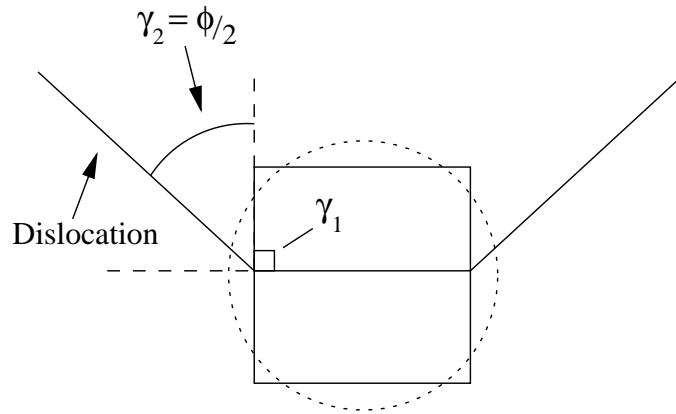
Figure 11.6: Calculation of ϕ using a cubic precipitate approximation.

11.2.2   Comparison with experimental data

Using the above method the calculated strengthening effect of a precipitate distribution was compared with the data of Pattanaik *et al.* [145] who used 1.6 at% Cu and 4.4 at% Cu

alloys tempered in the range 500–750 °C. Figure 11.7 shows that similar good agreement was found as was obtained by Russell and Brown [153].
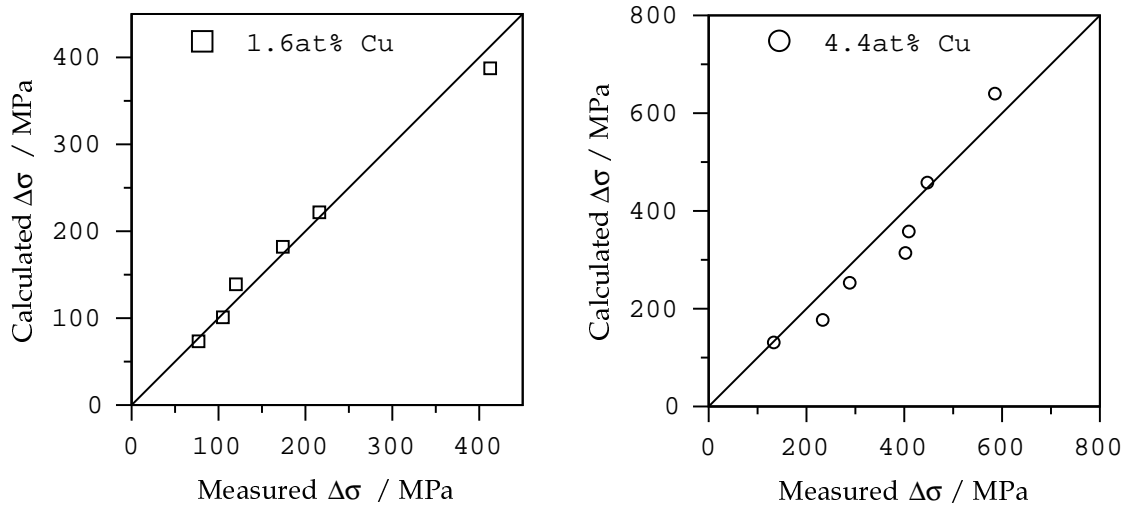
Figure 11.7: Comparison between calculated and measured Cu strengthening effects in a 1.6 at% Cu and 4.4 at% Cu Fe–Cu alloy [145].

11.2.3   Other strengthening effects

To further increase the accuracy of the model the solid solution strengthening effect of copper in ferrite was also included allowing approximate conversion to yield strength values. It is important to consider solid solution strengthening as the above model is incapable of allowing for the strengthening effect of particles of radius less than r_0. Experimental data due to Fujii *et al.* [72] were used to derive a linear relation between the strengthening effect of dissolved copper in ferrite $\sigma_{ss,Cu}$, and the copper content in solid solution for Fe-Cu alloys containing up to 6 at% Cu:-

$$\sigma_{ss,Cu} = 60.9 \times \text{at\% Cu} \qquad (\text{MPa}) \qquad (11.18)$$

The calculated solid solution effect is therefore significant particularly when compared to the yield strength of pure iron taken as 99 MPa from the same data. However, some inaccuracy is to be expected in these values due to the difficulty of removing the effect of the microstructure.

11.3 Combined precipitation and strengthening models

The data from the precipitation model, including the instantaneous matrix composition and a description of the number density and size of particles, were used to estimate the overall strength as a function of composition, temperature and time.

Figure 11.8 demonstrates the predicted effect of the Cu content on the yield strength of an Fe–Cu alloy tempered at 500 °C. Naturally the strength is higher at larger concentrations with the peak in strength occurring at shorter tempering times. The predicted behaviour is typical of precipitation strengthened alloys.
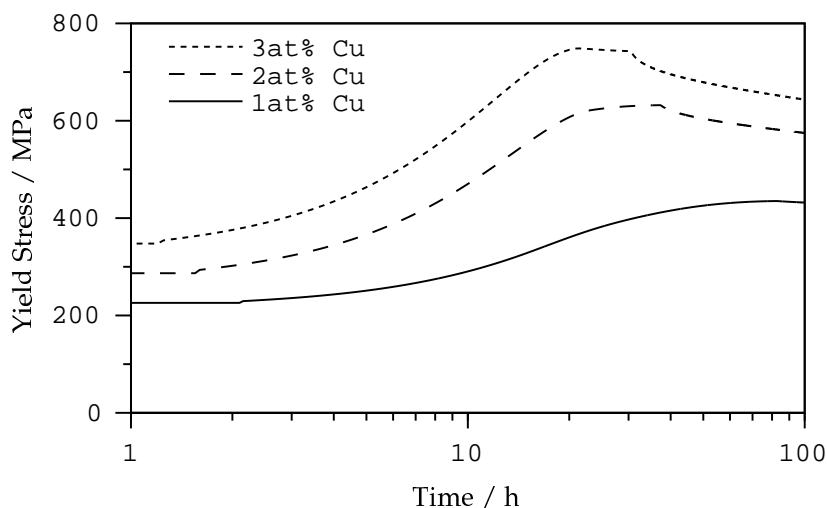
Figure 11.8: Predicted influence of Cu content upon the yield strength of an Fe–Cu alloy tempered at 500 °C.

The large effect of the tempering temperature is revealed in Figure 11.9. A increase in peak strength is predicted as the temperature is reduced.

Figure 11.10 shows the relative strengthening contributions of the precipitates and the ferrite lattice containing copper in solution for a 2 at% Cu alloy aged at 600 °C. Precipitation produces a reduction in the strengthening contribution from the ferrite, the peak in precipitation strengthening occurring where the lattice is no longer supersaturated.

11.4 Comparison with experimental data

Goodman *et al.* [73] measured yield strength values for their 1.4 at% alloy tempered at 500 °C. Comparing these data with the predictions of the model indicates that the peak
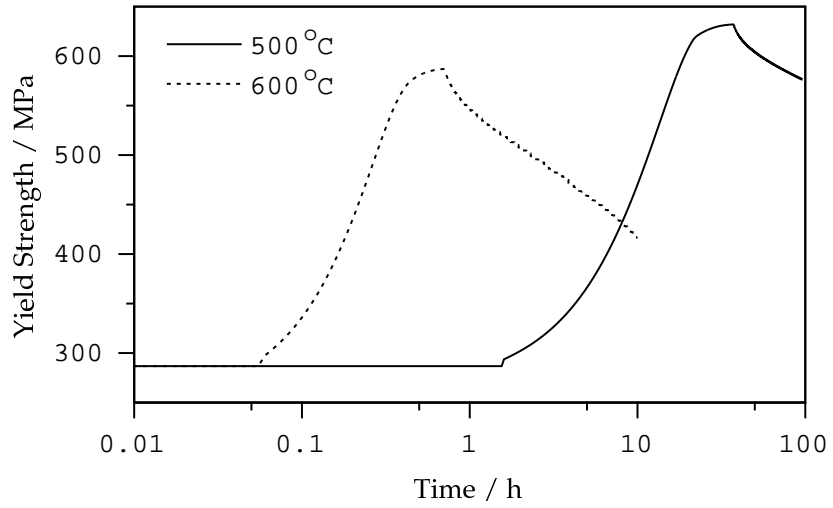
Figure 11.9: Predicted influence of temperature on a 2 at% Cu alloy tempered at 500 °C and 600 °C.
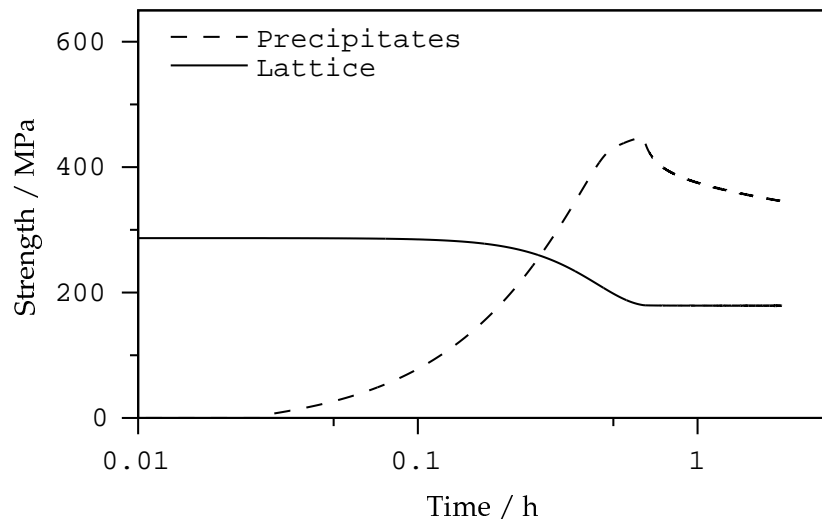
Figure 11.10: Typical strengthening contributions of the precipitates and the lattice containing dissolved Cu for a 2 at% Cu alloy aged at 600 °C.

strength is overestimated but more importantly that the time at which this occurs is approximately an order of magnitude later than in reality (Fig. 11.11).
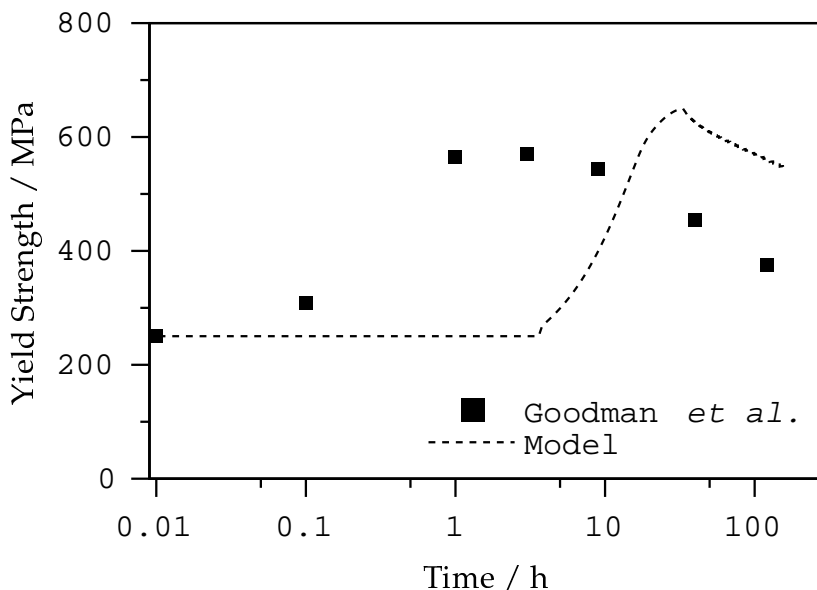
Figure 11.11: Comparison between yield strength calculations and measurements for a 1.4 at% Cu alloy tempered at 500 °C [73].

Experimental data due to Hornbogen [94] were used to further investigate this trend (Fig. 11.12). The calculations performed for a 0.9 at% alloy tempered at 500 °C again indicate an overestimation of strength and a separation of the measured and predicted peaks by approximately an order of magnitude in time.

The effect of the composition variations is captured correctly as can be seen in Figure 11.13 using data from Fujii *et al.* [72]. Again peak strengths are overpredicted and a similar order of magnitude difference in kinetics is observed. The figure contains data from a 6 at% alloy which is larger than the maximum copper content allowed in the model. A prediction using a 5 at% Cu alloy was used as an approximate substitute.

Interestingly, a decrease in temperature by 100 °C does not seem to significantly alter the accuracy of the calculations (Fig. 11.14). The kinetics of the reaction are considerably slower as would be expected but the peak in strength remains at a time approximately an order of magnitude later.

Further data due to Fujii *et al.* [72] provide evidence that a similar effect is observable at 600 °C although data for very short tempering timescales were not provided so the position of the peak is unclear (Fig. 11.15). The figure compares calculations and measurements on two alloys tempered at 600 °C.
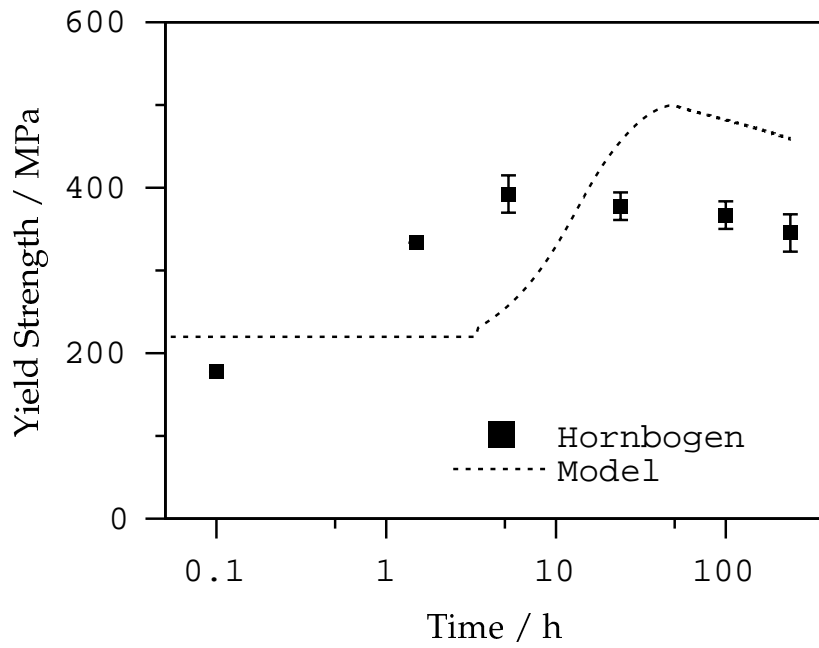
Figure 11.12: Comparison between yield strength calculations and measurements for a 0.9 at% Cu alloy tempered at 500 °C [94].
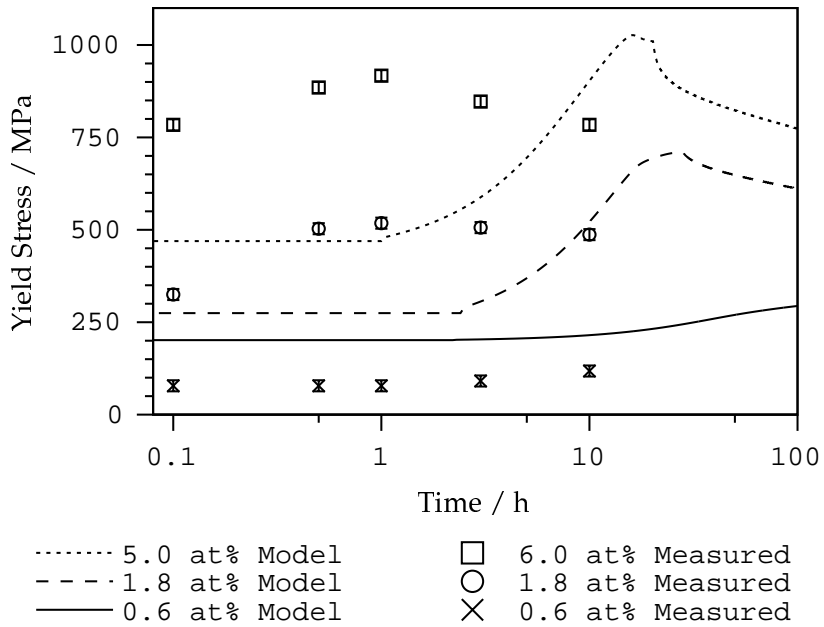
Figure 11.13: Comparison between yield strength calculations and measurements for 3 alloys tempered at 500 °C [72].
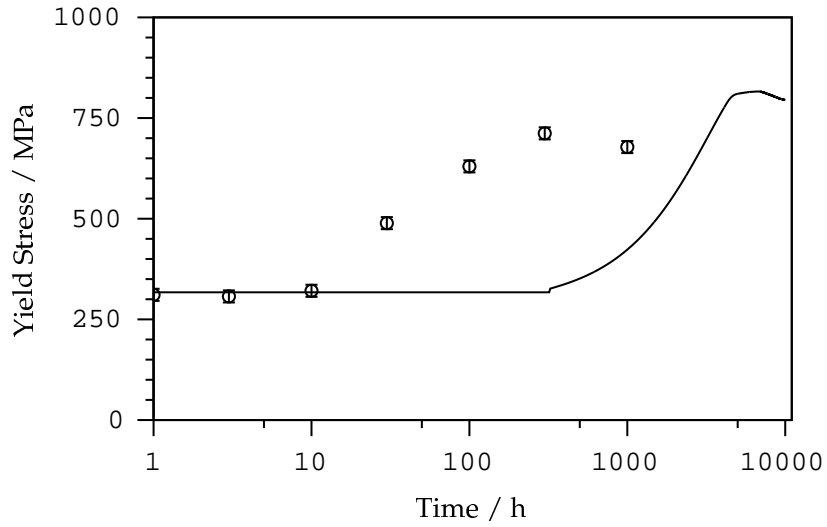
Figure 11.14: Comparison between yield strength calculations and measurements for a 2.5 at% Cu alloy tempered at 400 °C [72].
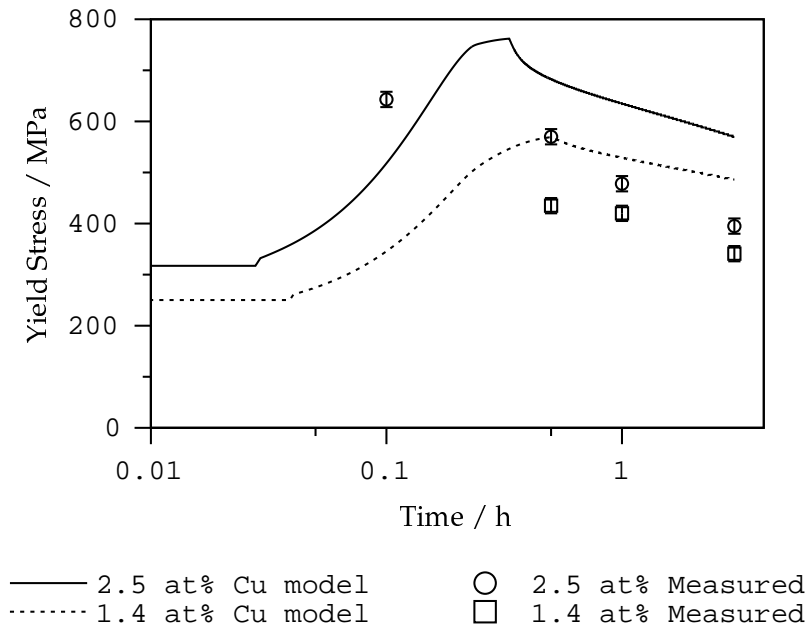
Figure 11.15: Comparison between yield strength calculations and measurements for 2 alloys tempered at 600 °C [72].

11.5   Summary

A numerical model has been produced to calculate the strengthening effect of copper precipitates in ferrite. A strength prediction is produced using the average radii and volume fraction of the precipitates. Adapting Russell and Brown's [153] methods based upon dislocation theory, the model was verified to produce similar good agreement with experiment. Data from the precipitate model were used in combination with this model to produce an estimate of the yield strength of Fe–Cu alloys. The calculations were found to behave according to metallurgical theory in terms of trends due to the effect of temperature and composition. However, significant discrepancies were found in comparison with experimental data probably due to shortcomings in the estimation of precipitation kinetics. The calculated peak strengths were achieved much later than found experimentally. The peak strength slightly overestimated measured values but this is consistent with the underestimation of reaction rates. It is probable that the discrepancies can be attributed to the formation of a transient body centred cubic phase of copper.

Chapter 12

Conclusions and Suggestions for Further Work

This work was undertaken in order to increase understanding of the microstructure and mechanical properties of ultra–high strength weld alloys. An initial series of welds based on a commercial composition was produced and their mechanical properties related to modifications in weld chemistry using a variety of experimental and modelling techniques.

One of the most interesting results of this study is the strong effect of the interpass temperature in these alloys. Using neural network modelling and dilatometry, previously unexplained strength variations were found to be caused by the intersection of the weld cooling rate with the CCT curve in a region of high gradient. More reliable and superior properties may now be obtained simply by careful control of this parameter.

Prediction of the tensile properties of these welds with a physical model identified large discrepancies between predicted and measured data. Long duration tempering experiments effected the removal of the microstructure, allowing measurement of the intrinsic lattice strength of the ferrite via hardness tests. The cause of the problems was identified as lying in the calculation of strengthening due to the grain size. Modifications were made to the model and new predictions showed great improvement. Gathering evidence concerning the microstructures and properties led to the production of new welds, the properties of which showed some promising although as yet not conclusive improvements.

Experiments showed that the high strength and toughness properties of the commercial electrode H1 were difficult to improve. Tungsten was found to have a strong solid solution strengthening effect but toughness was adversely effected. Increasing the nickel content in H1 at the expense of manganese indicated that an improvement in strength was possible. Future work on this alloy should consider the use of greater nickel levels but equally

requires strict control of the interpass temperature. Some other interesting experiments could be performed by increasing the hardenability of weld H1 although perhaps without significant increases in carbon levels to avoid toughness problems. The CCT curve of such alloys should be carefully measured in the context of natural weld cooling rates.

A rival weld to conventional compositions, containing higher levels of carbon and silicon was also studied in an attempt to produce increased strength using a bainitic ferrite–retained austenite microstructure. Despite good strength, toughness levels were less encouraging. Electron microscopy studies did show that the intended microstructure had been produced particularly in that carbide precipitation was prevented although some martensitic regions were also observed. The resistance of the austenite films to tempering was quantified using tempering experiments and microscopy, the precipitated carbide being identified as cementite in all cases.

The austenite films containing high levels of carbon may transform to martensite under the influence of stress and this may contribute to lower toughness levels. Further interesting work could be directed at attempting to confirm this hypothesis. Some modifications to the weld composition were also attempted. It was shown that the use of a lower silicon content was not detrimental to the mechanical properties. Further investigations were also performed into the effects of increasing the extent of the bainite reaction with cobalt whilst reducing the hardenability. These welds show some promise but a number of related compositions need to be investigated to estimate their true potential. In particular carbon, silicon and hardenability levels need to be optimized as it would appear that some toughness problems may result from high hardenability. As this is a new concept in high strength welds it is to be expected that further experimentation will be required.

Modifications to data used in conjunction with thermodynamic modelling software allowed calculation for the first time of the effect of silicon additions on the paraequilibrium Fe-Si-C phase diagram. Silicon was found to greatly increase the extent of the single phase (austenite) field under paraequilibrium conditions thus retarding or preventing the precipitation of cementite by this mechanism. Comparison with experimental data showed that the number of paraequilibrium carbides and their tempering resistance in an alloy can be explained in terms of the distance from the calculated paraequilibrium single phase boundary. Hence an upper bound in preventing paraequilibrium precipitation can now be evaluated in terms of temperature or composition. This represents a significant advance and there is now much scope for further testing of this modelling method. Although the high levels of alloying additions in the new bainitic welds may cause inaccuracies, it would certainly be interesting to correlate silicon levels, tempering treatments and observations of the carbides in the light of the thermodynamic predictions.

A more ambitious attempt at increasing strength was investigated using additions of copper. Through precipitation hardening, it was found that copper could indeed greatly improve the strength with a resultant reduction in toughness. Following a review of the relevant literature, a model was produced in a first attempt at predicting the strengthening behaviour of Fe–Cu alloys as a function of aging time. The observed peak in strength followed by a drop due to coarsening was reproduced consistently by this model. Comparison with published data agreed well but highlighted areas in which more work is required. Specifically, it was concluded that further work on the copper rich metastable phase is required. The transient nature of this phase and its small size may prove a challenging obstacle to improving the model's accuracy. Some further development is necessary before the effect of the rapid cooling cycles due to welding can be predicted. It is difficult to model the precipitation of Cu accurately in steels as the overall strengthening effect is produced by a combination of factors. Copper precipitation in welds adds complication due to the cooling rate but with sufficient data for comparison, the model may be capable of such predictions. Production of a weld series to investigate the effect of copper precipitation upon high strength welds would provide an valuable comparison with Fe–Cu alloys. The issue of copper additions is interesting in that such precipitates are clearly very effective at strengthening. As toughness levels in alloy H1 are high some copper could be added in a trade–off between toughness and strength.

On a final note, it is possible that a future hybrid weld could be produced which combines the best features of all the experimental welds detailed in this work. Following optimisation of compositions and strict control of parameters such as the interpass temperature, it might be hoped that such a weld could exhibit a yield strength well in excess of 1000 MPa. If this were accompanied by a UTS of perhaps 100 MPa higher and good toughness levels inherited from H1, a hybrid of this type would constitute a considerable development.

Appendix A

FORTRAN code for Cu strengthening model

The copper precipitate stengthening model described in this thesis was written in FOR-TRAN 77 under the UNIX (Solaris 2.5) operating system. The code should be portable to other platforms. Additional information is provided as comments within the code.

```
C===============================================================
C
C      MODEL TO CALCULATE THE PRECIPITATION STRENGTHENING
C      EFFECT OF COPPER PRECIPITATES IN IRON
C
C      Mike Lord. August 1998
C
C===============================================================
C
C Alteration of the following parameters will affect the
C predictions of the model. Subroutines in which they are
C found are given in parentheses.
C
C 1) Temperature TMP (K) (Main Program)
C 2) Cu content of material XFE (at. fr.) (Main Program)
C 3) Period of transformation TIMEND (s) (TRANSFN)
C 4) Iteration time step DT (s) (TRANSFN)
C    Note TIMEND/DT must be less than 10000
C 5) Extent of transformation before coarsening occurs
C    is altered using the line below (TRANSFN)
C    Note: this particular case is for 80% transformation.
C       IF ((XINF-XCU)/(XSS-XCU) .LT. 0.2D0) THEN
C 6) Nucleation site density SITE (m^-3) (NUCLN)
C 7) Force of fitting W( ) (THERMODYN) - weighting parameters
C    for the delta G curve.


C XSS - original copper concentration
```

```
C XFE - the same as XSS
C XCU - solubility of Cu in Ferrite
C XINF - variable which drops from XSS to XCU as pptn occurs


      IMPLICIT DOUBLE PRECISION (A-H,L-Z)
      IMPLICIT INTEGER (I-K)
C      EXTERNAL hand
C      ieeer=ieee_handler('set','common',hand)

      AVRAD=0.0D0
      XPPT=0.0D0

C Enter temperature and Cu composition below.

      TMP=673.0D0
      XFE=0.025D0

      OPEN(15,FILE='output1')
      OPEN(16,FILE='output2')

      CALL TRANSFN(TMP,XFE,XPPT,AVRAD)

      END



C-------------------------------------------------------------

      SUBROUTINE TRANSFN(TMP,XFE,XPPT,AVRAD)
      IMPLICIT DOUBLE PRECISION (A-H,L-Z)
      IMPLICIT INTEGER (I-K)

      DIMENSION PPTE(10000),PPVOL(10000),N(10000)
     &,GRWTH(10000),PPTRAD(10000)


C  Start, finish times and the iteration time step are entered here.
C  Note that there should be no more than 10000 iterations.

      DT=18000.0D0
      TIMEND=36000000.0D0
      TIMEST=DT

        TIMCHK=(TIMEND-TIMEST)/DT
        IF (TIMCHK .GT. 10000) THEN
         WRITE(6,*)'TIME STEP TOO SMALL'
        ENDIF


C====================================================================
C          MAIN PROGRAM LOOP FOR TRANSFORMATION CALCULATION
C====================================================================

C  Start of main time loop running between times TIMEST and TIMEND
```

```
C  the values of both are in seconds.

       ITIM=0
       XSS=XFE
       XINF=XFE
       X0=1.0D0
       ICFLAG=0
       IFIL=0
       SURF=0.15D0
       BOLZ=1.381D-23
       RMIN=0


       DO 799 TIME = TIMEST,TIMEND,DT


       ITIM=ITIM+1

       IT=0

C A new set of thermodynamic parameters is required at each iteration.


       CALL THERMODYN(TMP,XINF,XCU,DELGV)

C       WRITE(10,*) ITIM,EXTTRN




C Nested Loop to sum the amount of volume added to
C the transformation in time period DT. The increase in volume
C in each set of precipitates formed in subsequent DTs from start
C is monitored. Volumes of these pptes in total are stored in
C PPTE(I) - I counts up - oldest pptes are dealt with first.


       DO 699 T = TIME,TIMEST,-DT

IT=IT+1

C         WRITE(6,*) TMP,ITIM,DELGV

C  Nucleation rate is calculated in NUCLN subroutine



C  Coefficient 4.188790205D0 is 4/3*PI
C       WRITE(6,*)PPTE

       IF (T .EQ. TIMEST) THEN

       CALL NUCLN(N,TMP,ITIM,DELGV,BOLZ,SURF,EXTTRN,DT,RSTAR
      &,RMIN)
```

```
        PPTE(IT)=4.18879D0*(RSTAR**3)*N(IT)
        ENDIF


C       WRITE(6,*) PPTE(IT), PPTRAD(IT)

        CALL GROWTH(GRWTH,T,EXTTRN,XFE,XSS,XCU,XINF,TMP,IT
     &,TIME,TIMEST,TIMEND,AVRAD,PPTRAD,ITIM,N,DIFF,ICFLAG,
     &SURF,BOLZ,RMIN)



PPTE(IT)=PPTE(IT)+(2.0D0*12.56637D0*(PPTRAD(IT)**2)*N(IT)
     &*GRWTH(IT)*DT)

        TEMP11=0.23873D0*PPTE(IT)/N(IT)
        TEMP12=(TEMP11**(1.0D0/3.0D0))

        IF (PPTE(IT) .LE. 0.0D0) THEN
PPTE(IT)=0.0D0
        N(IT)=0.0D0
        ENDIF

        IF (TEMP12 .LE. RMIN) THEN
          PPTE(IT)=0.0D0
          N(IT)=0.0D0
        ENDIF

        CALL PPTVOLS(PPVOL,ITIM,PPTE,N,NTOT)
        EXTTRN=PPVOL(ITIM)
        XINF=(XSS-(EXTTRN*X0))/(1.0D0-EXTTRN)

699     CONTINUE
        TEMP30=N(ITIM)/DT
        TEMP31=TIME/3600D0
WRITE(16,*) TEMP31,TEMP30



C Nuclei distribution - Array PPTE (contains nuclei volume
C data) is printed out to screen and file.

C       WRITE(6,*)'Distribution of nuclei:-'
C       DO 101 COUNT=1,TIMEND,1
C       WRITE(6,798)PPTE(COUNT),COUNT,DT,TIME
C       WRITE(10,798)PPTE(COUNT),COUNT,DT,TIME

C101    CONTINUE

C  Increase in real volume is calculated
C  and placed in EXTARR array - can then monitor development.
C  Total volume of system is assumed unity - i.e. 1 cubic metre.
```

```
      CALL PPTRADCALC(N,PPTE,ITIM,PPTRAD)


      CALL AVERAD(PPTRAD,ITIM,N,AVRAD)


C        WRITE(11,*) TIME, AVRAD, EXTTRN



C      TEMP13=XINF+PPVOL(ITIM)
      TEMP14=TIME/3600.0D0
      WRITE(15,*) TEMP14,PPVOL(ITIM), NTOT,AVRAD
C797   FORMAT(4D12.5)
      XPPT=XSS-XINF
          CALL STRENGTHCALC(XPPT,XINF,XFE,AVRAD,TIME)


799   CONTINUE


803   CONTINUE



      WRITE(6,800) AVRAD
      WRITE(6,801) XPPT
      WRITE(6,802) XSS


800   FORMAT('Average PPT radius :   ',D11.4)
801   FORMAT('Containing atomic fraction Cu :',D11.4)
802   FORMAT('Original atomic fraction Cu :',D11.4)

      RETURN
      END

C==================================================================

      SUBROUTINE NUCLN(N,TMP,ITIM,DELGV,BOLZ,SURF,EXTTRN,DT,
     &RSTAR,RMIN)
      IMPLICIT DOUBLE PRECISION (A-H,L-Z)
      IMPLICIT INTEGER (I-K)
      DIMENSION N(10000)

C In this subroutine we need to make sure that the DELGV
C calculated by MTDATA is the one we are supposed to use
C in the equation below.
C Firstly convert DELGV into units of J per atom
      DELGV1=DELGV/6.022D23
C      WRITE(6,*) DELGV1
```

```
C Using eqns 46.2 and 46.20, 49.4 in Christian Nucleation Chapter
C Atomic volume Vl - unit cell ferrite volume divided by 2.
C ETA from page 420. eta = (36*pi)^.333333*(Vl^.66666)
C RSTAR=(2*sigma*vl)/DELGV1


      ETA=2.502360251D-19
C      WRITE(6,*)'ETA ... :- ',ETA,DELGV1
      SITE=1D22
C      SITE=2.561D7
C      SITE=8.897D5D
      BOLZ=1.381D-23
      PLANC=6.626D-34

      DELGCP=(4.0D0*(SURF**3.0D0)*(ETA**3.0D0))/(27.0D0*(DELGV1**2.0D0))

C DELSTR = interface transfer activation cost 240000Jmol / avagadro
C value from self diffusion in alpha iron.

C      WRITE(6,*) "DELGCP : ", DELGCP

      DELSTR=3.98519D-19
C      DELSTR=3.98519D-21

      COEF1=SITE*BOLZ*TMP/PLANC
C      COEF2=(DELGCP)/(BOLZ*TMP)
      COEF2=(DELGCP+DELSTR)/(BOLZ*TMP)

C The code below should stop the floating point error
C which occurs when the nucleation rate becomes too small.
C It calculates whether the coefficient inside the DEXP
C term will cause the total new nuclei volume to be less
C than the size of critical nucleus. If so the nucleus
C volume is set to zero.


      TEMP10=(RMIN**3)*4.18879D0
      COECH1=(TEMP10/COEF1)
      COECH2=-1.0D0*DLOG(COECH1)

      IF (COEF2 .GT. COECH2) THEN
        N(ITIM)=0.0D0
      ELSE

      N(ITIM)=COEF1*DEXP(-COEF2)*(1.0D0-EXTTRN)*DT
C      WRITE(6,*)"N(ITIM) : ", N(ITIM)

      RSTAR=(2.0D0*SURF*1.17706D-29)/DELGV1
      IF (RMIN .GT. RSTAR) THEN
        N(ITIM)=0
      ENDIF
      IF (N(ITIM) .LT. 1.0D0) THEN
        N(ITIM)=0.0D0
      ENDIF
```

```
C        WRITE(6,*) RSTAR
         ENDIF


C        TEMP20=DELSTR/(BOLZ*TMP)
C TEMP21=DEXP(-TEMP20)
C        TEMP22=DELGCP/(BOLZ*TMP)
C TEMP23=DEXP(-TEMP22)
C        WRITE(6,*)DELGCP,DELSTR
C WRITE(6,*) "NkT/h : ", COEF1
C        WRITE(6,*) "Total exponent term : ", COEF2
C        WRITE(6,*) "exp(-DELG/kT) : " , TEMP23
C WRITE(6,*) "exp(-delG/kT) : ",TEMP21
C        WRITE(6,*) "Total nucln rate : ", N(ITIM)


         RETURN
         END


C-----------------------------------------------------------

         SUBROUTINE GROWTH(GRWTH,T,EXTTRN,XFE,XSS,XCU,XINF,TMP,IT
     &,TIME,TIMEST,TIMEND,AVRAD,PPTRAD,ITIM,N,DIFF,ICFLAG,
     &SURF,BOLZ,RMIN)
         IMPLICIT DOUBLE PRECISION (A-H,L-Z)
         IMPLICIT INTEGER (I-K)
         DIMENSION GRWTH(10000),N(10000),PPTRAD(10000)
C  XSS is the original copper composition of the material (at.fr.)

C  X0 is the composition of the Cu rich phase (at.fr.=1)
         X0=1.0D0

C        DIFF=2.0D-13
         CALL DIFFUSN(TMP,DIFF)
C        DIFF=2.0D-16



         IF (EXTTRN .GT. XSS) THEN
           WRITE(6,*)'****************************'
           WRITE(6,*)' SUSPECTED ITERATION ERROR'
           WRITE(6,*)' REDUCE TIME STEP DT'
           WRITE(6,*)' TERMINATING EXECUTION'
           WRITE(6,*)'****************************'
STOP
         ENDIF


         IF (PPTRAD(IT) .GT. 0.0D0) THEN
           TEMP5=(2.0D0*SURF*1.177D-29/BOLZ/TMP/PPTRAD(IT))
           TEMP7=DEXP(TEMP5)
C WRITE(6,*)TEMP5,TEMP7
           XR=XCU*DEXP(TEMP5)
C          WRITE(6,*) XR, TEMP5
C          XR=XCU*(1.0D0+TEMP5)
           TEMP8=XINF/XCU
TEMP9=DLOG(TEMP8)
```

```
RMIN=2.0D0*SURF*1.177D-29/BOLZ/TMP/TEMP9
          A1=XINF-XR
          A2=X0-XR
          IF (X0 .LT. XR) THEN
WRITE(6,*) X0, XCU, XR, TEMP5, PPTRAD(IT)
WRITE(6,*)"X0 .LT. XR"
STOP
          ENDIF


        A3=A1/A2

        IF (XINF .LE. XR) THEN

        A3=-1.0D0*A1/A2
        A4=DSQRT(A3)
        GR=A4*DSQRT(DIFF)
        GRWTH(IT)=-0.5D0*GR*(1.0D0/(DSQRT(T)))
C        WRITE(16,*)
C        WRITE(16,*)
C
C        WRITE(16,*) A1,A2,A3,A4,GR,GRWTH(IT)

        ELSE

        A3=A1/A2
        A4=DSQRT(A3)
        GR=A4*DSQRT(DIFF)

        GRWTH(IT)=0.5D0*GR*(1.0D0/(DSQRT(T)))
C        WRITE(16,*)
C        WRITE(16,*)

C        WRITE(16,*) A1,A2,A3,A4,GR,GRWTH(IT)

        ENDIF
        ELSE
GRWTH(IT)=0.0D0
        ENDIF


        RETURN
        END


C----------------------------------------------------------

        SUBROUTINE PPTVOLS(PPVOL,ITIM,PPTE,N,NTOT)
        IMPLICIT DOUBLE PRECISION (A-H,L-Z)
        IMPLICIT INTEGER (I-K)
        DIMENSION PPVOL(10000),PPTE(10000),N(10000)

C Changed the Do loop to J=1 to ITIM from 10000

        TEMP3=0.0D0
        NTOT=0.0D0
```

```
      PPVOL(ITIM)=0
C     WRITE(6,*)'ITIM= ',ITIM
      DO 102 J=1,ITIM
C      WRITE(10,*) PPVOL(ITIM)

      PPVOL(ITIM)=PPVOL(ITIM)+PPTE(J)
      NTOT=NTOT+N(J)

102   CONTINUE



C      WRITE(6,*)'Total volume of pptes is: -',PPVOL(ITIM)

      RETURN
      END


C----------------------------------------------------------

      SUBROUTINE THERMODYN(TMP,XINF,XCU,DELGV)
      IMPLICIT DOUBLE PRECISION (A-H,L-Z)
      IMPLICIT INTEGER (I-K)
      DIMENSION X(7),Y(7),W(7),WORK1(21),WORK2(10),A(5,5),S(5),
     &COEF(5),ADIF(5),SSFE(7),SSCU(7),CPCU(7)
C     &AB(5,5),COEFB(5),RES(7)

C This subroutine calculates chemical potentials, the solubility of
C Cu in iron and the molar fraction of the epsilon phase all as a
C function of temperature - using fitted curves from MTDATA.
C Data for the curves was taken at 10K temperature intervals. Data
C are presented for 1,2,3,4,5 & 6 wt% copper (note weight%!!)


C I have checked and MTDATA uses the following molar masses:-
C      Fe = 55.847 g/mol
C      Cu = 63.546 g/mol

C Data below are coefficients for fitted quartic eqns of the form
C Y=A*X**4 + B*X**3 + C*X**2 + D*X + E
C Coefficients describe:-
C CPFE - chemical potential of iron in 2 phase common tangent
C         (where tangent hits Fe axis) as a function of temperature
C          in kelvin.
C CPCU - as above but for Cu (i.e. intercept on right hand axis).
C NCU  - literally the number of moles present of the Cu phase.
C XCU  - Solubility of Cu in iron as mole fraction (max=0.01762
C         at this composition).
C SSFE - As CPFE but only allowing the BCC phase to exist.
C SSCU - As CPCU but only allowing the BCC phase to exist.
C
C First digit following the name describes the copper content in
C wt%. The second digit is simply a label.
C The 0% calculations were performed with 1E-6wt% Cu.
```

```
C Firstly we need to check that the temperature range is within the
C limits of the fitted data curves. The maximum temperature at which
C the alpha phase existed was found for all of the compositions below.
C These, when plotted form a smooth curve (apart from the zero point
C which was removed) and a quartic eqn can be used to express this
C as here:-

      DATA TCHK1,TCHK2,TCHK3,TCHK4,TCHK5/
     &-0.416667D0,7.68518D0,-54.0278D0,223.585D0,843.333D0/


C I need to convert the incoming solid solution atomic fraction to a
C weight fraction as the routine below uses this.
C This is performed below.



      WPCU=(100.0D0*63.546D0*XINF)/((63.546D0*XINF)+
     &(55.847D0*(1.0D0-XINF)))


C      WRITE(10,*)'Copper concentration in wt%:- ',WPCU

      CALL QUARTIC(TCHK1,TCHK2,TCHK3,TCHK4,TCHK5,WPCU,OUT)
      TMPCHK=OUT

C      WRITE(10,*) 'At this composition, max temp is:- ',TMPCHK
      IF (TMP .GT. TMPCHK) THEN
       WRITE(6,*)'Temperature too high!!!!'
       WRITE(6,*)'EXITING SUBROUTINE...'
       RETURN
      ENDIF

C Thermodynamic data for the system is entered below.


      DATA CPFE01,CPFE02,CPFE03,CPFE04,CPFE05/
     &-5.60576D-09,1.98053D-05,-0.050637D0,-2.49628D0,-3346.91D0/
      DATA CPCU01,CPCU02,CPCU03,CPCU04,CPCU05/
     &2.42835D-08,-6.33349D-05,0.0205743D0,-187.454D0,47599.3D0/
      DATA SSFE01,SSFE02,SSFE03,SSFE04,SSFE05/
     &-5.60576D-09,1.98053D-05,-0.050637D0,-2.49628D0,-3346.91D0/
      DATA SSCU01,SSCU02,SSCU03,SSCU04,SSCU05/
     &4.46463D-08,-0.000128788D0,0.096396D0,-224.722D0,54109.5D0/
      DATA TMPMX1,TTMOL1/1020D0,1790.60647D0/

      DATA CPFE11,CPFE12,CPFE13,CPFE14,CPFE15/
     &-4.15942D-09,1.54337D-05,-0.0461647D0,-4.36705D0,-3074.95D0/
      DATA CPCU11,CPCU12,CPCU13,CPCU14,CPCU15/
     &-7.73269D-09,3.04568D-05,-0.0605255D0,-4.67276D0,-3839.9D0/
      DATA NCU11,NCU12,NCU13,NCU14,NCU15/
     &-2.15862D-10,4.50206D-07,-0.00035098D0,0.119525D0,0.88594D0/
      DATA XCU11,XCU12,XCU13,XCU14,XCU15/
     &1.19317D-13,-2.48235D-10,1.93148D-07,-6.5678D-05,0.00815117D0/
      DATA SSFE11,SSFE12,SSFE13,SSFE14,SSFE15/
     &-5.62456D-09,1.98533D-05,-0.0506792D0,-2.55447D0,-3345.6D0/
```

```
      DATA SSCU11,SSCU12,SSCU13,SSCU14,SSCU15/
     &4.93484D-08,-0.000141084D0,0.107576D0,-114.074D0,53936.6D0/
      DATA TMPMX0,TTMOL0/1020D0,1788.4366D0/

      DATA CPFE21,CPFE22,CPFE23,CPFE24,CPFE25/
     &-9.39586D-09,2.9469D-05,-0.059595D0,1.03648D0,-3842.47D0/
      DATA CPCU21,CPCU22,CPCU23,CPCU24,CPCU25/
     &-5.17382D-08,0.000147457D0,-0.171528D0,39.6067D0,-10085D0/
      DATA NCU21,NCU22,NCU23,NCU24,NCU25/
     &-2.49105D-10,5.32059D-07,-0.00042301D0,0.146315D0,13.074D0/
      DATA XCU21,XCU22,XCU23,XCU24,XCU25/
     &1.35354D-13,-2.86783D-10,2.26359D-07,-7.77972D-05,0.00972949D0/
      DATA SSFE21,SSFE22,SSFE23,SSFE24,SSFE25/
     &-5.68352D-09,2.00053D-05,-0.0508152D0,-2.57811D0,-3342.45D0/
      DATA SSCU21,SSCU22,SSCU23,SSCU24,SSCU25/
     &5.36871D-08,-0.000152236D0,0.117508D0,-111.977D0,53683.2D0/
      DATA TMPMX2,TTMOL2/1130D0,1786.2633D0/

      DATA CPFE31,CPFE32,CPFE33,CPFE34,CPFE35/
     &-6.78887D-09,2.22708D-05,-0.0525242D0,-1.87295D0,-3421.52D0/
      DATA CPCU31,CPCU32,CPCU33,CPCU34,CPCU35/
     &-5.58077D-09,2.48061D-05,-0.0552187D0,-6.77291D0,-3545.73D0/
      DATA NCU31,NCU32,NCU33,NCU34,NCU35/
     &-1.84356D-10,3.56372D-07,-0.000252751D0,0.0770007D0,38.7564D0/
      DATA XCU31,XCU32,XCU33,XCU34,XCU35/
     &9.66819D-14,-1.8094D-10,1.23201D-07,-3.56365D-05,0.00366352D0/
      DATA SSFE31,SSFE32,SSFE33,SSFE34,SSFE35/
     &-5.76954D-09,2.02204D-05,-0.0510001,-2.58758D0,-3334.22D0/
      DATA SSCU31,SSCU32,SSCU33,SSCU34,SSCU35/
     &5.761D-08,-0.000162103D0,0.12606D0,-111.667D0,53342.1D0/
      DATA TMPMX3,TTMOL3/1200D0,1784.0999D0/

      DATA CPFE41,CPFE42,CPFE43,CPFE44,CPFE45/
     &-1.4231D-09,6.77029D-06,-0.0366453D0,-8.65636D0,-2408.34D0/
      DATA CPCU41,CPCU42,CPCU43,CPCU44,CPCU45/
     &-1.7171D-08,5.90444D-05,-0.0910103D0,8.79018D0,-5904.65D0/
      DATA NCU41,NCU42,NCU43,NCU44,NCU45/
     &-1.36146D-10,2.20794D-07,-0.000116792D0,0.0199087D0,62.9048D0/
      DATA XCU41,XCU42,XCU43,XCU44,XCU45/
     &6.68422D-14,-9.59345D-11,3.72477D-08,6.55446D-07,0.00170348D0/
      DATA SSFE41,SSFE42,SSFE43,SSFE44,SSFE45/
     &-1.05915D-09,6.59449D-06,-0.0370192,-8.64423D0,-2416.94D0/
      DATA SSCU41,SSCU42,SSCU43,SSCU44,SSCU45/
     &5.26845D-08,-0.000145928D0,0.107499D0,-100.599D0,51233.6D0/
      DATA TMPMX4,TTMOL4/1260D0,1781.92659D0/

      DATA CPFE51,CPFE52,CPFE53,CPFE54,CPFE55/
     &2.81747D-10,1.58306D-06,-0.0310738D0,-11.1377D0,-2024.65D0/
      DATA CPCU51,CPCU52,CPCU53,CPCU54,CPCU55/
     &-1.33147D-08,4.84463D-05,-0.080714D0,4.62121D0,-5312.59D0/
      DATA NCU51,NCU52,NCU53,NCU54,NCU55/
     &-1.09714D-10,1.44824D-07,-3.87689D-05,-0.0136189D0,83.6827D0/
      DATA XCU51,XCU52,XCU53,XCU54,XCU55/
     &4.91755D-14,-4.3888D-11,-1.70288D-08,2.42074D-05,-0.00526726D0/
```

```
       DATA SSFE51,SSFE52,SSFE53,SSFE54,SSFE55/
      &7.223D-10,1.15987D-06,-0.0311665D0,-11.3311D0,-1983.4D0/
       DATA SSCU51,SSCU52,SSCU53,SSCU54,SSCU55/
      &3.9951D-08,-0.000106047D0,0.0635305D0,-78.7767D0,47387D0/
       DATA TMPMX5,TTMOL5/1310D0,1779.7632D0/

       DATA CPFE61,CPFE62,CPFE63,CPFE64,CPFE65/
      &1.57722D-09,-2.47937D-06,-0.0265874D0,-13.1854D0,-1701.47/
       DATA CPCU61,CPCU62,CPCU63,CPCU64,CPCU65/
      &-1.28183D-08,4.76604D-05,-0.0806045D0,4.86857D0,-5389.78/
       DATA NCU61,NCU62,NCU63,NCU64,NCU65/
      &-9.65553D-11,1.06923D-07,5.73183D-07,-0.0307632D0,102.033D0/
       DATA XCU61,XCU62,XCU63,XCU64,XCU65/
      &3.83747D-14,-1.11244D-11,-5.21279D-08,3.98048D-05,
      &-0.00767488D0/
       DATA SSFE61,SSFE62,SSFE63,SSFE64,SSFE65/
      &2.02231D-09,-2.94078D-06,-0.0266173D0,-13.4884D0,-1618.69D0/
       DATA SSCU61,SSCU62,SSCU63,SSCU64,SSCU65/
      &2.58552D-08,-6.09996D-05,0.0130084D0,-53.9837D0,42982.5D0/
       DATA TMPMX6,TTMOL6/1360D0,1777.5898D0/

C Calculation of data for the fitted G curve.
C Note SSFE(1) corresponds to approximately 0wt% copper, SSFE2 is
C for 1wt%Cu and so on.

       CALL QUARTIC(SSFE01,SSFE02,SSFE03,SSFE04,SSFE05,TMP,OUT)
       SSFE(1)=OUT
       CALL QUARTIC(SSFE11,SSFE12,SSFE13,SSFE14,SSFE15,TMP,OUT)
       SSFE(2)=OUT
       CALL QUARTIC(SSFE21,SSFE22,SSFE23,SSFE24,SSFE25,TMP,OUT)
       SSFE(3)=OUT
       CALL QUARTIC(SSFE31,SSFE32,SSFE33,SSFE34,SSFE35,TMP,OUT)
       SSFE(4)=OUT
       CALL QUARTIC(SSFE41,SSFE42,SSFE43,SSFE44,SSFE45,TMP,OUT)
       SSFE(5)=OUT
       CALL QUARTIC(SSFE51,SSFE52,SSFE53,SSFE54,SSFE55,TMP,OUT)
       SSFE(6)=OUT
       CALL QUARTIC(SSFE61,SSFE62,SSFE63,SSFE64,SSFE65,TMP,OUT)
       SSFE(7)=OUT
       CALL QUARTIC(SSCU01,SSCU02,SSCU03,SSCU04,SSCU05,TMP,OUT)
       SSCU(1)=OUT
       CALL QUARTIC(SSCU11,SSCU12,SSCU13,SSCU14,SSCU15,TMP,OUT)
       SSCU(2)=OUT
       CALL QUARTIC(SSCU21,SSCU22,SSCU23,SSCU24,SSCU25,TMP,OUT)
       SSCU(3)=OUT
       CALL QUARTIC(SSCU31,SSCU32,SSCU33,SSCU34,SSCU35,TMP,OUT)
       SSCU(4)=OUT
       CALL QUARTIC(SSCU41,SSCU42,SSCU43,SSCU44,SSCU45,TMP,OUT)
       SSCU(5)=OUT
       CALL QUARTIC(SSCU51,SSCU52,SSCU53,SSCU54,SSCU55,TMP,OUT)
       SSCU(6)=OUT
       CALL QUARTIC(SSCU61,SSCU62,SSCU63,SSCU64,SSCU65,TMP,OUT)
       SSCU(7)=OUT
       CALL QUARTIC(CPCU01,CPCU02,CPCU03,CPCU04,CPCU05,TMP,OUT)
```

```
        CPCU(1)=OUT
        CALL QUARTIC(CPCU11,CPCU12,CPCU13,CPCU14,CPCU15,TMP,OUT)
        CPCU(2)=OUT
        CALL QUARTIC(CPCU21,CPCU22,CPCU23,CPCU24,CPCU25,TMP,OUT)
        CPCU(3)=OUT
        CALL QUARTIC(CPCU31,CPCU32,CPCU33,CPCU34,CPCU35,TMP,OUT)
        CPCU(4)=OUT
        CALL QUARTIC(CPCU41,CPCU42,CPCU43,CPCU44,CPCU45,TMP,OUT)
        CPCU(5)=OUT
        CALL QUARTIC(CPCU51,CPCU52,CPCU53,CPCU54,CPCU55,TMP,OUT)
        CPCU(6)=OUT
        CALL QUARTIC(CPCU61,CPCU62,CPCU63,CPCU64,CPCU65,TMP,OUT)
        CPCU(7)=OUT


C Evaluate the maximum solubility of copper at this temperature

        CALL QUARTIC(XCU61,XCU62,XCU63,XCU64,XCU65,TMP,OUT)
        XCU=OUT
        IF (XCU .LT. 0.0D0) THEN
          XCU=1.0D-06
        ENDIF
C        WRITE(10,*) 'Max sol. of Copper at this temp is (at fr.):',XCU


C The code below calculates 7 points along the delta G curve and
C places them in the array Y. The array X is filled with the
C corresponding compositional data.
C This is all to give the NAG library the data in a manner
C consistent with the manual.


        DO 58 I=0,6,1
        Y(I+1)=SSFE(I+1)+((SSCU(I+1)-SSFE(I+1))*I/100.0D0)
C        WRITE(10,*) 'Y(I+1)=',Y(I+1),SSFE(I+1),SSCU(I+1)
58      CONTINUE


        X(1)=0.0D0
        X(2)=1.0D0
        X(3)=2.0D0
        X(4)=3.0D0
        X(5)=4.0D0
        X(6)=5.0D0
        X(7)=6.0D0

        IM=7
        IKPL1=5
        INRW=5

C The W array below is one which allows you to add weights to the
C calculated points on the G curve - by giving W(1) and w(2) higher
C numbers, the curve can be more strongly pinned at the sensitive
C low Cu end.
```

```
       W(1)=100.0D0
       W(2)=100.0D0
       W(3)=1.0D0
       W(4)=1.0D0
       W(5)=1.0D0
       W(6)=1.0D0
       W(7)=1.0D0

C      WRITE(6,*) X,Y,W
       IFAIL=0

C E02ADF - routine to fit a curve to the data points (x,y) using
C a Chebyshev polynomial of degree k (four for quartic)
C Note that the thermodynamics are extremely sensitive to composition
C around zero copper so the gradient may go below that of the eqm.
C This needs to be forseen and dealt with. In fact I have tried fitting
C a curve but it's too distorted so, as all of the values involved with
C most except very small Cu weights are approximately constant I have
C averaged these.

       CALL E02ADF(IM,IKPL1,INRW,X,Y,W,WORK1,WORK2,A,S,IFAIL)
C
       AVCPCU=0.0D0
           DO 47 I=1,6,1
           AVCPCU=CPCU(I+1)+AVCPCU
C           WRITE(10,*) 'CPCU(I+1)=',CPCU(I+1),SSFE(I+1),SSCU(I+1)
47         CONTINUE
           AVCPCU=AVCPCU/6.0D0
C          WRITE(10,*) 'Averaged CPCU = ',AVCPCU

       INP1=5
       XMIN=X(1)
       XMAX=X(7)
        DO 61 J=1,5
        COEF(J)=A(5,J)
61      CONTINUE
C       WRITE(6,*) COEF

       IA1=1
       ILA=5
       IADIF1=1
       ILADIF=5
       IFAIL=0

C  Test evaluation of fitting using E02AKF gives the y (RESULT) at
C  any position x (VALUE) on the curve. This basically plots out
C  the full fitted G curve


C  In this section I am forcing the model to give DELTAG = 0
C  when the eqm composition is reached.

       WPXCU=(100.0D0*63.546D0*XCU)/((63.546D0*XCU)+
```

```
     &(55.847D0*(1.0D0-XCU)))

C       WRITE(10,*)'Max weight pct. solubility of Cu',WPXCU
        VALUE = WPXCU
        CALL E02AKF(INP1,XMIN,XMAX,COEF,IA1,ILA,VALUE,RESULT,IFAIL)
        YEQM=RESULT
C       WRITE(6,*)'YEQM = ',YEQM
        CALL E02AHF(INP1,XMIN,XMAX,COEF,IA1,ILA,PATM1,ADIF,IADIF1,
     &ILADIF,IFAIL)
        CALL E02AKF(INP1,XMIN,XMAX,ADIF,IA1,ILA,VALUE,RESULT,IFAIL)

C       WRITE(10,*)'Curve fit eqm curve GRADIENT = ',RESULT
        INTCPT=YEQM-(VALUE*RESULT)
        DLGEQM=((100.0D0*RESULT)+INTCPT)-AVCPCU

        CHK3=(RESULT*100.0D0)+INTCPT
C       WRITE(10,*) 'CALC CPCU, REAL CPCU: ',CHK3,AVCPCU


C  Ideally DLGEQM = 0.0D0 but this will usually not be true.

        RESEQM=(AVCPCU-YEQM)/(100.0D0-WPXCU)

C       WRITE(10,*) 'In reality, gradient should be:- ',RESEQM

        CHK4=(RESEQM*(100.0D0-WPXCU))+YEQM
C       WRITE(10,*)'With new gradient AVCPCU= ',CHK4


C I need to convert the incoming solid solution atomic fraction to a
C weight fraction as the routine below uses this.
C This is performed below.


        VALUE=WPCU

        IF (VALUE .GT. 6.0D0) THEN
         VALUE=6.0D0
         WRITE(6,*) 'CU CONTENT TOO HIGH - ADJUSTED TO 6WT%'
        ENDIF
        IF (VALUE .LT. 0.0D0) THEN
         VALUE=0.0D0
         WRITE(6,*) 'CU CONTENT TOO LOW - ADJUSTED TO 0WT%'
        ENDIF

        CALL E02AKF(INP1,XMIN,XMAX,COEF,IA1,ILA,VALUE,RESULT,IFAIL)

C       RES(VALUE+1)=RESULT

        TMPRES=RESULT


C  E02AHF differentiates Chebyshev polynomial whose coefficients are held
C  in COEF.
```

```
      CALL EO2AHF(INP1,XMIN,XMAX,COEF,IA1,ILA,PATM1,ADIF,IADIF1,
     &ILADIF,IFAIL)


C  Again this differentiated polynomial is a polynomial itself and thus
C  can be evaluated at any point along the curve - gives the value of the
C  gradient at point x,y.


      CALL EO2AKF(INP1,XMIN,XMAX,ADIF,IA1,ILA,VALUE,RESULT,IFAIL)


C It is necessary to implement the correction to the gradient
C when within say 1% of the eqm concentration. This is done by
C comparing the calculated gradient with that of the correct
C value. The calculation is constrained so that the gradient is
C the ideal one at eqm, and the calculated one, 1% Cu away from
C eqm. This is done in a linear manner below.
C The calculated deltaG is then output to a file for plotting.
      CHK2=WPXCU


      CHK1 = VALUE-CHK2


      IF (CHK1 .LE. 1.0D0) THEN
        GRDNT = RESEQM + (CHK1*(RESULT-RESEQM))
        ELSE
        GRDNT=RESULT
      ENDIF


      IF (GRDNT .LT. RESEQM) THEN
        GRDNT=RESEQM
      ENDIF


C      INTCPT=TMPRES-(GRDNT*VALUE)
C       OUTPUT=((100.0D0*RESULT)+INTCPT)-AVCPCU
      CHK4=(RESEQM*(100.0D0-WPXCU))+YEQM
      INTCU=(GRDNT*(100.0D0-WPCU))+TMPRES
      OUTPUT=INTCU-AVCPCU


C      WRITE(10,*) VALUE,GRDNT,RESULT,OUTPUT
C      WRITE(10,*) GRDNT,WPCU,WPXCU,TMPRES,OUTPUT



C The result of this calculation is the free energy available
C for nucleation - DELGV.


796   FORMAT(D12.5,TR1,D12.5,TR1,D12.5,TR1,D12.5)
      DELGV=0.0D0
      DELGV = OUTPUT


C I can calculate the equilibrium free energy at this temperature
C because I have calculated the eqm maximum copper solubility in
C ferrite (XCU). I know that the driving force for nucleation is
C simply related to the difference between the stable free energy
C for the copper rich phase (in our case CPCU as we have 100% Cu
C assumed) and the intercept of the tangent to the solid solution
C free energy curve with the same 100% Cu axis. It should be easy
```

193

```
C to check when the pption stops as this difference may become close
C to or less than zero. This is why I have calculated CPCU for a
C number of different Cu contents and as expected the value is
C constant (approximately).

C However, experimentally this is not the case - the curves do not
C agree - the deltaG value does not go to zero as you approach the
C eqm concentration. Therefore it is necessary to apply some sort of
C forcing condition onto this. I propose to calculate the value at
C the eqm concentration first - then to apply some sort of maybe
C linear correction to the gradient in the last 1% Cu down to the
C eqm value. I have now done this.


      RETURN
      END


C------------------------------------------------------------

      SUBROUTINE QUARTIC(A,B,C,D,E,TMP,OUT)
      IMPLICIT DOUBLE PRECISION (A-H,L-Z)
      IMPLICIT INTEGER (I-K)

      OUT=(A*TMP**4.0D0)+(B*TMP**3.0D0)+(C*TMP**2.0D0)
     &+(D*TMP)+E

      RETURN
      END


C------------------------------------------------------------

      SUBROUTINE DIFFUSN(TMP,DIFF)
      IMPLICIT DOUBLE PRECISION (A-H,L-Z)
      IMPLICIT INTEGER (I-K)

C  Curie point marks a transition in diffusion coeff.
C  The fit for below Curie Temp only has 2 data points!!
C  Some inaccuracy likely. Units of DIFF are m^2/s

      IF (TMP .GE. 1032) THEN
        DZERO=13.5295D-4
        COEF=-30564.4
      ELSE
        DZERO=2.04942D-4
        COEF=-29999D0
      ENDIF

      DIFF=DZERO*DEXP(COEF*(1.0D0/TMP))

      RETURN
      END


C------------------------------------------------------------
```

```
      SUBROUTINE PPTRADCALC(N,PPTE,ITIM,PPTRAD)
      IMPLICIT DOUBLE PRECISION (A-H,L-Z)
      IMPLICIT INTEGER (I-K)
      DIMENSION N(10000),PPTE(10000),PPTRAD(10000)

TEMPPT=0.0D0
      DO 299 IPPT=1,ITIM
        IF ((N(IPPT) .GT. 0.0D0) .AND. (PPTE(IPPT)
     & .GT. 0.0D0)) THEN
        TEMPPT=(1.0D0/4.18879)*PPTE(IPPT)/N(IPPT)

        PPTRAD(IPPT)=(TEMPPT**(1.0D0/3.0D0))
        ELSE
        PPTRAD(IPPT)=0.0D0

      ENDIF
C     WRITE(6,795) N(IPPT),IPPT,TEMPPT,PPTRAD(IPPT)
795   FORMAT(D12.5,I5,2D12.5)

299   CONTINUE
      RETURN
      END




C--------------------------------------------------------

      SUBROUTINE AVERAD(PPTRAD,ITIM,N,AVRAD)
      IMPLICIT DOUBLE PRECISION (A-H,L-Z)
      IMPLICIT INTEGER (I-K)
      DIMENSION N(10000),PPTRAD(10000)
      AVRAD=0.0D0
      TOTRAD=0.0D0
      NTOT=0.0D0
      DO 200 IRAD=1,ITIM,1
        TOTRAD=(N(IRAD)*PPTRAD(IRAD))+TOTRAD
        NTOT=N(IRAD)+NTOT
C        WRITE(6,*) PPTRAD(IRAD)
200   CONTINUE
      AVRAD=(TOTRAD/NTOT)
      RETURN
      END




C--------------------------------------------------------
C Note that in this section of the program we use the variable
C AVRAD but this is in fact COMRAD

      SUBROUTINE STRENGTHCALC(XPPT,XINF,XFE,AVRAD,TIME)
      DOUBLE PRECISION AFCU,PPTR,ROCU,XFE,TIMEH,YIELDM
      DOUBLE PRECISION YIELD,SPC,RECIPSPC,RECIPR,PHIDEG
      DOUBLE PRECISION TAUFM,AVRAD,XPPT,TIME,XINF,SOLSTN,SOLSTO

      AFCU=XPPT
      PPTR=AVRAD
```

```
      OPEN(12,FILE='strengthoutput')
C      DO 99 COUNT=1,20
C  Need to define COUNT at start of subroutine if using this loop.
C      DO 99 PPTR=0.1,5,0.1
C      READ(9,*,END=100) AFCU,PPTR
C      WRITE(6,98)AFCU,PPTR,COUNT
      CALL COPPERPPTS(AFCU,PPTR,SPC,TAUFM,PHIDEG,ROCU)

C The Taylor factor can vary between 2.2 and 3.1 for cubic materials
C see page 341 of Strengthening Methods in Crystals.
C Using Fujii's data I am going to attach a linear fit to the substitutional
C solid solution data. This produces a predicted base ferrite strength of
C 98.8MPa. If I change the Taylor factor this will have to be altered.

      SOLST0=60.8945D0*(XFE*100.0D0)*1.0D6
      TIMEH=TIME/3600.0D0
      IF (TAUFM .GT. 0.0D0) THEN
      SOLSTN=60.8945D0*(XINF*100.0D0)*1.0D6
      YIELD=((TAUFM+75D6)*2.2D0)+SOLSTN
      YIELDM=YIELD/1D06
      RECIPSPC=1/SPC
      RECIPR=1/PPTR


C      WRITE(12,98)AFCU,RECIPR,RECIPSPC,YIELD,PHIDEG
C      WRITE(6,*)
C      WRITE(6,*)
C      WRITE(6,*)'Yield Stress is predicted as :-',YIELD
C      WRITE(6,*)'================================================='

      WRITE(12,*) TIMEH, YIELDM, YIELDM1, SOLSTN
      ELSE

      YIELD=((TAUFM+75D6)*2.2D0)+SOLST0
      YIELDM=YIELD/1D06

      WRITE(12,*) TIMEH, YIELDM, TAUFM, SOLSTN

      ENDIF

C 99      CONTINUE

98      FORMAT(5D12.5)
      RETURN
100      END


C ----------------------------------------------------------------

      SUBROUTINE COPPERPPTS(AFCU,PPTR,SPC,TAUFM,PHIDEG,ROCU)
      DOUBLE PRECISION AFCU,PPTR,PPTCR,SPC,PI,POIS,GFE,BURG,TENSN
      DOUBLE PRECISION POISFE,POISCU,GCU,BURGFE,BURGCU
      DOUBLE PRECISION BIGR,RZERO,THETA,PHI
```

196

```
        DOUBLE PRECISION TAUST,ROFE,ROCU
        DOUBLE PRECISION SIDEL,TAUFM
C        DOUBLE PRECISION TAUCW,BESTTAU,AFNTHETA
C        DOUBLE PRECISION I,Y,X,J
        DOUBLE PRECISION PHIDEG

C AFCU - atomic fraction of Cu
C PPTR - average radius of precipitates
C SPC - spacing of precipitates
C VPPT - volume of a precipitate
C PI - value of PI = 3.141592654

        PI=3.141592654D0
        BURGFE=2.48D-10
        BURGCU=2.56D-10

        PPTCR=0.0D0
        SPC=0.0D0
        TAUST=0.0D0

C Adjustable coefficients alter strength for ROFE and ROCU

        ROFE=1.5D0*BURGFE
        ROCU=1.5D0*BURGCU
C        RZERO=2*BURGFE
        TENSN=0.0D0


        CALL PPTSPACING(AFCU,PPTR,SPC,PI,PPTCR)
        CALL EQUIVSQRL(PPTCR,SIDEL,PI,ROCU,SPC,AFCU)


        POIS=0.29D0
        POISFE=0.29D0
        POISCU=0.35D0
        GFE=8.3D10
        GCU=4.85D10
        BURG=2.48D-10
        THETA=PI/2.0D0
        BIGR=SPC

C        WRITE(6,*)'BIGR (spacing between ppte edges) = ',BIGR
C        WRITE(6,*)
C        WRITE(6,*) 'For EDGE dislocations:'
C        WRITE(6,*)

        PHI=0.0D0


        IF (SIDEL .GT. ROCU) THEN

        CALL NEWSTUFF(GFE,GCU,BURGFE,BURGCU,POISFE,POISCU,PI,SPC
     &,PPTCR,ROFE,ROCU,SIDEL,BIGR,PHI,PHIDEG)
C        WRITE(6,*)'PHI IS:-',PHI
```

```
      TAUST=0.0D0

        CALL STRENFM(SPC,PPTCR,BURG,GFE,PHI,PI,TAUFM)
      PHI1=PHI/2.0D0

251      FORMAT(5D12.5)
       ENDIF
      RETURN
      END




C----------------------------------------------------------------------

      SUBROUTINE PPTSPACING(AFCU,PPTR,SPC,PI,PPTCR)
      DOUBLE PRECISION AFCU,PPTR,SPC,PI,PPTCR

C      WRITE(6,*) 'Atomic fraction of Cu?'
C      AFCU=0.03D0
C      READ(5,*)AFCU
C      WRITE(6,*)
C      WRITE(6,*) 'Average radius of precipitates (nm)?'
C      PPTR=25
C      READ(5,*)PPTR
C      WRITE(6,*)
C      PPTR=PPTR*1.0D-9
C      WRITE(6,*)'Radius in m:- ',PPTR


C Calculation of precipitate spacing assumes a random
C distribution of 100% Cu pptes. This calculates the mean
C circular section of a spherical precipitate on a random plane.
C The pptes are assumed to be distributed in a square array on
C this plane. The separation (taking the radius into account) is
C then easily calculated. Page 34.

      PPTCR = PPTR*DSQRT(2.0D0/3.0D0)

C      WRITE(6,*)
C      WRITE(6,*)'Averaged cut area of precipitate radius:- ',PPTCR

C      SPC = PPTCR*(DSQRT(PI/AFCU)-2)
      SPC = PPTCR*(DSQRT(PI/AFCU))

C      WRITE(6,*)
C      WRITE(6,*)'Calculated spacing of precipitates:- ',SPC
C      WRITE(6,*) SPC

      RETURN
      END




C----------------------------------------------------------------------
```

```
      SUBROUTINE LINETENSION(POIS,GSHEAR,BURG,THETA,BIGR,RZERO,TENSN,PI)
C TA-TC are parts of the line tension equation.
      DOUBLE PRECISION POIS,GSHEAR,BURG,THETA,BIGR,RZERO,TENSN,PI,TA

      TA=GSHEAR*(BURG**2.0D0)/(4.0D0*PI)
      TB=(1.0D0-(POIS*(DCOS(THETA)**2.0D0)))/(1.0D0-POIS)
      TC=DLOG(BIGR/RZERO)
C       WRITE(6,*)'TA = ',TA
C       WRITE(6,*)'TB = ',TB
C       WRITE(6,*)'TC = ',TC

      TENSN=TA*TB*TC
C       WRITE(6,*)'TENSION IS :-',TENSN

C       WRITE(6,*)
C       WRITE(6,*) 'POIS   :- ',POIS
C       WRITE(6,*) 'GSHEAR :- ',GSHEAR
C       WRITE(6,*) 'BURG   :- ',BURG
C       WRITE(6,*) 'THETA  :- ',THETA
C       WRITE(6,*) 'BIGR   :- ',BIGR
C       WRITE(6,*) 'RZERO  :- ',RZERO
C       WRITE(6,*) 'TENSN  :- ',TENSN
C       WRITE(6,*) 'PI     :- ',PI
C       WRITE(6,*)

      RETURN
      END



C-----------------------------------------------------------------

      SUBROUTINE STRENFM(SPC,PPTCR,BURG,GFE,PHI,PI,TAUFM)
      DOUBLE PRECISION SPC,PPTCR,BURG,GFE,PHI,TAUFM,PI
      DOUBLE PRECISION TAUFM1,TAUFM2,TAUFM3,TAUFM4
C       WRITE(6,*) SPC,PPTCR,GFE,BURG,PHI
      TAUFM1=(GFE*BURG)/(SPC)*(DCOS(PHI/2)**(3.0D0/2.0D0))
      TAUFM2=(GFE*BURG)/(SPC)*(DCOS(PHI/2)**(3.0D0/2.0D0))
      TAUFM3=TAUFM1*(0.8D0+(PHI/(5.0D0*PI)))
      TAUFM4=TAUFM2*(0.8D0+(PHI/(5.0D0*PI)))


C
C       WRITE(6,*)
C       WRITE(6,*) '------------------------------------------------'
C       WRITE(6,*)
C       WRITE(6,*)'Corrected Spacing gives :- ',TAUFM3
C       WRITE(6,*)'Original Spacing gives:- ',TAUFM4
      TAUFM=TAUFM3

C       WRITE(6,*)
C       WRITE(6,*)'Foreman and Makin strengthening is : ',TAUFM

      RETURN
      END
```

```
C-----------------------------------------------------------------

      SUBROUTINE NEWSTUFF(GFE,GCU,BURGFE,BURGCU,POISFE,POISCU,PI,SPC
     &,PPTCR,ROFE,ROCU,SIDEL,BIGR,PHI,PHIDEG)
      DOUBLE PRECISION GFE,GCU,BURGFE,BURGCU,POISFE,POISCU,PI,SPC
      DOUBLE PRECISION PPTCR,ROFE,ROCU,SIDEL,BIGR,TCU
      DOUBLE PRECISION TCU,TH,THETA,PHI
      DOUBLE PRECISION TENSN1,TENSN2,TENSN3
      DOUBLE PRECISION RESOLV,PHIDEG,CORE1,CORE2,CORE3,CORE
      TH=PI/4.0D0
      TENSN1=0.0D0
      TENSN2=0.0D0

      CALL LINETENSION(POISCU,GCU,BURGCU,TH,ROCU,ROCU,CORE1,PI)
      CALL LINETENSION(POISFE,GFE,BURGFE,TH,BIGR,ROCU,CORE2,PI)
      CALL LINETENSION(POISFE,GFE,BURGFE,TH,BIGR,ROFE,CORE3,PI)

      CORE=(CORE3-CORE2)

      CALL LINETENSION(POISCU,GCU,BURGCU,TH,SIDEL,ROCU,TENSN1,PI)
      CALL LINETENSION(POISFE,GFE,BURGFE,TH,BIGR,SIDEL,TENSN2,PI)
      CALL LINETENSION(POISFE,GFE,BURGFE,TH,BIGR,ROFE,TENSN3,PI)

      TCU=TENSN1+TENSN2

C      TCU=TENSN1+TENSN2+CORE
C      WRITE(6,*) TENSN1,TENSN2,TCU,CORE
C      WRITE(6,*) TENSN3

      RESOLV=TCU/TENSN3
      THETA=DACOS(RESOLV)


C      WRITE(6,*)'Theta is  :-',THETA
      PHI=2.0D0*((PI/2)-THETA)
C      WRITE(6,*)'PHI is at this point:-',PHI

      PHIDEG=PHI/PI*180.0D0

C      WRITE(6,*)'Phi is calculated as :- ',PHIDEG

      RETURN
      END

C-----------------------------------------------------------------
      SUBROUTINE EQUIVSQRL(PPTCR,SIDEL,PI,ROCU,SPC,AFCU)
      DOUBLE PRECISION CIRCLEA,PPTCR,SIDEL,PI,ROCU,EQN,SPC,AFCU
      DOUBLE PRECISION PPTR

      CIRCLEA=PI*(PPTCR**2.0D0)
C      SIDEL=(DSQRT(CIRCLEA))/2.0D0
C      I was going to equate the half-side length of a square
C      to SIDEL but now I have chosen the average radius of a
```

```
C      circle determined earlier - Root 2/3 of radius
C      The two numbers are very close anyway

       SIDEL=0.81649D0*PPTCR
C       SIDEL=PPTCR/2.0D0
C       WRITE(6,*) 'Square side (length/2) on slip plane = ',SIDEL
C       WRITE(6,*)'ROCU is : ',ROCU

       RETURN
       END


C ----------------------------------------------------
C Code for debugger error handling.

C       INTEGER FUNCTION hand(sig,code,context)
C         INTEGER sig,code,context(5)
C         WRITE(*, '("EXCEPTION AT PC", I5)') context(4)
C         RETURN
C       END
```

References

[1] *Naval Technology*, http://www.naval-technology.com/

[2] H. I. Aaronson, *The Decomposition of Austenite by Diffusional Processes*, eds. V. F. Zackay and H. I. Aaronson, Interscience, NY, (1962), 387

[3] H. I. Aaronson, H. A. Domian, G. M. Pound, *Trans. Met. Soc. AIME*, **236**, (1966), 753

[4] H. I. Aaronson, H. A. Domian, G. M. Pound, *Trans. Met. Soc. AIME*, **236**, (1966), 768

[5] H. I. Aaronson and H. A. Domian, *Trans. Met. Soc. AIME*, **236**, (1966), 781

[6] H. I. Aaronson, *Lectures on the Theory of Phase Transformations*, Metallurgical Society of AIME, (1975)

[7] H. I. Aaronson, M. G. Hall, D. M. Barnett, K. R. Kinsman, *Scripta Metall.*, **9**, (1975), 705

[8] D. J. Abson and R. J. Pargeter, *Int. Met. Rev.*, **31**, (1986), 141

[9] A. G. Allten and P. Payson, *Trans. ASM*, **45**, (1953), 498

[10] T. L. Altshuler and J. W. Christian, *Proc. Roy. Soc.*, **261A**, (1967), 253

[11] J. Aranzabal, I. Gutierrez, J. J. Urcola, *Mater. Sci. Technol.*, **10**, (1994), 728

[12] C. Atkinson, H. B. Aaron, K. R. Kinsman, H. I. Aaronson, *Metall. Trans.*, **4**, (1973), 783

[13] M. F. Ashby, *Physics of Strength and Plasticity*, ed. A. S. Argon, The M.I.T. Press, (1969), 113

[14] *ASM Metals Handbook*, 9th Edition, **8**, (1985), 90

[15] *ASM Metals Handbook*, 9th Edition, **9**, (1985), 130

[16] *Binary Alloy Phase Diagrams*, ASM International, **2**, (1990)

[17] S. Babu, K. Hono, T. Sakuri, *Applied Surface Science*, **67**, (1993), 321

[18] S. S. G. Banadkouki, D. Yu, D. P. Dunne, *ISIJ Int.*, **36(1)**, (1996), 61

[19] J. Barba, *Mem. Soc. Ing. Civ.*, **1**, (1880), 682

[20] S. J. Barnard, G. D. W. Smith, A. J. Garratt-Reed, J. Vander Sande, *Advances in the Physical Metallurgy and Applications of Steels*, Metals Society, London, (1981), 33

[21] H. K. D. H. Bhadeshia, *Ph.D. Thesis*, University of Cambridge, (1979), Chapter 1

[22] H. K. D. H. Bhadeshia, *Met. Sci.*, **15**, (1981), 175

[23] H. K. D. H. Bhadeshia, *Met. Sci.*, **15**, (1981), 178

[24] H. K. D. H. Bhadeshia, *Mat. Sci. Technol.*, **5**, (1989), 131

[25] H. K. D. H. Bhadeshia, *Bainite in Steels*, London, The Institute of Materials, (1992)

[26] H. K. D. H. Bhadeshia, *Materials Algorithms Project*, MAP_STEEL_MUCG46, http://www.msm.cam.ac.uk/map/steel/programs/mucg46-b.html, (1997)

[27] H. K. D. H. Bhadeshia, *Scripta Metall.*, **14**, (1980), 821

[28] H. K. D. H. Bhadeshia, *Acta Metall.*, **29**, (1981), 1117

[29] H. K. D. H. Bhadeshia and J. W. Christian, *Metall. Trans A*, **21A**, (1990), 767

[30] H. K. D. H. Bhadeshia and D. V. Edmonds, *Met. Sci.*, **17**, (1983), 411

[31] H. K. D. H. Bhadeshia and D. V. Edmonds, *Metall. Trans. A*, **10A**, (1979), 895

[32] H. K. D. H. Bhadeshia and D. V. Edmonds, *Acta Metall.*, **28**, (1980), 1265

[33] H. K. D. H. Bhadeshia and L. E. Svensson, *Mathematical Modelling of Weld Phenomena*, eds. H. Cerjak and K. E. Easterling, London, The Institute of Materials, (1993)

[34] H. K. D. H. Bhadeshia and L. E. Svensson, *Proc. of Int. Conf. Phase Transformations '87*, ed. G. W. Lorimer, London, The Institute of Metals, (1988)

[35] H. K. D. H. Bhadeshia and L.-E. Svensson, *J. Mater. Sci.*, **24**, (1989), 3180

[36] H. K. D. H. Bhadeshia and L.–E. Svensson, *Mathematical Modelling of Weld Phenomena*, eds. H. Cerjak and K. E. Easterling, London, The Institute of Materials, (1993), 160

[37] H. K. D. H. Bhadeshia, L.–E. Svensson, B. Gretoft, *J. Mater. Sci. Letters*, **4**, (1985), 305

[38] H. K. D. H. Bhadeshia, L.–E. Svensson, B. Gretoft, *J. Mater. Sci.*, **21**, (1986), 3947

[39] H. K. D. H. Bhadeshia, L.–E. Svensson, B. Gretoft, *Acta Metall.*, **33**, (1985), 1271

[40] J. R. Bradley, J. M. Rigbee, H. I. Aaronson, *Metall. Trans.*, **8a**, (1977), 323

[41] N. Bredzs, *Weld. J. Supplement*, November, (1954), 545s

[42] L. M. Brown, *Phil. Mag.*, **15**, (1964), 441

[43] L. M. Brown and R. K. Ham, *Strengthening Methods in Crystals.*, eds. A. B. Kelly and R. B. Nicholson, (1971), Chapter 2

[44] S. L. Case, *Steel Process*, **5**, (1950), 238

[45] D. E. Coats, *Metall. Trans.*, **4**, (1973), 2313

[46] J. Chance and N. Ridley, *Metall. Trans. A*, **21A**, (1981), 1205

[47] J. M. Chilton and P. M. Kelly, *Acta Metall.*, **16**, (1968), 637

[48] C. L. Choi and D. C. Hill, *Weld. J. Res. Supp.*, **57–8**, (1978), 23

[49] H. Conrad and S. Fredrick, *Acta Metall.*, **10**, (1962), 1013

[50] T. Cool, *Ph.D. Thesis*, Department of Materials Science, University of Cambridge, (1987)

[51] T. Cool and H. K. D. H. Bhadeshia, *Science and Technology of Welding and Joining*, **2(1)**, (1997) 36

[52] A. R. Cox, *JISI*, **37(3)**, (1967), 51

[53] J. W. Christian, *Strengthening Methods in Crystals.*, eds. A. B. Kelly and R. B. Nicholson, (1971), Chapter 5

[54] J. W. Christian, *The Theory of Phase Transformations in Metals and Alloys*, Part 1, 2nd edition, Pergamon, Oxford, (1965), Chapter 10

[55] J. W. Christian, *ICOMAT 79*, International conference on martensitic transformations, Cambridge, Massachusetts, (1979), 220

[56] J. Daigne, M. Guttmann, J. P. Naylor, *Mater. Sci. Eng.*, **56**, (1982), 1

[57] G. J. Davies and J. G. Garland, *Int. Metall. Rev.*, **20**, (1975), 83

[58] P. Deb, K. D. Challenger, A. E. Therrien, *Metall. Trans. A*, **18A**, June, (1987), 987

[59] J. H. Devletion and W. E. Wood, *Metals Handbook*, 9th Edition, **6**, June, (1983), 21

[60] G. E. Dieter, *Mechanical Metallurgy*, 3rd Edition, McGraw-Hill, (1986)

[61] G. DeWit and J. S. Koehler, *Physical Review*, **116(5)**, (1959), 1113

[62] K. Easterling, *Introduction to physical metallurgy of welding*, London, Butterworths, (1987), 152

[63] T. Edvardson, H. Fredricksson, I. Svensson, *Met. Sci.*, **10**, (1976), 298

[64] G. R. Edwards and S. Liu, *Symp. Proc. on Advances in Welding Technology*, First US–Japan Symposium AWS/JWS/JWES, SF, U.S.A. and Yokohama, Japan, (1990), 215

[65] A. J. E. Foreman, *Acta. Met.*, **3**, (1955), 322

[66] A. J. E. Foreman and M. J. Makin, *Phil. Mag.*, **14**, (1966), 911

[67] A. J. E. Foreman and M. J. Makin, *Can. J. Phys.*, **45**, (1967), 511

[68] G. Fourlaris, A. J. Baker, G. D. Papadimitriou, *Acta Mater.*, **44(12)**, (1996), 4791

[69] H. Fredriksson, *Acta Universitats Ouluensis*, Series C, 26–4, Proceedings of the 3rd Scandinasm Symposium on Materials Science, (1983), 1

[70] J. Fridberg, L.–E. Torndahl, M. Hillert, *Jerkont. Ann.*, **153**, (1969), 263

[71] J. Friedel, *Dislocations*, Pergamon Press, Oxford, (1964)

[72] A. Fujii, M. Nemoto, H. Suto, K. Monma, *Int. Conf. on Strength of Metals and Alloys, Tokyo (Supplement)*, **9**, (1968), 374

[73] S. R. Goodman, S. S. Brenner, J. R. Low Jr, *Metall. Trans.*, **4**, (1973), 2363

[74] J. Gordine and I. Codd, *J. Iron Steel Inst.*, April, (1969), 461

[75] J. L. Gregg, *Alloys of Iron and tungsten*, 1st Edition, The Engineering Foundation, (1934), 190

[76] O. Grong and D. K. Matlock, *Int. Met. Rev.*, **31**, (1986), 27

[77] P. Haasen, *Proc. 1st. Int. Conf. Strength of Metals and Alloys*, Supp. Trans. Japan Inst. Metals, **9**, (1968), XL

[78] F. S. Ham, *J. Phys. Chem. Solids*, **6**, (1958), 335

[79] R. K. Ham, *Trans. JIM Supplement*, **9**, (1968), 52

[80] E. G. Hamburg and A. D. Wilson, *Processing, Microstructure and Properties of HSLA Steels*, ed. A. J. DeArdo, The Minerals, Metals and Materials Society, (1988)

[81] P. L. Harrison and R. A. Farrar, *Int. Mater. Rev.*, **34**, (1989), 35

[82] L. S. Harsha, *CPGS Dissertation*, University of Cambridge, (1998)

[83] M. J. Hawkins and J. Barford, *J. Iron Steel Inst.*, **210**, (1972), 97

[84] R. F. Hehemann, K. R. Kinsman, H. I. Aaronson, *Metall. Trans.*, **3**, (1972), 1077

[85] J. E. Hilliard, *Trans. JIM Supplement*, **9**, (1968), 52

[86] M. Hillert, *Acta Metall.*, **3**, (1955), 34

[87] R. M. Hobbs, G. W. Lorimer, N. Ridley, *J. Iron Steel Inst.*, October, (1972), 757

[88] S. M. Hodson, MTDATA – Metallurgical and Thermochemical Databank, National Physical Laboratory, Teddington, U.K., (1989)

[89] R. W. K. Honeycombe and H. K. D. H. Bhadeshia, *Steels - Microstructure and Properties*, Edward Arnold, London, 2nd Edition, (1995)

[90] E. Hornbogen and R. C. Glenn, *Trans. Metall. Soc. AIME*, **218**, (1960), 1064

[91] E. Hornbogen, *Precipitation from Iron–Base Alloys*, eds. G. R. Speich, J. B. Clark, Gordon and Breach, New York, (1965), 1

[92] E. Hornbogen, *Acta Met.*, **10**, (1962), 525

[93] E. Hornbogen, *TMS-AIME*, **224**, (1962), 906

[94] E. Hornbogen, *Trans. ASM*, **57**, (1964), 120

[95] Y. Horii, M. Wakabayashi, S. Ohkita, M. Namura, *Nippon Steel Technical Report*, Nippon Steel Company, Japan, No. 37, April, (1986), 1

[96] F. J. Humphreys and M. Hatherly, *Recrystallization and related annealing phenomena*, 1st Edition, Pergamon, (1996), 271

[97] R. F. Hehemann, *Phase Transformation*, ASM, Metals Park, Ohio, U.S.A., (1970), 397

[98] K. J. Irvine and F. B. Pickering, *J. Iron Steel Inst.*, **201**, (1963), 518

[99] Y. Ito and K. Bessyo, *Int. Inst. Weld.*, Document XII–113–75, (1975)

[100] Y. Ito and M. Nakanishi, *The Sumitomo Search (Technical Report)*, **15**, Sumitomo Metal Industries Ltd., Japan, (1976), 42

[101] Y. Ito and M. Nakanishi, *Metal Constr.*, **14(9)**, (1982), 472

[102] A. S. Keh and W. C. Leslie, *Mater. Sci. Res.*, **1**, Plenum Press, New York, (1963), 208

[103] A. S. Keh and S. Weissmann, *Electron Microscopy and the Strength of Crystals*, ed. G. Thomas, J. Washburn, New York, Interscience, (1963), 231

[104] M. Kehoe and P. M. Kelly, *Scripta Metall.*, **4**, (1970), 473

[105] J. D. Embury, *Strengthening Methods in Crystals.*, eds. A. B. Kelly and R. B. Nicholson, Chapter 6, (1971), 341

[106] Y. Kimura and S. Takaki, *ISIJ Int.*, **37(3)**, (1997), 290

[107] H. Kimura, H. Matsui, S. Takaki, A. Kimura, K. Oguri, *Mechanical Properties of BCC Metals*, Proc. Conf. The Metallurgical Society of AIME, ed. M. Meshii, **37(3)**, (1981), 125

[108] K. R. Kinsman, E. Eichen, H. I. Aaronson, *Metall. Trans.*, **6**, (1975), 303

[109] E. P. Klier and T. Lyman, *Trans. AIMME*, **158**, (1944), 394

[110] K. Kitajima, Y.Aono, H. Abe, E. Kuramoto, *Strength of Metals and Alloys*, Proc. Conf., ed. P. Haasen, Pergamon Press, **2**, (1979), 965

[111] A. O. Kluken, T. A. Siewert, R. Smith, *Welding Research Supplement*, (1994), 193-s

[112] T. Ko and S. A. Cottrell, *J. Iron Steel Inst.*, **172**, (1951), 307

[113] U. F. Kocks, *Metall. Trans.*, **1**, (1970), 1121

[114] O. Kriesement and F. Wever, *Mechanism of Phase Trans. in Met.*, Institute of Metals, Monoraph and Report. Ser. No. 18, London, (1956), 253

[115] G. V. Kurdjumov, G. Sachs, *Z. Phys.*, **64**, (1930), 325

[116] W. Kurz, *Mathematical Modelling of Weld Phenomena 2*, eds. H. Cerjak and H. K. D. H. Bhadeshia, London, The Institute of Materials, (1995), 42

[117] G. Langford and M. Cohen, *Trans. ASM*, **62**, (1969), 623

[118] T. W. Lau, M. M. Sadowsky, T. H. North, G. C. Waetherly, *Welding Metallurgy of Structural Steels*, ed. J. Y. Koo, TMS–AIME, Warrendale, PA, (1987), 349

[119] T. W. Lau, M. M. Sadowsky, T. H. North, G. C. Waetherly, *Mater Sci Technol.*, **4**, (1988), 52

[120] E. Levine and D. C. Hill, *Metall. Trans.*, **8A**, (1977), 1453

[121] W. C. Leslie, *Metall. Trans.*, **3**, (1972), 5

[122] I. M. Lifshitz and V. V. Slyozov, *J. Phys. Chem. Solids*, **19(1/2)**, (1961), 35

[123] D. J. C. MacKay, *Neural Computation 4*, **3**, (1992), 415

[124] D. J. C. MacKay, *Neural Computation 4*, **3**, (1992), 448

[125] D. J. C. MacKay, *Neural Computation 4*, **5**, (1992), 698

[126] D. J. C. MacKay, *Darwin College Journal (Cambridge)*, March, 1993, 81

[127] D. J. C. MacKay, *University of Cambridge Programme for Industry — Modelling Phase Transformations in Steels*, March, (1995)

[128] S. J. Matas and R. F. Hehemann, *Trans. Met. Soc. AIME*, **221**, (1961), 179

[129] P. Maynier, J. Dollet, P. Bastien, *Hardenability Concepts with Applications to Steel*, eds. D. V. Doane, J. S. Kirkaldy, The Metallurgical Society of AIME, (1978), 163

[130] W. G. Moffatt, *The Handbook of Binary Phase Diagrams*, General Electric Company, (1986)

[131] T. Nakamura and S. Nagakura, *International Conference on Martensitic Transformations ICOMAT 86*, Japan Inst. Met., (1986), 386

[132] J. P. Naylor, *Metall. Trans.*, **10A**, July, (1979), 861

[133] K. Nishioka and H. Tamehiro, *Microalloying '88: Int. Symp. on Applications of HSLA Steel*, Chicago, IL (1988), 1

[134] L.-Å. Norström, *Scand. J. Metall.*, **5**, (1976), 159

[135] J. T. Norton, *Trans. AIME*, **116**, (1935), 386

[136] J. A. Oates, *Modern Arc Welding Practice*, George Newnes Ltd., (1961)

[137] H. Ohtani, H. Suda, K. Ishida, *ISIJ Int.*, **37(3)**, (1997), 207

[138] H. Ohtsuka, G. Ghosh, K. Nagai, *ISIJ Int.*, **37(3)**, (1997), 296

[139] P. T. Oldland, C. W. Ramsay, D. K. Matlock and D. L. Olson, *Welding Research Supplement*, April, (1989), 158

[140] R. A. Oriani, *Acta Met.*, **12**, (1964), 1399

[141] E. Orowan, *Dislocations in Metals*, AIME Publ. No. 128, (1954)

[142] H. O'Neill, *Hardness Measurement of Metals and Alloys*, 2nd Edition, Chapman and Hall, London, (1967), 45

[143] W. S. Owen, *Trans. ASM*, **46**, (1954), 812

[144] S. V. Parker, *Ph.D. Thesis*, Department of Materials Science, University of Cambridge, (1997)

[145] S. Pattanaik, D. Tromans, J.A. Lund, *Int. Conf. on Strength of Metals and Alloys, Tokyo (Supplement)*, **9**, (1968), 381

[146] F. B. Pickering, *Phase Transformations*, Inst. Metallurgists, London, (1979), series 3, **2k(11)**, VI 7

[147] D. A. Porter and K. E. Easterling, *Phase Transformations in Metals and Alloys*, 2nd Edition, Chapman and Hall, (1992)

[148] M. M. Rao and P. G. Winchell, *Trans. Met. Soc. AIME*, **239**, (1967), 956

[149] G. Rees, *Ph.D. Thesis*, Department of Materials Science, University of Cambridge, (1992)

[150] R. Reed and H. K. D. H. Bhadeshia, *Recent Trends in Welding Science and Technology*, (eds. S. A. David and J. Vitek), ASM International, OH, (1989), 205

[151] R. Reed, *Ph.D. Thesis*, Department of Materials Science, University of Cambridge, (1990)

[152] B. G. Reisdorf, *Trans. Met. Soc. AIME*, **227**, (1963), 1334

[153] K. C. Russell and L. M. Brown, *Acta Met.*, **20**, (1972), 969

[154] R. A. Ricks, *Ph.D. Thesis*, Department of Materials Science, University of Cambridge, (1979), Chapter 2

[155] B. P. J. Sandvik, *Metall. Trans.*, **13A**, (1982), 777

[156] B. P. J. Sandvik, *Metall. Trans.*, **13A**, (1982), 789

[157] W. F. Savage and A. H. Aaronson, *Weld J.*, **44**, (1965), 175

[158] Y. Sawaragi, A. Iseda, S. Yamamoto, F. Masuyama, *The Sumitomo Search (Technical Report)*, **59**, Sumitomo Metal Industries Ltd., Japan, September, (1997), 113

[159] R. Siems, P. Delavignette, S. Amelinckx, *Phys. Stat. Sol.*, **2**, (1962), 636

[160] F. T. Sisco, *Nickel in Iron and Steel*, 1st Edition, The Engineering Foundation, (1954), 194

[161] R. Smith and J. Nutting, *Brit. J. Appl. Phys.*, **7**, (1956), 214

[162] R. Smith and J. Nutting, *J. Iron Steel Inst.*, **187**, (1957), 314

[163] G. R. Speich and R. A. Oriani, *Trans. AIME*, **233**, (1965), 623

[164] G. R. Speich, J. A. Gula, R. M. Fisher, *The Electron Microprobe*, John Wiley, (1966), 525

[165] G. R. Speich and H. Warlimont, *J. Iron Steel Inst.*, **206**, (1968), 385

[166] W. Steven and A. G. Haynes, *J. Iron Steel Inst.*, **183**, (1956), 349

[167] A. A. B. Sugden and H. K. D. H. Bhadeshia, *Metall. Trans. A*, **19A**, (1988), 1597

[168] A. A. B. Sugden and H. K. D. H. Bhadeshia, *Metall. Trans. A*, **20A**, (1989), 1811

[169] T. Suzuki, *Proc. 2nd. Int. Conf. Strength of Metals and Alloys*, **1**, ASM, Cleveland, Ohio, (1970), 237

[170] M. Strangwood, *Ph.D. Thesis*, Department of Materials Science, University of Cambridge, (1992)

[171] M. Strangwood and H. K. D. H. Bhadeshia, *Advances in Welding Technology and Science*, ASM, Metals Park, Ohio, U.S.A., (1987), 209

[172] L.-E. Svensson, *Private communication*, March 28th, (1996)

[173] L.-E. Svensson, *Control of Microstructures and Properties in Steel Arc Welds*, CRC Press, (1988)

[174] L.-E. Svensson, H. K. D. H. Bhadeshia, *Weld Quality: The Role of Computers*, Proc. Int. Conf. Improved Weldment Control, Vienna, International Institute of Welding, July, (1988), 71

[175] L.-E. Svensson, B. Gretoft, H. K. D. H. Bhadeshia, *Scand. J. Metallurgy*, **15**, (1986), 97

[176] M. Takahashi and H. K. D. H. Bhadeshia, *Mater. Sci. Technol.*, **6**, (1990), 592

[177] S. Takeuchi, *J. Phys. Soc. Japan*, **27**, (1969), 167

[178] S. Takeuchi, H. Yoshida, T. Taoka, *Trans. Japan Inst. Metals Supplement*, Proc. Conf., **9**, (1968), 715

[179] G. I. Taylor, *J. Inst. Met.*, **63**, (1938), 307

[180] K. A. Taylor, G. B. Olson, M. Cohen, J. B. Vander Sande, *Metall. Trans. A*, **20A**, (1989), 2749

[181] K. A. Taylor, L. Chang, G. B. Olson, G. D. W. Smith, M. Cohen, J. B. Vander Sande, *Metall. Trans. A*, **20A**, (1989), 2772

[182] G. Thewlis, J. A. Whiteman, D. K. Senogles, *Mater. Sci. Technol.*, **13**, (1997), 257

[183] S. W. Thompson and G. Krauss, *Metall. Trans.*, **27A**, (1996), 1573

[184] S. W. Thompson, D. J. Colvin, G. Krauss, *Scripta Metall.*, **22**, (1988), 1069

[185] Y. Tomita, T. Haze, N. Saito, T. Suzuki, Y. Tokunaga, K. Okamoto, *ISIJ Int.*, **34(10)**, (1994), 836

[186] Y. Tomita and K. Okabayashi, *Metall. Trans.*, **14A**, (1983), 485

[187] Y. Tomita and K. Okabayashi, *Metall. Trans.*, **14A**, (1983), 2387

[188] Y. Tomita and K. Okabayashi, *Metall. Trans.*, **16A**, (1985), 73

[189] Y. Tomita and K. Okabayashi, *Metall. Trans.*, **16A**, (1985), 83

[190] Y. Tomita, *Metall. Trans.*, **18A**, (1987), 1496

[191] Y. Tomita, *Metall. Trans.*, **18A**, (1987), 2513

[192] J. H. Tweed and J. F. Knott, *Acta Metall.*, **35**, (1987), 1401

[193] G. F. Vander Voort, *Metallography Principles and Practice*, McGraw-Hill, (1984), 350

[194] C. Wagner, *Z. Electrochem.*, **65**, (1961), 581

[195] J. D. Watson and P. G. McDougall, *Acta Metall.*, **21**, (1973), 961

[196] P. G. Winchell and M. Cohen, *Trans. ASM*, **55**, (1962), 347

[197] H. C. Yakel, *Int. Met. Rev.*, **30**, (1985), 17

[198] J. R. Yang and H. K. D. H. Bhadeshia, *Advances in Welding Technology and Science*, ASM, Metals Park, Ohio, U.S.A., (1987), 187

[199] J. R. Yang and H. K. D. H. Bhadeshia, *Proc. Int. Conf. Welding Metallurgy of Structural Steels*, TMS–AIME, Warrendale, PA, U.S.A., (1987), 549

[200] J. R. Yang, *Ph.D. Thesis*, Department of Materials Science, University of Cambridge, (1987)

[201] A. Youle and B. Ralph, *Met. Sci.*, **6**, (1972), 149

[202] C. H. Young and H. K. D. H. Bhadeshia, *Mater. Sci. Technol.*, **10**, (March 1994), 209

[203] C. Zener, *J. Applied Phys.*, **20**, (1949), 950